SHEAR-WAVE IMAGING AND BIREFRINGENCE IN A COMPLEX NEAR-SURFACE GEOLOGICAL ENVIRONMENT

DISSERTATION

A dissertation submitted in partial fulfillment of the
requirements for the degree of Doctor of Philosophy in the
College of Arts and Sciences at the University of Kentucky

By
Ali Z. Almayahi

Lexington, Kentucky

Director: Dr. Edward W. Woolery, Associate Professor of Geophysics

Lexington, Kentucky

2013

ABSTRACT OF DISSERTATION

SEAR-WAVE IMAGING AND BIREFRINGENCE IN A COMPLEX NEAR-SURFACE GEOLOGICAL ENVIRONMENT

Multiple geophysical and geological data sets were compiled, reprocessed, and interpreted using state-of-the-art signal processing and modeling algorithms to characterize the complex post-Paleozoic geology that overlies the southwestern projection of the Fluorspar Area Fault Complex (FAFC) in western Kentucky. Specific data included 21.5 km of SH-wave seismic reflection, 1.5 km of P-wave seismic reflection, 2 km of electrical resistivity, vertical seismic profiles, Vp and Vs sonic-suspension logs, and 930 lithologic borehole logs. The resultant model indicates three general northeast–southwest-oriented fault zones pass through the study area as southwestern extensions of parts of the FAFC. These fault zones form two significant subparallel grabens with ancillary substructures. The geometry of the interpreted fault zones indicates that they have undergone episodic tectonic deformation since their first formation. Evidence of thickening and steeply dipping reflectors within Tertiary and Quaternary sediment in the downthrown blocks indicate syndepositional movement. Subtle thickening and lack of steeply dipping intraformational reflectors in the Cretaceous suggest a more quiescent period, with sediment deposition unconformably draping and filling the earlier Paleozoic structural surface. There is also evidence that the Tertiary and early Quaternary reactivation was associated with an extensional to compressional regional stress reversal, as manifested by the antiformal folds seen in the hanging wall reflectors and the potential small-amplitude force folds in the Quaternary alluvium, as well as a clear displacement inversion along the Metropolis-loess seismic horizon in two high-resolution reflection images.

A surface shear-wave splitting experiment proved to be an efficient and effective tool for characterizing shallow subsurface azimuthally anisotropic geologic inclusions in low-impedance water-saturated sediment environments. The measured azimuthal anisotropy across a well-constrained N60ºE-striking fault exhibited a natural coordinate system that had a fast direction coincident with the fault strike and an orthogonal slow direction. This is also one indicator that faults inactive during significant geologic intervals (i.e., Holocene) do not "heal". Integrated shear-wave velocity models and electrical resistivity tomography profiles across the fault zones exhibit lower shear-wave velocities and resistivities within the deformation zones compared with values outside the boundaries. This is additional evidence that the deformed sediment does not reconsolidate or heal, but that the sediment particle configuration remains more loosely packed, providing an increase in the overall porosity (i.e., hydraulic conductivity). This can wholly or in large part explain the anomalous contaminant plume migration path that is coincident with the deformed zones of the regional gravel groundwater aquifer.

SHEAR-WAVE IMAGING AND BIREFRINGENCE IN A COMPLEX NEAR-SURFACE GEOLOGICAL ENVIRONMENT

By
Ali Z. Almayahi

Dr. Edward W. Woolery

Director of the Dissertation

Dr. Alan Fryar

Director of Graduate Studies

Date

ACKNOWLEDGEMENT

The author would gratefully thank the Iraqi ministry of higher education and scientific research for granting a fully funded scholarship to study abroad. Special thanks go to the Department of Energy and the Kentucky Consortium for Energy and Environment for funding the research component of the dissertation. The author wish to particularly thank the committee members, Dr. Woolery, Dr. Ravat, Dr. Wang, Dr. Kalinski, and Dr. Sottile for their review and input. More thanks go to Mr. Steve Hampson for DOE database access. Also, I wish to thank my family for their time and patience.

TABLE OF CONTENTS

LIST OF TABLES

LIST OF FIGURES

CHAPTER ONE

1 INTRODUCTION

1.1 Problem Statement

1.1.1 General

Seismic imaging and characterization of subtle, yet complex, geologic features in low-velocity near-surface (often saturated) unlithified sediments can be problematic because of limitations with the traditional industry-oriented approach to data acquisition and processing, as well as fundamental resolution limitations. The Fluorspar Area Fault Complex (FAFC) in the sediment-filled northern Mississippi Embayment of western Kentucky provides an excellent field laboratory in which to evaluate near-surface seismic methods and procedures in a complex geologic setting (i.e., situated at the junction of two ancient rifts that have reactivated structures exhibiting deformation that extend into Quaternary sediments). In addition, a large and unique geological and geophysical database associated with the U.S. Department of Energy's Paducah Gaseous Diffusion Plant is available to constrain modeled data and interpretations.

1.1.2 Specific Problems

The Paleozoic and post-Paleozoic geologic conditions south of the Ohio River in the Jackson Purchase Region of western Kentucky are generally not well constrained because of the lack of subsurface exposure that is the result of the masking effect associated with the sediment fill of the northern Mississippi Embayment. The inherently weak soft-sediment cover and relatively long recurrence interval between large earthquakes, apart from a few exceptions (e.g., Reelfoot Scarp, Benton Hills, and Crowleys Ridge), fail to produce significant or noticeable tectonic-related surface manifestations. Consequently, geophysical imaging surveys, seismic reflection in particular, are generally required to characterize the subsurface geology in these environments; however, accurate identification and characterization of stratigraphy, as well as structure, using traditional P-wave seismic imaging can also be limited by the physical resolving power (i.e., inherent wavelength), and by masking of the low-velocity sediment by water saturation. In addition, subtle lateral and vertical features associated with or caused by faults can be

difficult to image and characterize by conventional seismic reflection and refraction methods in low-impedance sediment/soil environments; however, these features impart a mechanical azimuthal anisotropy that can be detected and measured by the birefringence properties of the shear wave. Moreover, as a shorter-wavelength framework wave, the shear wave is insensitive to water and propagates strictly in the solid matrix, thus providing a higher-resolution measure of the lithologic material.

1.2 Specific Project Objectives and Significance

1.2.1 Objectives:

- Construct seismic data-processing flowcharts that offer better-resolution images of stratigraphic and/or structural changes within the limits of the overall seismic resolution in water-saturated, unlithified, low-velocity media.

- Adapt, evaluate, and apply conventional industry-scale shear-wave birefringence surface methods to azimuthally anisotropic geologic features (i.e., faults, etc.) in near-surface sediments that typically have subtle manifestations in the low-impedance-contrast material, which are thus difficult to detect by conventional seismic-reflection/refraction techniques.

- Process and integrate ~27.5 km of P- and SH-wave seismic CMP reflection profiles, ~930 shallow bore logs, and 2 km of electrical-resistivity profiles to construct a subsurface model of the complex post-Paleozoic geology in the Fluorspar Area Fault Complex of western McCracken County, Kentucky.

1.2.2 Significance and Broader Impact:

Results from this work provide an improved fundamental understanding of the post-Paleozoic geologic (i.e., structural and stratigraphic) conditions in the FAFC. The higher-resolution characterization of reactivated faults also provides the practical benefit of lessening the spatial and temporal uncertainties associated with regional seismic hazard evaluations. In addition, the near-surface structure and stratigraphy can, to some extent, to control a preferential flow path for a local contaminant plume. These methods can be used in similar environments to better evaluate subsurface conditions. More important,

using these higher-resolution seismic methods for better characterization of geohazard conditions improves mitigation strategies and allows valuable and often scarce resources to be more effectively allocated and applied.

1.3 General Study Location

The Fluorspar Area Fault Complex is a group of fault systems (Kolata and Nelson, 1991; Nelson et al., 1997) at the juncture of two late Precambrian–Early Paleozoic rifts: the Reelfoot Rift and the Rough Creek Graben (Fig. 1.1). The Rough Creek Graben, which lies mostly in western Kentucky, is bounded on the north by the Rough Creek–Shawnee Fault System and on the south by a series of faults that includes the Pennyrile Fault System. The Rough Creek–Shawnee Fault System extends from Kentucky into southern Illinois for approximately 25 km, then turns abruptly to the southwest and joins the Lusk Creek and Raum Fault Zones, which form the northwestern boundary of the FAFC (Nelson and Lumm, 1987). The surface manifestation of the FAFC continues to the southwest toward western Kentucky, but disappears beneath the embayment sediment near the Ohio River (Kolata and Nelson, 1991; Nelson et al., 1999; McBride and Nelson., 2001). South of the Ohio River is the Jackson Purchase Region of western Kentucky. The study area is located about 15.5 km west of Paducah, the largest city in the Jackson Purchase, and approximately 4 km south of the river. The study area includes the Paducah Gaseous Diffusion Plant (PGDP), a property of the U.S. Department of Energy (Fig. 1.2).

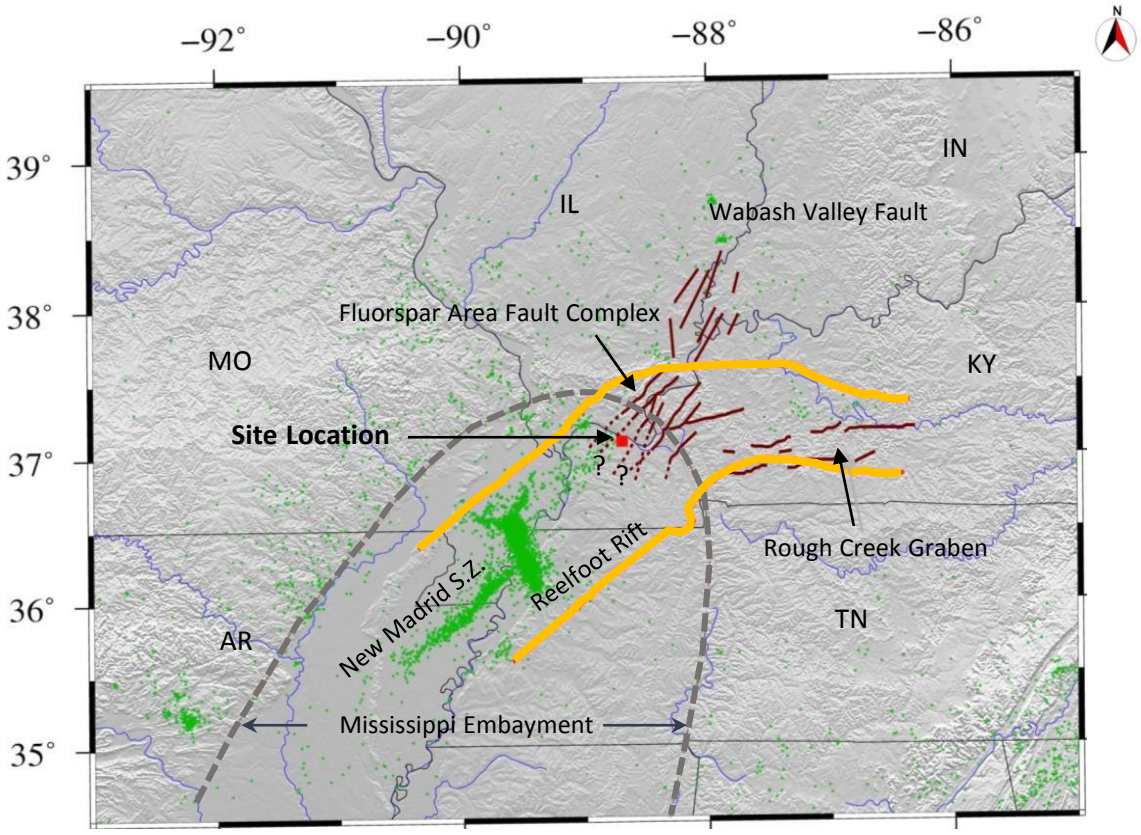

Figure 1.1: Major structural elements in the central United States. The site location in shown in relation to the major structural features in the central Mississippi Valley. The projected locations of the Fluorspar Area Fault Complex, Rough Creek Graben, and Reelfoot Rift are after Kolata and Nelson (1997).

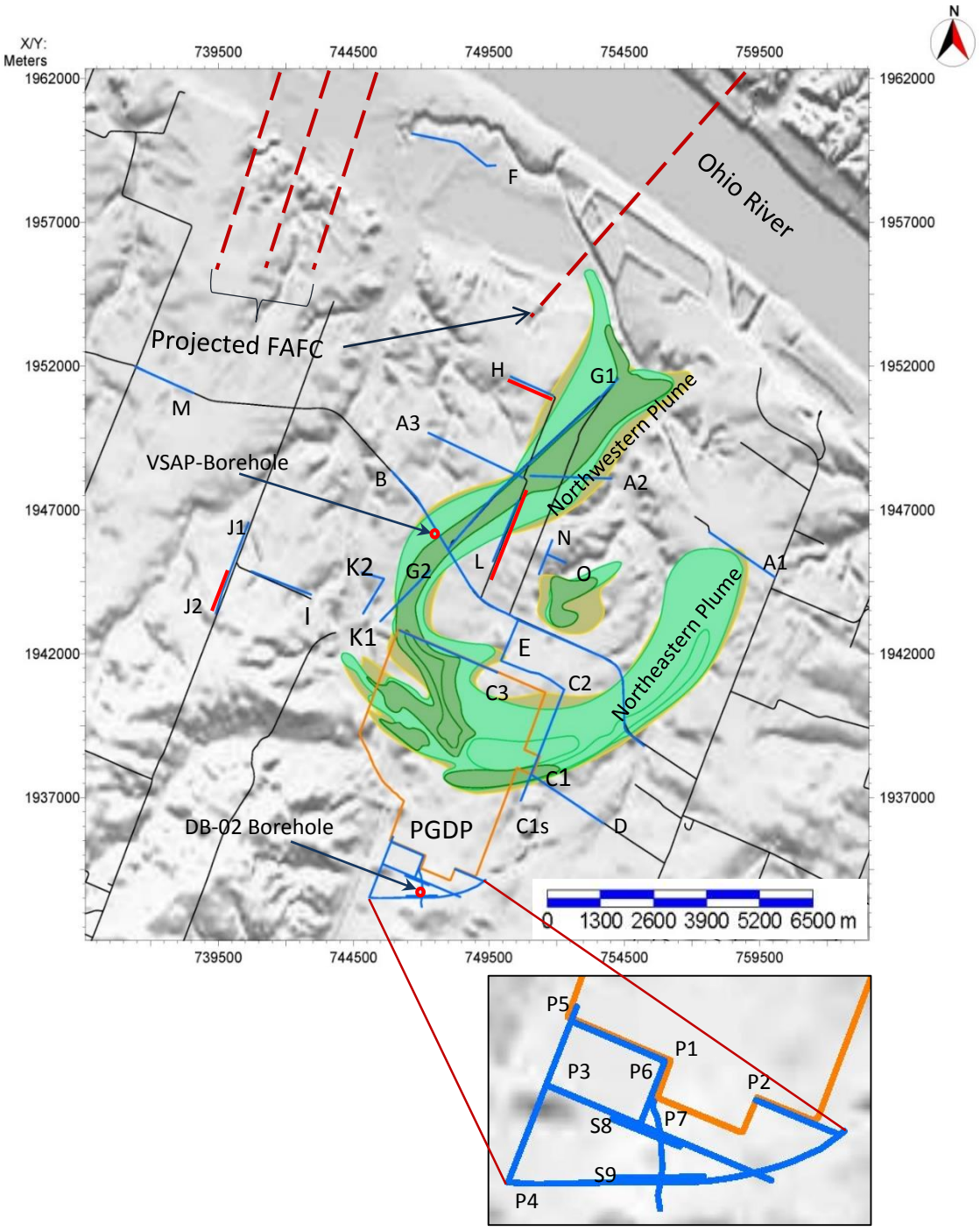

Figure 1.2: Topographic map of the study area shows the locations of seismic profiles (light blue lines), electrical resistivity profiles (red lines), the contamination plume, and the projected faults of the Fluorspar Area Fault Complex.

1.4 Geologic and Seismotectonic Setting

Western Kentucky and southernmost Illinois have undergone recurrent tectonic activity during the geologic past. Specifically, multiple phase reversals of stress fields have occurred since the Late Mississippian (Chesterian), when the supercontinent Pangaea was assembled, resulting in an intricate and complex structural framework for the region. Structures are associated with both compressional (e.g., reverse and transpressional strike-slip faulting, folding, etc.) and extensional (e.g., normal faults and wide rifting) stress regimes. The most prominent relic structures and features in western Kentucky and southernmost Illinois are the FAFC, Reelfoot Rift, Rough Creek Graben, and Mississippi Embayment. The FAFC lies at the junction of the Reelfoot Rift and the Rough Creek Graben, and forms an approximately 40-km-wide assemblage of steeply dipping, northeast-striking fault systems (Fig. 1.1) (Kolata and Nelson, 1991). Most of the complex is covered by the northern part of the Mississippi Embayment, which was described physiographically by Mooney et al. (1983) as a broad, elongate, southwest-plunging reentrant of the Coastal Plain Province that extends northward into the North American Craton to approximately the confluence of the present-day Ohio and Mississippi Rivers. The major fault systems included with the FAFC are the Lusk Creek, Raum, Hobbs Creek, and Barnes Creek Fault Zones (Fig. 1.3) (Nelson et al, 1999; McBride et al., 2002). The mapped outcrops of the FAFC faults primarily reside in the fluorspar-mining area of southeastern Illinois; however, Hildebrand et al. (1983), Kolata and Nelson (1991), and Nelson et al (1999), among others, have suggested that the FAFC continues to the southwest beneath the embayment fill into the Jackson Purchase Region of western Kentucky. Langston et al. (1998) and Woolery and Street (2002) used high-resolution seismic images to show that the fault complex does continue into the Jackson Purchase of western Kentucky, with reactivated displacement extending into Quaternary sediments. The primary northeast-southwest orientation of the FAFC suggests that is an accommodation zone in the transition between the Reelfoot Rift and the Rough Creek Graben that likely formed during the late Precambrian–Early Paleozoic (Braile et al., 1982; Kolata and Nelson, 1991; Kolata and Hildebrand, 1997). The FAFC's northwestern boundary, the Lusk Creek Fault System, projects southwest beneath the embayment sediment and appears to form the northwestern margin of the Reelfoot Rift, the host

geologic structure for the New Madrid Seismic Zone (Fig. 1.1). The Reelfoot Rift extends from east-central Arkansas through southwestern Missouri toward southernmost Illinois (Braile et al., 1986; Kolata and Nelson, 1997), approximately 300 km long (Kane et al., 1981); it is 70 km wide (Kane et al., 1981) and approximately 4 to 8 km deep (Nelson and Zhang, 1991). The rift is also coincident with a Mesozoic-Tertiary Mississippi Embayment (Burke and Dewey, 1973), and is defined as several half grabens tied together by transfer zones (Kolata and Nelson, 1997). The southern end of the rift was deformed and truncated by the Ouachita Orogeny (Kolata and Nelson, 1997), and the northern edge of the Reelfoot Rift is transitioned to the Rough Creek Graben by the FAFC (Kolata and Nelson, 1997). The eastern extent of the Rough Creek Graben is not well resolved (Thomas, 2011), but Hickman (2011) and Harris (1975) agreed that it is connected with the Rome Trough across the Cincinnati Arch in central Kentucky. The east–west-oriented Rough Creek Graben is filled with Cambrian sediments and is approximately 161 km long. It is 1.7 to 8.0 km wide and thicker than 2.5 km (Thomas, 2011). Although the Reelfoot Rift and Rough Greek Graben are connected and/or adjacent, the Rough Creek Graben is relatively aseismic compared with the Reelfoot Rift and its associated significant earthquake activity of the New Madrid Seismic Zone (Wheeler, 1997). In addition to the similar northeast-southwest orientations of the Reelfoot Rift and the FAFC, the FAFC structures are also coincident with a northeast-oriented band of diffuse microseismicity, interpreted by Wheeler (1997) as a potential projection of New Madrid seismicity (Fig. 1.1). This northeast-projected weak microseismicity pattern suggests that the poorly defined FAFC may have similar architecture and behavior as the faults in the New Madrid Seismic Zone do (i.e., oblique dextral strike-slip faults that have extension and compression deformation components). Consequently, Wheeler (1997) inferred that the Holocene deposits in the FAFC could exhibit tectonic deformation. Nelson et al. (1999) and McBride et al. (2002) found evidence of Pliocene to Early Pleistocene displacement along the Lusk Creek Fault Zone in southern Illinois, but saw no Holocene sediment displacement. They also observed undisturbed Holocene sediments in the neighboring Raum Fault. Specifically, it is the FAFC's Raum and Lusk Creek Faults Systems that lie beneath the subject study area. McBride et al. (2002) further described the Raum Fault Zone in southern Illinois as a 50-

km-long by 1.6-km-wide zone of north- to northeast-trending, steeply dipping faults bounding horst and graben structures. They found that the faults extended upsection of the Paleozoic bedrock into the Late Quaternary sediment. Their mapped outcrop contacts between Pleistocene and Holocene horizons showed no evidence of deformation. Likewise, McBride et al. (2002) characterized the Lusk Creek Fault Zone by subparallel high-angle normal and reverse faults with vertical displacements of up to 70 m in the deeper sediment (Cretaceous) and up to 5 m in the shallower horizons (Pleistocene). The Hobbs Creek and Barnes Creek Fault Systems have similar characteristics, but their projections are not thought to affect the data sets for the subject study.

1.5 Stratigraphy

The Paleozoic bedrock (Mississippian carbonates) in the study area is unconformably overlain by Late Cretaceous and younger unlithified sediments that are restricted to the Jackson Purchase and form the northeastern part of the Mississippi Embayment (Olive and McDowell, 1986). The Cretaceous and younger sediments thicken westward from the Jackson Purchase Region toward the axis of the Mississippi Embayment, which is approximately coincident with the current course of the Mississippi River (Olive and McDowell, 1986). The general lithology of these sediments consists of unlithified marine and continental gravels, sands, silts, and clays caped with alluvium, loess, and latest Tertiary and Quaternary Continental deposits (Olive and McDowell, 1986). The Late Cretaceous Tuscaloosa Formation (Kt), a narrow belt of light-gray gravels with scattered lenses of sand, silt, and clay, appears east of the Jackson Purchase. This formation is not present at the study site according to the geologic map of Olive and McDowell (1986). Harrison and Litwin (1997) showed that the Tuscaloosa Formation is much older than Late Cretaceous (middle to late Campanian age and perhaps late Cenomanian or older). Hence, they named it the Post Creek Formation as a substitute for the Tuscaloosa Formation. SAIC Engineering Inc. (2004) stated that a rubble zone, possibly the Post Creek Formation, immediately overlies bedrock at the PGDP. It is 0 to 6 m thick and

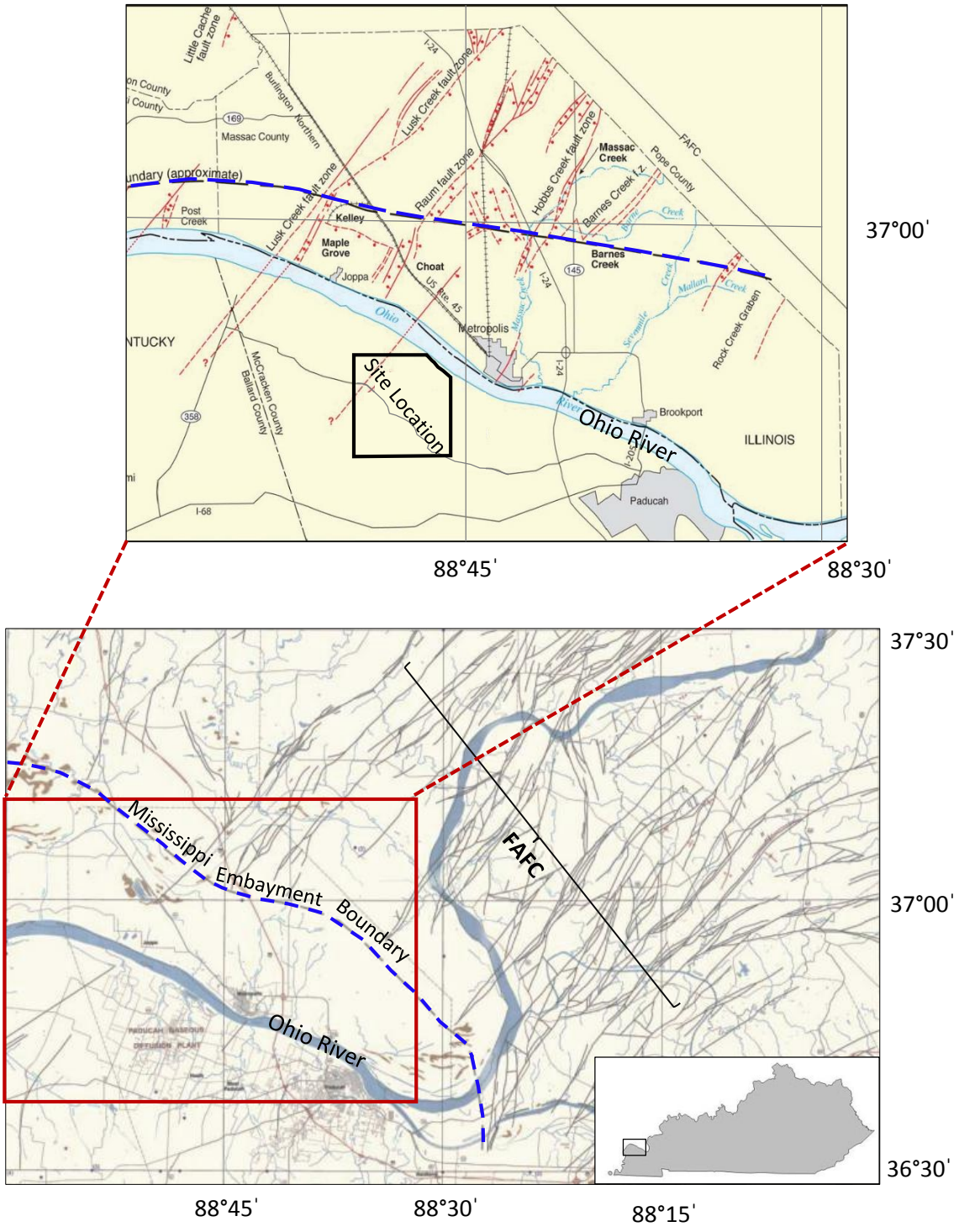

Figure 1.3: Regional structural features of the Paducah and Murray 30×60 minute quadrangles, after Drahovzal and Hendricks (1996). In the insert which is after McBride et al. (2002) and Woolery and Street (2002), the northeast-southwest projection of FAFC normal fault is directly oriented toward the study site.

consists of subangular chert and silicified limestone fragments. The rubble zone has not been determined to exist approximately 200 m south of the PGDP.

In general, the late Paleozoic bedrock at the site is unconformably overlain by the Upper Cretaceous (Maastrichtian) McNairy Formation (Nelson et al. 1999), which is overlain by the Paleocene Clayton Formation. Because of the difficulty in distinguishing between the McNairy and Clayton Formations in most places in the field, it is a common practice to classify them as one geologic unit (Olive and McDowell, 1986). The McNairy-Clayton Formation consists mainly of light- to dark-gray, fine to medium sand, but sometimes weathers to yellow or reddish brown (Olive, 1980; Olive and McDowell, 1986). The Porters Creek Clay (Tp) is a Paleocene micaceous clay that overlies the McNairy-Clayton Formation. Sexton (2006) showed that the Porters Creek Clay has been removed across much of the study site by the ancestral Tennessee River. Tertiary deposits overlie the Porters Creek immediately south of the PGDP, but they unconformably overlie McNairy-Clayton Formation beneath the PGDP and north to the Ohio River (Fig. 1.4). These sediments are Early Eocene age and called the Wilcox Formation. The Wilcox Formation is composed of interbedded light-gray and brown sand, clay, and silt (Olive and McDowell, 1986). The thickness varies depending upon which surface it was deposited on, as well as erosion of its own surface (Olive and McDowell, 1986).

The Wilcox Formation is overlain by the Claiborne and Jackson Formations. The Claiborne and Jackson Formations are undifferentiated and combined into a single geologic unit. They are Middle and Upper Eocene, respectively. Boring information at the study site has not identified the Wilcox, Claiborne, and Jackson Formations (Woolery and Street, 2002; SAIC Engineering Inc., 2004) (Fig. 1.4). This suggests that Miocene(?), Pliocene, and Pleistocene Continental deposits unconformably overlie the McNairy-Clayton Formation in most of the subject site. The Miocene-Pliocene-Pleistocene Continental deposits include a sedimentary sequence in the Jackson Purchase and northern Mississippi Embayment, referred to as a single unit, called the Lafayette Formation or Lafayette Gravel (Olive, 1980). At the study site, SAIC Engineering Inc. (2004) divided the Continental deposits into two parts: lower and upper Continental deposits. Based on their lithology and age, Nelson et al. (1999) and Woolery et al. (2009)

called the Continental deposits the Mounds Gravel and Metropolis Formation. The reddish-orange to brown chert of the Mounds Gravel is overlain by Pleistocene silt and sand with lesser amounts of clay and gravel (fluvial terrace) of the Metropolis Formation (Olive, 1980; Nelson et al., 1999). The Continental deposits are capped by three layers of Late Quaternary deposits, Pleistocene loess, and Pleistocene and Holocene alluvium (Olive, 1980). Previous seismic studies (Woolery and Street, 2002; Woolery et al., 2009) showed that the stratigraphic tops of the bedrock, McNairy-Clayton Formations, and lower Continental deposits (i.e., Mounds Gravel) are high-acoustic-impedance boundaries that define the primary seismic-stratigraphy marker horizons (Fig.1.5).

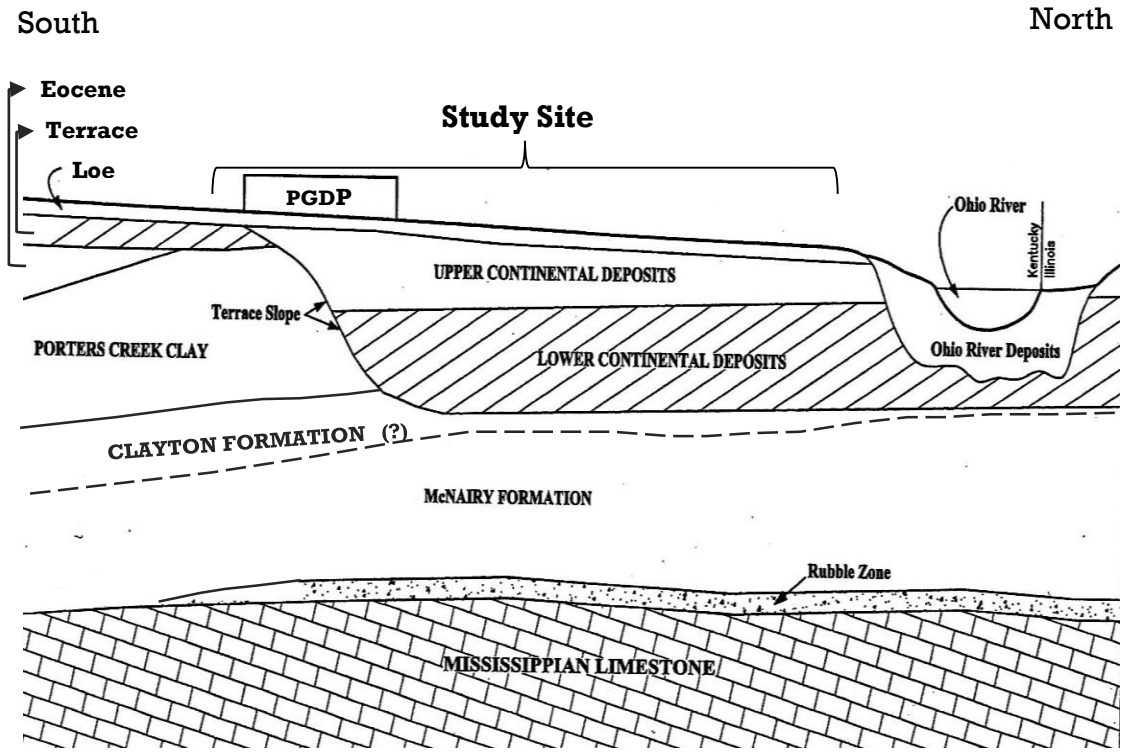

Figure 1.4: Schematic geologic cross section of the study site and adjacent areas. Modified from SAIC Engineering Inc. (2004) and Clausen et al. (1992). The Porters Creek Clay exits in the southern part and fades out underneath the PGDP. The dashed line between Clayton and McNairy refers to uncertain boundary separating them. In most of study site, Continental deposits unconformably underlain by McNairy Formation.

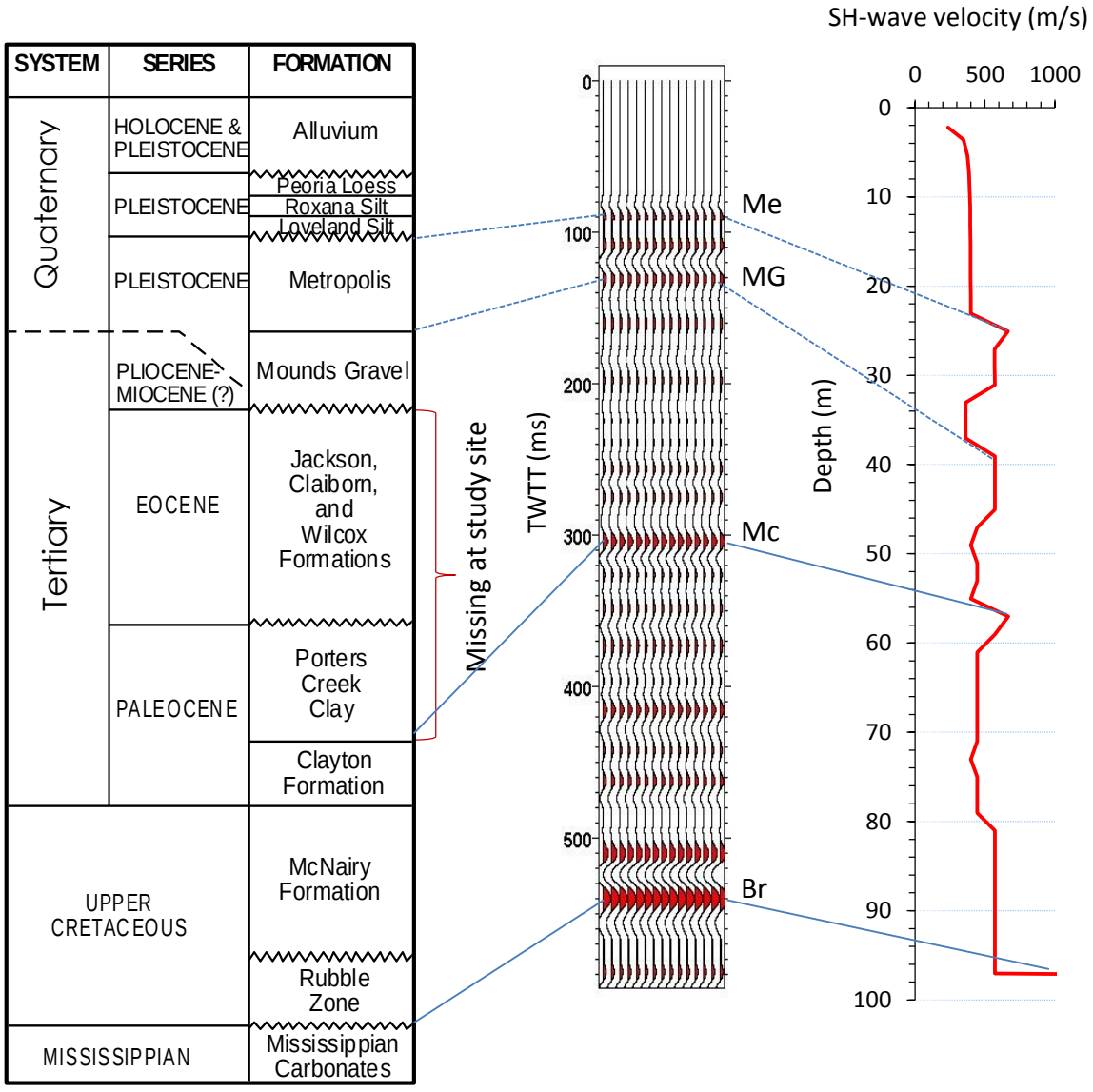

Figure 1.5: Site stratigraphy and velocity profile are correlated to corridor stack VSP data from a borehole in profile B. Metropolis top (Me), Mounds Gravel top (MG), McNairy-Clayton top (Mc), and bedrock top (Br) are the interpreted acoustic impedance boundaries.

1.6 PGDP Background and Environmental Conditions

The U.S. Atomic Energy Commission constructed the Paducah Gaseous Diffusion Plant between 1951 and 1955 (Clausen et al., 1992). It is located about 15.5 km west of Paducah, the largest city in the Jackson Purchase, and approximately 4 km south of the Ohio River. In 1952, the plant first produced enriched uranium through the gaseous diffusion of uranium hexafluoride (Garner et al., 1995). Currently, it is operated by United States Enrichment Corporation and owned by the U.S. Department of Energy. In August of 1988, contaminated materials were discovered approximately 1.6 km north of the plant in several privately owned offsite wells (Clausen et al., 1992). Three months later, the Department of Energy recognized the PGDP as the source of contamination and entered into an Administrative Consent Order with the U.S. Environmental Protection Agency (EPA). The main components of the contamination materials are trichloroethylene (TCE) and technetium-99 (Tc-99). TCE, a common chlorinated solvent, was primarily used at PGDP as a cleaning agent in degreasing facilities (Clausen et al., 1992). Over extended periods of time, it has been mixed with groundwater that is a water resource for humans. Drinking water containing concentrations of TCE over the maximum contaminant level of 5 parts per billion can cause damage to the liver, kidneys, immune and endocrine systems, and contribute to an increased cancer risk (EPA, 2000). Tc-99, a fission byproduct, is believed to have been introduced through the reprocessing of nuclear reactor tails (Clausen et al., 1992). It is assigned a maximum contaminant level of 4 millirems per year, the general level associated with manmade radionuclides (EPA, 2007). The ingestion of drinking water with levels of Tc-99 exceeding this concentration can lead to an increased risk of cancer and other adverse radiation-related health effects (EPA, 2007). Thus, intensive and comprehensive site investigations were conducted in order to localize the source and to estimate the extent of groundwater contamination. These studies, both on and off site, were prepared for PGDP, which was designated a superfund site in 1994, and made a priority effort for remediation (Jacobs, 1997). The results of the investigations delineated the spatial extent of the contamination, a TCE plume extending approximately 4 km to the northeast and a plume containing both TCE and Tc-99 extending almost 5 km northwest (Clausen et al., 1992) (Fig. 1.2). The migration rate and direction of these plumes within the regional shallow gravel aquifer is

of particular significance because of the proximity of the northeastern plume to multiple residences along Metropolis Lake Road (McCracken County, Kentucky) and the proximity of the northwestern plume to Little Bayou Creek and the Ohio River (Clausen et al., 1992).

Various remediation strategies were considered to reduce the expected adverse health effects of TCE and Tc-99 coupled with the increasing probability of human contact, predominantly through the consumption of contaminated drinking water. As precautions, a potable water supply was added to the impacted areas, public access to areas of known surface contamination (including parts of Little Bayou Creek) was restricted, silt fences were constructed around above-ground disposal areas, and certain identified waste area groupings (WAG's) were remediated. Remediation must continue within the area through the use of established techniques as well as developing technologies.

1.7 Previous Related Studies

The central United States has been studied to understand its structural complexity and tectonic activity. Seismic imaging has been the principal technique to decipher most subsurface conditions. In this context, Sexton and Jones (1986) investigated and better characterized the structural geology of the Reelfoot Scarp in northwestern Tennessee using denser-arrayed, higher-resolution P-wave reflection profiles. Odum et al. (1998) integrated geomorphic data and high-resolution seismic-reflection P-wave data to develop a tectonic model of the near surface in the New Madrid, Mo., area. Using high-resolution seismic-reflection P-wave data, Stephenson et al. (1999) concluded that the history of Cretaceous faulting associated with the Commerce Lineament in southeastern Missouri extends into the Quaternary. Palmer et al. (1997) did shallow high-resolution seismic-reflection P-wave surveys in the southern escarpment of the Benton Hills segment of Crowleys Ridge to image Cretaceous faults and folds. In most of the near-surface seismic P-wave reflection investigations, the seismic data processing and interpretation have been limited by low-velocity sediments and a water-saturated environment. This kind of environment has been shown to be better imaged by SH-wave

mode reflection (Omens, 1978; Helbig, 1986; Woolery et al., 1993; Harris, 1996; Deidda and Balia, 2001; Woolery, 2002; Woolery and Street, 2002; Woolery et al., 2009). SH-waves have provided more accurate geologic imaging in near-surface unlithified sediments (< 100 m). Technically, SH-waves resolve near-surface problems better than P-waves because SH-waves are a function of rigidity and P-waves a function of compressibility, so that the SH-wave travels with the lithologic matrix and not fluid/water. Also, the lower-velocity SH-wave propagation shifts the optimal collecting window to the near offset behind the coherent noise (i.e., refraction, etc.) and expands the temporal window, which better separates the individual signals. SH-wave resolution is generally higher than P-wave by factor of 2 to 3 in an unlithified sediment environment because S-waves often have 0.5 to 0.6 percent of the P-wave velocity and 0.33 to 0.5 percent of the P-wave frequency content (Woolery and Street, 2002). SH-wave propagation in a stratified media is easier than for P- and SV-waves because there is no mode conversion (Helbig, 1986).

Integrating P- and SH-wave seismic-reflection surveys is generally optimal for characterizing the subsurface geology. The more field-efficient P-wave surveys are used for reconnaissance and target location, with the more labor-intensive SH-wave survey applied to shorter profiles over the discrete targets. This becomes more important when there is no surface expression of the deeper Paleozoic and Cretaceous to Late Tertiary and Quaternary structure (McBride and Nelson, 2001; Bexfield et al., 2006).

In the northern part of the study site, Blits (2008) used five SH-wave seismic-reflection profiles totaling 8 km in length and 2 km of electrical-resistivity profiles to characterize the post-Paleozoic geology that related to the PGDP's northwest contaminant plume. She found a correlation between the results of the two methods in terms of fault location and degree of near-surface offset. She interpreted multiple high-angle normal faults striking between N40°E and N45°E that outline a number of asymmetric grabens. She used this framework to hypothesize that a preferable flow path for contaminant migration possibly had been formed by faults in the regional gravel aquifer, but this was considered speculative and equivocal because an integrated model comparing all of the structure data spatially with the contaminant plume was incomplete. Also, in the northern part of the

study area, Bechtel Jacobs Co. LLC (2003) obtained two SH-wave seismic-reflection lines (369 m east-west and 518 m north-south) at the C-746-U landfill site. They were able to identify the top of the regional gravel aquifer, but the tops of the deeper McNairy Formation and Paleozoic bedrock were abnormally discontinuous, incoherent, and frequently absent. Potential faults were determined, depending on disrupted reflectors associated with structural features. Although all the field configurations, equipment, and acquisition parameters were identical to those of the previously acquired high-quality data about 8 km away, no pre-survey array testing was performed and is likely the reason for the poor data quality. Using seismic-reflection profiling, Woolery et al. (2009) studied the Late Quaternary sediments in the eastern part of the study area. They defined five deformation zones of high-angle faults. These faults extended to within approximately 7 m of the ground surface. Their results are supported by coincident core sampling, detailed logging, stratigraphic correlations, and numerical age determinations.

In the southern part of the study area (i.e., PGDP potential waste site 3A), SAIC Engineering Inc. (2004) conducted a comparative seismic-reflection study for the Department of Energy using P- and SH-wave high-resolution seismic-reflection surveys, as well as trial ground-penetrating radar profiles. They acquired seven P-wave reflection lines of 4.877 km total length. Two SH-waves seismic-reflection lines totaling 700 m in length were acquired as suggested from the P-wave surveys to delineate the deformation zone in the Porters Creek Clay. The P-wave surveys suggested reactivated faults extending above the limestone bedrock into the Porters Creek Clay. The SH-wave survey was able to detect the top of the Porters Creek Clay, an overlying firm sand unit, and some parts of the loess. Also, a number of potential faults at shallow depth near the bottom of the loess unit were picked.

Drahovzal and Hendricks (1996) reviewed the geologic and remote-sensing literature of the region and concluded that the southern part of the study area (i.e., the Paducah plant) is underlain by a series of northeast-oriented lineaments that possibly correlate with the Fluorspar Area Fault Complex. They also concluded that Mississippi Embayment sediment was most likely masking these structures. They also noticed that the lineaments

were oriented similarly to the direction of the contamination plume migration in the regional gravel aquifer (RGA).

CHAPTER TWO

2 METHODOLOGY

Although various seismic-reflection surveys have been widely used since the 1950s in the oil and gas industry, shallow seismic exploration has only become a routine technique in the last three decades, primarily as the result of cost-effective microcomputer technology. The typical use of near-surface seismic-reflection imaging is to map bedrock and to characterize the overlying stratified sediments related to engineering, mining, hazard, and groundwater studies. Numerous applications of near-surface seismic-reflection work has addressed these topics (e.g., Hunter et al., 1984; Steeples and Miller, 1990; Guy et al., 2003; Pugin et al., 2004; Francese et al., 2005; Woolery et al., 2009; Stephenson et al., 2012;). Seismic- reflection technique is divided into two subcategories based on the controlled seismic-energy source that creates seismic waves. Thus, for seismic-reflection prospecting, P- and/or S-body waves are used. The seismic-reflection method and its subsequent innovations were originally developed in relation to deep industry targets (e.g., Mayne, 1962, 1967; Oliver et al., 1976); consequently, as these methods have been scaled to the near surface, many of the standard industry procedures and applications have followed, including the P-wave as the primary energy source. In addition to being easier and more cost-effective to generate and apply, greater amounts of P-wave energy can be coupled to the ground compared with S-waves; thus, greater depths can generally be sampled. In most rock environments, the higher-frequency P-waves will also yield higher-resolution images, because the S-wave velocity is not sufficiently smaller to produce a shorter wavelength wavelet. The S-wave has special characteristics that can often make it more effective in near-surface studies, however. The S-wave, unlike the P-wave, has birefringence properties and is categorized into SH-waves (horizontal) and SV-waves (vertical) according to its polarization direction (Helbig, 1986). The SH-wave has the further useful property of self-consistency, where it neither interacts with nor converts to a P-wave or SV-wave; neither do other wave types convert or interact with it at horizontal impedance boundaries. Thus, the SH-wave is often preferable to the SV-wave

because it leads to a seismic section; in theory, there are only SH-wave reflections and no other modal contamination (Helbig, 1986). Furthermore, SH-waves resolve near-surface problems better than P-waves because SH-waves travel with the lithologic matrix and not fluid/water (Fig. 2.1); unlithified sediments are often water-saturated and have low seismic velocity in the near-surface environment. The lower-velocity SH-wave propagation shifts the optimal collecting window to the near offset behind the coherent noise (i.e., refraction, etc.) and expands the temporal window, which better separates the individual signals (Fig. 2.2). In this type of environment, the SH-wave typically has frequencies one-third to one-half that of the P-wave, but the S-wave velocity is often five to 10 times less than the P-wave, thus yielding an overall shorter wavelength and improved resolution factor between two and three (Fig. 2.3). The polarization property of the S-wave allows or induces it to split into two waves travelling at two different velocities when travelling in an azimuthally anisotropic medium (Crampin, 1985; Thomsen, 1988; Tatham and McCormack, 1991) (Fig. 2.4). The two shear-waves travel parallel (fast shear-wave) and orthogonal (slow shear-wave) to the azimuth of the anisotropic element or inclusion. Historically, the shear-wave splitting or birefringence method has been used by industry to evaluate fracture direction in oil/gas-bearing rock formations (e.g., Winterstein and Meadows, 1991) and by earthquake seismologists to illuminate deep crust and/or mantle architecture (Clement et al., 1994; Long and Silver, 2009); however, Harris (1996, 2005) was the first to show that surface and downhole birefringence methods can be used to reveal near-surface sediment microfractures associated with in situ stress conditions in seismic and slope-stability hazard areas. Because of the subsurface geologic complexity of the study area, seismic-reflection and shear-wave birefringence techniques were combined in this project. SH-wave and P-wave seismic reflections were used to resolve the stratigraphic and structural geology, and surface-arrayed shear-wave splitting was used to assess the near-surface material anisotropy caused by faults. Electrical resistivity, vertical seismic profiling (VSP), and well-log data were employed as supporting geophysical techniques.

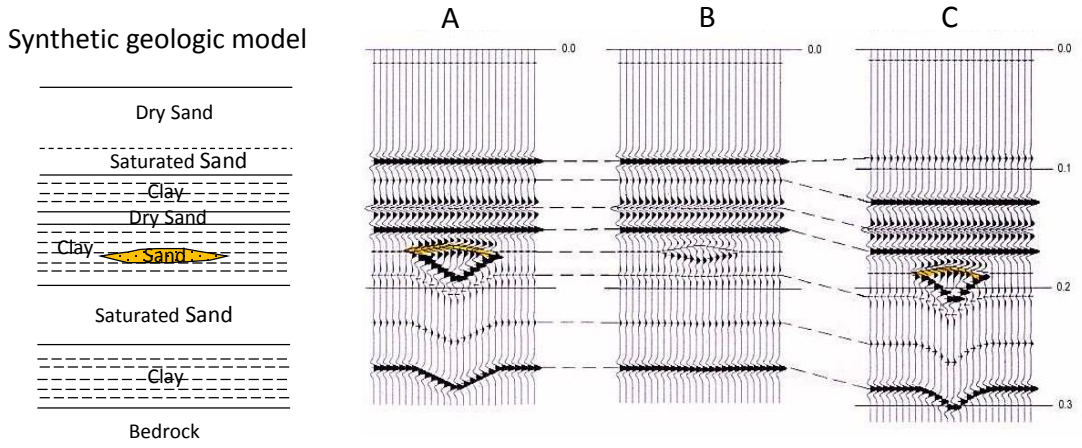

Figure 2.1: Synthetic P- and SH-wave seismic-reflection profiles were used to image a sand body in a synthetic geologic model. (A) The P-wave imaged the sand body in dry conditions, but (B) water-saturated condition masked the sand body in the P-wave profile. (C) The SH-wave (framework wave) is not affected by water saturation; therefore, the SH-wave profile samples the low-velocity geologic/particulate medium. After Bay Geophysical, Inc. (2004).

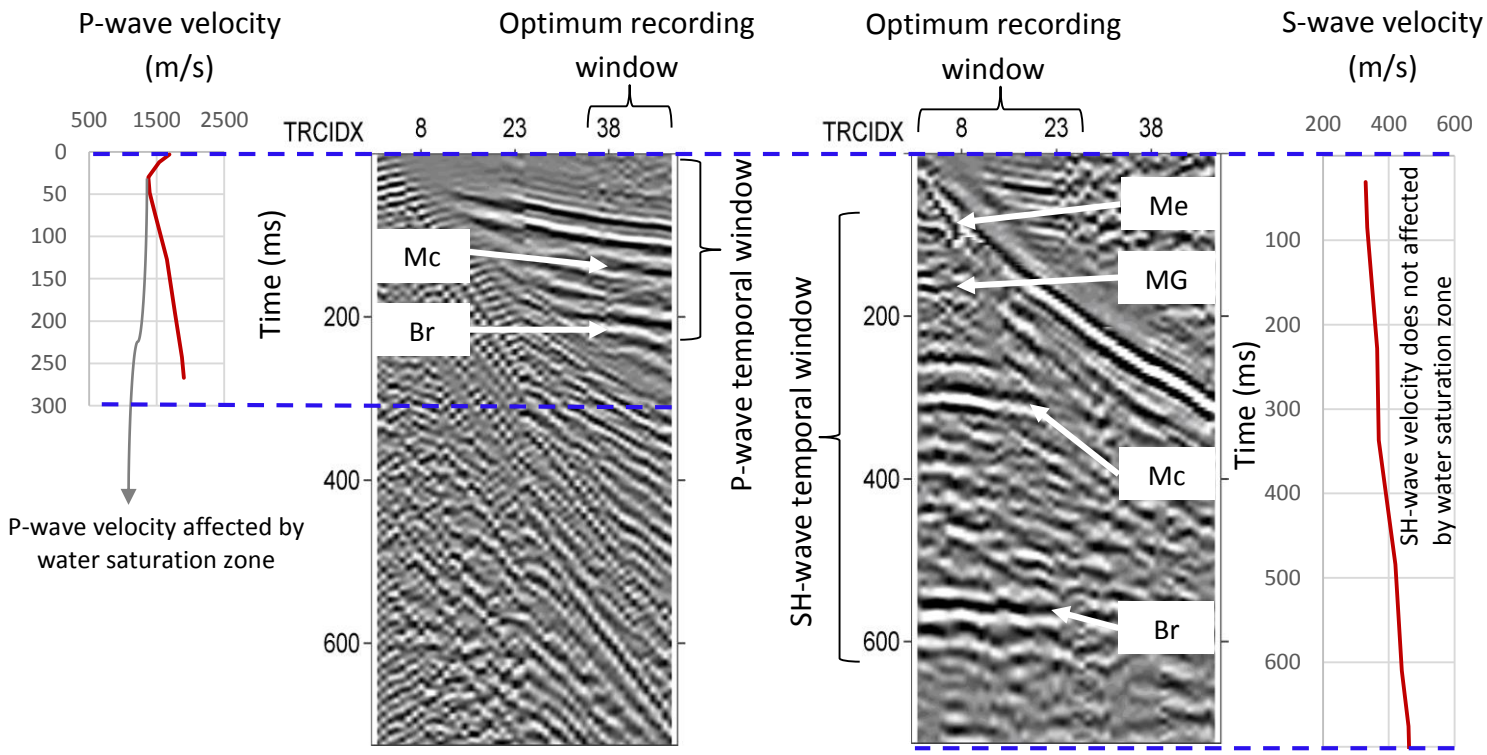

Figure 2.2: Optimum recording and temporal windows. (A) P-wave. (B) SH-wave. In the P-wave velocity curve on the left, the water-saturated zone masks the framework matrix characteristics because the P-wave is capable of traveling through water, but the S-wave velocity curve was not affected by the presence of water because the S-wave travels through the matrix, not in the water.

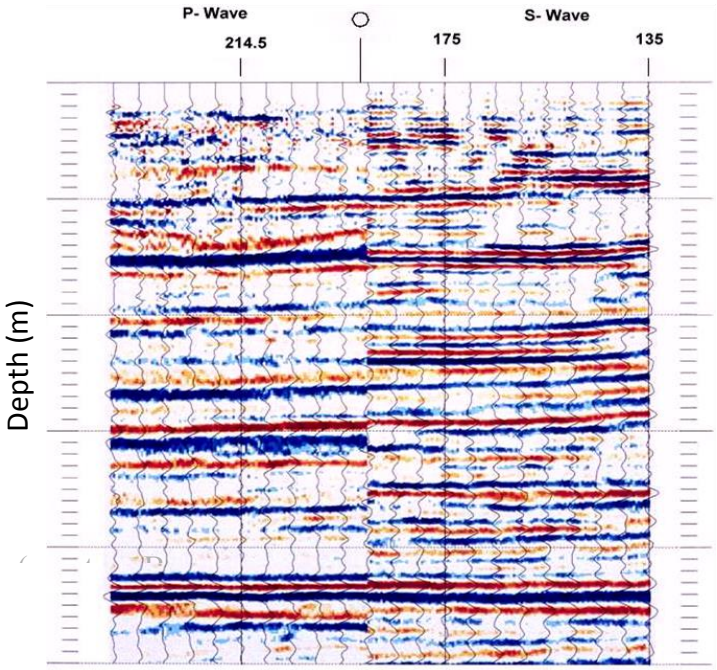

Figure 2.3: Vertical resolution of P-wave versus SH-wave profiles. Although S-waves have one-half to one-third of P-waves' frequency and five to 10 times less velocity than P-waves, they have shorter wavelength; therefore, S-wave vertical resolution improved by a factor of 2 to 3. Courtesy Bay Geophysical, Inc. (2004).

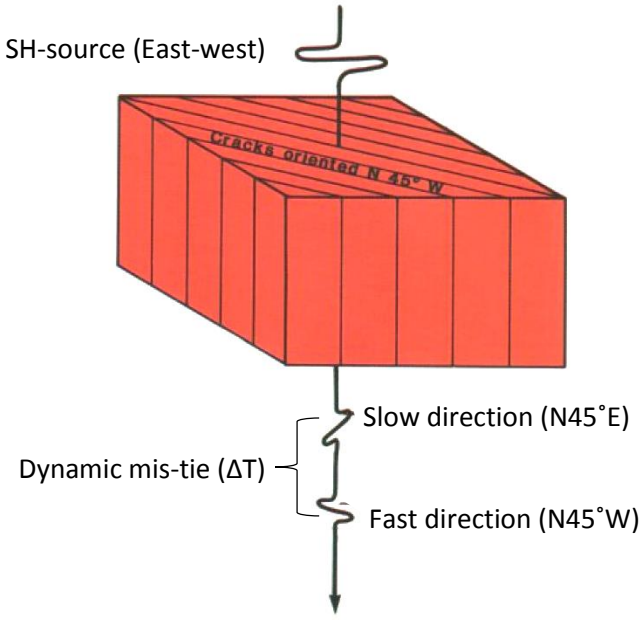

Figure 2.4: A horizontally east-west polarized shear-wave encounters azimuthal anisotropic medium caused by N45˚W crack orientation. The shear-wave splits into two polarized waves with two different velocities. The shear-wave of parallel polarization to the crack orientation propagates with fast velocity, and the other shear-wave of perpendicular polarization to crack orientation propagates with slow velocity. After (Martin and Davis, 1987).

2.1 Seismic-Reflection Method

A large Department of Energy database contains a significant amount of unprocessed geophysical data. For this study, all available nonproprietary seismic-reflection data from Langston and Street (1998), Bechtel Jacobs Co. LLC (2003), Woolery and Street (2003), SAIC Engineering Inc. (2004), and Blits (2008), were gathered, reprocessed, and integrated into a single geologic model, which included approximately 21 km of SH-wave seismic-reflection and approximately 6 km of P-wave seismic-reflection data. Langston and Street (1998) collected SH-wave data with a 48-channel, 24-bit, IFP Geometrics StrataView RX Engineering seismograph. The energy source was 5.4-kg sledgehammer and 12-kg steel I-beam. SH-wave reflection data from Woolery et al. (2003) and Blits (2008) were acquired with a 48-channel Geometrics NZXP StrataVisor seismograph with a dynamic range of 115 dB; but line L was collected with 24-channel Geometrics Geodes with an instantaneous dynamic range of 110 dB. The energy source was a 1.4-kg engineer's hammer striking a steel H-pile. Horizontally polarized 30-Hz geophones were used in all these SH-wave reflection surveys. SAIC Engineering Inc. (2004) collected seven P-wave reflection lines and two SH-wave reflection lines. P-wave data were collected with 144-channel, 24-bit, 2 OYO DAS-1 seismographs, master and slave. The data were collected with a Vibroseis 30- to 350-Hz energy source (IVI MiniVib) and vertical-component 40-Hz geophones. SH-wave reflection data were collected with a 96-channel, 24-bit, OYO DAS-1 seismograph. The vibratory energy source was an in-house-designed SH-microvib, 20- to 200-Hz. Horizontal-component 40-Hz OYO SMC70 receivers were used. Two more SH-wave reflection lines were collected by Bechtel Jacobs Co. LLC (2003) with a 96-channel OYO DAS-1 seismograph. The energy source was also the SH-microvib 20- to 200-Hz with single horizontal-component 40-Hz OYO SMC70 geophones. Figure 1.2 shows the locations of the existing seismic-reflection lines and Tables 2.1 and 2.2 summarize the field acquisition parameters. Seismic data were processed using VISTA12, 2-D/3-D interactive commercial signal processing software. VISTA12 licenses are available from the University of Kentucky/Department of Earth and Environmental Sciences Seismic Lab. The data-processing flowcharts that were created to produce final-stack seismic sections are discussed in detail in the next chapter. Another available software package, Kingdom

Suite version 8.7.1, for advanced and complex interpretation, also available from the Seismic Lab, was used to interpret the seismic data, produce synthetic seismograms, and plot time-structure and isopach maps. The interpretation details are discussed in chapter four.

2.2 Shear-Wave Birefringence

2.2.1 Method Justifications

Two types of anisotropic media can be considered. The first is simple anisotropy, which occurs when only one anisotropic layer splits or polarizes an incident shear-wave into specific fast and slow directions. Normally, the two directions are orthogonal to each other and result in an elapsed time or time differential between the split waves. The second type is complex anisotropy (Fig. 2.5), which occurs if more than one anisotropic layer affects the shear-wave propagation through these layers (Silver and Savage, 1994). In order to simplify the shear-wave splitting application, researchers frequently assume a single anisotropic layer, although there is actually more than one layer beneath the receiving station (Silver and Savage, 1994). This assumption is valid for regional-scale studies and the deep-earth interior (e.g., mantle flow) with various anisotropic layers; however, this assumption is not needed in near-surface applications that focus on mesoscopic features (e.g., faults, fractures, depositional fabric, etc.) because the time delay is very small (Crampin and Lovell, 1991). Shear-wave splitting is used in various applications and at a wide range of depths. In the deep-earth interior, for instance, it can be a tool to make inferences about the style and geometry of mantle flow because it is a direct consequence of deformation processes (Long et al., 2009). In near-surface applications, Schoenberg and Sayers (1995) found that shear-wave birefringence provides specific information related to the internal structure of rock (e.g., strike of vertical cracks can determine the orientation of cracks) and thus preferred fluid flow directions. Traditionally, the shear-wave splitting technique is used in rock conditions, but Harris (1996) concluded that the surface shear-wave splitting technique is an effective approach to determine the extent and location of surface/near-surface stress orientation in the New Madrid Seismic Zone (NMSZ) in a sediment environment. Most of the near-surface geologic conditions at the study site are low-velocity unlithified (often saturated)

sediments. A shear-wave experiment was carried out in order to further support the fault-orientation assessment and interpretation, measure the significance of shear-wave splitting in unlithified sediments, and identify the presence of azimuthal anisotropy strictly caused by fault deformation/orientation and not because of deposition fabric, microfracture sets, stress field, and mineral content.

2.2.2 Data Acquisition

The location of the shear-wave-splitting experiment was selected according to a clearly identified, constrained, and correlated striking fault on three seismic-reflection profiles (i.e., profiles J1, J2, and I (Fig. 2.6). Shear-wave-splitting data across the 200-m deformation zone were collected on the south-southwest part of profile J1 with a 48-channel Geometrics NZXP StrataVisor seismograph. Traditionally, surface-arrayed shear-wave-splitting experiments need either broadband seismometers that are used mainly in earthquake seismology or three-component geophones that are used mainly in the oil and gas industry. However, not enough receivers were available to collect CMP datasets; as a substitute, pairs of single-component horizontal-polarization 30-Hz geophones were orthogonally planted along a line oriented south-southwest–north-northeast (Fig. 2.7). The two geophones (the pair) in each recording station were arrayed perpendicularly to each other. This configuration resolved the transverse and radial polarized shear-wave components that were split from the single seismic source. For better near-surface sampling, geophone pairs and shot-point intervals were 2 m. Because two channels were required for each geophone group, the general 24-channel recording window was reduced to 12-channels. A 1.8-kg engineer's hammer and 6-kg modified H-pile section were used as the energy source. At the same shotpoint location, the H-pile section was oriented in two perpendicular directions: north-south and east-west (Fig. 2.7). The east-west H-pile and hammer impact were used to generate transverse polarization (SH-waves); the north-south H-pile and hammer impact were used to generate radial polarization (SV-waves). In any source direction, six total impacts were applied at each shot location—three strikes on each side. Double-sided hammer impacts and acquisition polarity reversals were performed in order to allow constructive SH-wave interference

and destructive P-wave interference to ensure initial accurate identification of SH-wave arrivals. The data were saved after every hammer impact to avoid the field auto-stack and to allow a visual laboratory inspection of the data for potential trigger delays. The seismic data were collected at a sample interval of 0.25 ms with a total record length of 1.024 ms. The acquisition field filter was 15 Hz low-cut and out high-cut. The collected data were processed using VISTA12, and the processing procedure details are discussed in chapter four.

2.3 Vertical Seismic Profiling (VSP)

The oil industry first introduced the vertical seismic profiling technique as another exploration tool. Traditionally, VSP is used to tie time-based 2D seismic-reflection profiles with depth-based borehole data to support subsurface lithosequence correlation and interpretation. This constrains seismic waves to follow a prescribed path between the source and downhole geophone; therefore, the VSP technique can detect layered velocity inversion. In the last three decades, the practice of VSP expanded beyond time-depth correlation to become a tool for seismic anisotropy measurement. A polarized source combined with a three-component downhole geophone form a dataset of the desired elements and provide insight into the physics of wave generation and seismic wave propagation. Thus, detailed information about fracture- and/or fault-related anisotropy can be resolved. Downhole anisotropy measurements were not collected during the downhole velocity surveys, however. Future work at the site should include these measurements.

Table 2.1: Acquisition parameters for SH-wave seismic-reflection profiles.

Line Name	Near-offset (m)	Shot interval (m)	Receiver interval (m)	Sample interval (ms)	Acqu. Filter Low-cut	Acqu. Filter High-cut	Notch Filter (Hz)	Receiver Frequency (Hz)	Total subsurface sampling length (m)
A1*	0	4	4	0.5	10	250	60	30	1091
A2*	0	4	4	0.5	10	250	60	30	703
A3*	0	4	4	0.5	10	250	60	30	1677
B*	0	4	4	0.5	10	250	60	30	4327
C1*	0	4	4	0.5	10	250	60	30	1229
C1s*	0	4	4	0.5	10	250	60	30	236
C2*	0	4	4	0.5	10	250	60	30	713
C3*	0	4	4	0.5	10	250	60	30	781
D*	0	4	4	0.5	10	250	60	30	547
E*	0	4	4	0.5	10	250	60	30	471
F**	0	4	4	0.25	15	250	NaN	30	1025
G1*	0	4	4	0.5	10	250	60	30	2721
G2*	0	4	4	0.5	10	250	60	30	1095
H***	2	2	2	0.25	15	out	NaN	30	500
J1**	2	2	2	0.5	15	out	60	30	789
K1*	0	4	4	0.5	10	250	60	30	427
K2*	0	4	4	0.5	10	250	60	30	245
L***	4	4	4	0.25	15	out	NaN	30	713
N****	0.3048	0.6096	0.6096	0.5	3/18	out	NaN	40	554
O****	0.3048	0.6096	0.6096	0.5	3/18	out	NaN	40	433
S8*****	0.3048	0.6096	0.6096	0.5	3/18	out	NaN	40	344
S9*****	0.3048	0.6096	0.6096	0.5	3/18	out	NaN	40	374

*Langston and Street (1998) data
** Woolery and Street (2003)
*** Blits (2008) data
**** Bechtel Jacobs Co. LLC (2003) data data
***** SAIC Engineering Inc. (2004) data

Table 2.2: Acquisition parameters for P-wave seismic-reflection profiles.

Line Name	Near-offset (m)	Shot interval (m)	Receiver interval (m)	Sample interval (ms)	Acqu. Filter Low-cut	Acqu. Filter High-cut	Notch Filter (Hz)	Receiver Frequency (Hz)	Total subsurface sampling length (m)
J2	50	2	2	0.25	15	out	NaN	40	200
I**	60.96	3.048	3.048	0.25	25	out	NaN	40	761
M**	40	4	4	0.25	15	out	NaN	40	617
P1*****	0.762	3.048	1.524	0.5	3/18	out	NaN	40	463
P2*****	0.762	3.048	1.524	0.5	3/18	out	NaN	40	393
P3*****	0.762	3.048	1.524	0.5	3/18	out	NaN	40	1164
P4*****	0.762	3.048	1.524	0.5	3/18	out	NaN	40	1441
P5*****	0.762	3.048	1.524	0.5	3/18	out	NaN	40	865
P6*****	0.762	3.048	1.524	0.5	3/18	out	NaN	40	216
P7*****	0.762	3.048	1.524	0.5	3/18	out	NaN	40	506

** Woolery and Street (2003) data ***** SAIC Engineering Inc. (2004) data

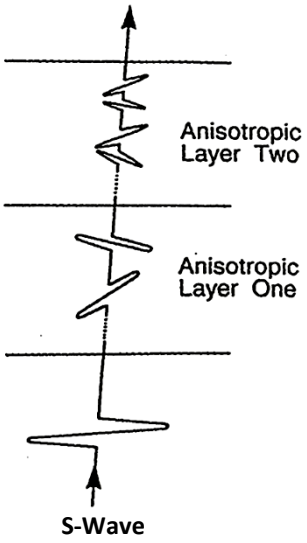

Figure 2.5: Diagram of shear-wave splitting resulting from more than one anisotropic layer. The incoming shear wave is splitting two times to produce four individual waves that could be detected at a receiver (Silver and Savage, 1994).

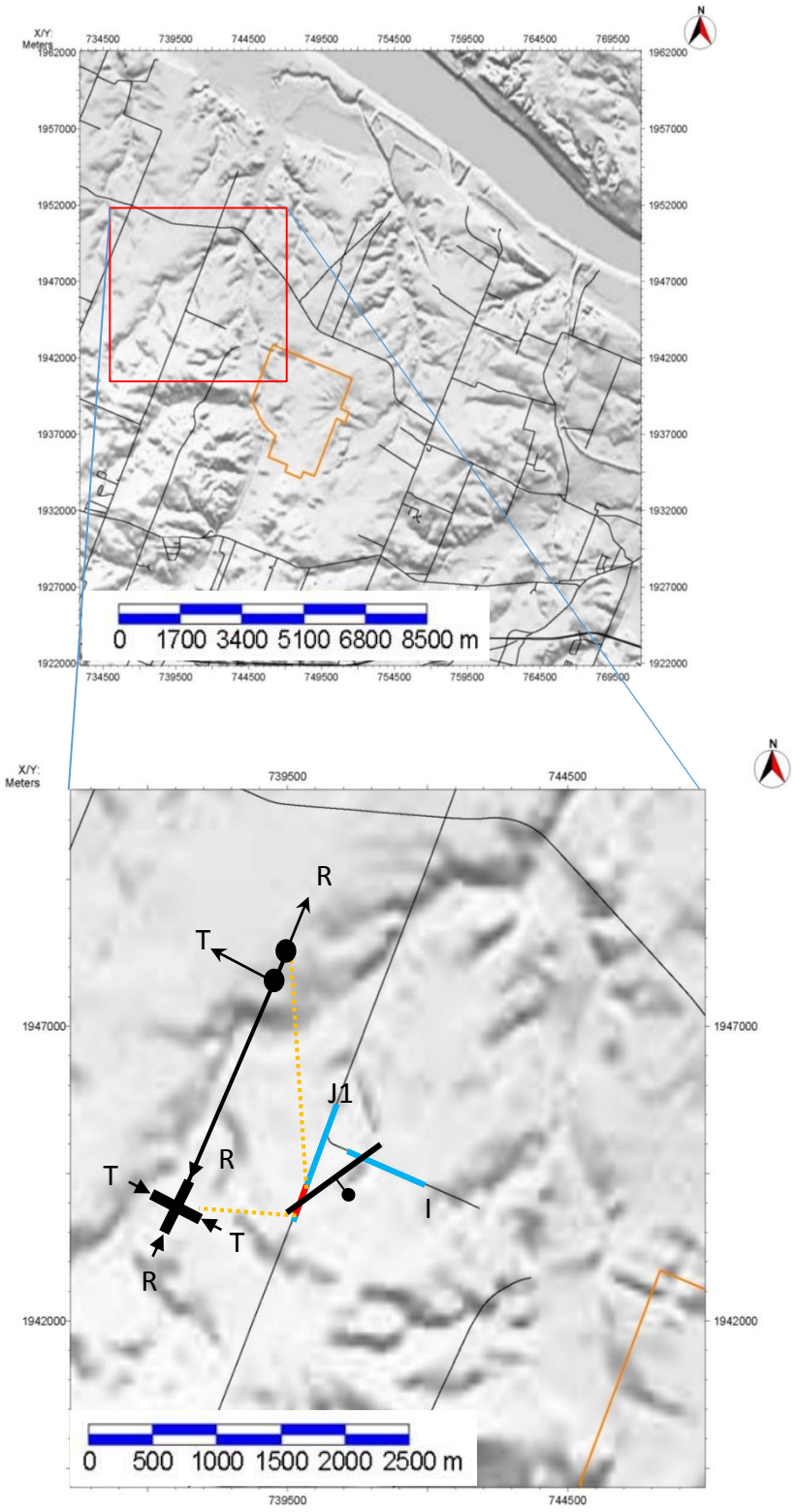

Figure 2.6: Location of profiles I and J and SH-wave and P-wave reflection profiles. The small red line is the location of the shear-wave splitting experiment. The insert shows the field source-receiver configuration.

Figure 2.7: (A) Shear-wave splitting line direction. (B) A pair of two single-component horizontal-polarization 30-Hz geophones aligned perpendicular (90°) to each other. (C) East-west SH-wave source in-line with east-west geophone and perpendicular with the north-south geophone. (D) North-south SH-wave source in-line with north-south geophone and perpendicular with the east-west geophone.

2.3.1 Data Acquisition

In VSP data collection, the principal field equipment includes an active source to generate SH-waves, downhole three-component geophone, digital recording system, and cased vertical borehole. The S-wave energy-source system consisted of an H-pile and 1-kg hammer. The hold-down weight on the H-pile was approximately 70 to 80 kg (i.e., includes weight of hammer swinger standing on H-pile). The energy source was placed on the ground surface 2 m from the borehole opening (Fig. 2.8). To improve the energy coupling, the H-pile flanges were embedded into a prepared slot in the ground. The Geostuff model BHG-2c 14-Hz was the three-component downhole geophone with flux-gate compass. The geophone was coupled to the borehole wall by a motor-driven piston that expands and contracts a wall-lock spring. The data were collected with 24-channel Geometrics geodes with instantaneous dynamic range of 110 dB. The field acquisition by Woolery and Wang (2005) was part of a ground-motion response study. They measured the differential travel times of the seismic waves from the energy source at the ground surface to a three-component geophone, which was lowered in a vertical borehole and fixed at various elevations. These downhole data collection points were 1 m apart. The arrival times of shear-waves from orthogonal horizontal directions and a converted SP-wave from a vertical direction were recorded. In order to improve the signal-to-noise ratio, 10 to 15 stacks were applied at each collection point. The two horizontal components (i.e., the transverse and longitudinal directions) were arbitrarily oriented at each collection point. Unfortunately, this acquisition procedure invalidated the data for in-situ seismic anisotropy application.

To ensure proper identification of shear-waves, an initial test of uncorrected polarization was performed so that polarity correction was carried out (Fig. 2.9), as well as other corrections (e.g., bandpass filtered, gain controlled, and spliced into an overall downhole composite). The raw dataset (Fig. 2.10) was processed using VISTA12 software. The resultant VSP stacked section was used for bed marker identification on seismic-reflection profiles (Fig. 1.5).

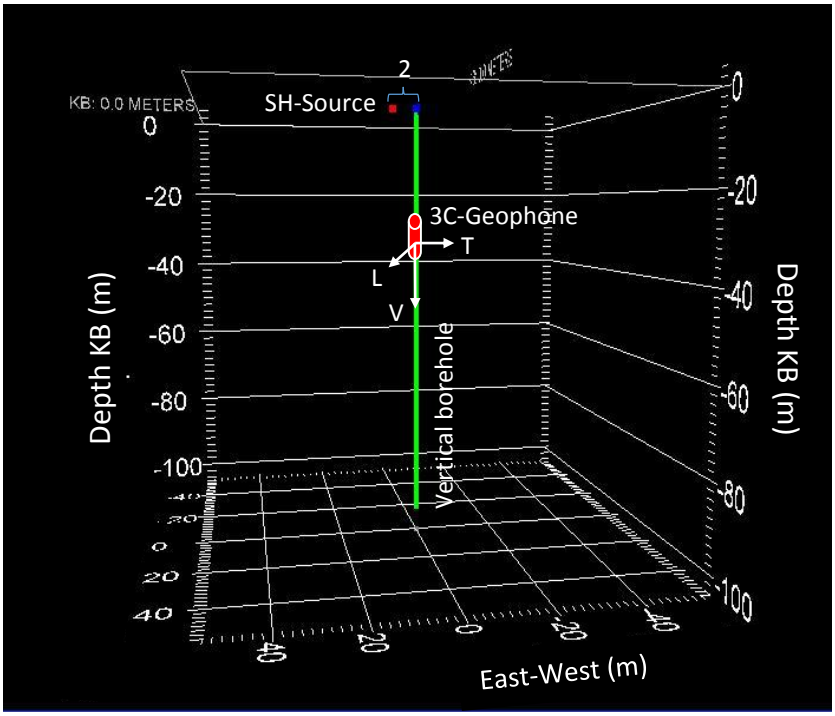

Figure 2.8: Schematic cross section of the field setup used for a downhole seismic experiment (not to scale).

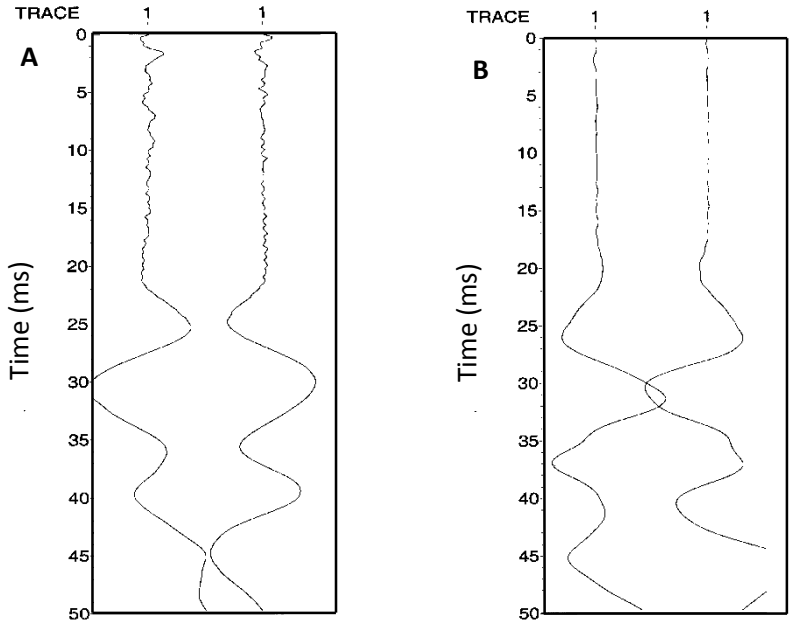

Figure 2.9: Shear-wave arrival identification assurance. (A) Uncorrected polarity field tests were performed on the longitudinal component of the downhole 3-C geophone. (B) Uncorrected polarity field tests were performed on the transverse component of the downhole 3-C geophone.

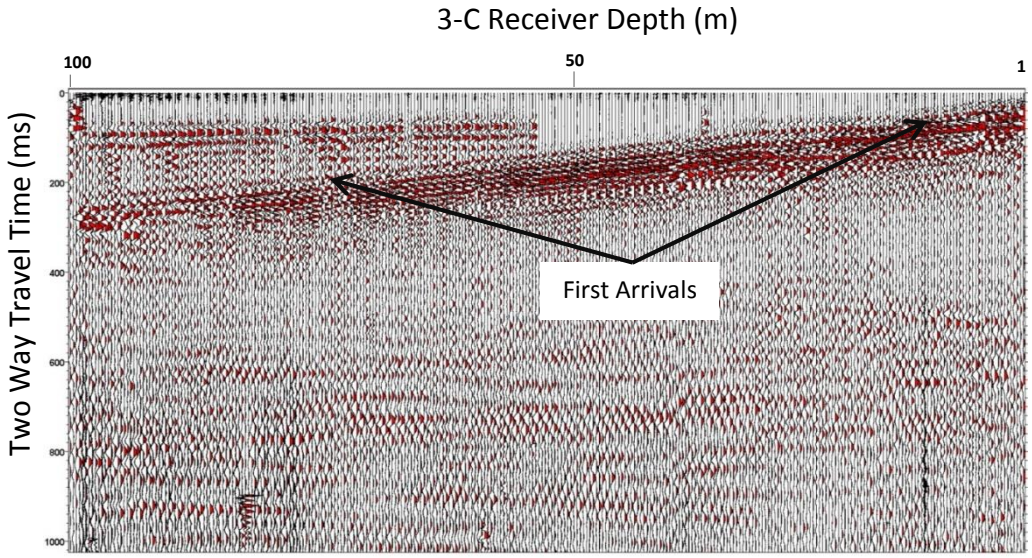

Figure 2.10: Raw VSP three-component data set (longitudinal, vertical, transfers) before component separation step.

2.4 Synthetic Seismograms

A synthetic seismogram is a forward one-dimensional model of acoustic impedance boundaries. It ties or correlates a seismic-reflection section with borehole data and helps interpretation by identifying geologic formation markers. The synthetic seismogram is created by convolving the earth's reflectivity with an equivalent wavelet. Earth's reflectivity is derived from velocity and density logs. In the subject area, SAIC Engineering Inc. (2004) acquired SH-wave and P-wave velocity logs (Fig. 2.11) in DB-02 borehole of 120 m total depth. Also, Woolery and Wang (2005) surveyed shear-wave velocity (Fig. 2.12) using the 3-C downhole geophone in the VSAP borehole to 100 m total depth. Street et al. (1997) calculated density values in the VSAP borehole, and they were plotted as a density log (Fig. 2.13). Each velocity log was convolved with the density log using Kingdom Suite version 8.7.1 to generate an acoustic impedance log. The amplitudes of the acoustic impedance logs were converted into a reflectivity log. The earth's reflectivity data are measured in the space (z-depth) domain with higher

frequency content than seismic signal; thus, the reflectivity log was convolved with an equivalent theoretical wavelet to produce seismic-like responses (i.e., synthetic seismogram). Ricker and Ormbsy wavelets were chosen to be convolved with the reflectivity log because they best match the seismic-data response. The optimum wavelet parameters (Table 2.3) varied according to the velocity log-type and SH-wave or P-wave convolution. Wavelet parameters were often repeatedly tested to achieve an acceptable visual match with the seismic data. Also, filter points were selected depending on the designed band-pass filter used for processing the seismic-reflection data (Figs. 2.14–2.19). Perfect matching between the synthetic seismograms and seismic-reflection data was not expected because of density variations, random noise, and subsurface sample-point variance. In general, synthetic seismograms of Ricker wavelets matched better with seismic data than Ormbsy wavelets. Thus, Ricker wavelets were used for reflector identifications on the reflection profiles (Figs. 2.20–2.21. The actual seismic-data wavelets were not considered because the nearest seismic trace manifests poor quality. Also, the synthetic seismogram that was created with the SH-velocity log from the VSP experiment correlated poorly with SH-wave reflection profile J1.

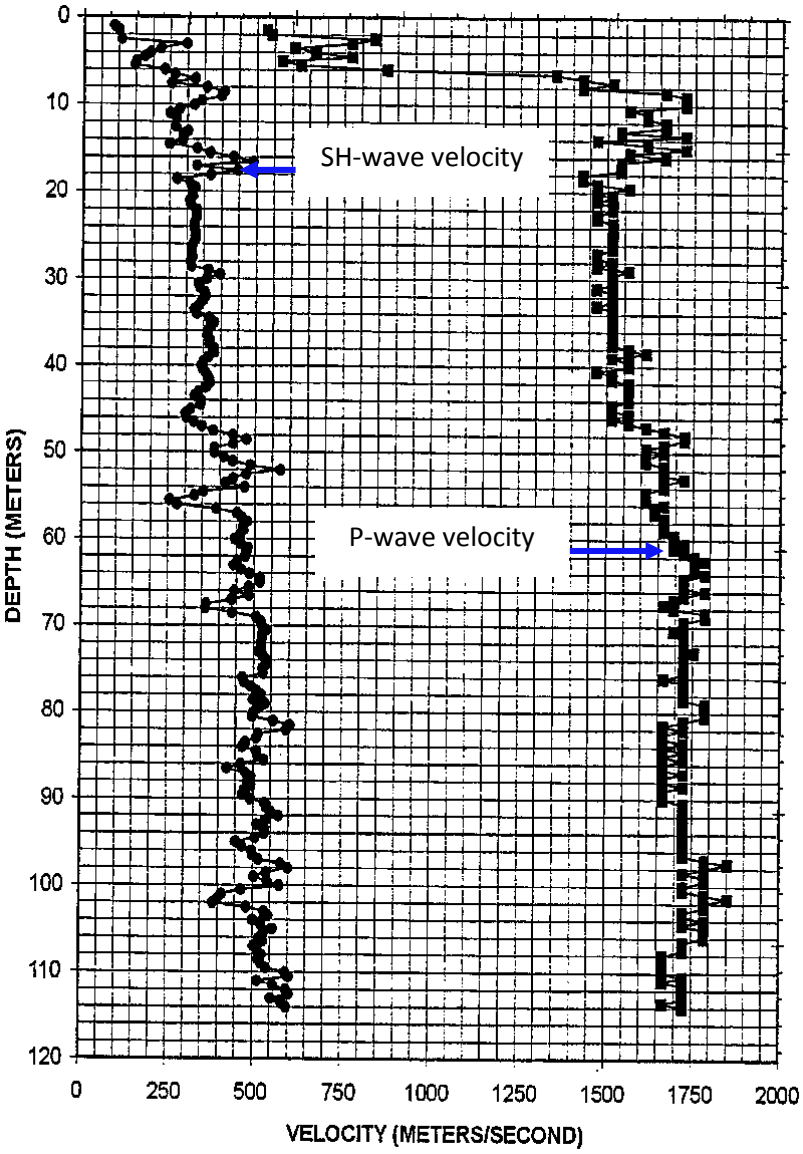

Figure 2.11: SH-wave and P-wave velocity logs from borehole DB-02 (SAIC Engineering Inc., 2004).

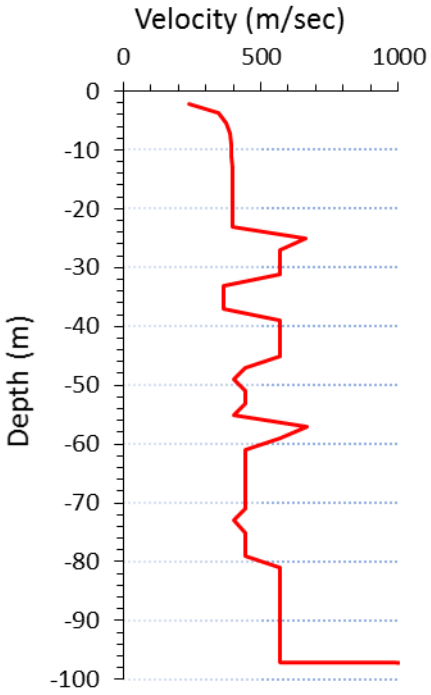

Figure 2.12: SH-wave velocity log from borehole VSAP. After Woolery and Wang (2005).

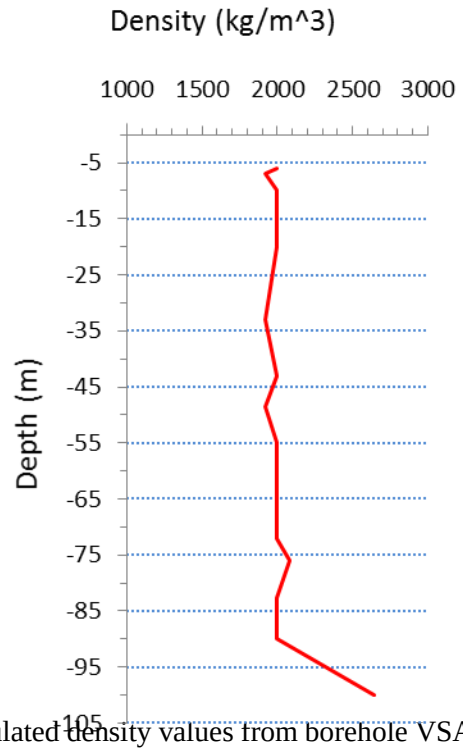

Figure 2.13: Calculated density values from borehole VSAP, after (Street et al., 1997).

Table 2.3: Ormbsy and Ricker theoretical wavelet parameters that were used to generate the synthetic seismograms.

Ormbsy Wavelet			Ricker Wavelet		
Wavelet Parameter	SH-wave	P-wave	Wavelet parameters	SH-wave	P-wave
Frequency (F1)	15 Hz	30 Hz	Peak Frequency (F0)	35 Hz	40 Hz
Frequency (F2)	25 Hz	50 Hz	Sample interval	0.0025 Sec	0.0025 Sec
Frequency (F3)	70 Hz	120 Hz	Phase	0	0
Frequency (F4)	80 Hz	140 Hz			
Sample Interval	0.0025 Sec	0.0025 Sec			
Length in time	0.25 Sec	0.25 Sec			
Phase	0	0			

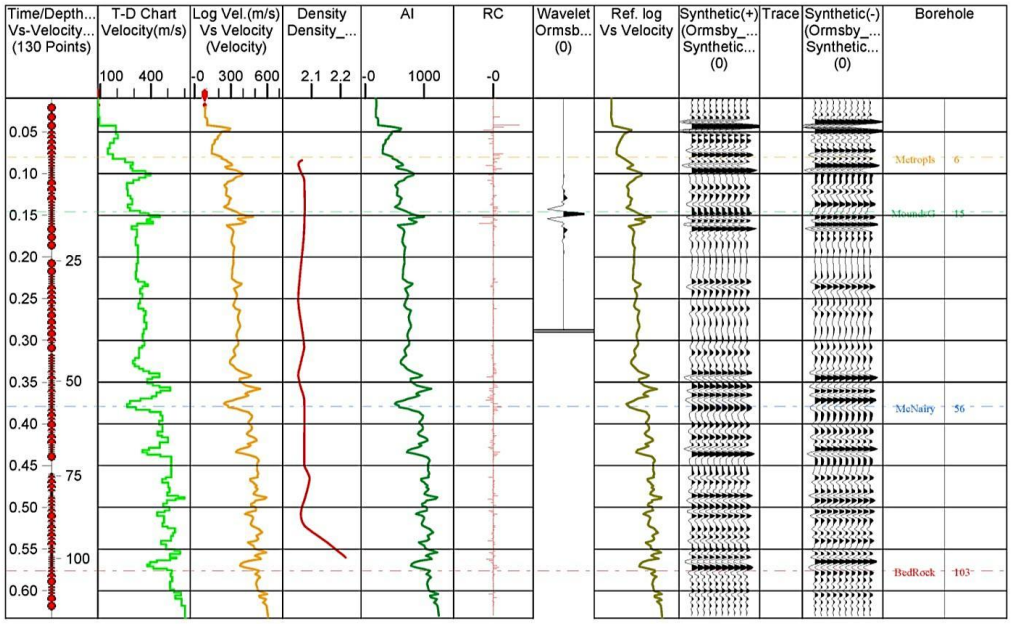

Figure 2.14: Synthetic seismogram of Ormbsy wavelet. SH-wave velocity log from borehole DB-02 and density data from borehole VSAP.

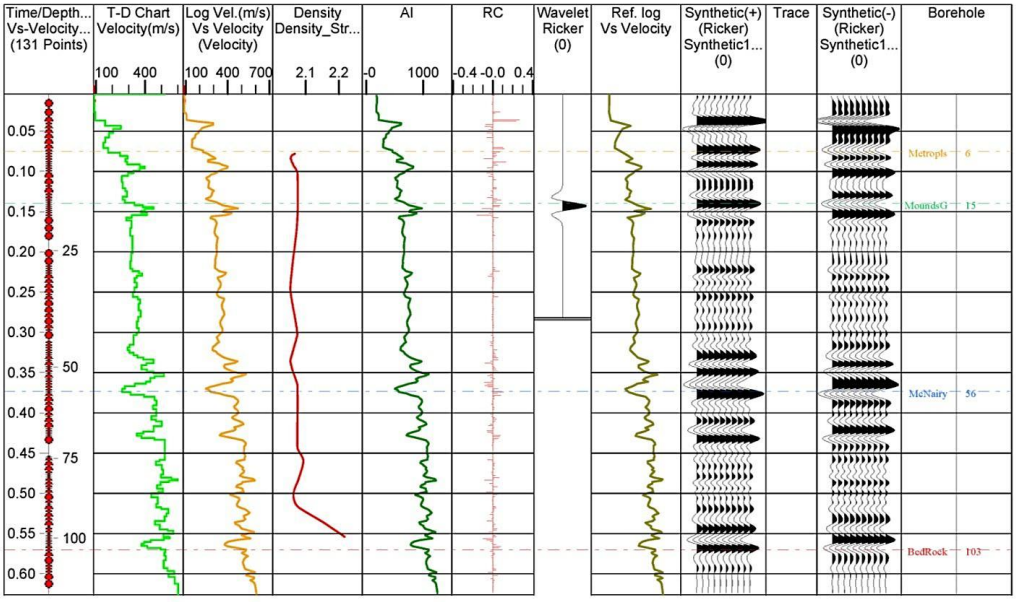

Figure 2.15: Synthetic seismogram of Ricker wavelet, SH-wave velocity log from borehole DB-02 and density data from borehole VSAP.

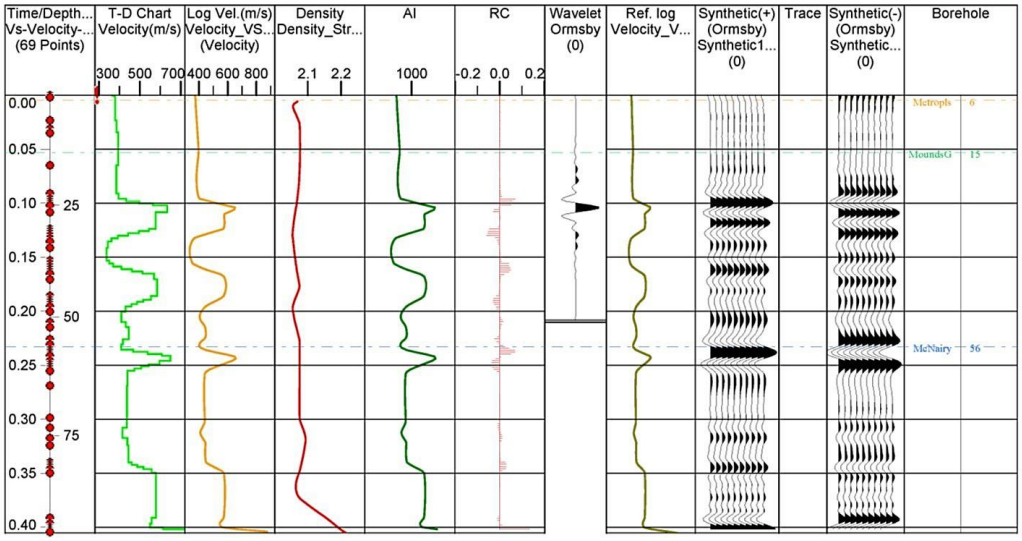

Figure 2.16: Synthetic seismogram of Ormbsy wavelet. SH-wave velocity and density logs from borehole VSAP.

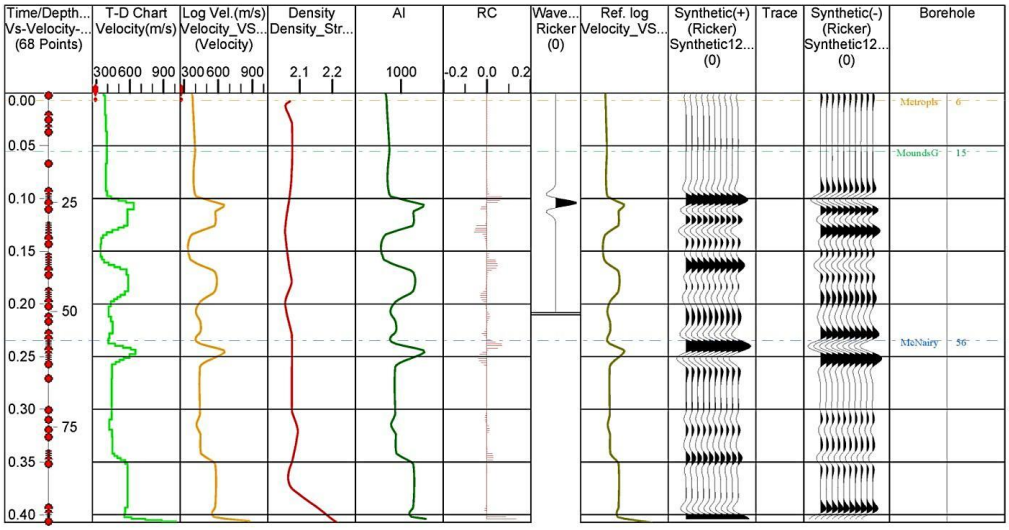

Figure 2.17: Synthetic seismogram of Ricker wavelet. SH-wave velocity and density logs from borehole VSAP.

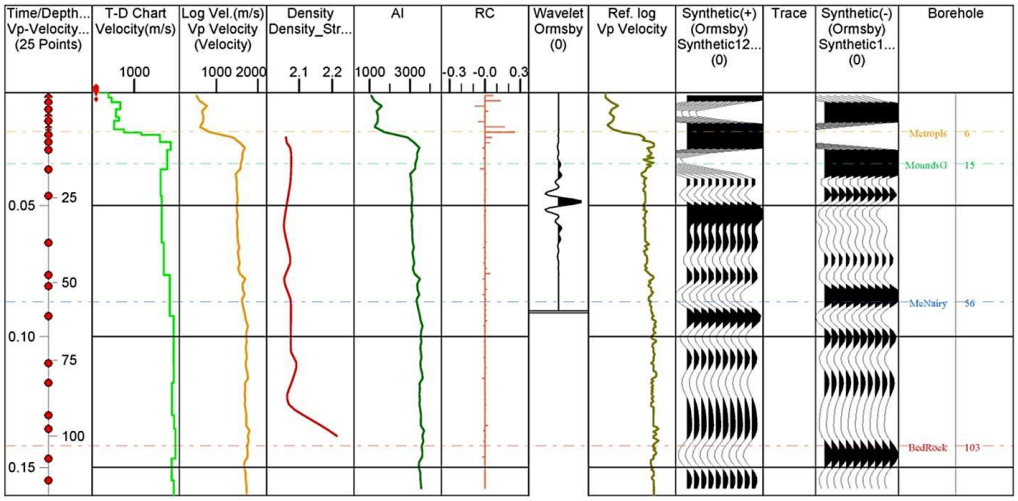

Figure 2.18: Synthetic seismogram of Ormbsy wavelet. P-wave velocity log from borehole DB-02 and density data from borehole VSAP.

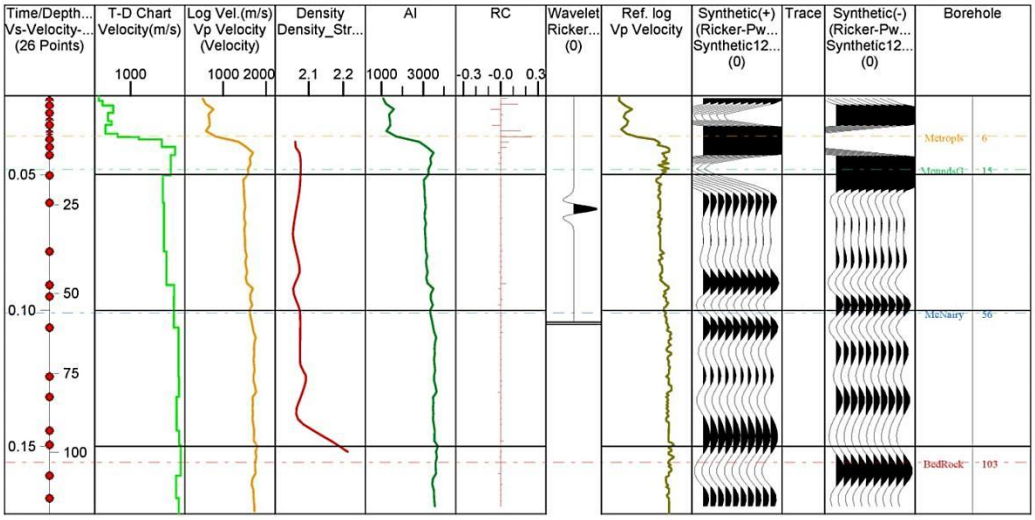

Figure 2.19: Synthetic seismogram of Ricker wavelet. P-wave velocity log from borehole DB-02 and density data from borehole VSAP.

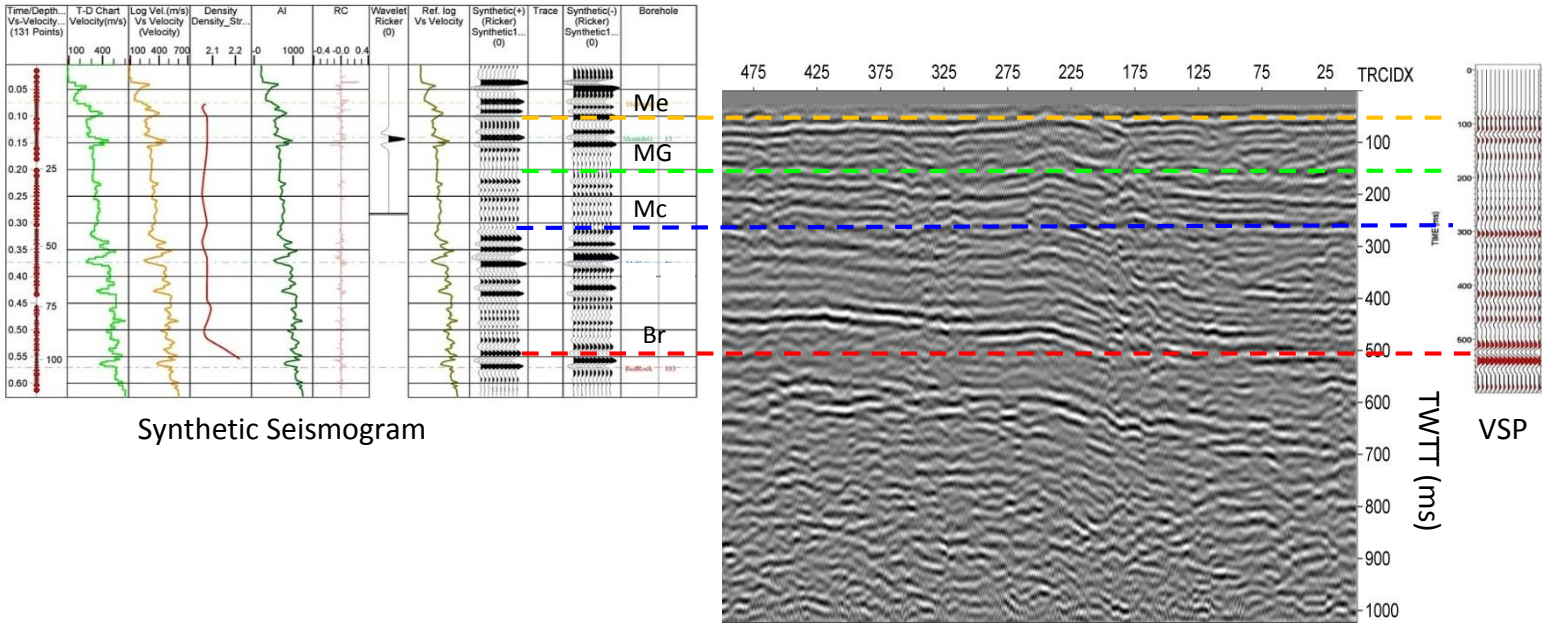

Figure 2.20: Matching *s*ynthetic seismogram and VSP with corresponding SH-wave reflection profile J1.

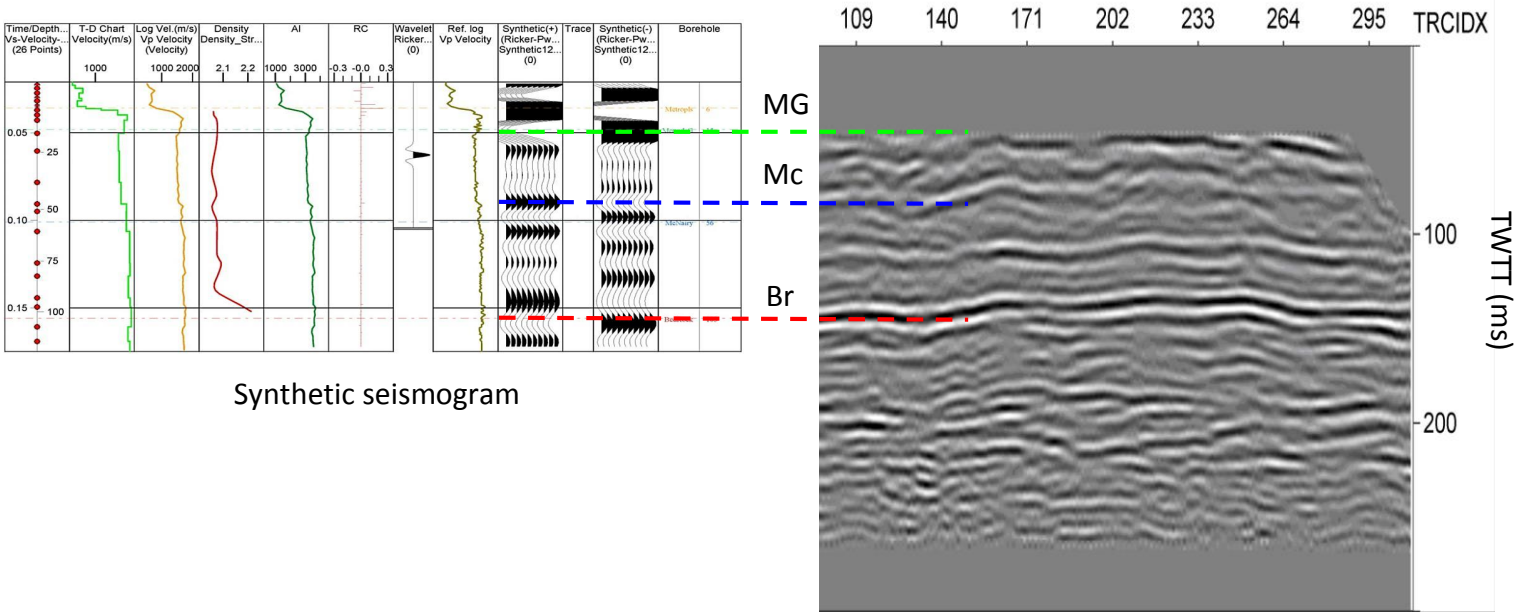

Figure 2.21: Matching synthetic seismogram with corresponding P-wave reflection profile J2.

2.5 Supporting Techniques

2.5.1 Borehole Data

The DOE database containing data from 930 boreholes was available; however, only logs located inside the study site were considered (Fig. 2.22). The lithologic-description logs were used to follow the formation tops across the study area and to support and constrain the seismic data interpretation. The depths of continuous lithologic units were picked for each borehole. Because the majority of the boreholes do not penetrate the Mississippian limestone bedrock, no depth picks were considered for this formation top. Although all boreholes penetrate the near-surface Metropolis Formation, its top was not picked because of difficulty in identifying the corresponding seismic-reflection horizon for a meaningful comparison. Consequently, the picked lithologic units were the tops of the McNairy Formation and Mounds Gravel. The depths of the McNairy and Mounds Gravel tops were gridded and contoured. The contours lines showed the general lows and highs in the formation tops across the study area (Figs. 2.23–2.224).

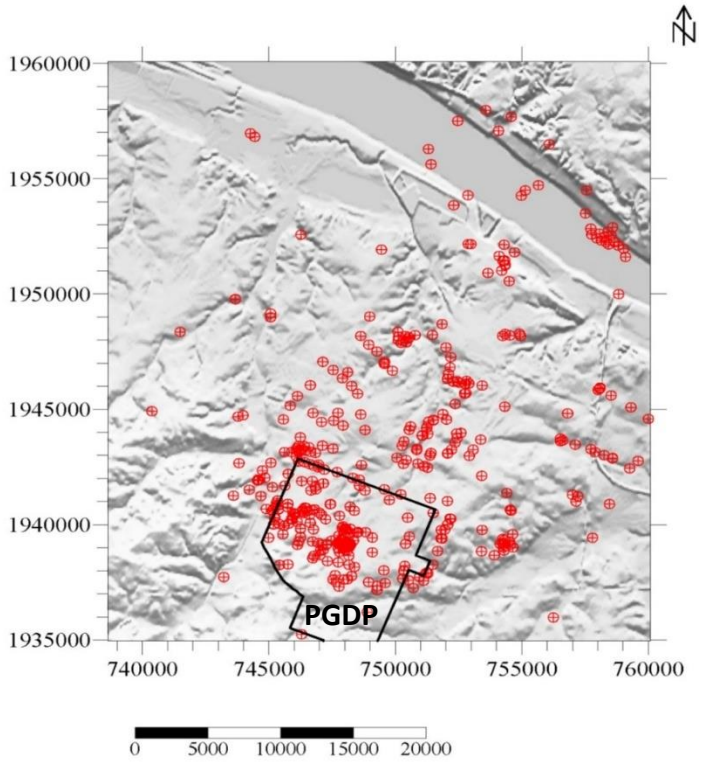

Figure 2.22: Topographic map of the study site shows the locations of the boreholes.

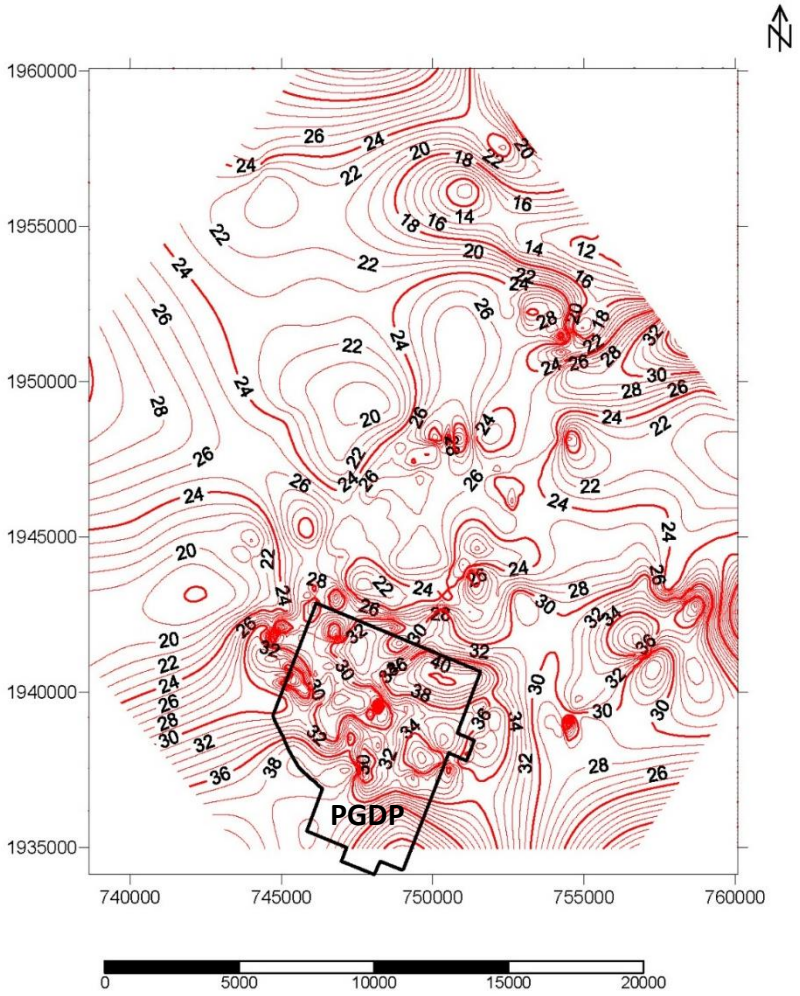

Figure 2.23: Depth contour map of the top of the McNairy Formation. Sandy gravel and sandy silt were the target lithologies for the depth picks.

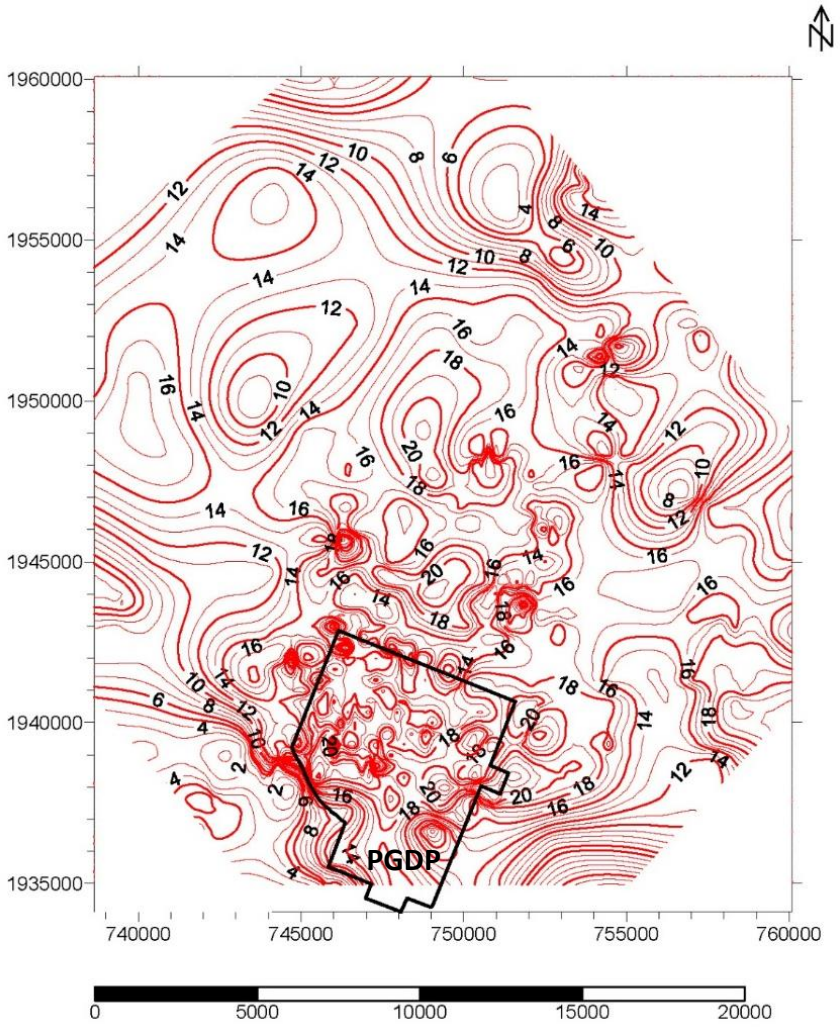

Figure 2.24: Depth contour map of the top of the Mounds Gravel. The upper Continental deposits basal sand (silty) and some lower Continental gravel were the target lithologies for the depth picks.

2.5.2 Electrical- Resistivity Method

The minerals of the rock matrix are inherently very poor conductors, whereas groundwater is a good conductor, so porous sediments and sedimentary rocks are strongly affected by the existence of groundwater. This suggests that water-filled fractures or deformation zones increase the sediment conductivity and vice versa (Lowrie, 2007). Chambers et al. (2006) showed that electrical resistivity in a hard-rock environment is capable of imaging a fault zone. They found that a fault is delineated by relative resistivity drops in dolerite and a high-resistivity response in mafic sills and dikes. The enormous variation in electrical resistivity associated with different subsurface materials makes it a legitimate supporting geophysical technique for interpretation of faults and deformation zones for this project. Blits (2008) collected three electrical-resistivity lines of 2 km total length; these data were reprocessed and utilized for this project. The lines ERT-1, ERT-2, and ERT-3 were collected to determine the locations of SH-wave seismic-reflection profiles H, L, and J1, respectively (Fig. 1.2).

2.5.2.1 Data Acquisition

The electrical-resistivity data-acquisition system consisted of a single-channel AGI SuperSting earth-resistivity meter with internal memory and switching for up to 56 electrodes, a 12-volt deep-cycle battery energy source, and four passive cables. Each stainless-steel electrode was 45 cm in length. The electrodes were tamped into the ground approximately 28 to 32 cm and coupled to the passive cables with a spring collar. The acquisition configuration for the electrodes was a dipole-dipole array. The arrays used a 6-m electrode spacing and were moved, or "rolled-along," in order to extend the survey length. Advanced Geosciences Inc. (2007a) suggested the use of the dipole-dipole array over Wenner and Schlumberger arrays in similar investigations, because it combines the array's resolution advantage for vertical or near-vertical features and 56-electrode spread to offer minimum data-collection time. The administrative software (SSAdmin) creates a command file for setting the electrode configuration according to array type and optimum data-acquisition parameters (Table 2.4). AGI "smart-electrode" internal switching used four electrodes for each measurement, with the electrode selected by the command file. In order to reduce the noise level, the maximum dipole separation was set at six times the

current-electrode spacing and the maximum n-values were set at eight (Advanced Geosciences Inc., 2007b). For every electrode configuration, two cycles of current injection lasting 1.2 s each were used. Current injection was set at 2000 mA maximum. The acceptable error percentage between any two measurements was 2 percent. If the acceptable error percentage exceeded the set limit, measurement was repeated once. For proper operating conditions, a contact resistance test was considered in all survey measurements.

2.5.2.2 Data Processing and Inversion

The data of the three electrical resistivity lines were reprocessed and inverted into 2D electrical resistivity tomography (ERT) profiles using EarthImager 2D version 2.3.0. The main goal of data processing and inversion is to accurately fit the resulted inversion model with the measured field data. This goal can be met by bringing down the root mean square (RMS) error value as low as possible. Three inversions algorithms are available in EarthImager: damped least squares, smooth model inversion, and robust least-squares inversion. Method selection was driven by numerical efficiency as well as subsurface geologic conditions. Numerically, robust least-squares inversion minimizes the absolute value of data misfit, which is an efficient technique in removing noise from the desired signal (Dahlin and Zhou, 2004). In homogeneous subsurface geology with sharp boundaries and fault-like features as current surveys targets, the robust least-squares inversion gives significantly better results than the other algorithms (Dahlin and Zhou, 2004; Advanced Geosciences Inc., 2006). The available data preparation and inversion parameters in EarthImager that were tested for optimum inversion results are categorized into initial forward modeling and inversion settings (Table 2.5). In the initial setting, minimum and maximum limits of voltage, absolute V/I, apparent resistivity, and reciprocal error were set to consider values outside these limits as an excess noise to be automatically removed. The forward modeling settings were a finite-element scheme to create a model with the Dirichlet boundary condition and Cholesky decomposition solutions. Blits (2008) and Tripathi (2009) assumed that layer thicknesses increase with depth, which means the resolution decreases with depth; therefore, thickness increment and depth factors were set at 1.1, and the number of mesh divisions set at 2. The

resistivity inversion settings are shown in Table 2.4. Smoothing and damping factors were set at 10 to avoid over-smoothing the resultant model (Tripathi, 2009). Both model width and height were set at 1 because it is necessary to preserve a 1:1 scale ratio, and the horizontal and vertical roughness ratio was set at 1.5 to enhance the effect of lateral variations along the profile (Tripathi, 2009).

Table 2.4: Electrical-resistivity field data acquisition parameters.

ERT-line	Array Type	Electrode Spacing (m)	Total Length (m)	Max. n	Max. Dipole	Measure Time (s)	Cycles	Max. Error (%)	Max. Repeat	Max. Current (mA)
ERT-1	Dipole-Dipole	6	498	8	6	1.2	2	2.0	1	2000
ERT-2	Dipole-Dipole	6	972	8	6	1.2	2	2.0	1	2000
ERT-3	Dipole-Dipole	6	498	8	6	1.2	2	2.0	1	2000

Table 2.5: The applied EarthImager inversion parameters to 2D electrical resistivity data.

Initial Settings		
Minimum voltage (mV)	0.2	
Minimum absolute (V/I)-ohm	0.0005	
Maximum repeat error	3%	
Minimum apparent resistivity (ohm-m)	1	
Maximum apparent resistivity (ohm-m)	10,000	
Maximum reciprocal error	5	
Inversion method	robust inversion	
Forward Modeling Settings		
Forward modeling method	finite element	
Forward equation solver	Cholesky decomposition	
Type of boundary condition	Dirichlet	
Number of mesh divisions	2	
Thickness incremental factor	1.1	
Depth factor	1.1	
Resistivity Inversion Settings		
Number of iterations	Stop Criteria	8
Maximum RMS error		2%
Error reduction		5%
Smoothing factor/damping factor	10	
Starting model	average apparent resistivity	
Model parameter width	1	
Model parameter height	1	
Resolution	0.2	
Horizontal/vertical roughness ratio	0.5-2.0	

CHAPTER THREE

3 SEISMIC DATA PROCESSING

3.1 Seismic-Reflection Data Processing

Seismic-reflection data are generally acquired in a common-midpoint (CMP) fashion. Common-midpoint surveys provide a subsurface sampling redundancy known as a "fold" of coverage that defines the number of linear superposition additions available to enhance the signal quality and decimate the noise. After field data are collected, seismic data processing is the next step. The acquisition parameters and conditions (e.g., field geometry, penetrating depth, surface condition, and survey purpose) are defined and written into the file headers. The data processing incorporates state-of-the art algorithms that yield a subsurface image represented by the response of the variation in lithologic elastic properties. Traditionally, the processed images are displayed in time domain. Relatively good raw-data quality is followed by a suitable processing strategy that makes the required corrections and delivers an interpretable seismic section in which the two-way travel time is a proxy for depth; however, it is indispensable to validate the subsurface information characterized by the seismic section with borehole information. Thus, migrating from the time domain to the depth (space) domain is beneficial.

Seismic-reflection data processing for shallow CMP-profiles (i.e., generally between 5 and 100 m) is different than the processing prescription for industry-scale hydrocarbon exploration. In this study, the first 500 and 200 ms are the time windows of interest for near-surface S- and P-wave surveys, respectively; however, these windows are often statically removed in oil-industry procedures. Thus, special attention needs to be paid to shallow reflections because they are embedded and/or overwhelmed with coherent, but nonreflective events (e.g., refracted and coherent noise events, etc.). Reflective and nonreflective events are identified and the coherent nonreflective events removed by careful muting. Otherwise, the resultant seismic-reflection profile will be biased by stacking nonreflective signal artifacts, which leads to misinterpreted geologic models.

Often, part or all of the shallowest reflective signal are top-muted along with refraction events because they cannot be effectively separated. Top-muting in this case becomes very difficult to apply using the available processing algorithms. Other processing steps are similar to those used in the oil industry, yet processing parameters are significantly different (e.g., deconvolution operator length > 100 ms, time variant BP filter, time variant AGC, and starting velocity of adaptive subtraction higher since the reflectors of interest are deeper).

Seismic-reflection SH-wave and P-wave data were processed on a Pentium-based microcomputer using the commercial signal-processing software Vista 12.0. Shallow-reflection processing procedures were considered to improve the prestack quality of the desired reflected signals in the raw field data. Each profile dataset was processed individually, but all the area-based parameters (e.g., bandpass filter, time-variant scaling, and deconvolution) were identical for uniformity. A general processing flow-chart (Fig. 3.1) was designed for all CMP reflection after preprocessing tests. Optimum processing parameters (Table 3.1) were sought throughout the preprocessing tests in order to make certain neither pitfalls nor over- or underestimated processing parameters exist in the final seismic sections (e.g., f-k filter, etc.). The preprocessing tests included bandpass filter, f-k filter, deconvolution type and operator length, and depth migration smoothing parameters. Frequency bandpass filtering is a mainstay to improve the signal-to-noise ratio. In order to design the high- and low-cut filters, a frequency spectrum was calculated for the raw SH-wave and P-wave data in order to characterize the overall frequency content (Fig. 3.2). Baker (1999) suggested the trial-and-error technique to estimate the effective reflection signals. Consequently, multiple bandpass filters were applied to the same dataset in order to determine the best frequency band that has minimal noise and highest reflective signals (Appendices A and B). A visual inspection method was used to compare the same dataset with different bandpass filters. The selected band pass filters were 20-30-75-85 Hz and 50-70-140-160 Hz for SH-wave and P-wave datasets, respectively. To attenuate the coherent noise, a frequency-wavenumber (f-k) filter was applied. Figure 3.3 is an example of an interactive f-k filter designation window. As a nontraditional practice, the f-k filter was applied in two steps. First, the

noise was rejected from the dataset using the f-k filter. Second, the rejected noise was adaptively subtracted from the original dataset. Adaptive subtraction eliminates the coherent noise and preserves the effective signal about the frequency component (Shaowu et al., 2009). The traditional method of f-k filtering was considered as a validation process for the nontraditional f-k filtering. The same f-k filter was therefore applied directly to the same dataset (Fig. 3.4). The results of the two methods were compared and the result demonstrated that adaptive subtraction eliminates much of the coherent noise, even multiples, more effectively than applying the f-k filter directly to the data (Fig. 3.5). The persistent high-frequency air-wave coherent noise was muted. At this level of data processing, reverberations and short-period multiples remain in the shot gathers. Yilmaz (2008) suggested that prestack deconvolution is capable of removing this noise as well as compressing the basic wavelet. In VISTA 12.0 software, three types of deconvolution are available: spiking, predictive, and zero-phase. All deconvolution algorithms require an operator length to run. In order to estimate the operator length, the VISTA 12.0 autocorrelation function was used to plot a normalized autocorrelation seismic trace. The normalized trace indicated that the largest amplitude was concentrated around 80 ms, thus providing the suitable operator length for the deconvolution (Fig. 3.6). As a preprocessing test, the selected operator length was further tested by applying spiking, predictive, and zero-phase deconvolution to the same dataset. This test helped determine the best algorithm for removing reverberation and multiples (Fig. 3.7). After careful visual inspection of the result of the three algorithms, the spiking deconvolution was selected. Figure 3.8 compares the final spiking deconvolution with the same dataset prior to spiking deconvolution. The same bandpass filter was reapplied after deconvolution to remove the added frequencies beyond the desired frequency band.

As a part of the detailed reflection-velocity analysis, the output of spiking deconvolution process was utilized to create the common velocity stack (CVS) and offset gathers. The traces of the same data set were sorted again from common-shot to CMP gathers to create the velocity semblance. Semblance, offset gathers, CMP gathers, and common velocity stack were synchronized in an interactive velocity window so that the estimated interval velocities and common velocity stack (reflection velocity model) could be

instantaneously cross-checked with the corrected offset and CMP gathers. The interactive velocity measurements were assumed equal to the normal-move-out (NMO) velocities. This assumption is valid only when the structural dips and/or lateral velocity changes are small (Baker, 1999). In case of steep structural dips, dip-move-out (DMO) correction is required along with NMO correction; thus, the two-way travel-time arrivals need to be corrected for both NMO and steep dipping reflector effects. Subsurface geologic information of the study area indicated no steep structural dip, so only NMO correction was necessary for the dataset.

Throughout the velocity model development in the interactive window, a top mute was designed. Since the velocities of refraction signals are faster than the velocities of reflection signals, correct velocity estimation for reflection signals is considered underestimated for refraction events at the same time and distance. Thus, the refraction events are stretched far more than the reflection signal so that the reflections stand out (Fig. 3.9). In other words, applying top mute after NMO correction separates refraction signals more efficiently with minimal reflection signal losses.

NMO correction and top mute were followed by two residual statics correction passes. The stack-power optimization function in VISTA 12 was used to compute the 2D surface-consistent statics. The output of this function was applied to the NMO-corrected, top-muted, and CMP-order dataset. Stack was performed to the static-corrected and CMP-gather traces. Often, in near-surface active-source seismic prospecting, strong hammer strikes generate more energy than needed. The excess energy is trapped in the near-surface bedding as reverberations as well as generating multiples. These reverberations and multiples are often preserved in the final-stacked seismic sections. Thus, three poststack processing methods were taken into account to improve the stacked data quality and to eliminate residual noises. First, GEDCO (2012) confirmed that the F-X 2D Prediction function in VISTA 12.0 smooths the data spatially in the frequency domain by eliminating random noise; therefore, it was applied to the stacked data. Subsequently, a poststack spiking deconvolution was applied to most of the seismic sections in order to remove the remnant reverberations and multiples. Third, after

applying deconvolution, the optimal bandpass filter was reapplied to the poststack data to aid in removing the added frequencies beyond the desired frequency band.

As an interpretation aid, as well as improving subsurface representation, a depth migration was applied to the poststack processed seismic sections. The calculated interval velocity was first smoothed to avoid signal stretches due to sharp velocity changes. Visual inspection followed in order to choose the optimum smoothing parameters for the final velocity model. An accurate velocity model is critical for calculating reflector depths. Thus, the velocity model used to generate the depth migration section was validated by comparing the migrated and unmigrated sections. The calculated depths were also compared with the corresponding borehole information for further assurance of accurate depth calculations. The results of processing procedures and depth migration are presented in chapter four.

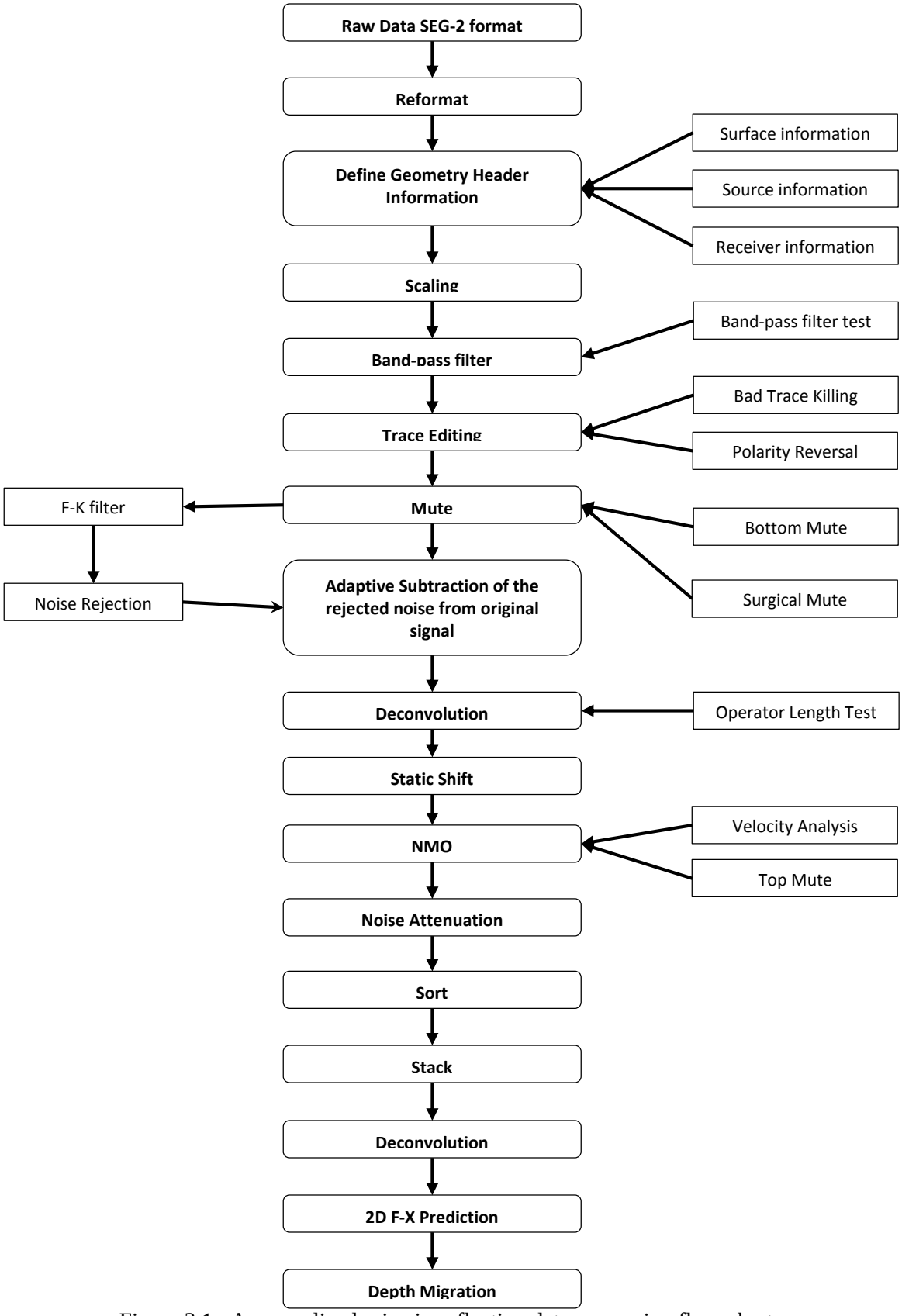

Figure 3.1: A generalized seismic-reflection data processing flow-chart.

Table 3.1: General shallow seismic-reflection data processing steps for the entire dataset using VISTA 12 software.

	Processing Functions	Parameters
1	Reformat	Convert the data from SEG-2 to VISTA12 internal format
2	Geometry	Geometry definition
3	Time-Variant Scaling	Scale: 1.000 RMS Trim Median Window Type: DYNAMIC SC Interpolation: LOGARITHMIC Define Time Windows by User Defined Time Windows 1: Start: 0.00 End: 100.00 Apply: 50.00 2: Start: 50.00 End: 150.00 Apply: 100.00 3: Start: 100.00 End: 300.00 Apply: 200.00 4: Start: 200.00 End: 400.00 Apply: 300.00 5: Start: 300.00 End: 500.00 Apply: 400.00 6: Start: 400.00 End: 600.00 Apply: 500.00
4	Data Scaling	Scale: 1.000 Mean Scale Gate Window: ENTIRE TRACE
5	Ormsby Band-Pass	20.00/30.00-75.00/85.00 Hz Domain Filter Application: Frequency Restore Mutes after Filtering Percent Zero Padding for FFT: 10.00 %
6	FK_Filter	F-K Designed Filter File Power: 1.00 TrcSmooth: 7 FreqSmooth: 5 F-K Filter Operation: PASS
7	Adaptive Subtraction	Time Domain Adaptive Subtraction Operator Lag: 10.00 ms Moving Window Shift: 80.000 % Output: Subtraction Start Time: 100.00 ms End Time: 1024.00 ms Start Time defined by NMO Velocity: 300.00 M/S Operator Len: 50.00 ms Pre-Whitening: 2.000 % Moving Window:300.00

Table 3.1: Continued.

	Processing Functions	Parameters
8	Surface consistent Deconvolution	Type: Spiking Decon Operator Length: 80.000 Pre-Whitening: 1.000 Components to Apply: 1 - Line Component 1 - SHOT_SEQUENCE_NUMBER : SC Decon Solve 2 - RECV_SEQUENCE_NUMBER : SC Decon Solve
9	Ormsby Band-Pass	20.00/30.00-75.00/85.00 Hz Domain Filter Application: Frequency Restore Mutes after Filtering Percent Zero Padding for FFT: 10.00 %
10	Normal Move-Out	Velocity Percent: 100.00 %
11	Muting	Interpolating, Offset[Trace] Dependent Taper Mute Zones by 4 Samples
12	Statics Shifts	Shot Static: STATIC_SRC [APPLY Shot Static] Recv Static: STATIC_REC [APPLY Recv Static] Combined Static: STATIC_TOTAL
13	Noise Attenuation	2D/3D Threshold Median Noise Attenuation/Replacement Window Length millisec. 75.000000, N Cdps to Smash 3 Median Length 13, Attenuation Multiplier 3.000000 Min Apply Freq: 0.00 Hz Max Apply Freq: 100000.00 Hz Sort Super-Gather by offset Threshold - Freq: 30.000000 Amplitude 2.000000
14	Common Mid-Points Stack	Stack: No Normalization of Stack CMP Stack Geometry Header Update: ON
15	2D F-X Prediction	Predicition Filter: 3 Design: 100 Cut: 60.000000 Power: 1.000000
16	Deconvolution	Type: Zero-Phase Decon Pre-Whitening: 1.000 Operator Length: 80.000 ms Apply Operator Taper: 10.00 ms Gate Window: ENTIRE TRACE
17	Ormsby Band-Pass	20.00/30.00-60.00/70.00 Hz Domain Filter Application: Frequency Restore Mutes after Filtering Percent Zero Padding for FFT: 10.00 %

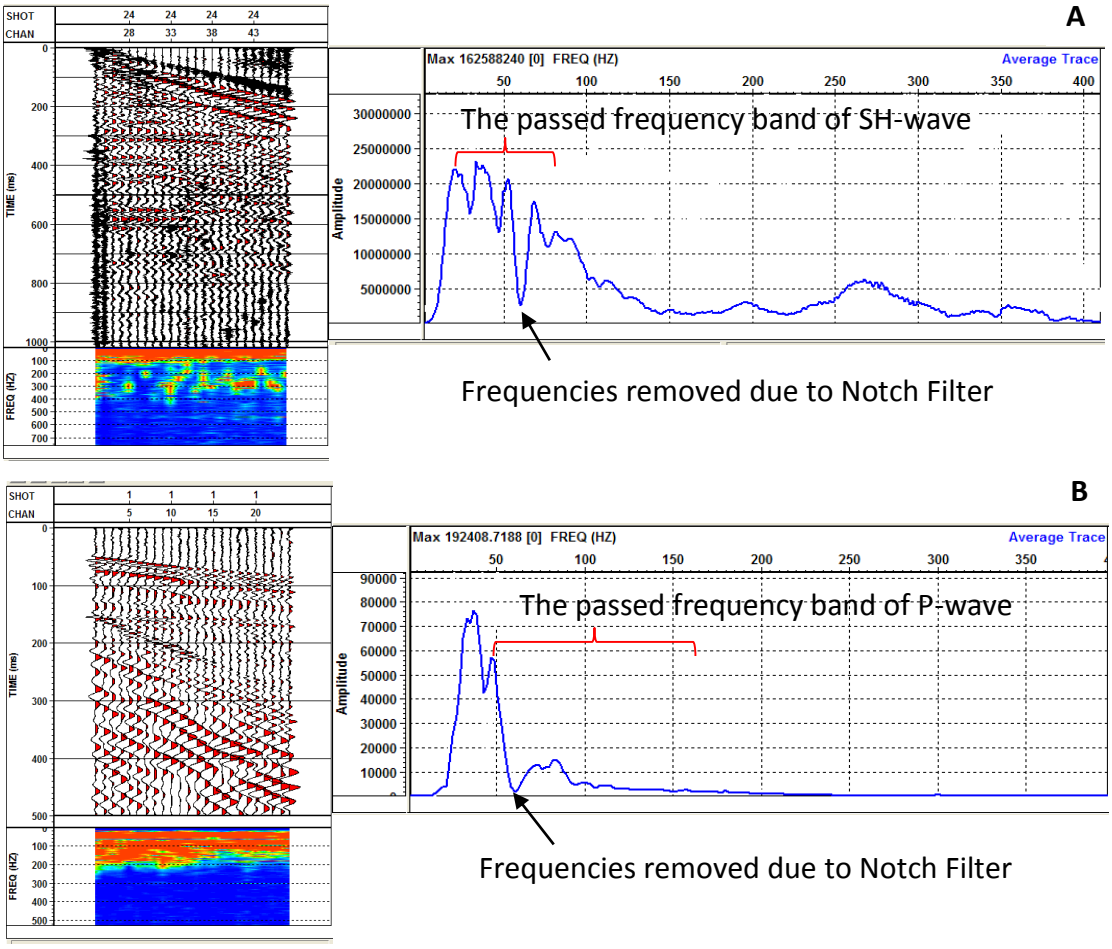

Figure 3.2: Frequency spectrum analysis. (A) SH-wave data. (B) P-wave data. Frequency spectrum indicates the overall frequency content, and trial-and-error method helped to resolve the optimum bandpass filter to improve effective reflective events and harsh the noise.

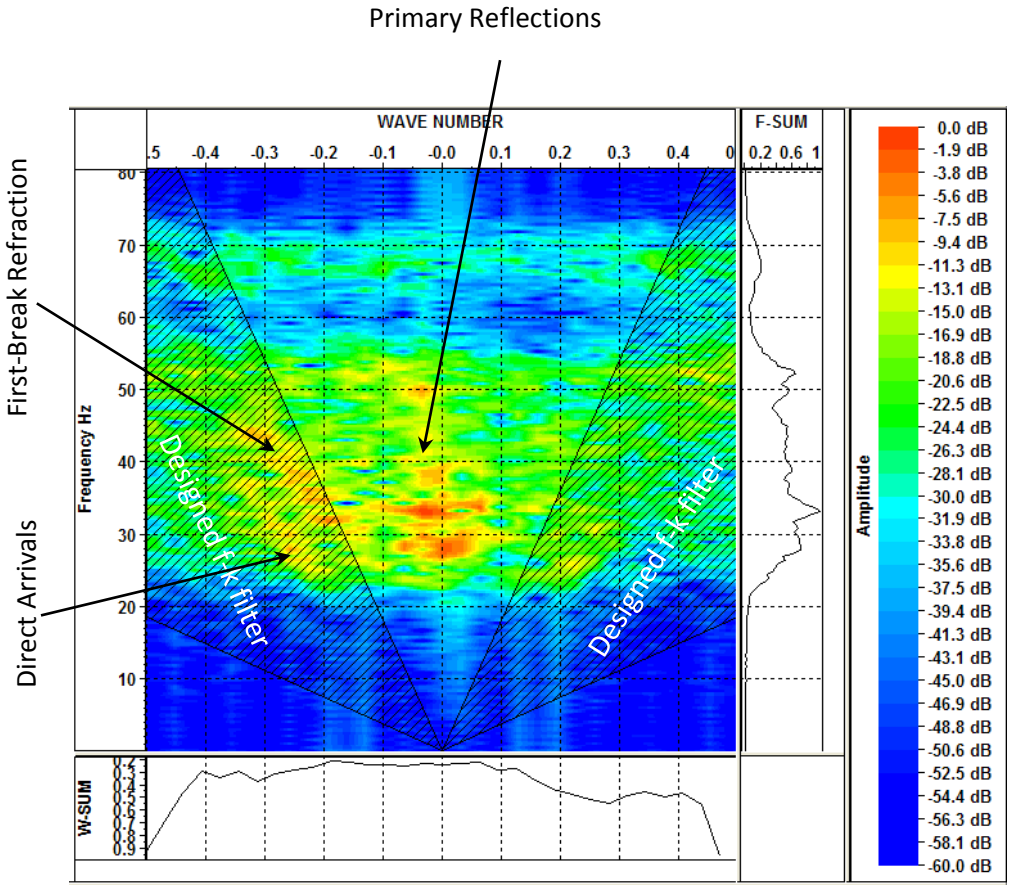

Figure 3.3: An example of interactive f-k filter designation window. Direct arrivals and first-break refraction were removed by the designed f-k filter so that the primary reflection events were enhanced.

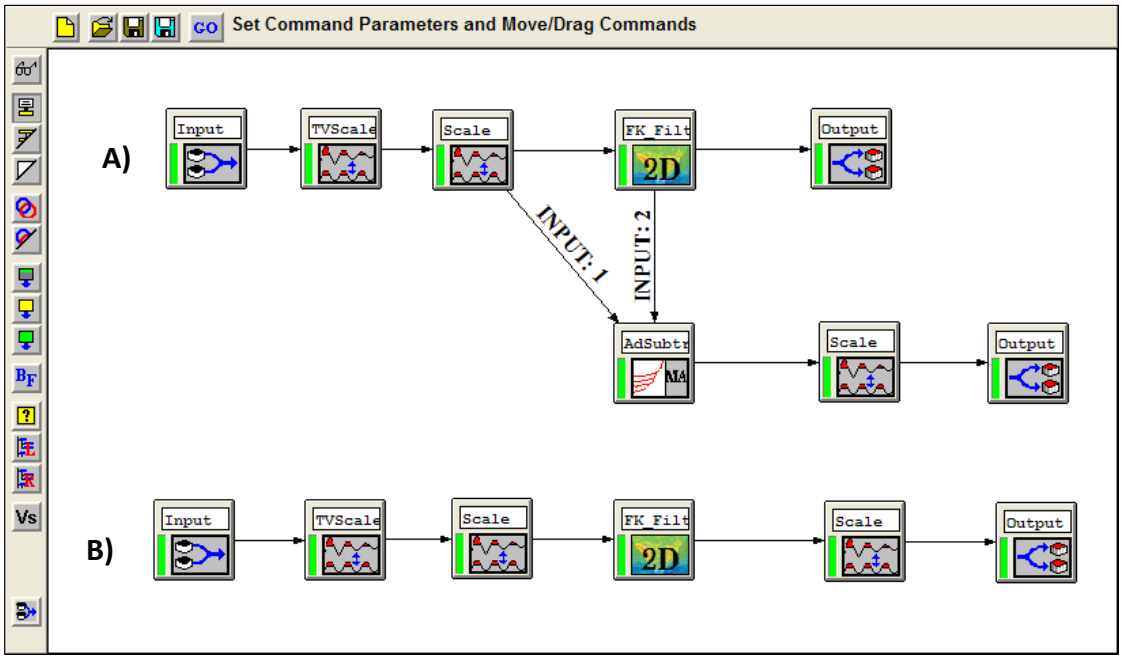

Figure 3.4: Flow-chart of f-k filter tests. (A) F-k noise rejected is adaptive subtracted from the data. (B) F-k filter is applied directly to the data.

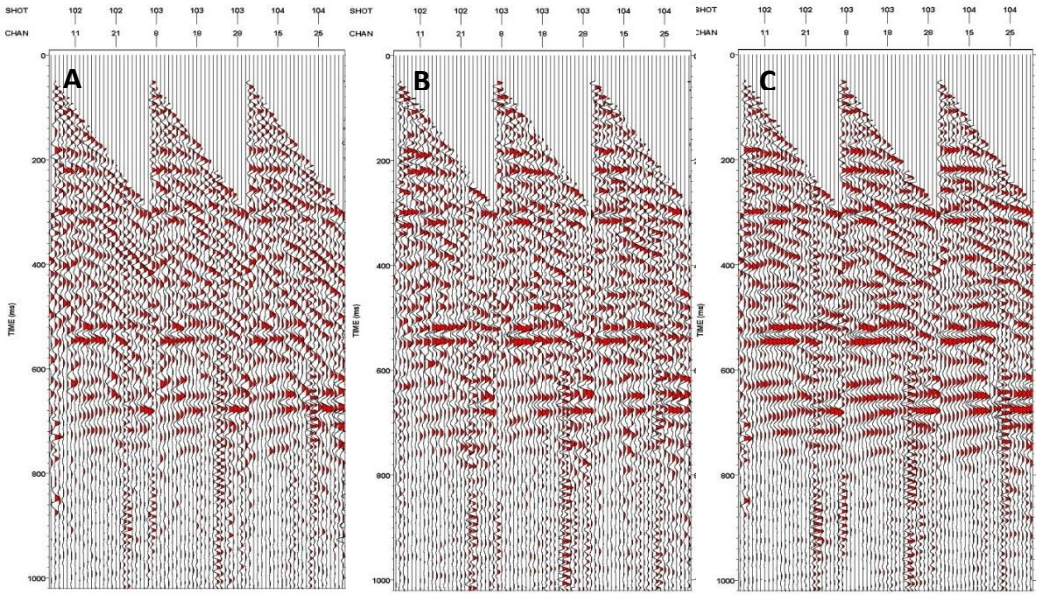

Figure 3.5: F-K filter test applied to field files records. A) Shot gathers before f-k filter B) Adaptive subtraction of f-k filtered noise from the original signal C) Same f-k filter applied directly to the data. F-K filter with adaptive subtraction showed better noise removal than the other method.

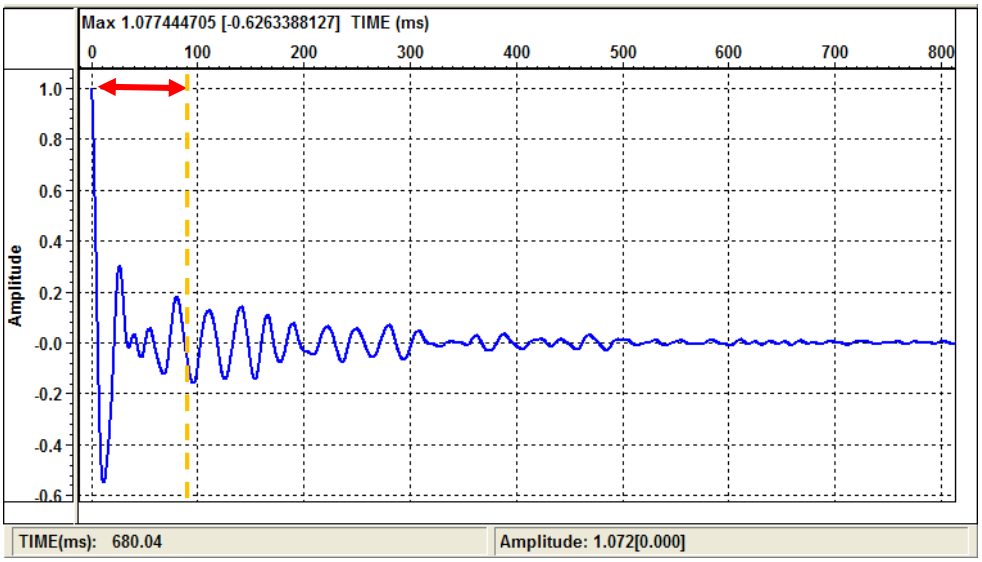

Figure 3.6: A normalized autocorrelation seismic trace. The effective signal is focused around 80 ms (red arrow), which refers to the best deconvolution operator length.

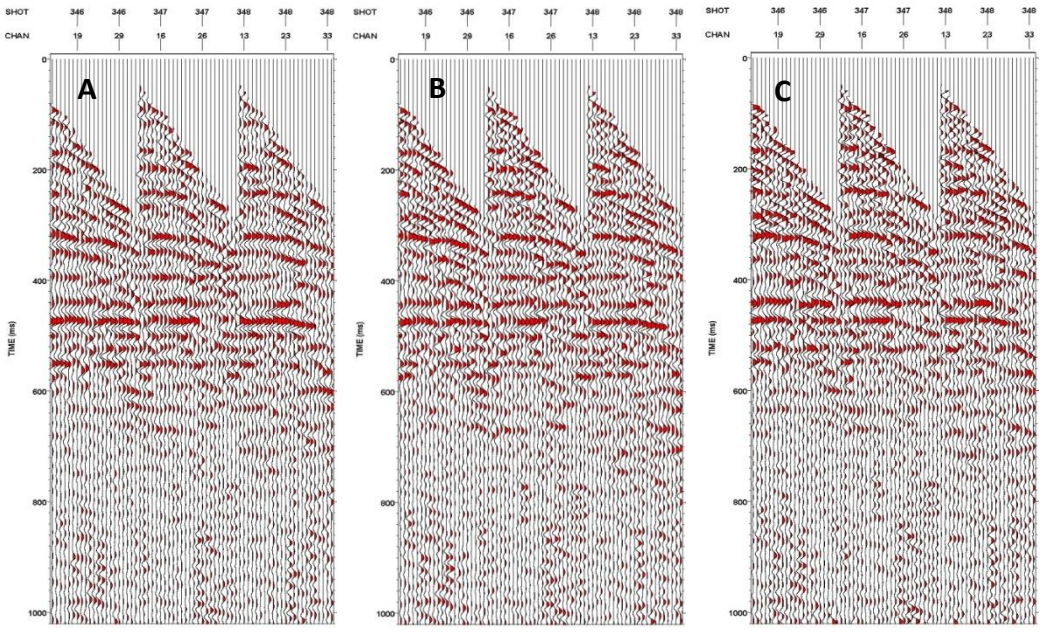

Figure 3.7: Deconvolution types tests. A) Zero-phase Deconvolution B) Predictive Deconvolution C) Spiking Deconvolution. The spiking Deconvolution showed better noise removal that the other two types.

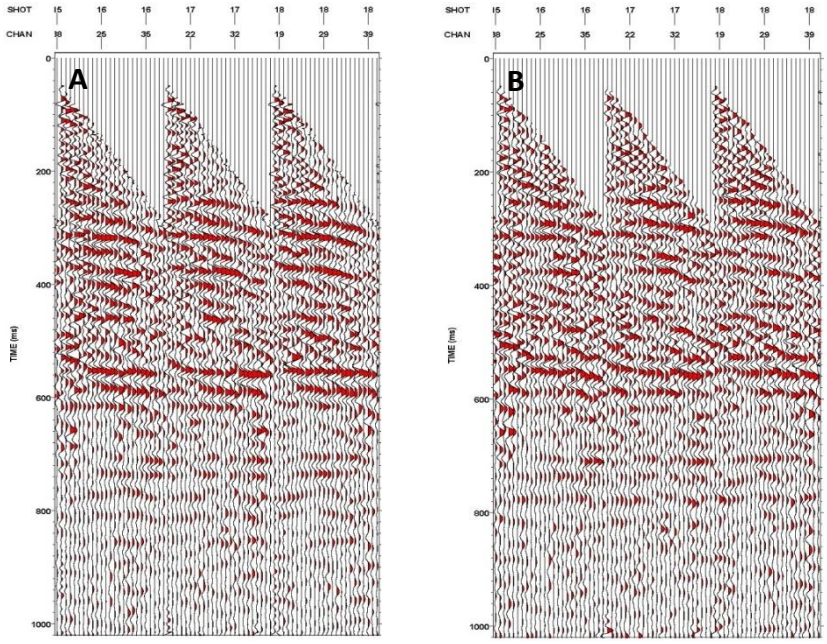

Figure 3.8: (A) Three consecutive field files before deconvolution and (B) after deconvolution. Spiking deconvolution attenuated the multiples and reverberations and enhanced the reflection signals.

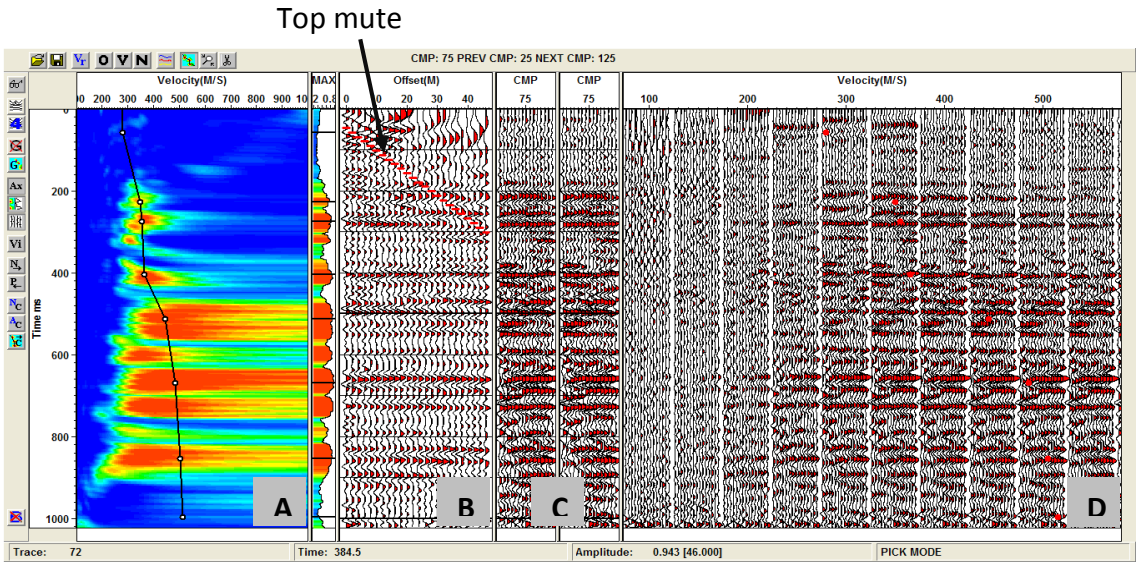

Figure 3.9: Interactive velocity window. A) Semblance velocity B) Offset gather C) CMP-gather D) Common stack velocity (CVS). Interval and common stack velocities as well as top mute were picked throughout this window. This is an effective procedure to ensure the correct velocity estimation by synchronizing the velocity picks and offset-gathers, CMP-gather, and semblance. Also, top mute designation at this processing step helps minimum reflection losses and maximum refraction removals.

3.2 Vertical Seismic Profile (VSP) Data Processing

A general procedure for processing VSP data was developed by combining the Lee and Balch (1983) and GEDCO (2012) methods (Fig. 3.10). Since each VSP dataset is unique in shooting and recording conditions, the detailed processing steps and parameters were optimized for this dataset by preprocessing tests. The data were collected with a three-component downhole geophone so that the dataset is a combination of three different oscillation directions (e.g., transverse, longitudinal, and vertical). Likely, the vertical component corresponded to converted SP-wave propagation and the horizontal components corresponded to two SH-wave propagation perpendicular to each other. Because the VSP borehole location was nearby, the SH-wave seismic-reflection sections (i.e., profile B), only horizontal components were considered. First-break picking, geometry setup, scaling, trace editing, and bandpass filtering were the primary process sequences in VSP data processing (Table 3.2). For best matching between VSP and SH-wave reflection sections, the same bandpass filter was applied to the dataset. The same f-k filter procedure was also applied to eliminate/attenuate the tube waves. Prestack deconvolution was considered to diminish multiples. To correct the VSP data for spherical divergence or transmission losses in the downgoing waves from the source to the 3C-geophone, and any possible borehole coupling effects, a 20-ms mean scale centered on the first arrivals at ~75–100 ms was applied. At this level of data processing, the dataset includes upgoing and downgoing wave fields. The upgoing wave field corresponds to the reflected waves; therefore, it was a useful signal to isolate downgoing wave fields in the dataset. Using the first-break picks, the downgoing wave field was flattened to an arbitrary datum (e.g., 100.00).

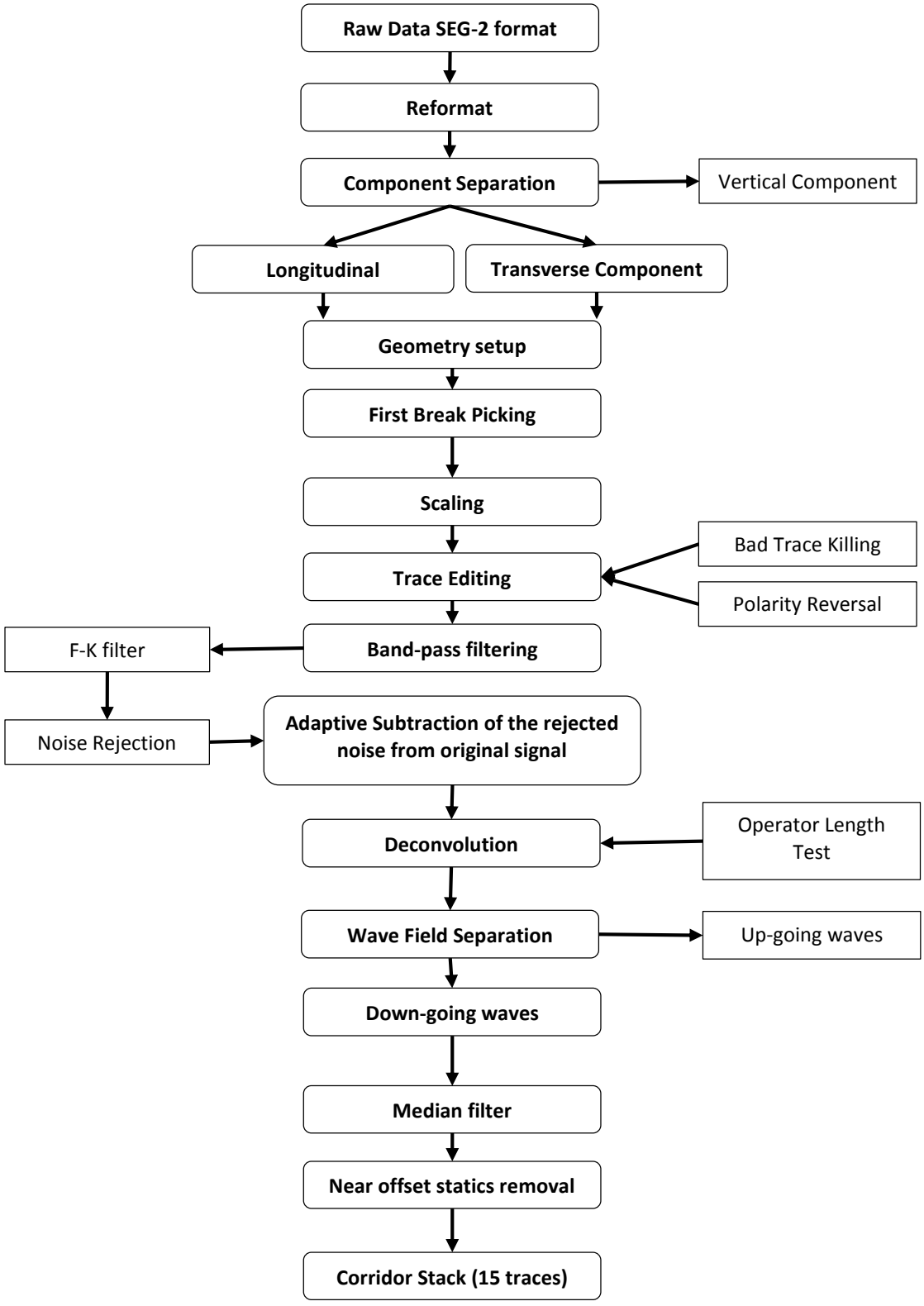

Figure 3.10: A generalized vertical seismic profile data processing flow-chart.

The upgoing wave field was separated from the downgoing wave field by applying a 13-point median filter (i.e., alpha trim mean filter). The flattened downgoing wave field was then arithmetically subtracted from the upgoing wave field. Near-offset statics removal was performed to the upgoing wave field. The data were aligned at the time coordinate equal to the two-way travel time in the 2D stacked seismic-reflection sections. Thus, the data were stacked into one single trace in the time domain. The stacked trace for both horizontal components was replicated to 15 traces (Fig. 3.11) in order to assist visual matching with 2D SH-wave seismic-reflection profiles. Again, the two horizontal components (the transverse and longitudinal directions) were arbitrarily oriented at each collecting point due to lack of orientation control of the 3C geophone. The final stacked VSP trace of the transverse and longitudinal components was visually inspected to decide which component better matched the seismic-reflection section. The stacked section in Figure 3.11A indicates the impedance boundaries that better match the SH-wave seismic-reflection section (Fig. 2.20) compared with the section in Figure 3.11B.

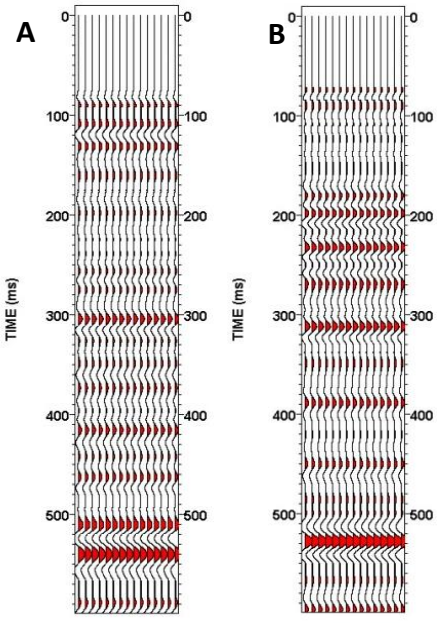

Figure 3.11: Vertical Seismic profile 15 traces stack of two horizontal components. A and B represent longitudinal and horizontal components that are arbitrarily aligned.

Table 3.2: Processing steps for vertical seismic profiling (VSP) data.

	Processing Functions	Parameters
1	Reformat	Convert the data from SEG-2 to VISTA12 internal format
2	Component Separation	Vertical, Two horizontal components (Longitudinal and Transverse)
3	Geometry set up	
4	First break picking	
3	Time-Variant Scaling	Scale: 1.000 RMS Trim Median Window Type: DYNAMIC SC Interpolation: LOGARITHMIC Define Time Windows by User Defined Time Windows 1: Start: 0.00 End: 100.00 Apply: 50.00 2: Start: 50.00 End: 150.00 Apply: 100.00 3: Start: 100.00 End: 300.00 Apply: 200.00 4: Start: 200.00 End: 400.00 Apply: 300.00 5: Start: 300.00 End: 600.00 Apply: 500.00
4	Data Scaling	Scale: 1.000 Mean Scale Gate Window: ENTIRE TRACE
5	Ormsby Band-Pass	20.00/30.00-75.00/85.00 Hz Domain Filter Application: Frequency Restore Mutes after Filtering Percent Zero Padding for FFT: 10.00 %
6	FK_Filter	F-K Designed Filter File Power: 1.00 TrcSmooth: 7 FreqSmooth: 5 F-K Filter Operation: PASS
7	Adaptive Subtraction	Time Domain Adaptive Subtraction Operator Lag: 10.00 ms Moving Window Shift: 80.000 % Output: Subtraction Start Time: 100.00 ms End Time: 1024.00 ms Start Time defined by NMO Velocity: 300.00 M/S Operator Len: 50.00 ms Pre-Whitening: 2.000 % Moving Window:300.00
8	Deconvolution	Type: Spiking Decon Operator Length: 80.000 Pre-Whitening: 1.000 Components to Apply: 1 - Line Component 1 - SHOT_SEQUENCE_NUMBER : SC Decon Solve 2 - RECV_SEQUENCE_NUMBER : SC Decon Solve
9	Ormsby Band-Pass	20.00/30.00-75.00/85.00 Hz Domain Filter Application: Frequency Restore Mutes after Filtering Percent Zero Padding for FFT: 10.00 %
10	Flatten (Statics)	Flatten Datum: 100.000 Header Item: Data first break
11	Alpha Trim Mean Filter (Median Filter)	ATM filter traces: 13 (1 samples)
12	Mute	Apply Top Mute Header Item: DATA_FIRSTBREAK Taper Mute Zones by 4 Samples
13	Exponential Gain	Exp. Gain: 1.500000
14	VSP Stack	Replicate Output Traces: 15

CHAPTER FOUR

4 RESULTS

4.1 Seismic Reflection Data

4.1.1 Resolution and Reflector Identification

In the seismic-reflection technique, vertical resolution is a direct relationship between the wavelength (i.e., seismic wave velocity and dominant frequency) and the vertical dimension separating the upper and lower boundary of a geologic feature. The minimum thickness of a subsurface geologic layer, or the threshold, in order to resolve its top and bottom is specifically defined by a quarter of the dominant wavelet length (Yilmaz, 2008). The shorter wavelength/higher dominant frequency yields a better vertical resolution according to the following equation:

$$\text{Vertical Resolution} = \frac{1}{4} Wavelength = 0.25 \text{ X } \frac{Velocity}{Frequency} \quad \ldots.(4.1)$$

Table 4.1 shows the calculated vertical resolution for the SH-wave seismic-reflection profile J1 and P-wave seismic-reflection profile J2. In the SH-wave reflection image, the vertical resolution for the Metropolis Formation and Mounds Gravel are between approximately 1 and 2 m. Thus, the Mounds Gravel, for instance, with a thickness greater than 2 m, will have its top and bottom boundaries resolved, but if the thickness is less than 2 m the formation will be detected as a single reflector. As the SH-waves travel deeper, the predominant frequency is decreased because of attenuation in the subsurface layering acting as a low-pass filter. Consequently, vertical resolution at bedrock is diminished to ~ 3 m. Although the P-wave reflection data have a higher predominant frequency than the SH-wave data, the vertical resolution is lower because the P-wave propagates at a much higher velocity than the SH-wave. Overall, this diminishes the P-wave resolvable thickness at bedrock to ~ 5 m.

Horizontal resolution is defined as the minimum distance between two geologic points that can be distinguished as two separate points along the total subsurface sampling of a

seismic-reflection profile. The total subsurface sampling length is calculated according to equation 4.2, which was modified after Dobrin (1976).

$$\text{Total subsurface sampling length} = \left(\frac{Geophone\ Spacing \times Max.\ CMPs\ number}{2}\right) - 1 \quad \ldots(4.2)$$

More specifically, the horizontal resolution is characterized by the fundamental Fresnel radius. This means that if two reflecting points fall within the first Fresnel zone, they are not recognized as separate and are indistinguishable on seismic images (Yilmaz, 2008). Fresnel radius and horizontal resolution can be quantitatively estimated by the following equation:

$$Horizontal\ Resolution = \frac{1}{2} V \sqrt{t/f} \quad \ldots.4.3 \qquad \text{(Yilmaz, 2008)}$$

where: V is velocity (m/s)

t is the two-way travel time to a specific reflector

f is frequency (Hz).

Table 4.2 shows the calculated horizontal resolution for SH-wave seismic-reflection profile J1 and P-wave seismic-reflection profile J2.

Table 4.1: The acceptable threshold for vertical resolution of most seismic-reflection profiles in the study area.

	P-wave					SH-wave				
	Interval Velocity (m/s)	Dominant Frequency (Hz)	Wave Length (λ) m	Vertical Resolution	Detectable Resolution	Interval Velocity (m/s)	Dominant Frequency (Hz)	Wave Length (λ) m	Vertical Resolution	Detectable Resolution
Metropolis (Me)	-	-	-	-		283.5	47.10	6.0	1.5	0.7
Mounds Gravel (MG)	-	-	-	-		341.1	46.56	7.3	1.8	0.9
McNairy (Mc)	1629.75	92.07	17.7	4.5	2.2	343.5	46.54	7.4	1.8	0.9
Bedrock (Br)	1873.75	91.93	20.3	5.1	2.5	510	38.66	13.2	3.3	1.6

Table 4.2: The acceptable threshold for horizontal resolution of the seismic-reflection profiles in the study area.

	P-wave				SH-wave			
	Interval Velocity (m/s)	Dominant Frequency (Hz)	Tow way Travel Time (ms)	Lateral Resolution (m)	Interval Velocity (m/s)	Dominant Frequency (Hz)	Tow way Travel Time (ms)	Lateral Resolution (m)
Metropolis (Me)	-	-	-	-	283.5	47.10	75	178.8
Mounds Gravel (MG)	-	-	-	-	341.1	46.56	200	353.3
McNairy (Mc)	1629.75	92.07	75	735.4	343.5	46.54	300	436
Bedrock (Br)	1873.75	91.93	150	1196.7	510	38.66	500	917

Within the available vertical resolution limits, these data can resolve layers as thin as ~1 m at shallow depths and ~ 3 m at 100 depths. Synthetic seismograms and VSP data were calculated from nearby boreholes in order to stratigraphically identify reflection events (Fig. 1.2). These data also spectrally matched the seismic-reflection sections relatively well (Figs. 2.20–2.21). The Paleozoic–Mississippian bedrock top (Br) is the deepest and often most prominent reflector in all profiles at approximately 500 ms two-way travel time (TWTT), or ~100 m depth. Normally, Br has a strong signal because of the high acoustic-impedance contrast/boundary it represents between lithified rock and the overlying semi- to unlithified sediment. A shallower and relatively high acoustic-impedance boundary at approximately ~300 ms TWTT (~50 m) is the Upper Cretaceous–Late Paleocene McNairy-Clayton (Mc) top. In the typical stratigraphic column, the McNairy-Clayton is overlain by the Paleocene Porters Creek Clay; however, the Porters Creek Clay has been eroded from most of the study site by the ancestral Tennessee River (Sexton, 2006). As a result, this reflector marks an erosional unconformity boundary between the McNairy-Clayton and the Pliocene Mounds Gravel (MG) (locally named Continental deposits). A shallower third reflector, the Mounds Gravel (MG), is exhibited at approximately 200 ms TWTT (~30 m). This impedance boundary segregates gravel and sand of the Mounds Gravel from overlying sandy clay and gravelly clays of the Late Miocene–Early Pleistocene Metropolis Formation. The Metropolis (Me) is the shallowest identified reflector at about 75 ms TWTT (~10 m). The boundary separates the surface deposits that are mainly silt and/or loess from the top of the Metropolis. The last three reflectors (Mc, MG, and Me) can sometimes appear weak and exhibit a discontinuous nature relative to the Br reflector because of their inherently much lower impedance contrasts. Figure 4.1 is an example of three consecutive field files from SH-wave reflection profile J1 in which the identified reflectors are present. In addition, the identified reflectors are consistent with previous investigators' findings (e.g., Woolery and Street, 2002; Sexton, 2006; Woolery et al., 2009). The final stacked seismic-reflection profiles in time domain were compared with the interpreted poststack depth-migrated sections (Figs. 4.2−4.23).

The TWTT of each identified reflector on each seismic profile was picked and then binned with the TWTT for the equivalent reflector on other seismic profiles. The

binned TWTT for each reflector was gridded and contoured in order to produce an individual time-structure map for each stratigraphic surface (Figs. 4.24−4.26). This is important to demonstrate the spatial or structural relationship for individual horizons as a function of TWTT. These time-structure surfaces were combined into a 3D view that enhances the vertical or "depth-wise" characteristics and the overall structural definition and geometric relationship (Fig. 4.27). The time-structure maps of Mounds Gravel and McNairy-Clayton tops were overlain with the depth-contour maps of Mounds Gravel and McNairy-Clayton tops from borehole information (Figs. 4.28−4.29). The combined maps showed agreement in the overall relative highs and lows between the seismic interpretation and borehole information. The IHS Kingdom Suites software license agreement expired before the time-structure map could be transformed to depth surfaces for comparison with the borelog-derived surfaces.

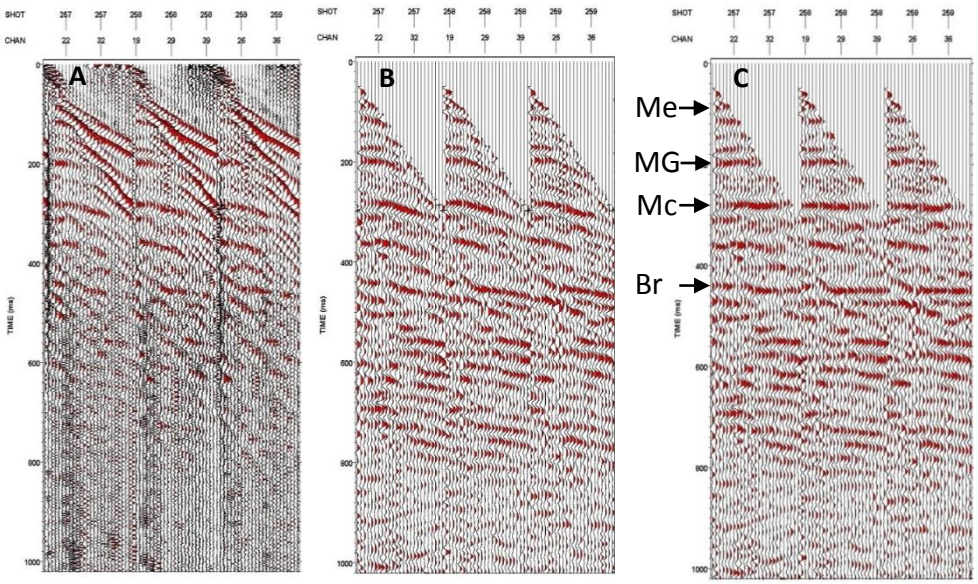

Figure 4.1: Three consecutive field records from SH-wave profile J1 showing the observed reflectors. (A) Raw data. (B) Filtered, top-muted, and scaled. (C) NMO corrected.

4.1.2 General Interpretation

The stratigraphic impedance boundaries and structural features seen on each subsurface image were interpreted using depth-migrated seismic-reflection sections. Depth-migrated sections provide a more accurate representation of the subsurface geology and can be directly related to the borehole information. The interpreted reflectors indicated very gentle slope or flat layering with some exceptions caused by structural interposed offsets. Hence, horizontal and vertical reflection discontinuities or "washed out" zones were used to interpret structural observations on the seismic-reflection images. In addition, fault interpretations were defined by (1) offset reflectors, (2) abrupt termination of strong reflection signals, (3) abrupt change in reflection dips, (4) diffraction patterns, and (5) associated folds. These rubrics were correlated between profiles to trace any major structural feature spatially across the study area, and to determine the feature's geographic orientation. Any minor structural feature on a particular seismic profile that could not be correlated with other profiles was considered an in-situ minor feature; these features are discussed in the next section. The Paleozoic bedrock reflector (Br), a strong and coherent impedance boundary in most of the seismic-reflection profiles, was the main guide for identifying structural features; most of the structural features that were seen at the Paleozoic bedrock reflector extend to as deep as Pleistocene sediments. But because of the inherently unconsolidated nature of the shallow sediments, near-surface reflectors manifested relatively smaller fault offsets and broader washouts zones than exhibited along the Br reflector. Total offsets were delineated by measuring depth displacements across a particular fault from intact points. More details about specific fault offsets on every seismic-reflection profile are addressed in the next section.

In general, structures across the bedrock appeared as normal faults on the bedrock reflector, but there is clear evidence of post-Paleozoic episodic tectonic activity that has deformed Cretaceous, Tertiary, and Quaternary sediments. The major structural features that were correlated on multiple seismic images were classified as northeast-southwest normal displacement fault sets (Fig. 4.30). These fault sets are parallel with and extensions of the surface mapped normal displacement faults in southern Illinois, called the Fluorspar Area Fault Complex (Fig. 1.3). The intense faulting with parallel strikes of northeast-southwest trend may provide a preferential flow path for groundwater

movement. The structure appears coincident with the northeastern and northwestern paths of contamination plume migration (Figs. 4.24B, 4.25B, 4.26B).

4.1.3 Profile Interpretations

4.1.3.1 Profile A1

Line A1 is an SH-wave profile and consists of 262 shotpoints to represent 1091 m total subsurface sampling length. It was acquired along an unpaved road that is oriented east-southeast−west-northwest. Langston et al. (1998) collected the nonproprietary raw data for a general reconnaissance survey related to groundwater investigations. Data quality is fair and representative of the entire line. Reflector identification on this line was controlled by information from nearby boreholes and vertical seismic profile data (Fig. 1.2) available from the seismic lab at the Department of Earth and Environmental Sciences at the University of Kentucky and the U.S. Department of Energy. Three seismic marker beds were identified on the section: Br, Mc, and MG (Fig. 4.2). The Br reflector is a prominent contact between unlithified sediment and the underlying bedrock at about 155 m depth at the eastern end of the line and about 105 m depth at the western end. Mc was interpreted as the top of the McNairy at about 250 ms (50 m) and MG was interpreted as the top of the Mounds Gravel at ~150 ms (25 m). They appear weak and less coherent than Br. Depth differences across the relatively short line suggest structural displacements. A reflector washout zone was observed between trace numbers 432 and 120. It is interpreted as part of a series of normal faults merged into Fault Zone 1 (FZ-1) or a deformation zone that fades out the reflectors. The structural feature that was seen on the Br also extends across the Mc and MG, Cretaceous and Pliocene/Pleistocene sediments. The total displacement across the area from intact points is approximately 50 m. The strong Br reflector exhibits apparent downthrow to the east-southeast. Although Mc and MG reflectors are intermittent and have less coherent characteristics, the measured displacements are 25 and 20 m, respectively. These observations lead to the conclusion that high-angle normal faults evident at Br have occurred in the post-Paleozoic, with small-scale reactivation events having occurred in post-Cretaceous and younger sediments.

4.1.3.2 Profile A2

Line A2 is an SH-wave profile and consists of 165 shotpoints representing 703 m total subsurface sampling length. It was acquired along an unpaved road that is oriented east-west. Langston et al. (1998) collected the nonproprietary raw data for a general reconnaissance survey related to groundwater investigations. Data quality is fair and representative of the entire line. Reflector identification on this line was controlled by nearby borehole information and VSP data (Fig. 1.2) available from the UK seismic lab and DOE. Three seismic marker beds were identified on the section: Br, Mc, and MG (Fig. 4.3). The bedrock marker (Br) was picked at about 500 ms (~120 m average) and was expected to be a prominent contact between unlithified sediment and the underlying bedrock. However, it is faded out across nearly two-thirds of the line. This may be a result of faulting/deformation. Mc and MG were interpreted as tops of McNairy and Mounds Gravel, respectively. They appear weak and less coherent than Br and were picked at about 300 ms (70 m) and 200 ms (40 m), respectively. Depth of the bedrock reflector at the eastern end of the line is ~110 m, but it deepens to ~125 m at the western end. Changes in Br depth are because of a series of fault set displacements merged into Fault Zone 2, a major fault zone. It was observed at about trace numbers 84 to 276. The fault sets within the fault zone are aligned close enough to each other, so that Fault Zone 2 appears to be deformation areas or washout. Such structural characteristics have led to difficulty in distinguishing individual faults within a fault zone. The structural feature that was seen along the Br extends across the Mc and MG, Cretaceous and Pliocene/Pleistocene sediments. The total displacement across Fault Zone 2 from intact points is approximately 15 m. The relatively strong Br reflector exhibits apparent downthrow to the west- northwest. The intermittent and less coherent characteristics of the Mc and MG reflectors have reduced the confidence level of assessing the magnitude of near-surface displacement and dip angle. These observations indicate that the structures evident at Br have occurred in the post-Paleozoic with small-scale reactivation in post-Cretaceous and younger sediments.

4.1.3.3 Profile A3

Line A3 is an SH-wave profile and consists of 408 shotpoints representing 1677 m total subsurface sampling length. It was acquired along an unpaved road that is oriented east-southeast−west-northwest. Langston et al. (1998) collected the nonproprietary raw data for a general reconnaissance survey related to groundwater investigations. Data quality is fair and representative of the entire line. Reflector identification on this line was controlled by nearby borehole information and VSP data (Fig. 1.2) available from the UK seismic lab and DOE. Three reflectors were identified on the section: Br, Mc, and MG (Fig. 4.4). The bedrock horizon (Br) is a prominent contact between unlithified sediment and the underlying bedrock, and was picked at about 500 ms (~120 m average). Mc and MG were interpreted as tops of McNairy and Mounds Gravel, respectively. They appear weak and less coherent than Br and were picked at about 300 ms (70 m) and 200 ms (40 m), respectively. Depth of the bedrock reflector at the eastern end of the line is ~150 m, but it deepens to ~115 m at the western end. Changes in Br depth are caused by a series of fault set displacements merging into Fault Zone 3. Fault Zone 3 manifests as a washout area seen between trace numbers 135 and 675. The fault sets within the fault zone are aligned close to each other. Such a structural setting has led to difficulty in distinguishing individual faults within the fault zone. The structural feature that was seen at Br occurs at Mc and MG, which means Paleozoic tectonic deformation has extended into Cretaceous and Pliocene/Pleistocene sediments. The total displacement across Fault Zone 3 from intact points is approximately 14 m. The relatively strong Br reflector exhibits apparent downthrow to the east-southeast. Although Mc and MG reflectors are intermittent and have less coherent characteristics, the measured displacements are 7 and 4 m, respectively. These observations lead to the conclusion that high-angle normal faults evident at Br have occurred in the post-Paleozoic, with small-scale reactivation in post-Cretaceous and younger sediments.

4.1.3.4 Profile B

Line B is an SH-wave profile and consists of 1071 shotpoints representing 4327 m total subsurface sampling length. It was acquired along a paved highway that is oriented west-northwest−east-southeast. Langston et al. (1998) collected the nonproprietary raw data for a general reconnaissance survey related to groundwater investigations. Data quality is good and representative of the entire line, but signal/noise ratio is reduced between trace numbers 1250 and 1750 because the profile passes beneath overhead power lines. Hence, the noticeable amplitude decrease within this area does not necessarily indicate a change in the subsurface geologic conditions. Reflector identification on this line was controlled by nearby borehole information and VSP data (Fig. 1.2) available from the UK seismic lab and DOE. Three reflectors were identified on the section: Br, Mc, and MG (Fig. 4.5). The bedrock horizon (Br) is a prominent contact between unlithified sediments and the underlying bedrock, and was interpreted at an average of 500 ms (~115 m). Mc and MG were interpreted as tops of McNairy and Mounds Gravel, respectively. They appear weak and less coherent than Br and were picked at about an average of 300 ms (50 m) and 200 ms (30 m), respectively. The first structural feature was seen at the Br reflector between trace numbers 150 to 800. This feature consists of a series of normal faults that extend into Cretaceous and Pliocene/Pleistocene sediments. The fault setting within the structure forms a graben-like structure. This structure appears in line with Fault Zone 2 and Fault Zone 3 that were observed on profiles A2 and A3. Improved data quality along this profile provides a better image of the faults compared with profiles A2 and A3. Normal faulting in the bedrock and the overlying unconsolidated sediments are interpreted from the downdropped structure. The offsets of the normal faults within the graben-like feature vary between 5 and 24 m. The close association between the normal fault offsets of this structure and Fault Zones 2 and 3 suggests a spatial along-strike correlation with these structures. The composite orientation for the structures is northeast-southwest (~ N45°E). Most of the structural features seen at Br extend into the Mc and MG, Cretaceous, and much of the Pliocene/Pleistocene sediments. The mapped location of the northwest plume falls between trace numbers 200 and 550, coincident with this structure. This suggests that the structure provides a preferential fluid-flow path. Between trace numbers 810 and 918, two normal faults with down-to-east displacement were interpreted. Total offset of

both faults is about 16 m. The interpreted faults at bedrock appear to cut through Cretaceous and much of the Pliocene/Pleistocene sediments. A horst-like structure was noticed between traces 1000 and 1458. The average fault displacements at the Br reflector is 27 m. A set of normal faults with total offset of about 33 m was interpreted as the Br reflector between trace numbers 1674 and 2106. This feature was formed by three normal faults that extend into Cretaceous and Pliocene/Pleistocene sediments. The fault sets are aligned with Fault Zone 1, which was seen on profile A1. Improved data quality for this profile provides a better image of the fault compared with profile A1. The similar characteristics between this fault and Fault Zone 1 on profile A1 indicate a structural correlation and continuation between the two lines. The mapped location of the northeast plume is between trace numbers 1800 and 2150, coincident with this structure. This suggests that the structure provides a preferential flow path for groundwater and the contamination plume. Although the Mc and MG reflectors are intermittent and have less coherent characteristics, fault displacements appear less than the Br reflector. These observation lead to the conclusion that the high-angle normal faults evident at Br have occurred in the post-Paleozoic, with small-scale reactivation in post-Cretaceous and younger sediments.

4.1.3.5 Profile C1

Line C1 is an SH-wave profile and consists of 297 shotpoints to represent 1229 m total subsurface sampling length. It was acquired along a paved road that is oriented north-northeast−south-southwest. Langston et al. (1998) collected the nonproprietary raw data for a general reconnaissance survey related to groundwater investigations. Data quality is fair and representative of the entire line. Reflector identification on this line was controlled by nearby borehole information and VSP data (Fig. 1.2) available from the UK seismic lab and DOE. Three reflectors were identified on the section: Br, Mc, and MG (Fig. 4.6). The bedrock marker (Br) is a prominent contact between unlithified sediment and the underlying rock, and was picked at about an average of 500 ms (~130 m). Mc and MG were interpreted as tops of McNairy and Mounds Gravel, respectively, and appear weak and less coherent than Br. They were picked at about an average of 300 ms (~70 m)

and 200 ms (~40 m), respectively. Depth of the bedrock reflector at the northern end of the line is ~113 m, but it deepens to ~154 m at the southern end. Br depth differences across the relatively short line are caused by a series of normal fault set displacements. This feature was seen at trace number 75 and continues toward the end of the line. The total offset is about 32 m and appears to be closely associated with the Fault Zone 1 total offset on profiles A1 and B. Spatially, this structure, which was seen on Br, is in line with Fault Zone 1 and extends across the Mc and MG, Cretaceous, and Pliocene/Pleistocene sediments. The relatively strong Br reflector exhibits apparent downthrow to the east-southeast. The estimated displacement on Mc and MG were 25 and 20 m, respectively. These observations lead to the conclusion that the high-angle normal faults evident at Br have occurred in the post-Paleozoic, with small-scale reactivation in post-Cretaceous and younger sediments.

4.1.3.6 Profile C1-S

Line C1-S is an SH-wave profile and consists of 48 shotpoints to represent 236 m total subsurface sampling length. It was acquired along a paved road that is oriented north-northeast−south-southwest. Langston et al. (1998) collected the nonproprietary raw data for a general reconnaissance survey related to groundwater investigations. Data quality is fair and representative of the entire line. Reflector identification on this line was controlled by nearby borehole information and VSP data (Fig. 1.2) available from the UK seismic lab and DOE. Three reflectors were identified on the section: Br, Mc, and MG (Fig. 4.7). The bedrock marker (Br) is a prominent contact between unlithified sediment and the underlying bedrock, and was picked at about an average of 600 ms (~130 m). Mc and MG were interpreted as tops of McNairy and Mounds Gravel, respectively. They were picked at about an average of 300 ms (~60 m) and 200 ms (~30 m), respectively. Depth of the bedrock reflector at the northern end of the line is ~150 m, but it deepens to ~135 m at the southern end. Br depth differences across a short line are caused by normal fault set displacements. The fault was seen between trace numbers 17 and 50, with total offset of about 32 m and apparent downthrow to the northwest. These fault characteristics are closely associated with the offset measured for Fault Zone 1 on profiles A1 and B.

The structural features that were seen at Br also occur at Mc and MG, which means Paleozoic tectonic disruptions have extended to Cretaceous and Pliocene/Pleistocene sediments. This observation leads to the conclusion that a high-angle fault at Br occurred in the post-Paleozoic, with small-scale reactivation in post-Cretaceous and younger sediments.

4.1.3.7 Profile C2

Line C2 is an SH-wave profile and consists of 168 shotpoints to represent 713 m total subsurface sampling length. It was acquired along a paved road that is oriented east-southeast−west-northwest. Langston et al. (1998) collected the nonproprietary raw data for a general reconnaissance survey related to groundwater investigations. Data quality is fair and representative of the entire line. Reflector identification on this line was controlled by nearby borehole information and VSP data (Fig. 1.2) available from the UK seismic lab and DOE. Three reflectors were identified on the section: Br, Mc, and MG (Fig. 4.8). The bedrock marker (Br) was picked at about 500 ms(~120 m average) and expected to be a prominent contact between unlithified sediment and the underlying bedrock. However, it fades out along the line. This may be a result of intense faulting/deformation areas. Mc and MG were interpreted as tops of McNairy and Mounds Gravel, respectively. They appear weak and incoherent and were picked at about ~300 ms (50 m) and ~200 ms (30 m), respectively. Depth of Br at the eastern end of the line is ~150 m, but it shallows to ~125 m at the western end. Br depth differences across a short line are caused by normal fault set displacements. The faults sets at Br were seen between trace numbers 50 and 300, with total offset of about 20 m and apparent downthrow to the east- southeast. This structure is not correlated with other fault zones. The fault sets that were seen at Br extend into Mc and MG (i.e., Paleozoic tectonic deformation has occured in Cretaceous and Pliocene/Pleistocene sediments). Mc and MG have less coherent characteristics, showing displacements of about 10 and 7m, respectively. Post Cretaceous and younger sediments manifest slight thickening eastward, which suggests a tectonic component (i.e., sediments onlapped the preexisting normal faults). These observations

lead to the conclusion that the high-angle normal faults evident at Br have occurred in the post-Paleozoic, with small-scale reactivation in post-Cretaceous and younger sediments.

4.1.3.8 Profile C3

Line C3 is an SH-wave profile and consists of 204 shotpoints to represent 781 m total subsurface sampling length. It was acquired along a paved road that is oriented east-southeast−west-northwest. Langston et al. (1998) collected the nonproprietary raw data for a general reconnaissance survey related to groundwater investigations. Data quality is fair and representative of the entire line. Reflector identification on this line was controlled by nearby borehole information and VSP data (Fig. 1.2) available from the UK seismic lab and DOE. Three reflectors were identified on the section: Br, Mc, and MG (Fig. 4.9). The bedrock marker (Br) is a prominent contact between unlithified sediment and the underlying bedrock, and was picked at an average of about 500 ms (~100 m). Mc and MG were interpreted as tops of McNairy and Mounds Gravel, respectively. They appear weak and less coherent than Br and were picked at about an average of 300 ms (~50 m) and 200 ms (~25 m), respectively. Depth of the bedrock reflector is at approximately ~123 m on the eastern end of the line and at about ~95 m at the western edge. Depth differences across the relatively short line suggest structural offset. Two primarily normal fault zones were observed on the profile. The first fault zone caused Br and other reflectors to be laterally discontinuous between trace numbers 1 and 100. The total displacement is about 28 m. The second fault zone is limited to within trace numbers 225 and 300. The fault zone displacement is about 13 m. Both fault zones are in line with graben-like structure seen on profile B. The relatively strong Br reflector exhibits apparent downthrow to the east- southeast. The structural features that were seen at Br occur at Mc and MG (i.e., Paleozoic tectonic disruptions have extended to Cretaceous and Pliocene/Pleistocene sediments). Mc and MG are less coherent and intermittent, leading to a less confidence in assessing the magnitude of near-surface displacement and dip. These observation lead to the conclusion that the structures evident at Br have occurred in the post-Paleozoic, with small-scale reactivation in post-Cretaceous and younger sediments.

4.1.3.9 Profile D

Line D is an SH-wave profile and consists of 132 shotpoints representing 547 m total subsurface sampling length. It was acquired along a paved road that is oriented west-northwest−east-southeast. Langston et al. (1998) collected the nonproprietary raw data for a general reconnaissance survey related to groundwater investigations. Data quality is fair and representative of the entire line. Reflector identification on this line was controlled by nearby borehole information and VSP data (Fig. 1.2) available from the UK seismic lab and DOE. Three reflectors were identified on the section: Br, Mc, and MG (Fig. 4.10). The bedrock marker (Br) is a prominent contact between unlithified sediment and the underlying bedrock, and was picked at an average of about 580 ms (~105 m). Mc and MG were interpreted as tops of McNairy and Mounds Gravel, respectively. They appear weak and less coherent than Br and were picked at about an average of 275 ms (~46 m) and 92 ms (~13 m), respectively. Depth of the bedrock reflector is at ~125 m on the western end of the line and ~105 m on the eastern edge. Depth differences across the relatively short profile suggest three normal fault zone displacements. The first fault zone was seen between trace numbers 36 and 70 and has a total offset of about 10 m, and the displacements were measured at 6 m on Mc. There are two possible interpretations pertaining to this fault zone on MG: (1) The movement did not propagate into the younger sediments (i.e., Tertiary and Quaternary) and a channel feature exists and defines the abrupt MG downbend between trace numbers12 and 65 and (2) The fault zone extended to MG, but with reverse reactivation movement associated with a compressive stress regime. The second fault zone was observed between trace numbers 125 and 156. The total offset across the fault zone is about 5−7 m. Both fault zones form a downdropped block. The structural features that were seen on Br also extend into the Mc and MG, Cretaceous, and Pliocene/Pleistocene sediments, with less offset across both faults zones. These observations suggest that the structures evident at Br have occurred in the post-Paleozoic, with small-scale reactivation in post-Cretaceous and younger sediments.

4.1.3.10 Profile E

Line E is an SH-wave profile and consists of 120 shotpoints representing 471 m total subsurface sampling length. It was acquired along a paved road that is oriented north-northeast−south-southwest. Langston et al. (1998) collected the nonproprietary raw data for a general reconnaissance survey related to groundwater investigations. Data quality is fair and representative of the entire line. Reflector identification on this line was controlled by nearby borehole information and VSP data (Fig. 1.2) available from the UK seismic lab and DOE. Three reflectors were identified on the section: Br, Mc, and MG (Fig. 4.11). Bedrock (Br) and McNairy (Mc) were traced at an average of 500 ms (~128 m) and an average of 300 ms (~55 m), respectively. Br was expected to be a prominent contact between unlithified sediment and the underlying bedrock. However, it is intermittent and incoherent along the line. This may be a result of intense faulting/deformation or in-situ poor impedance boundary. MG was interpreted as top of Mounds Gravel and was picked at an average of ~126 ms (16 m). A normal fault was interpreted between trace numbers 60 and 110. An apparent downthrow to the north-northeast was noticed on both Br and MG. The fault displacement at Br is 18 m and decreased at MG to 3 m. These observation lead to the conclusion that high-angle faults evident at Br have occurred in the post-Paleozoic, with small-scale reactivation in post-Cretaceous and younger sediments.

4.1.3.11 Profile F

Line F is an SH-wave profile and consists of 252 shotpoints to represent 1025 m total subsurface sampling length. It was acquired along a paved road that is oriented east-southeast−west-northwest. Woolery and Street (2003) collected the nonproprietary raw data for a general reconnaissance. Data quality is poor and representative of the entire line. Three reflectors were traced and identified on the section: Br, Mc, and MG (Fig. 4.12). The bedrock marker (Br) was picked at about 500 ms (~100 m average) and expected to be a prominent contact between unlithified and the underlying bedrock. However, it fades out along most of the line. This may be a result of intense faulting/deformation or poor impedance boundary. Mc and MG were interpreted as tops of McNairy and Mounds Gravel, respectively. They appear weak and incoherent and

were picked at ~300 ms (65 m) and ~175 ms (30 m), respectively. Poor data quality did not allow any fault displacement to be interpreted.

4.1.3.12 Profile G1

Line G1 is an SH-wave profile and consists of 710 shotpoints to represent 2721 m total subsurface sampling length. It was acquired along an unpaved road that is oriented northeast-southwest. Langston et al. (1998) collected the nonproprietary raw data for a general reconnaissance survey related to groundwater investigations. Data quality is fair and representative of the entire line. Reflector identification on this line was controlled by nearby borehole information and VSP data (Fig. 1.2) available from the UK seismic lab and DOE. Three reflectors were identified on the section: Br, Mc, and MG (Fig. 4.13). The bedrock marker (Br) is a prominent contact between unlithified sediment and the underlying bedrock, and was picked at an average of 515 ms (~125 m). Mc and MG were interpreted as tops of McNairy and Mounds Gravel, respectively. They appear weak and less coherent than Br and were picked at about 260 ms (55 m) and 170 ms (32 m), respectively. The line runs approximately between Fault Zone 2 and Fault Zone 3. At the northern end of the line to trace number 650, a wide normal fault zone (F1) was interpreted on the Br reflector. The profile intersects the fault zone at a sharp angle, which showed a wide apparent width of the fault zone. The total fault displacement is about 25 m. The bedrock marker showed apparent downthrow toward the northwest. At trace numbers 870 to 1000, another normal fault zone (F2) was interpreted. The fault displacement is about 10 m. The bedrock reflector exhibited apparent downthrow to the northwest. Both structural features that were seen at Br occur at Mc and MG. This suggests that Paleozoic tectonic disruption extends to Cretaceous and Pliocene/Pleistocene sediments. Mc and MG are less coherent and intermittent, leading to less confidence in assessing the magnitude of near-surface displacement and dip. These observation lead to the conclusion that the structures evident at Br have occurred in the post-Paleozoic, with small-scale reactivation in post-Cretaceous and younger sediments.

4.1.3.12 Profile G2

Line G2 is an SH-wave profile and consists of 422 shotpoints representing 1095 m total subsurface sampling length. It was acquired along an unpaved road that is oriented northeast-southwest. Langston et al. (1998) collected the nonproprietary raw data for a general reconnaissance survey related to groundwater investigations. Data quality is fair and representative of the entire line. Reflector identification on this line was controlled by nearby borehole information and VSP data (Fig. 1.2) available from the UK seismic lab and DOE. Three reflectors were identified in the section: Br, Mc, and MG (Fig. 4.14). The bedrock marker (Br) is a prominent contact between unlithified sediment and the underlying bedrock, and was picked at an average of 500 ms (~105 m). Mc and MG were interpreted as tops of McNairy and Mounds Gravel, respectively. They appear weak and less coherent than Br and were picked at an average of about 260 ms (50 m) and 170 ms (27 m), respectively. A fault zone was seen between trace numbers 240 and 345. The average offset is 10 m. The relatively strong Br reflector showed apparent downthrow to the south-southwest. The structural feature that was seen at Br occurs at Mc and MG, which means Paleozoic tectonic disruptions extended to Cretaceous and Pliocene/Pleistocene sediments. Mc and MG are less coherent and intermittent, leading to less confidence in assessing the magnitude of near-surface displacement and dip. These observation lead to the conclusion that the structures evident at Br have occurred in the post-Paleozoic, with small-scale reactivation in post-Cretaceous and younger sediments.

4.1.3.13 Profile H

Line H is an SH-wave profile and consists of 240 shotpoints representing 500 m total subsurface sampling length. It was acquired along a paved road that is oriented west-northwest−east-southeast. Blits (2008) collected the nonproprietary raw data for her master's thesis on imaging the subsurface geologic conditions. Data quality is excellent for this area and representative of the entire line. Reflector identification on this line was controlled by nearby borehole information and VSP data (Fig. 1.2) available from the UK seismic lab and DOE. Tighter acquisition geometry, smaller energy source, and a decreased sampling interval helped the near-surface resolution. Therefore, four reflectors were identified on this section: Br, Mc, MG, and Me (Fig. 4.15). The bedrock marker

(Br) is a prominent contact between unlithified sediment and the underlying bedrock, and was picked at an average of about 500 ms (~100 m). Mc, MG, and Me were interpreted as tops of McNairy, Mounds Gravel, and Metropolis, respectively. They were picked at an average of about 270 ms (~47 m), 100 ms (~20 m), and 70 ms (~10 m), respectively. Four prominent high-angle normal faults were observed along the line. The first fault (F1), which was between trace numbers 20 and 100, has a relative apparent throw along the Br reflector to the southeast. The total measured fault displacement across Br is about 6−10 m. The fault effect appears to propagate through the entire sediment section (i.e., Mc, MG, and Me) at measured offsets of 5, 3, and 1 m, respectively. Although the predominant character is normal displacement across Br and Mc, an onlap character of MG and Me as well as slight offset reversal along the horizons occur at this fault zone. These observations suggest that the feature was formed by episodic tectonic activity. In addition, a force fold in the hanging wall with no sharp offset emphasizes the structural inversion. In other words, at MG and Me, the upgoing wall reversed to the downgoing wall. The second (F2) and third (F3) normal faults were observed between trace numbers 125 and 260, and have total displacement across the Br reflector of about 5 and 12 m, respectively. Both of them form a downdropped block. The reflector discontinuity crosses Mc, MG, and Me of approximate displacement between 1 and 5 m. The structural movement across the Cretaceous has left a noticeable thickening of the profile eastward. The fourth normal fault was observed between trace numbers 350 and 430. The total displacement was measured at 5 m. The bedrock reflector exhibits apparent downthrow to the southeast. The fault planes of the fault sets appear to be in line with the northeast−southwest-oriented Fault Zone 3 observed on profiles B and A3. The orientation of the fault sets is associated with the Fluorspar Area Fault Complex. Clearly, structural features that were seen at Br also occur at Mc and MG, which means Paleozoic tectonic disruptions have extended to Cretaceous and Pliocene/Pleistocene sediments. These observations lead to the conclusion that the structures evident at Br have occurred in the post-Paleozoic, with small-scale reactivation in post-Cretaceous and younger sediments.

4.1.3.13 Profile I

Line I is a P-wave profile and consists of 235 shotpoints representing 761 m total subsurface sampling length. It was acquired along a paved road that is oriented east-northeast−west-southwest. Woolery and Street (2003) collected the nonproprietary raw data for general imaging of subsurface geologic conditions. Data quality is good for this area and representative of the entire line. Reflector identification on this line was controlled by nearby borehole information and VSP data (Fig. 1.2) available from the UK seismic lab and DOE. Two reflectors were identified on the section: Br and Mc (Fig. 4.16). The bedrock marker (Br) is a prominent contact between unlithified sediment and the underlying bedrock, and was picked at an average of about 130 ms (~107 m). Mc was interpreted as top of McNairy and appears to be a relatively strong reflector. It was picked at about an average of 70 ms (~45 m). At trace numbers 115 to 180, a normal fault zone (F1) was observed. The measured total displacement across Br is about 15 m. The fault zone has apparent downthrow to the west-northwest. Another normal fault zone (F2) of 18 m total displacement was interpreted between trace numbers 300 and 380. It has apparent downthrow to the south-southeast. F2 seems to be part of Fault Zone 3, which was observed on profiles H, A3, and B. Clearly, structural features that were seen at Br extended to Mc, the Cretaceous, and even younger sediments.

4.1.3.13 Profile J1

Line J1 is an SH-wave profile and consists of 384 shotpoints represent 789 m total subsurface sampling length. It was acquired along a paved highway that is oriented south-southwest−north-northeast. Blits (2008) collected the nonproprietary raw data for her master's thesis related to imaging of subsurface geologic conditions. Data quality is excellent for this area and representative of the entire line. Reflector identification on this line was controlled by nearby borehole information and VSP data (Fig. 1.2) available from the UK seismic lab and DOE. Tighter acquisition geometry, smaller energy source, and a decreased sampling interval have helped the near-surface resolution. Therefore, four reflectors were identified on the section: Br, Mc, MG, and Me (Fig. 4.17). The bedrock marker (Br) is a prominent contact between unlithified sediment and the underlying bedrock, and was picked at an average of about 450 ms (~100 m). Mc and

MG were interpreted as tops of McNairy and Mounds Gravel, respectively. They appear to be relatively strong reflectors and were picked at an average of about 192 ms (~44 m) and 145 ms (~24 m), respectively. The Me reflector was interpreted as the top of the Metropolis Formation (base of the loess deposits). It was picked at an average of 56 ms (~10 m). The structures observed on this line included four high-angle normal fault zones. The first normal fault zone (F1) is between trace numbers 110 and 225. The total offset across the Br reflector is nearly 19 m. The structure is correlated with Fault Zone 3, which was interpreted on profiles I, B, A3, and H. It has apparent downthrow to the south-southeast. Although the predominant character of this feature is normal displacement across Br, the onlap character of Mc and the above sediments (i.e., MG and Me), as well as slight offset reversal along the horizons, are presented at this fault zone. These observations suggest that the feature was formed in episodic tectonic activity. In addition, a force fold in the hanging wall with no sharp offset emphasizes the structural inversion. In other words, at MG and Me, the upgoing wall reversed to a downgoing wall. The second observed fault zone (F2) is between trace numbers 290 and 360. The total offset across the faulted area at the Br reflector is nearly 5 m. The strong bedrock reflector exhibits apparent downthrow to the south-southwest. The relatively small fault displacement indicates a minor in-situ structural feature. The third (F3) and fourth (F4) normal faults were observed between trace numbers 275 and 680, and have total displacement across the Br reflector of about 5 to 7 m, respectively. Both of them form a downdropped block. The reflectors discontinuously cross Mc, MG, and Me with approximate displacement between 1 and 3m. The majority of the observed structural features intersect the profile at an oblique angle so that fault planes obscure the true displacement and exaggerate the width of the overall structure. Structural features that were seen at Br extend up to Mc, MG, and Mc, with smaller offsets of younger sediments. These observation provide evidence for a slight thickening southward along the profile and suggest recurrent small-scale reactivation events.

4.1.3.14 Profile J2

Line J2 is a P-wave profile consisting of 144 shotpoints representing 308 m total subsurface sampling length. It was acquired coincident with part of the SH-wave profile J1 between trace numbers 50 and 325 along a paved highway that is oriented south-southwest to north-north-east−north-northeast. The data were collected for this study in order to directly compare P-wave and SH-wave seismic-reflection data for the near-surface (Fig. 4.18). Thus, vertical and horizontal resolution capabilities were calculated (Tables 4.1−4.2) to evaluate the resolving and detecting limits for SH-wave and P-waver reflection profiles. The optimum and temporal windows for SH-waves and P-waves are different, so that very shallow reflectors within ~ 10 to 20 m depth can be identified on SH-wave profiles, but cannot be seen on P-wave profiles with excellent data quality for this area. Thus, only two reflectors were identified on the section: Br and Mc (Fig. 4.19). The bedrock marker (Br) is a prominent contact between unlithified sediment and the underlying bedrock, and was picked at an average of about 130 ms (~103 m). Mc was interpreted as the top of the McNairy. It appears to be a relatively strong and coherent reflector and was picked at an average of about 75 ms (~ 45 m). The structure feature (F1) that was seen on profile J1 was also observed on this profile. The total offset across the faulted area at the Br reflector is nearly 20 m. The measured offset across the same fault zone on SH-wave data was 19 m, which means a 4.76 percent miscalculation between the two datasets. The correlated structure on both P-wave and SH-wave profiles is oriented northeast-southwest and has apparent downthrow to the south-southwest.

4.1.3.15 Profile K1

Line K1 is an SH-wave profile and consists of 100 shotpoints representing 427 m total subsurface sampling length. It was acquired along an unpaved road that is oriented south-southwest−north-northeast. Langston et al. (1998) collected the nonproprietary raw data for a general reconnaissance survey related to groundwater investigations. Data quality is fair and representative of the entire line. Reflector identification on this line was controlled by nearby borehole information and VSP data (Fig. 1.2) available from the UK seismic lab and DOE. Three reflectors were identified on the profile: Br, Mc, and MG (Fig. 4.20). The bedrock marker (Br) is a prominent contact between unlithified sediment

and the underlying bedrock, and was picked at an average of 480 ms (~115 m). Mc and MG were interpreted as tops of McNairy and Mounds Gravel, respectively. They appear weak and less coherent than Br and were picked at an average of about 250 ms (51 m) and 114 ms (23 m), respectively. Between trace numbers 25 and 100, a normal fault was observed. The offset of the interpreted fault zone across the Br reflector is 8 m. The strong Br reflector exhibits apparent downthrow to the south-southeast. This fault seems to be part of Fault Zone 3 that was observed on profiles H, A3, and B. The structural feature that was seen at Br also occurs at Mc and MG. These observations suggest that the Paleozoic tectonic disruptions extend to Cretaceous and Pliocene/Pleistocene sediments. Mc and MG are less coherent and intermittent, leading to less confidence in assessing the magnitude of near-surface displacement and dip.

4.1.3.15 Profile K2

Line K2 is an SH-wave profile and consists of 58 shotpoints representing 245 m total subsurface sampling length. It was acquired along an unpaved road that is oriented east-west. Langston et al. (1998) collected the nonproprietary raw data for a general reconnaissance survey related to groundwater investigations. Data quality is fair and representative of the entire line. Reflector identification on this line was controlled by nearby borehole information and VSP data (Fig. 1.2) available from the UK seismic lab and DOE. Three reflectors were identified on the profile: Br, Mc, and MG (Fig. 4.21). The bedrock marker (Br) is a prominent contact between unlithified sediment and the underlying bedrock, and was picked at an average of 480 ms (~115 m). Mc and MG were interpreted as tops of the McNairy and Mounds Gravel, respectively. They appear weaker and less coherent than Br and were picked at an average of about 250 ms (51 m) and 114 ms (23 m), respectively.

4.1.3.16 Profile L

Line L is an SH-wave profile and consists of 169 shotpoints representing 713 m total subsurface sampling length. It was acquired along a paved road that is oriented northeast-southwest. Blits (2008) collected the nonproprietary raw data for her master's thesis related to imaging of subsurface geologic conditions. Data quality is good and representative of the entire line. Reflector identification on this line was controlled by nearby borehole information and VSP data (Fig. 1.2) available from the UK seismic lab and DOE. Three reflectors were identified on the profile: Br, Mc, and MG (Fig. 4.22). The bedrock marker (Br) is a prominent contact between unlithified sediment and the underlying bedrock, and was picked at an average of 520 ms (~110 m). Mc and MG were interpreted as tops of the McNairy and Mounds Gravel, respectively. They appear weaker and less coherent than Br and were picked at about 230 ms (45 m) and 80 ms (13 m), respectively. There are noticeable depth changes at the bedrock reflector between the northern and southern ends of the line. Depth differences across the relatively short profile suggest displacement of two normal fault zones. The first fault zone is observed clearly between trace numbers 150 and 240. It exhibits ~10 m total displacement across the fault zone. The strong Br reflector shows apparent downthrow to the south-southeast. The fault plane of the structure probably intersects this profile at an oblique angle, which obscures the true offsets and broadens the distortion seen on the Br reflector. The fault effect appears to propagate through most of the sediment section (i.e., Mc and MG) at measured offsets of 5 and 3 m, respectively. At trace numbers 290 to 320, another fault zone of 5 m displacement is interpreted. A relatively strong Br reflector shows apparent downthrow to the south-southwest. The relatively small offset indicates a sharp intersection angle between the fault plane and the seismic line, which results in obscuring the true offsets and broadens the distortion seen on the Br reflector. Again, the fault effect appears to propagate through the entire sediment section (i.e., Mc and MG) at measured offsets of 5 and 3 m, respectively. These observations suggest the Paleozoic tectonic disruptions extend to Cretaceous and Pliocene/Pleistocene sediments, with small-scale reactivation in post-Cretaceous and younger sediments.

4.1.3.17 Profile M

Line M is a P-wave profile and consists of 144 shotpoints representing 617 m total subsurface sampling length. It was acquired along a paved road that is oriented west-northwest–east-southeast. Woolery and Street (2003) collected the nonproprietary raw data for general imaging of subsurface geologic conditions. Data quality is poor and representative of the entire line. Reflector identification on this line was controlled by nearby borehole information and VSP data (Fig. 1.2) available from the UK seismic lab and DOE. Two reflectors were identified on the section: Br and Mc (Fig. 4.23). The bedrock marker (Br) was picked at about 140 ms (~111 m average) and expected to be a prominent contact between unlithified sediment and the underlying bedrock. However, it appears weak in almost half of the line. The Mc reflector was interpreted as the top of the McNair and appears weak and incoherent. It was picked at ~55 ms (35 m average). The data quality is not coherent enough to interpret any fault displacement, but it was useful for estimating reflector depth.

4.1.3.18 Multiple SH-Wave and P-Wave Reflection Profiles

Profiles P1 P7 and profiles S8 and S9 are P-wave and SH-wave reflection data, respectively. P-wave and SH-wave total subsurface sampling lengths were 1686 m and 719 m, respectively. Both datasets were acquired by SAIC Engineering Inc. (2004) as part of a geophysical feasibility study for imaging subsurface geology. These datasets were reprocessed (Appendices C and D); however, they were acquired in a small area and do not provide significant supporting information toward the objectives of this study. Two additional SH-wave reflection profiles (N and O) were acquired adjacent to the C-746-U landfill. The data were reprocessed, but were not interpreted because of high noise content that obscured the effective signal.

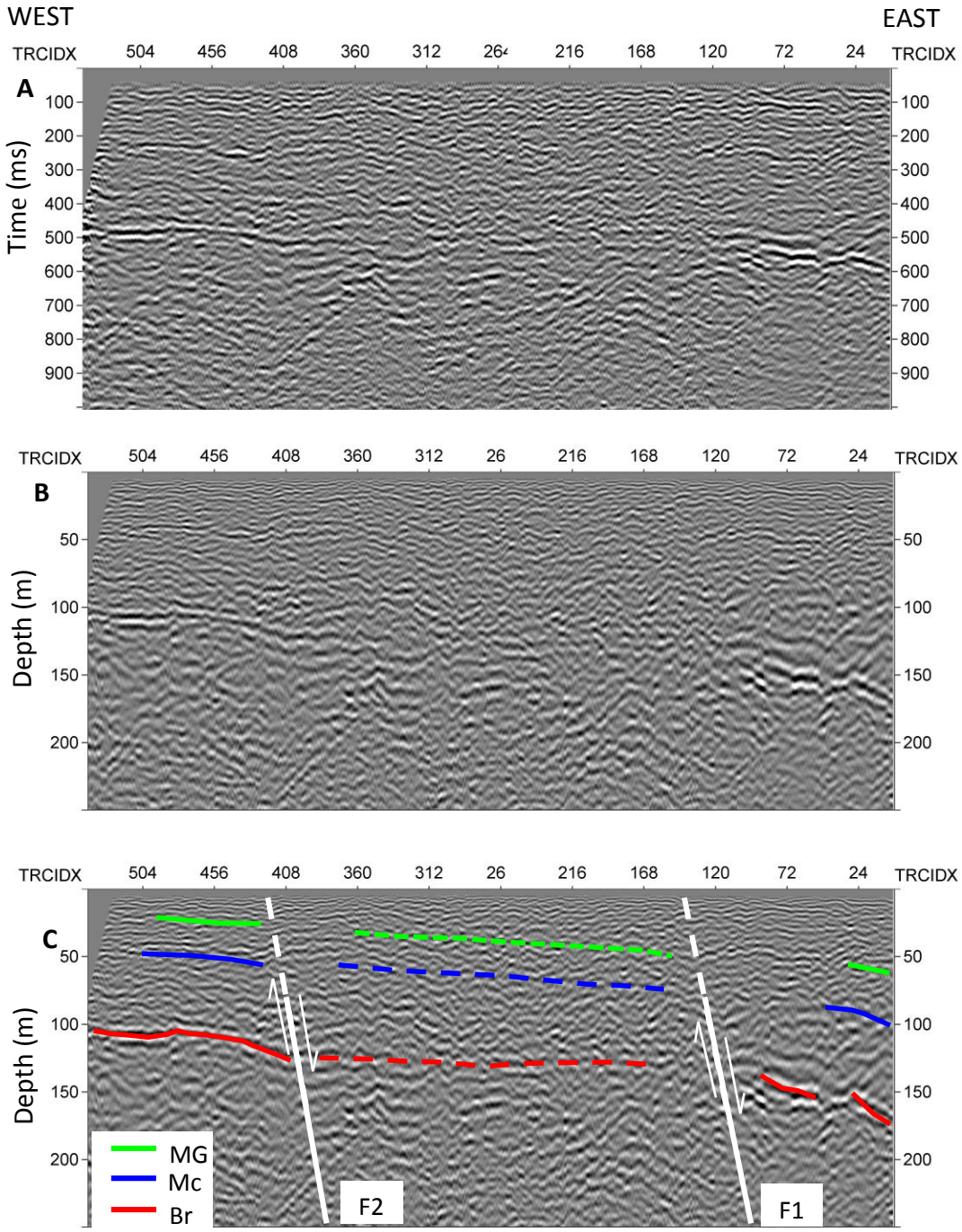

Figure 4.2: SH-wave seismic-reflection profile A1. (A) Unmigrated. (B) Depth-migrated uninterpreted. (C) Depth-migrated interpreted.

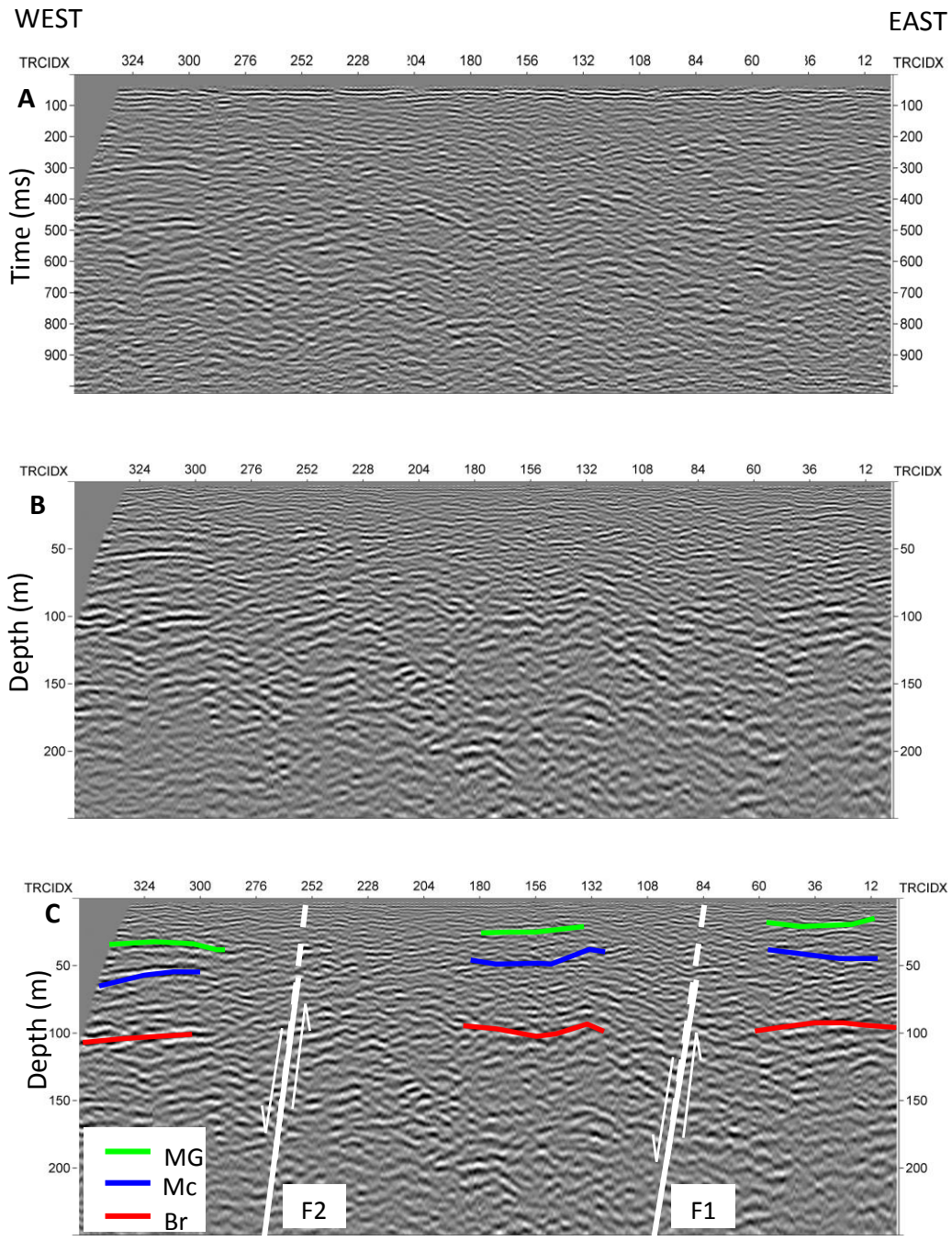

Figure 4.3: SH-wave seismic-reflection profile A2. (A) Unmigrated. (B) Depth-migrated uninterpreted. (C) Depth-migrated interpreted.

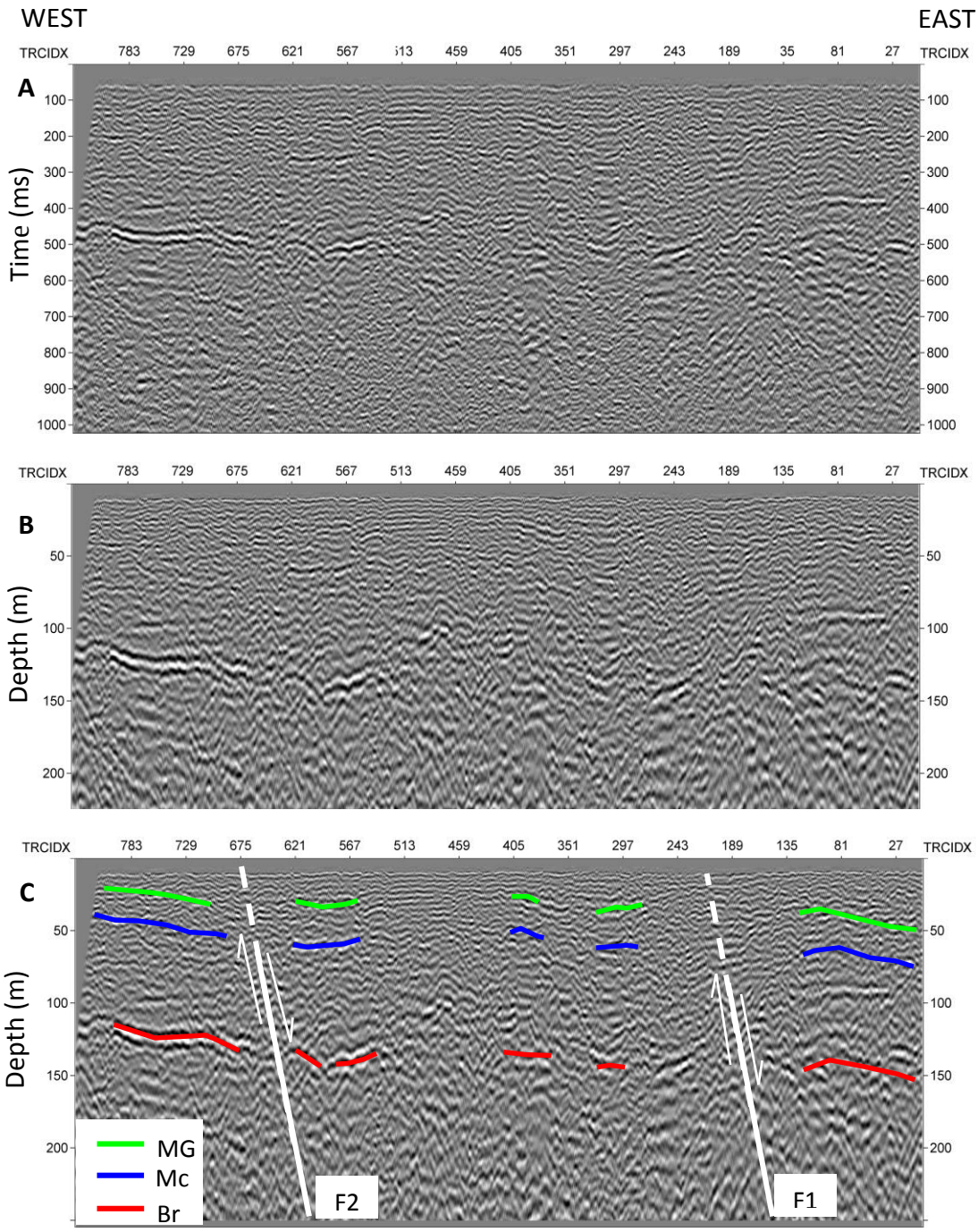

Figure 4.4: SH-wave seismic-reflection profile A3. (A) Unmigrated. (B) Depth-migrated uninterpreted. (C) Depth-migrated interpreted.

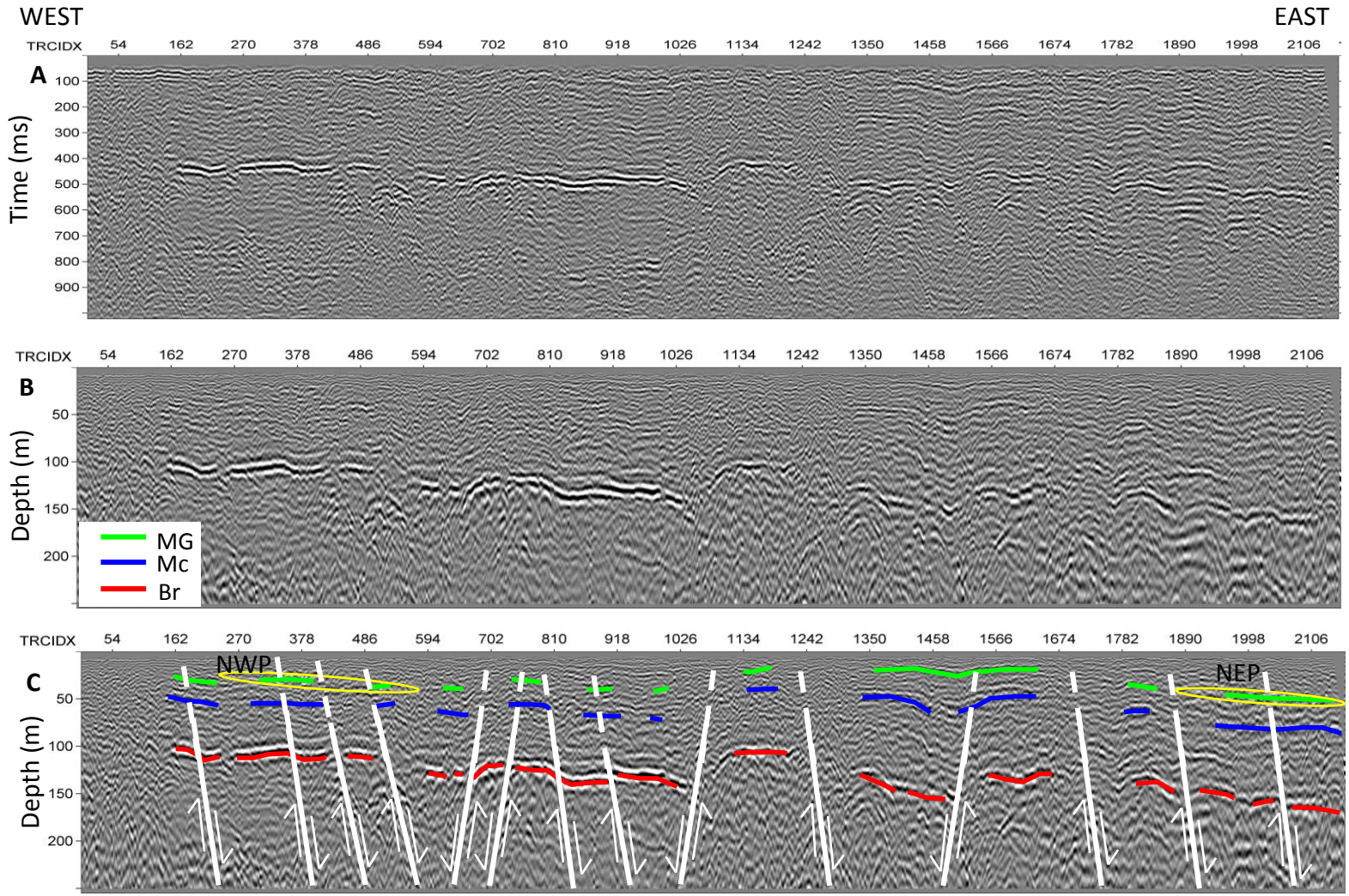

Figure 4.5: SH-wave seismic-reflection profile B. (A) Unmigrated. (B) Depth-migrated uninterpreted. (C) Depth-migrated interpreted.

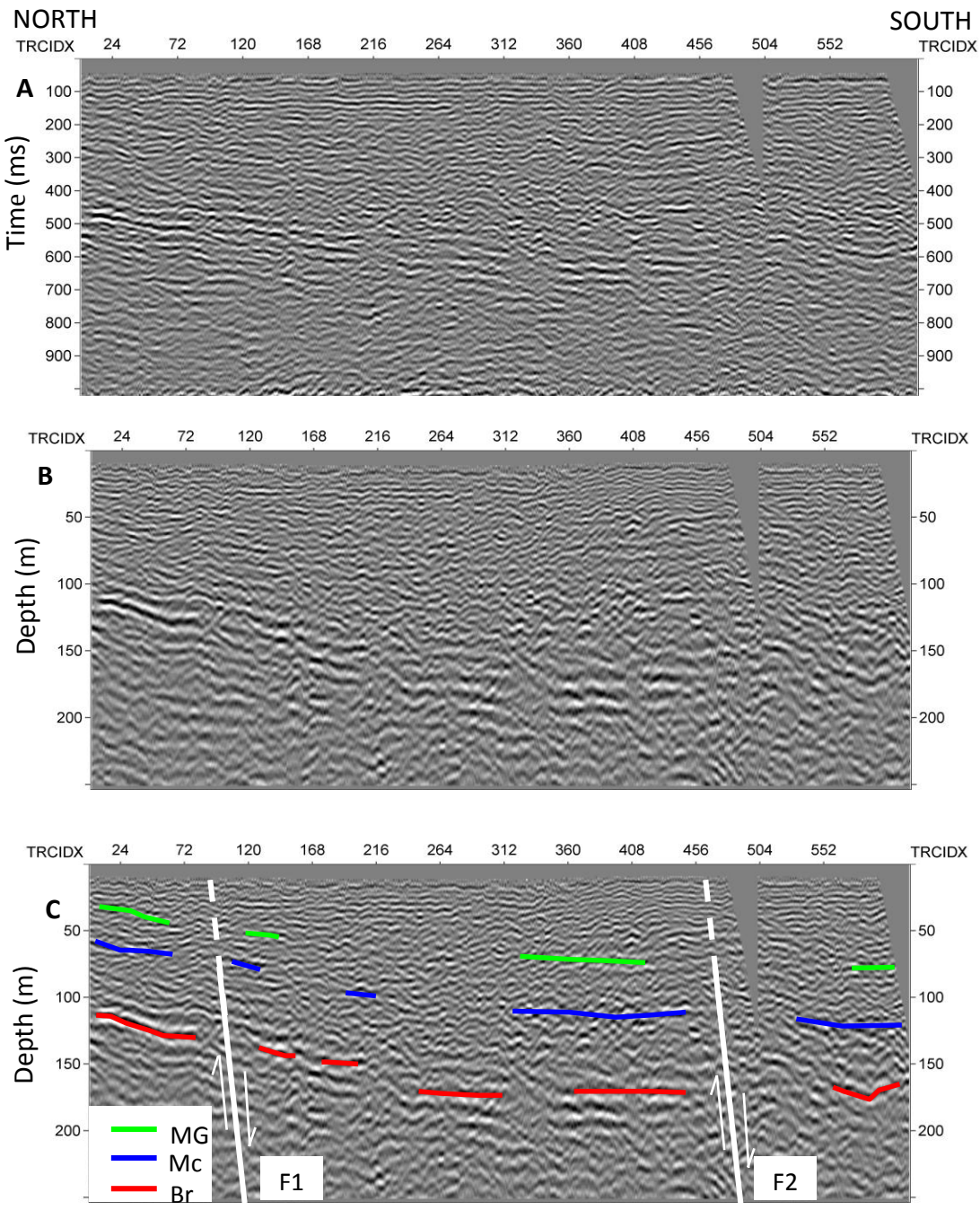

Figure 4.6: SH-wave seismic-reflection profile C1. (A) Unmigrated. (B) Depth-migrated uninterpreted. (C) Depth-migrated interpreted.

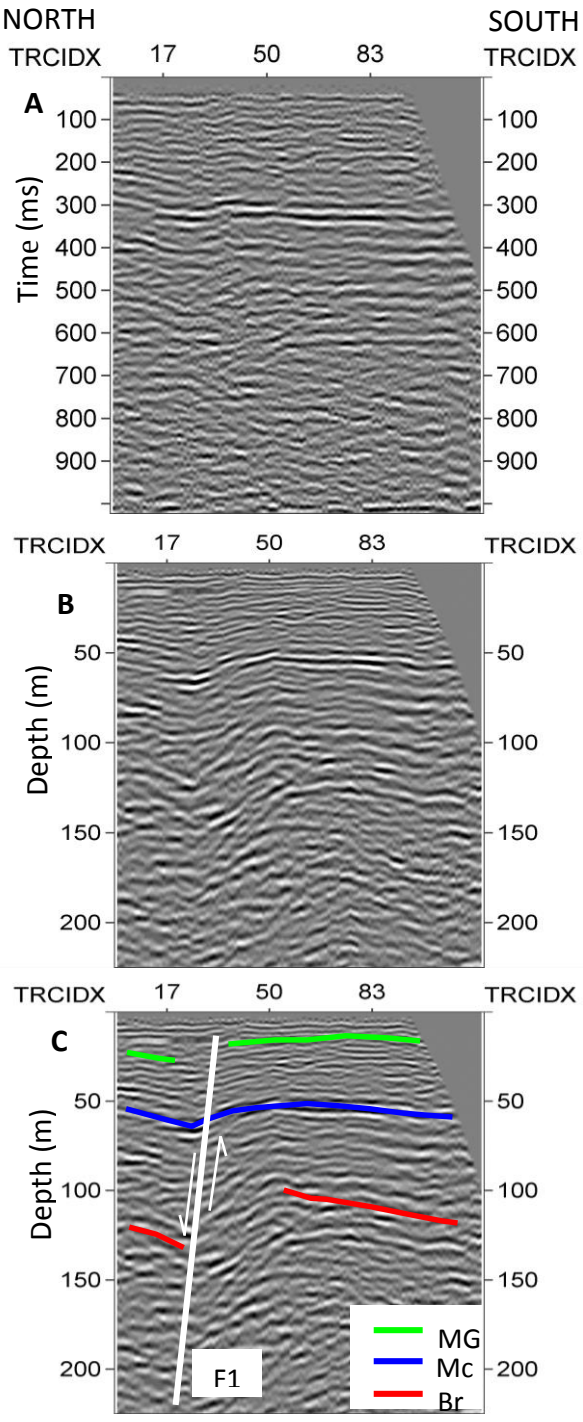

Figure 4.7: SH-wave seismic-reflection profile C1_S. (A) Unmigrated. (B) Depth-migrated uninterpreted. (C) Depth-migrated interpreted.

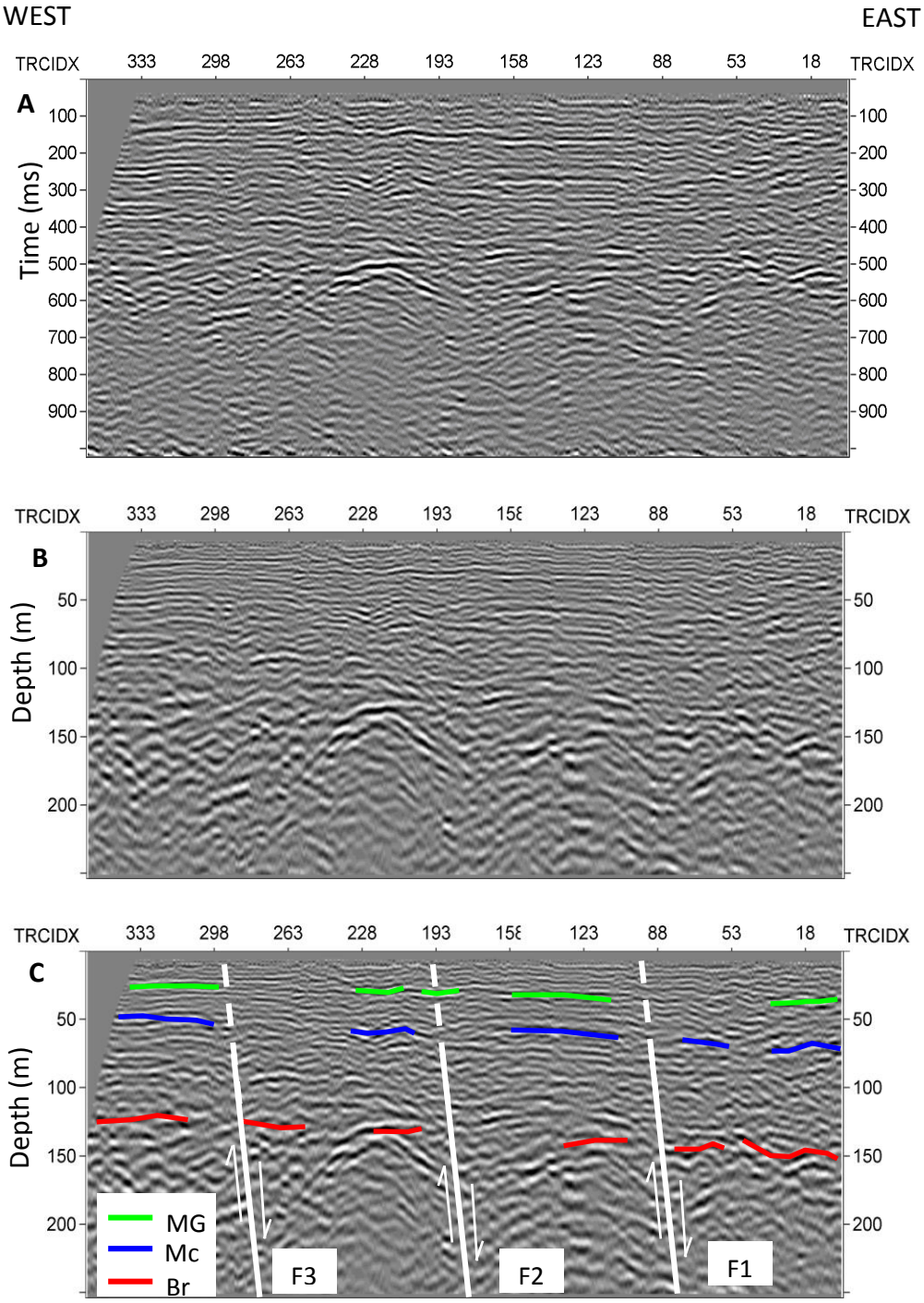

Figure 4.8: SH-wave seismic-reflection profile C2. (A) Unmigrated. (B) Depth-migrated uninterpreted. (C) Depth-migrated interpreted.

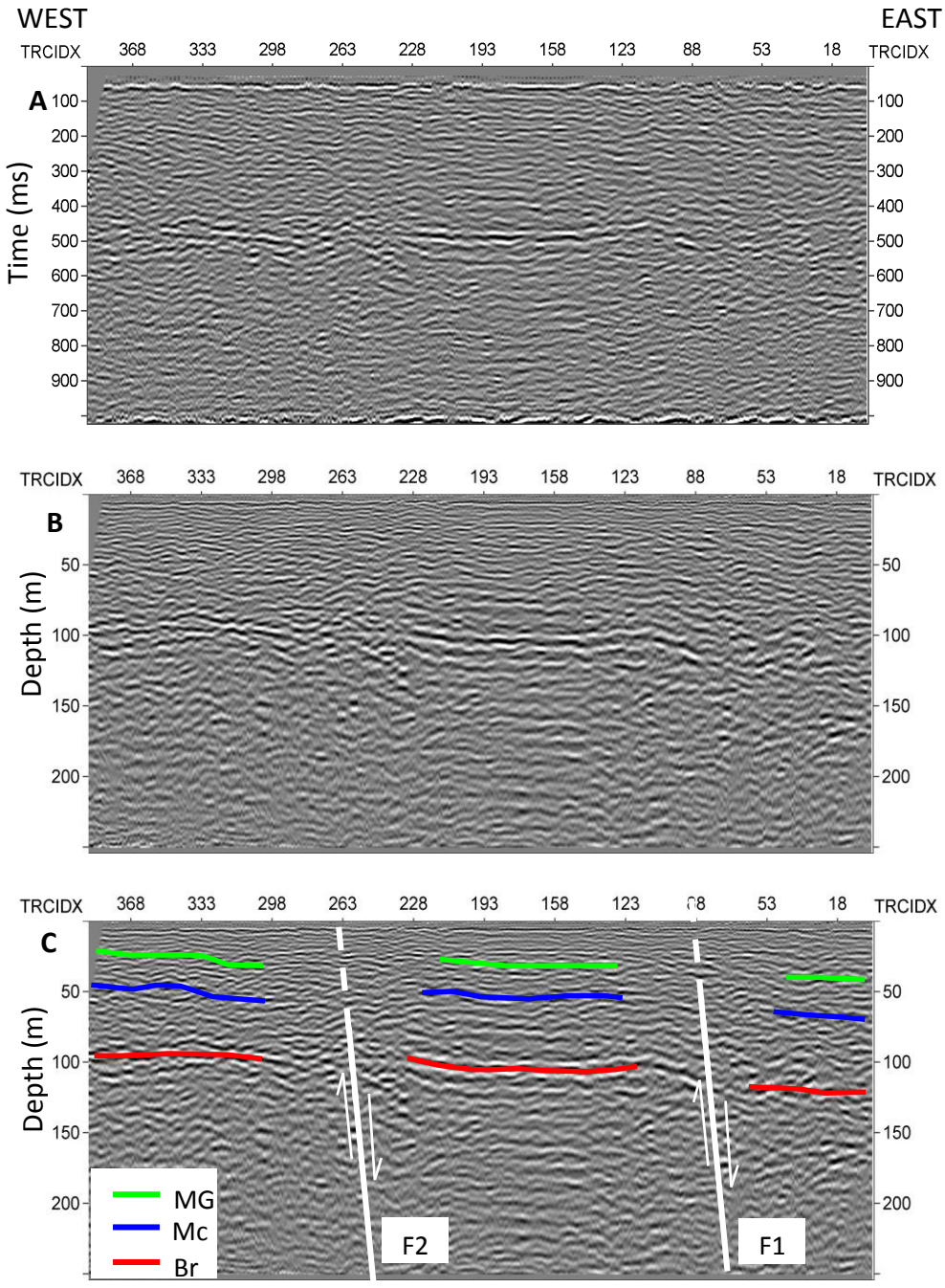

Figure 4.9: SH-wave seismic-reflection profile C3. (A) Unmigrated. (B) Depth-migrated uninterpreted. (C) Depth-migrated interpreted.

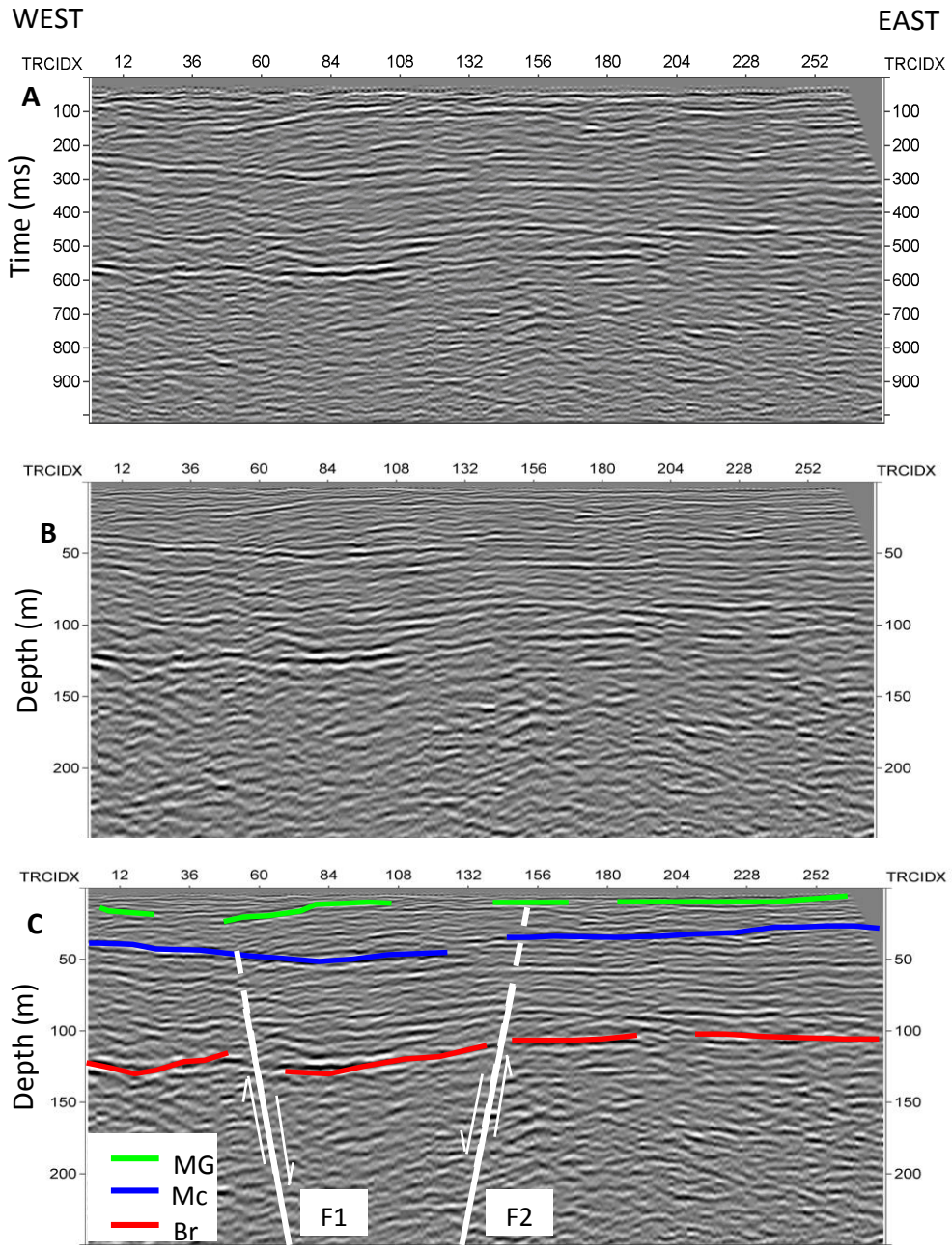

Figure 4.10: SH-wave seismic-reflection profile D. (A) Unmigrated. (B) Depth-migrated uninterpreted. (C) Depth-migrated interpreted.

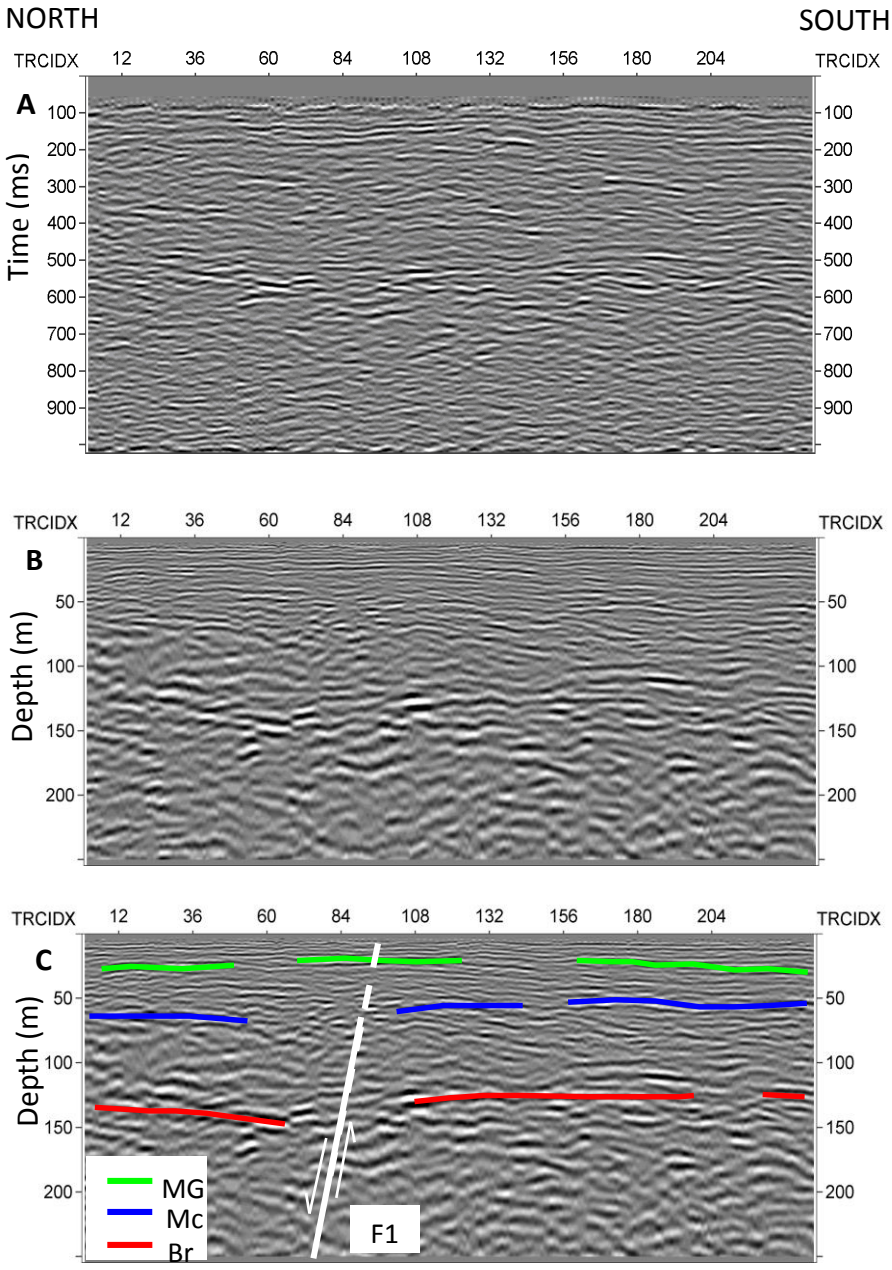

Figure 4.11: SH-wave seismic-reflection profile E. (A) Unmigrated. (B) Depth-migrated uninterpreted. (C) Depth-migrated interpreted.

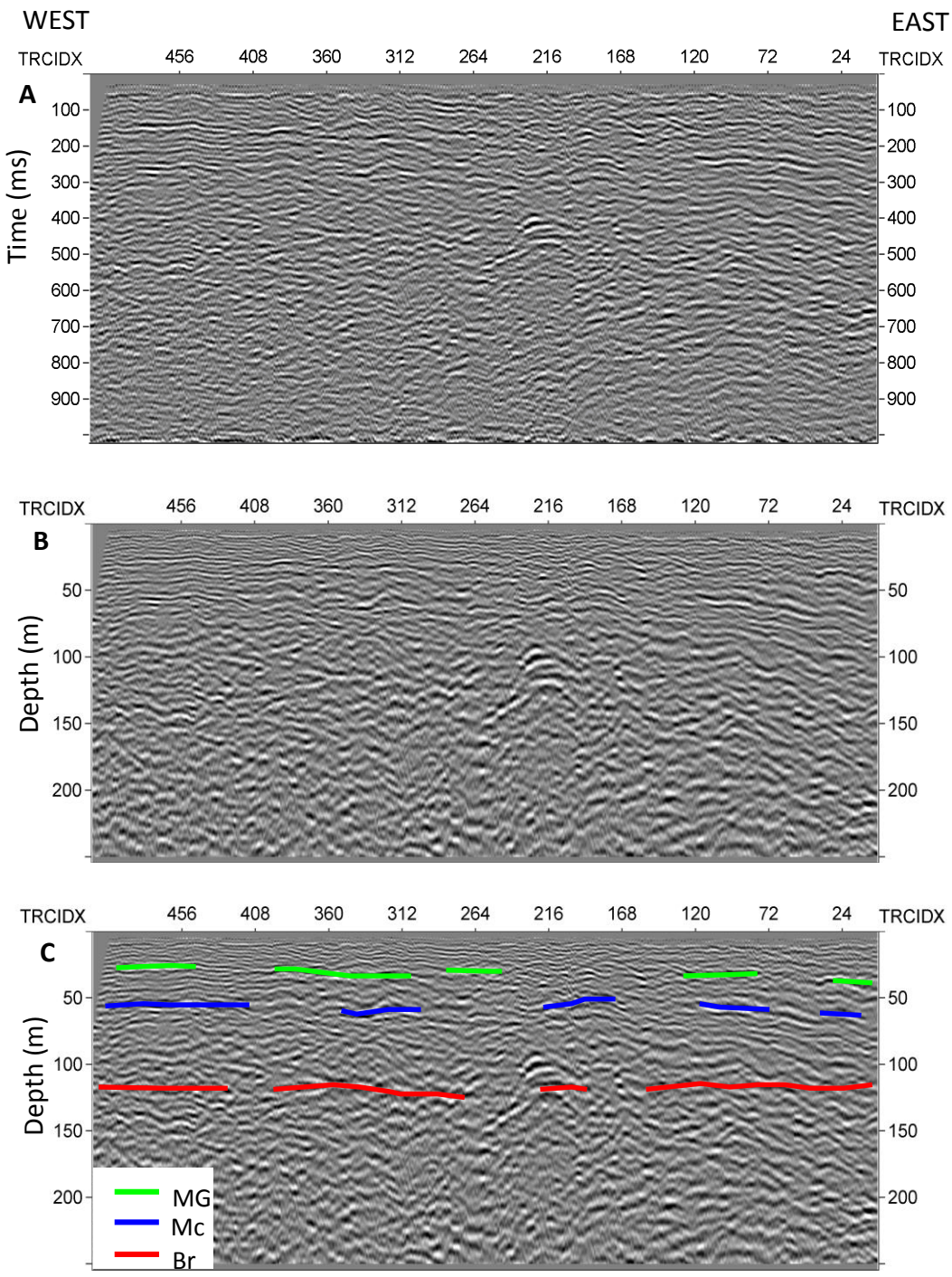

Figure 4.12: SH-wave seismic-reflection profile F. (A) Unmigrated. (B) Depth-migrated uninterpreted. (C) Depth-migrated interpreted.

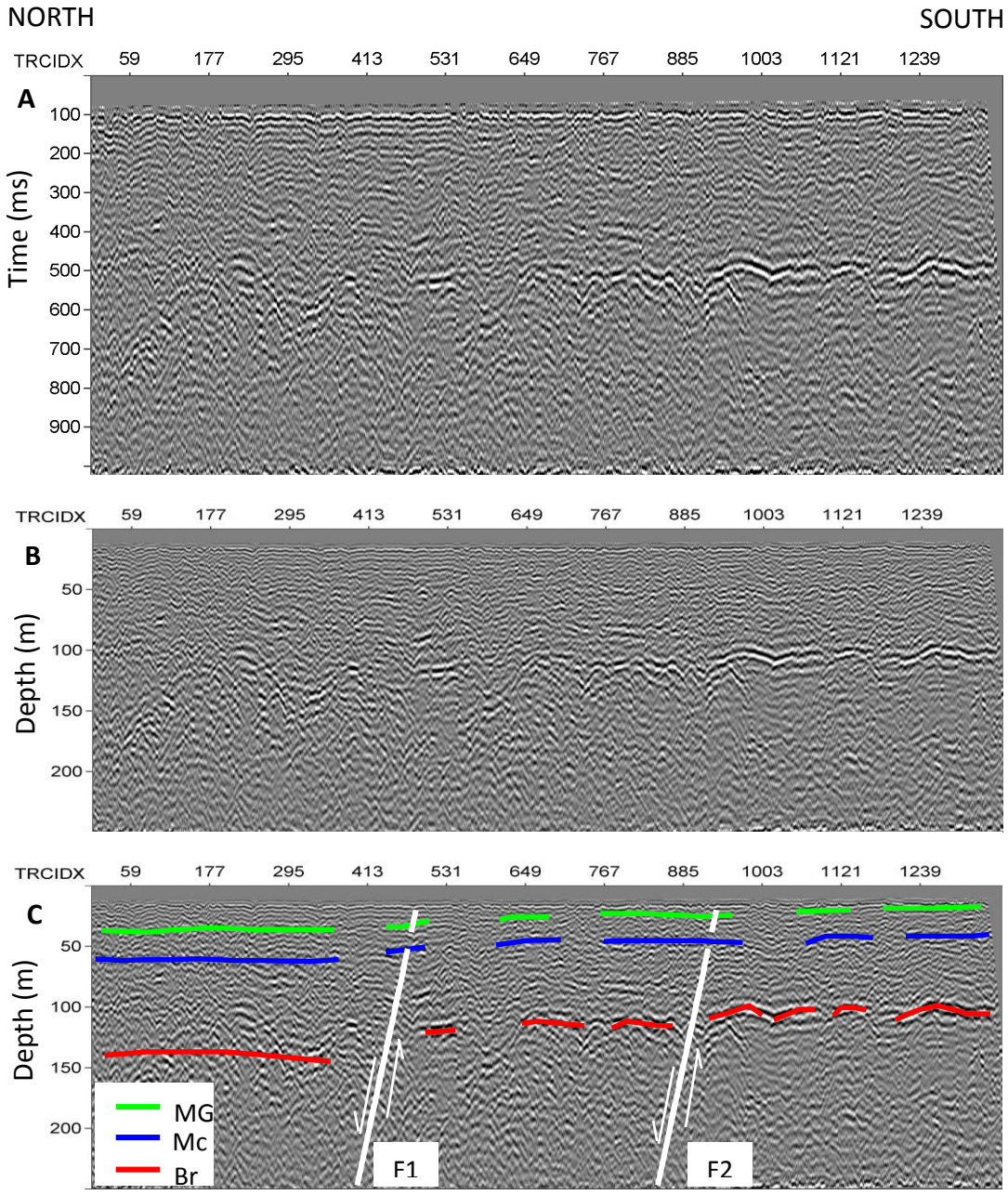

Figure 4.13: SH-wave seismic-reflection profile G1. (A) Unmigrated. (B) Depth-migrated uninterpreted. (C) Depth-migrated interpreted.

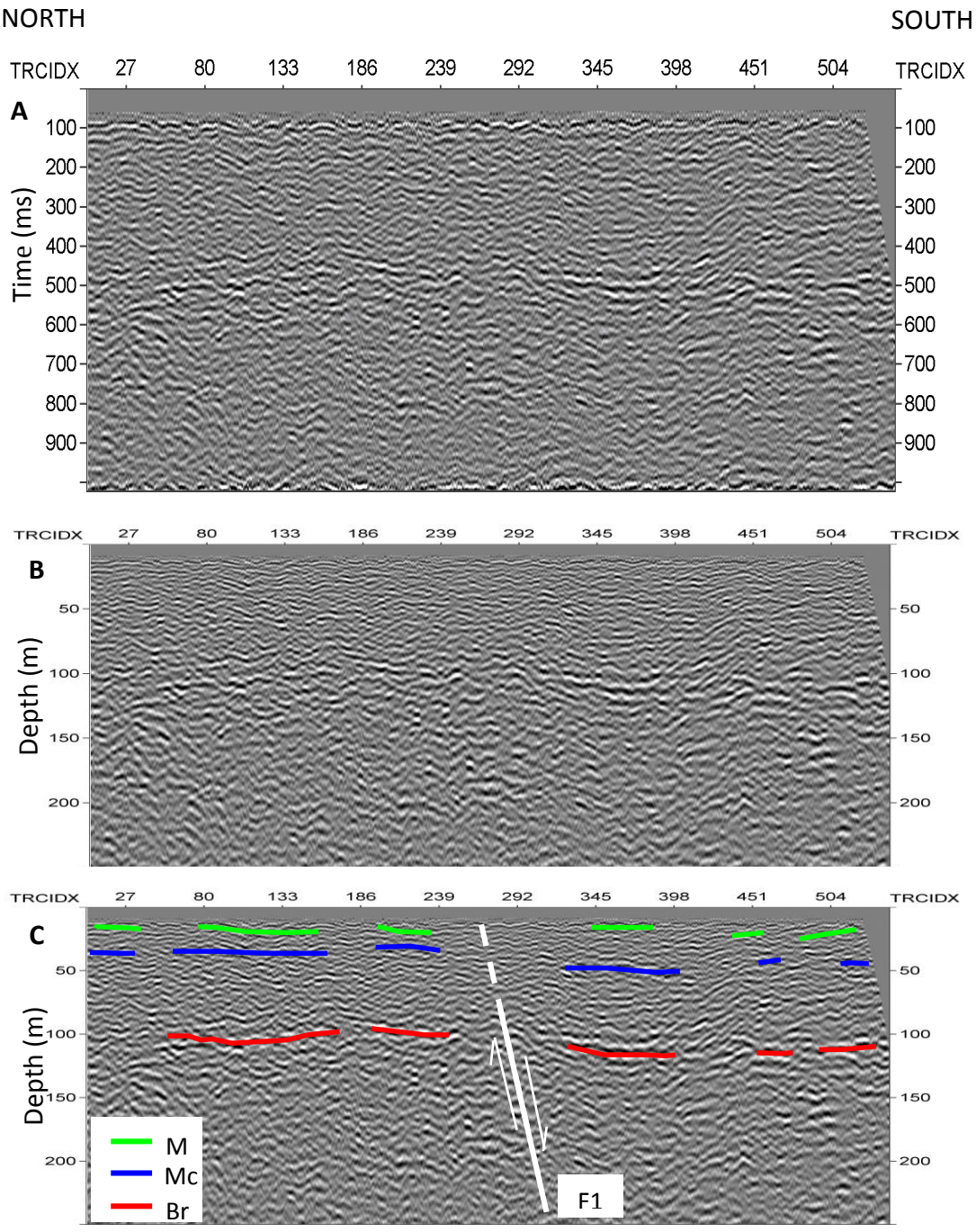

Figure 4.14: SH-wave seismic-reflection profile G2. (A) Unmigrated. (B) Depth-migrated uninterpreted. (C) Depth-migrated interpreted.

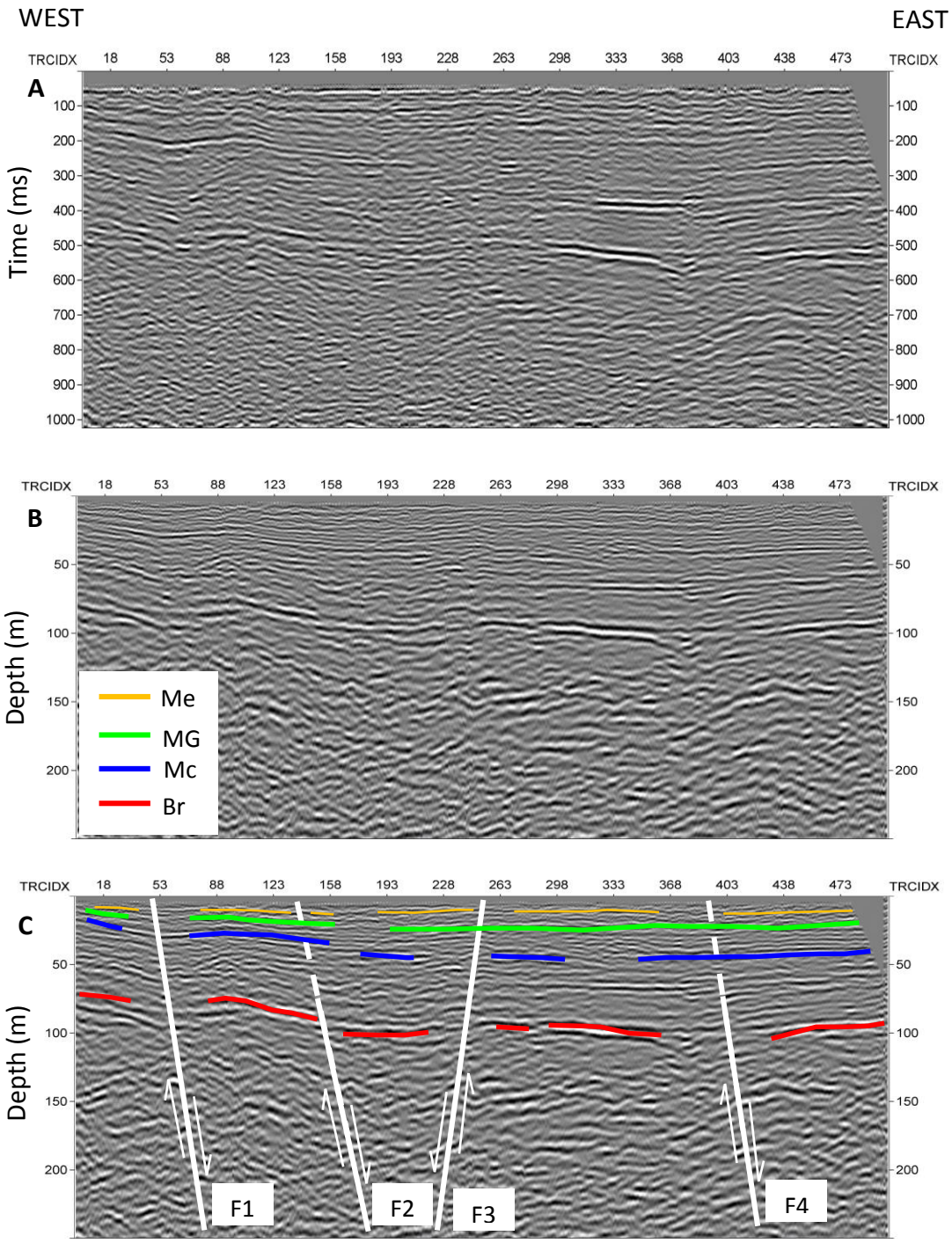

Figure 4.15: SH-wave seismic-reflection profile H. (A) Unmigrated. (B) Depth-migrated uninterpreted. (C) Depth-migrated interpreted.

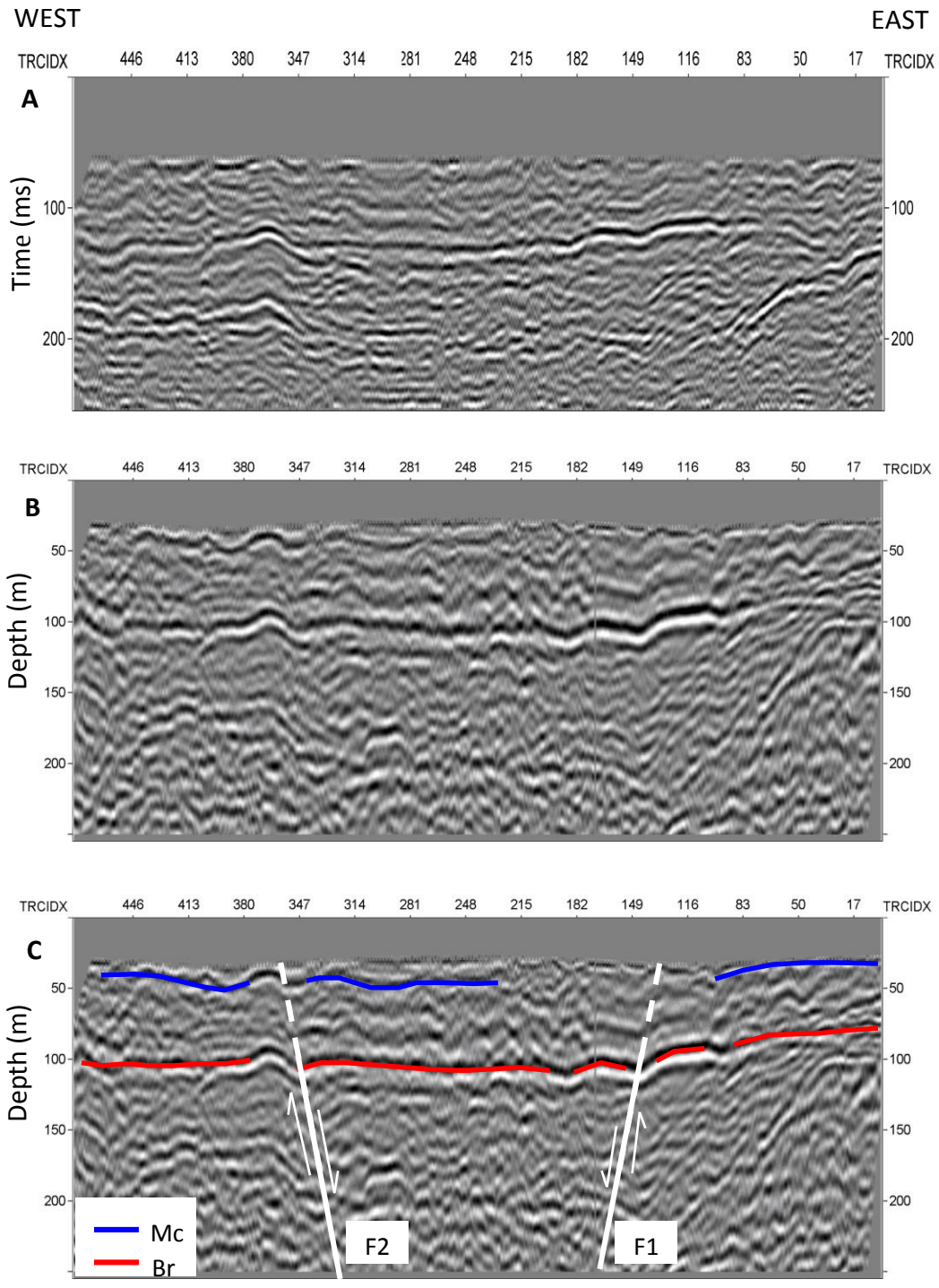

Figure 4.16: SH-wave seismic-reflection profile I. (A) Unmigrated. (B) Depth-migrated uninterpreted. (C) Depth-migrated interpreted.

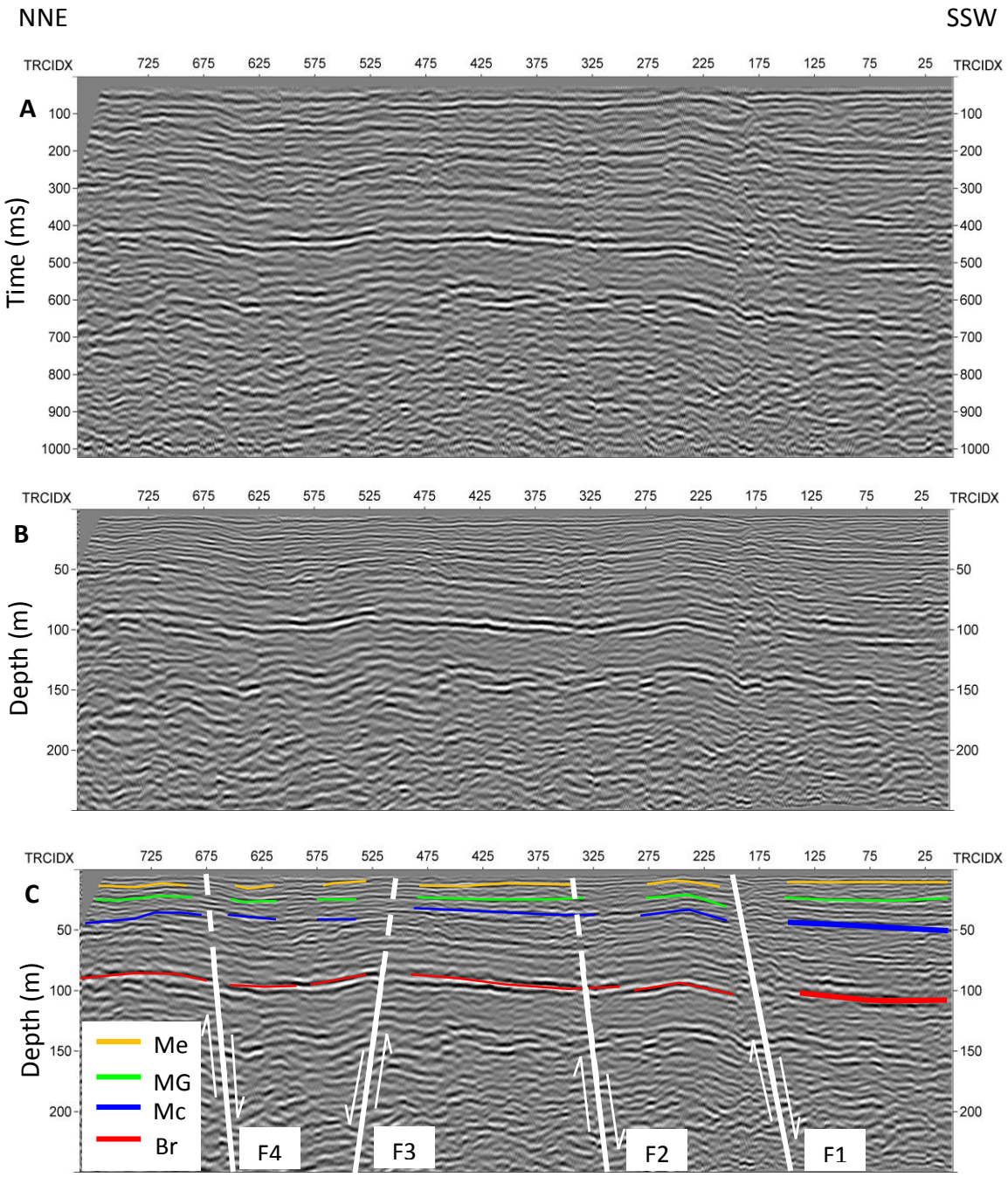

Figure 4.17: SH-wave seismic-reflection profile J1. (A) Unmigrated. (B) Depth-migrated uninterpreted. (C) Depth-migrated interpreted.

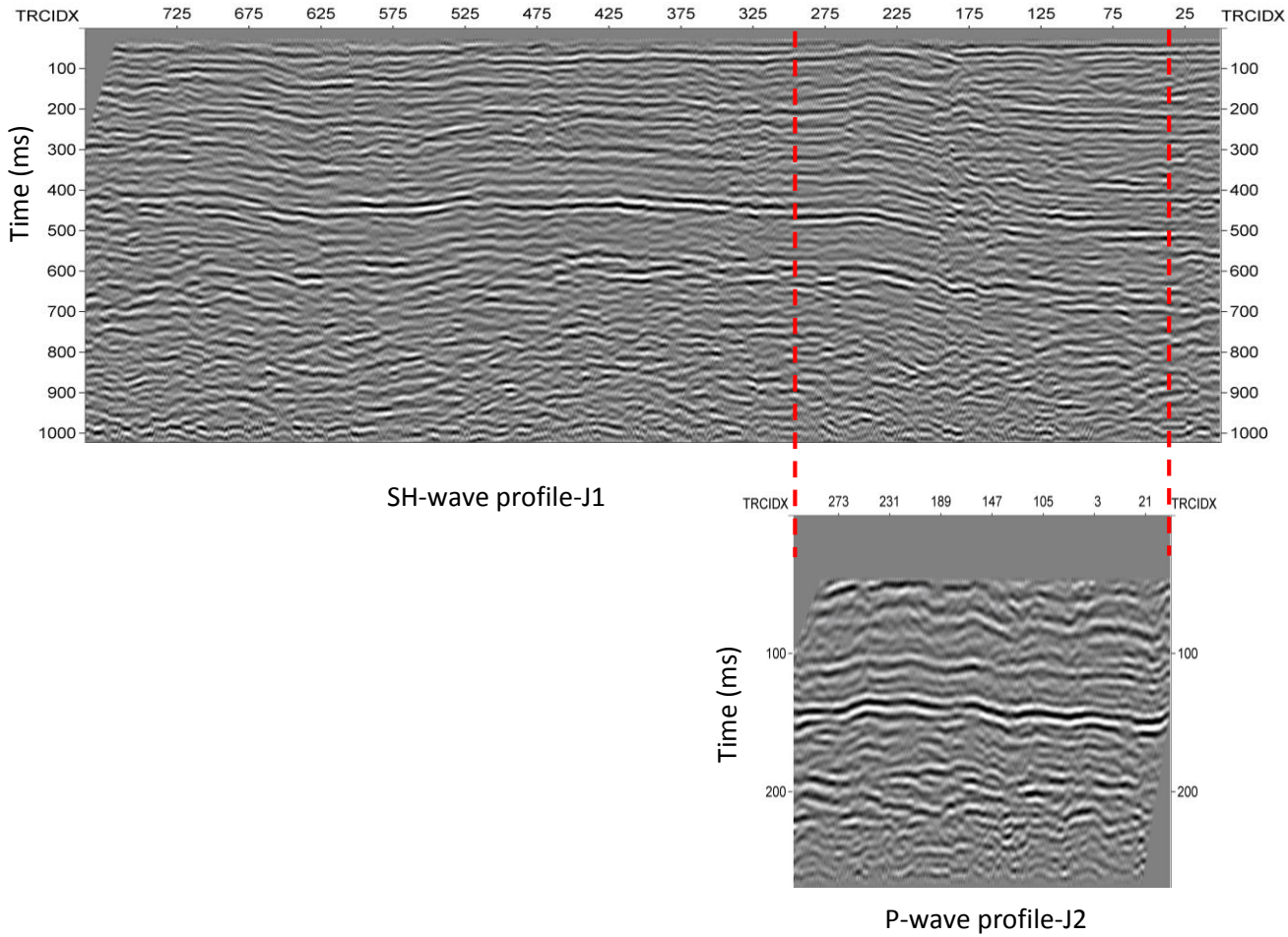

Figure 4.18: Coincident P-wave and S-wave seismic-reflection profiles Comparison.

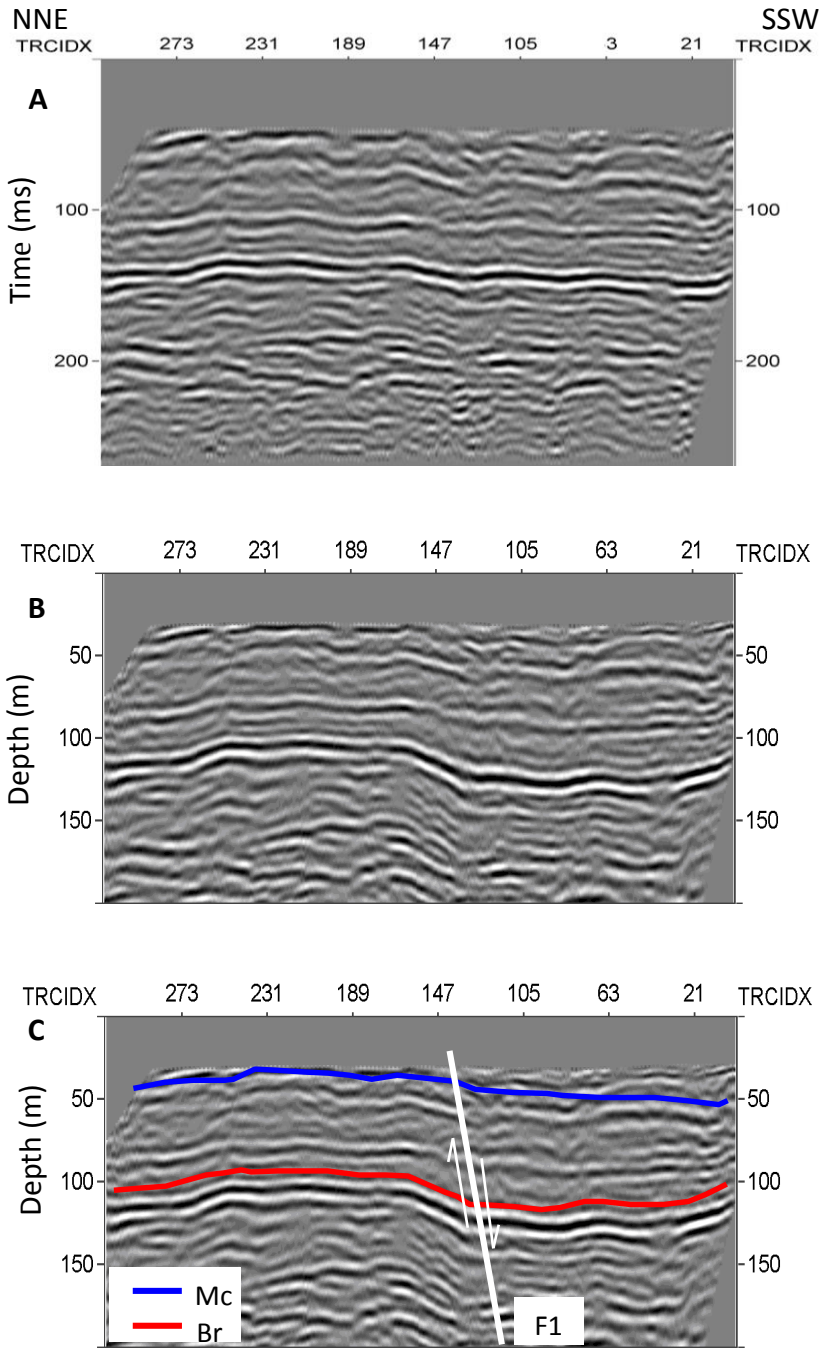

Figure 4.19: SH-wave seismic-reflection profile J2. (A) Unmigrated. (B) Depth-migrated uninterpreted. (C) Depth-migrated interpreted.

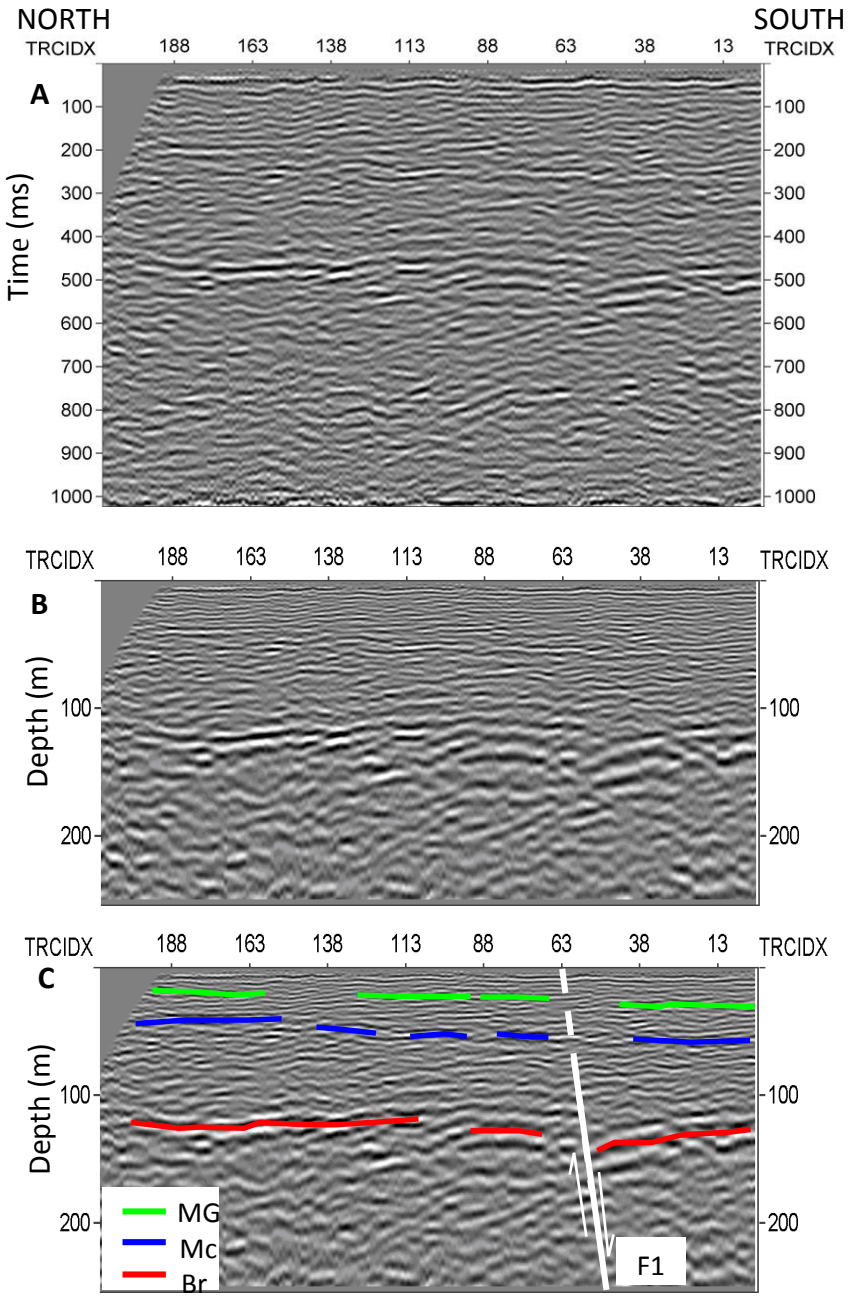

Figure 4.20: SH-wave seismic-reflection profile K1. (A) Unmigrated. (B) Depth-migrated uninterpreted. (C) Depth-migrated interpreted.

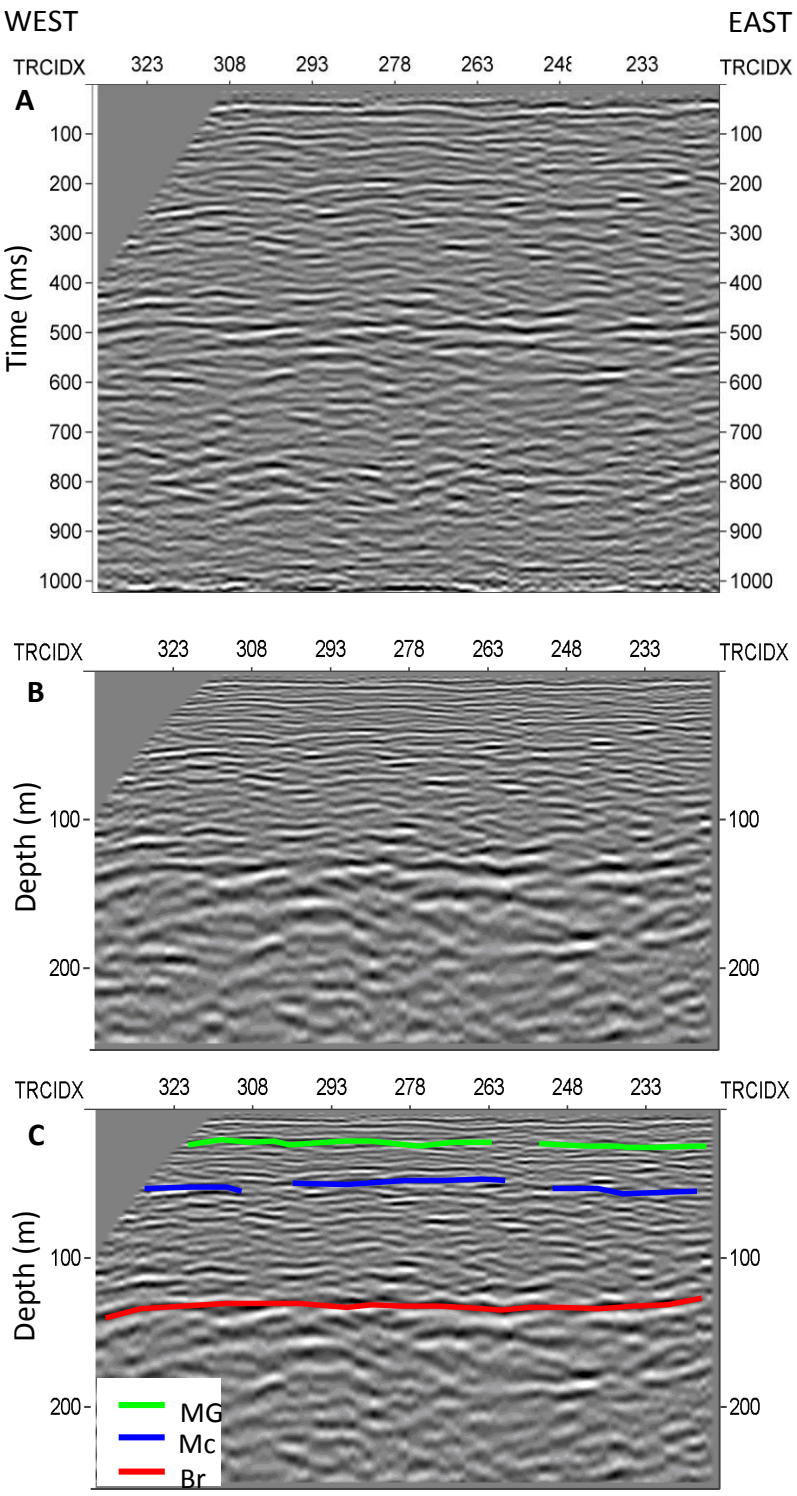

Figure 4.21: SH-wave seismic-reflection profile K2. (A) Unmigrated. (B) Depth-migrated uninterpreted. (C) Depth-migrated interpreted.

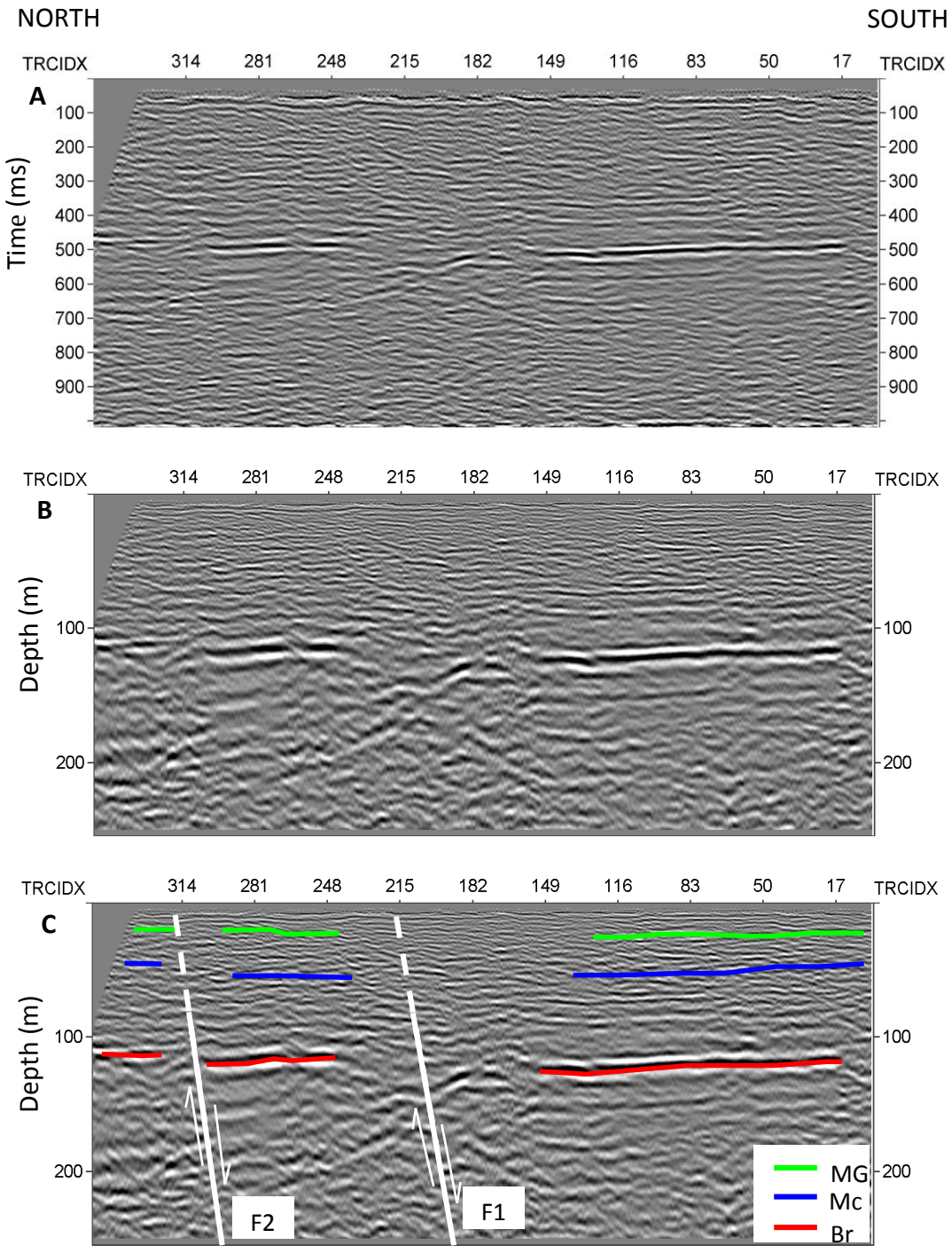

Figure 4.22: SH-wave seismic-reflection profile L. (A) Unmigrated. (B) Depth-migrated uninterpreted. (C) Depth-migrated interpreted.

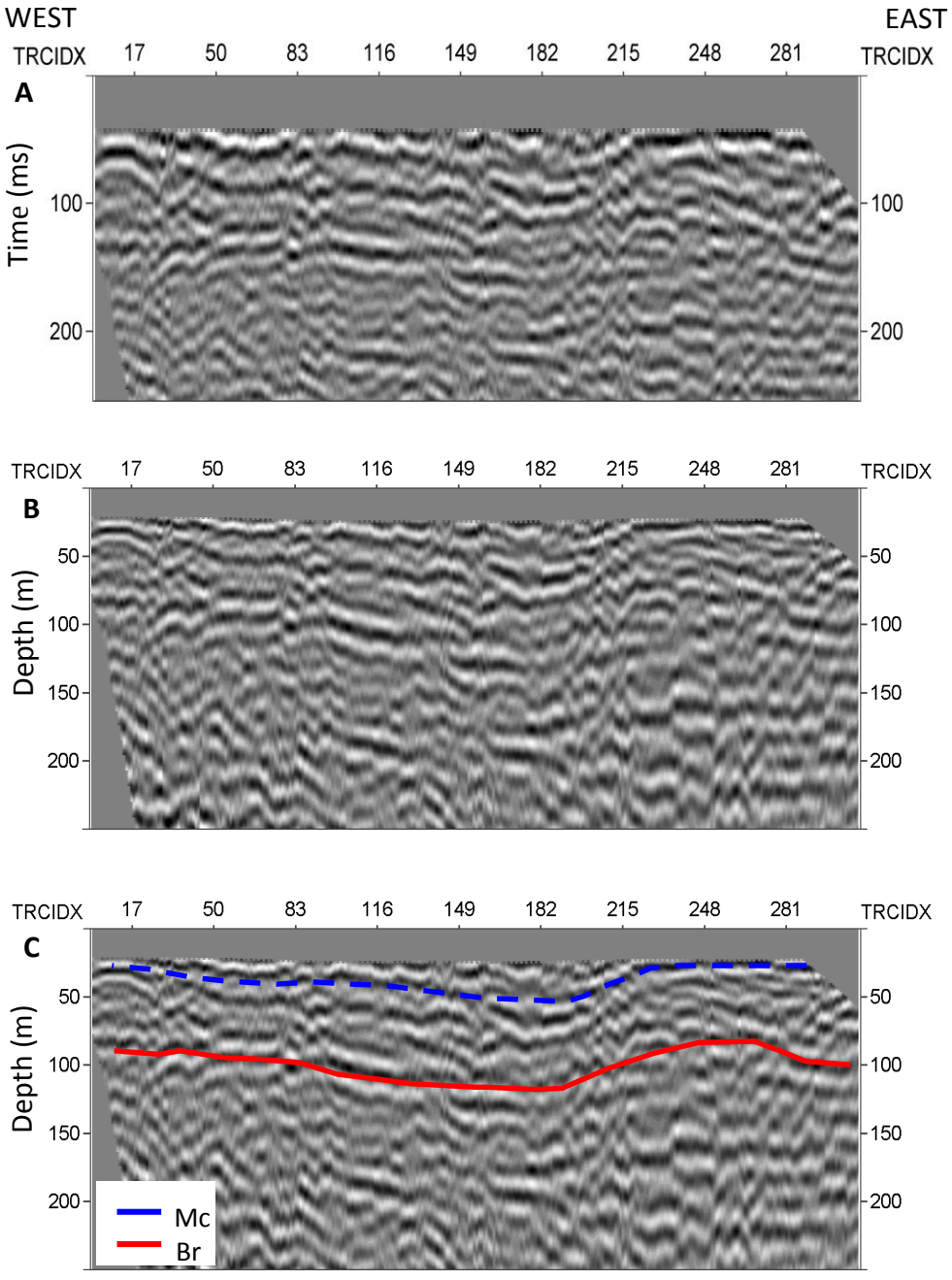

Figure 4.23: SH-wave seismic-reflection profile M. (A) Unmigrated. (B) Depth-migrated uninterpreted. (C) Depth-migrated interpreted.

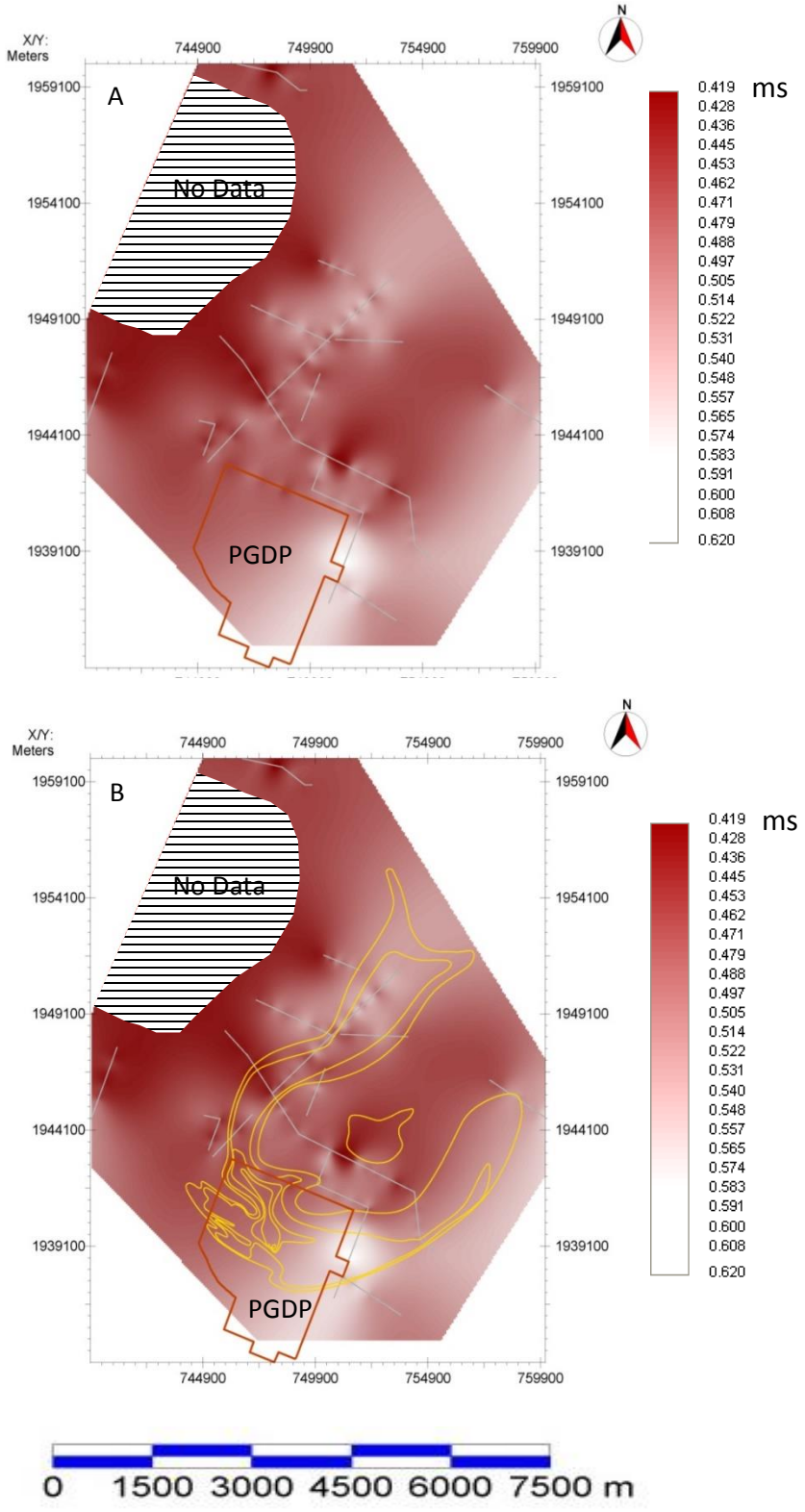

Figure 4.24: (A) Time-structure map of Paleozoic bedrock. (B) Time-structure map of Paleozoic bedrock correlated spatially with the contamination plume.

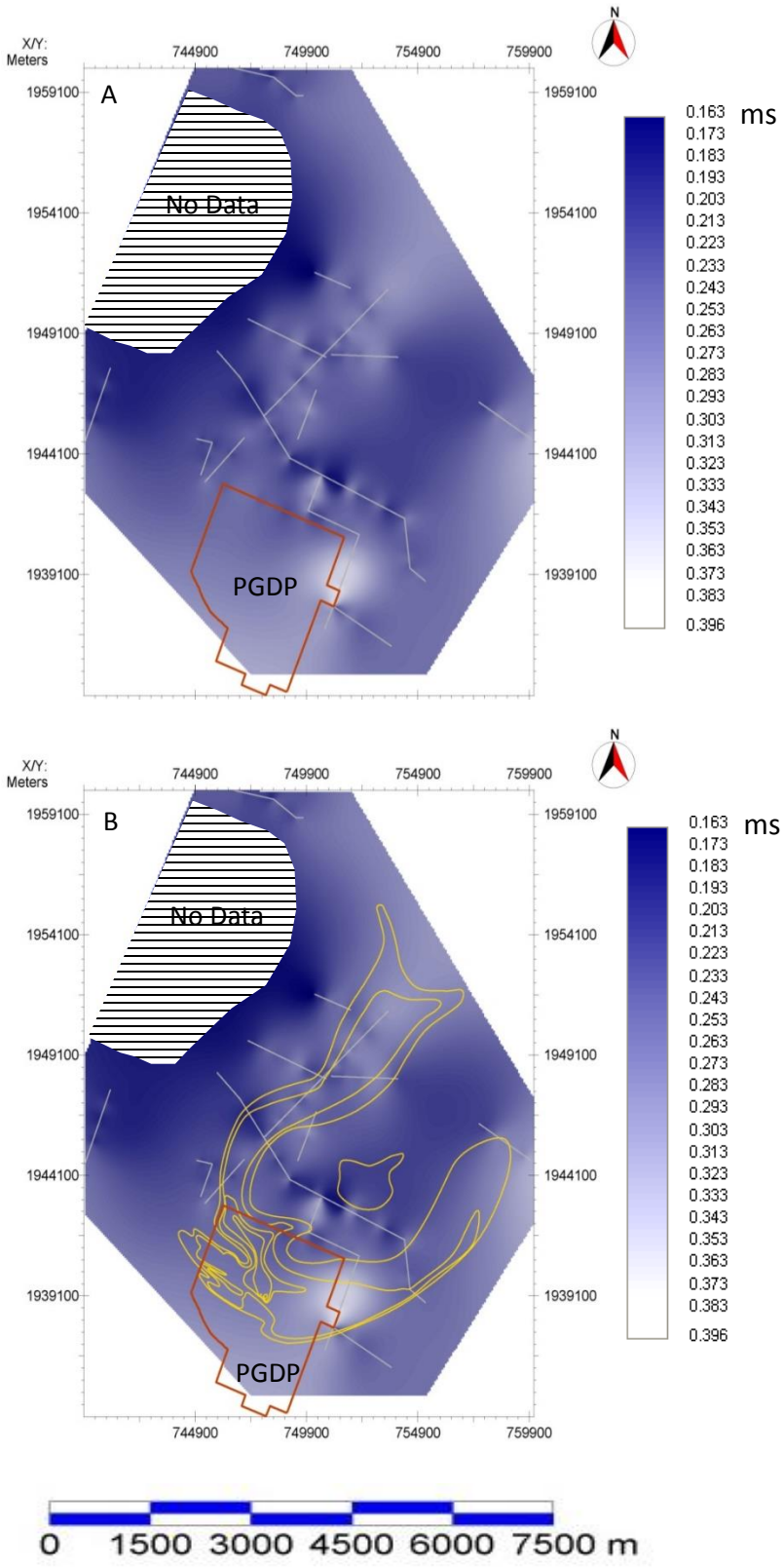

Figure 4.25: (A) Time-structure map of McNairy. (B) Time-structure map of McNairy correlated spatially with the contamination plume.

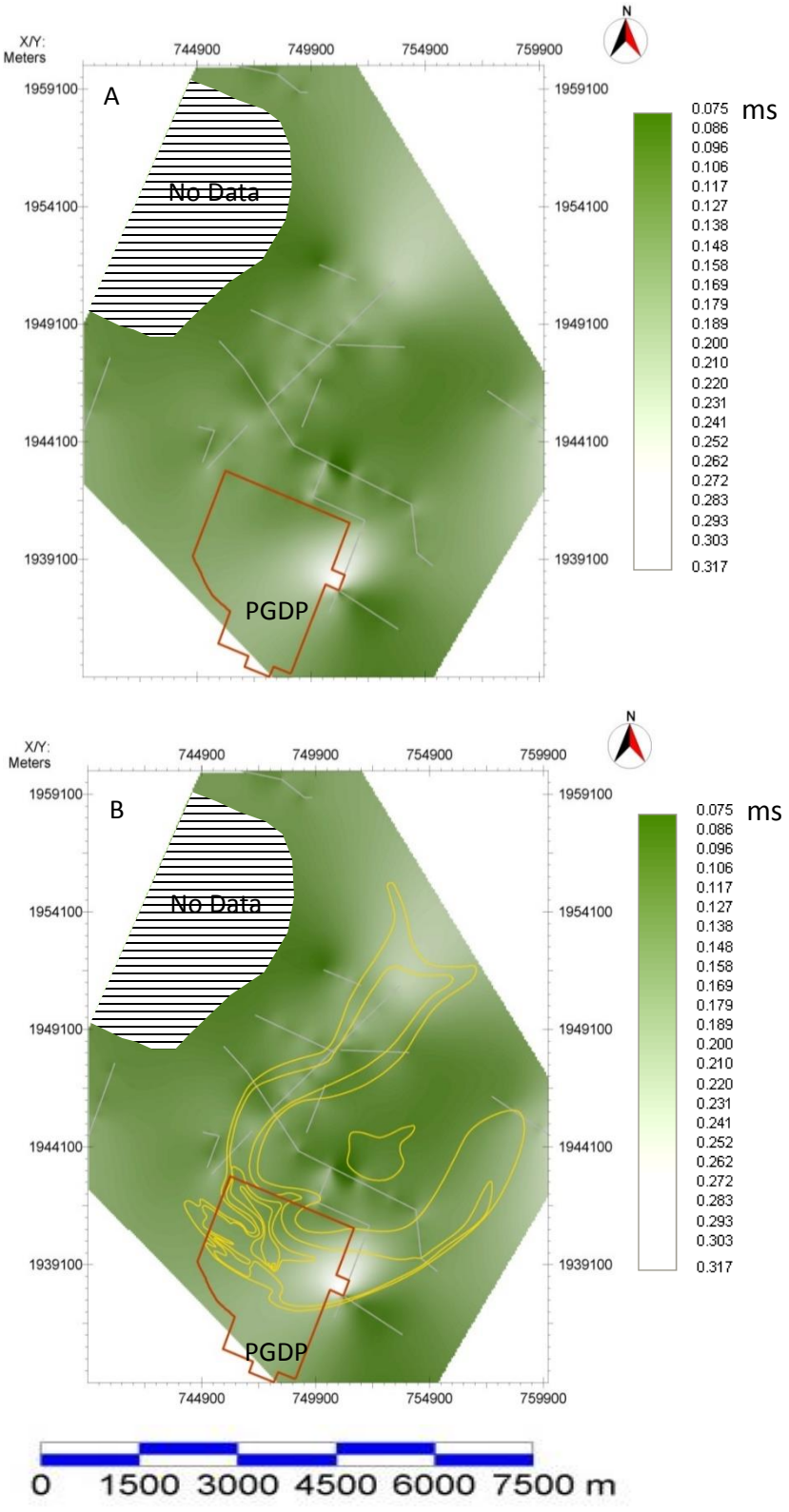

Figure 4.26: (A) Time-structure map of Mounds Gravel. (B) Time-structure map of Mounds Gravel correlated spatially with the contamination plume.

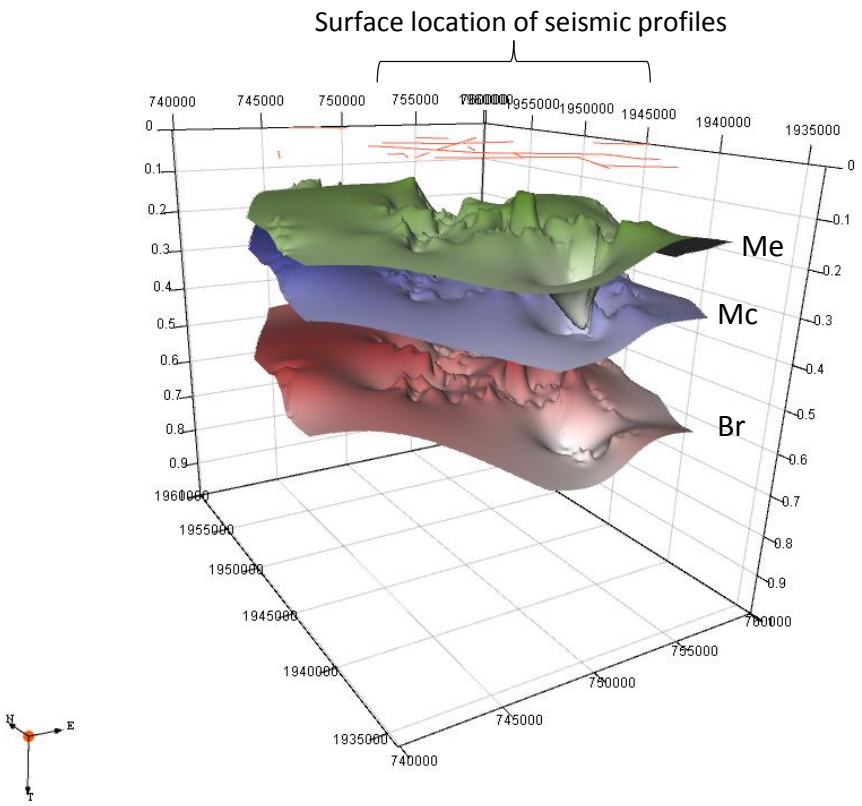

Figure 4.27: A 3D view of the combined time-structure surfaces of the identified reflectors in relation to the surface location of the seismic profiles.

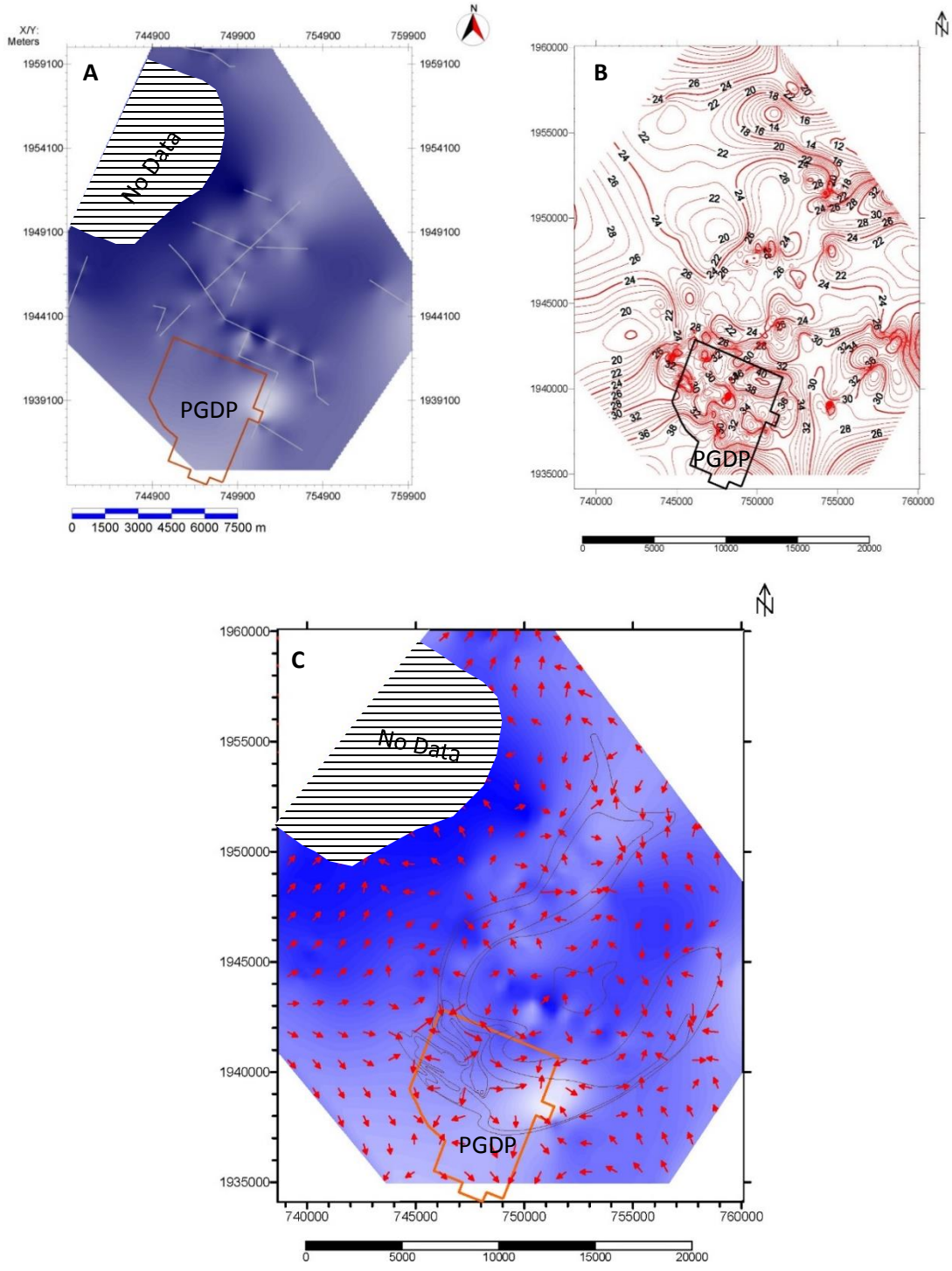

Figure 4.28: (A) Time-structure map of the McNairy top. (B) Depth contour map of the McNairy Formation top. (C) Time-structure map and depth vector map of the McNairy Formation top, correlated spatially with the contamination plume. Depth vector heads point to the deeper areas that are consistent with deeper (white) areas in the time structure map.

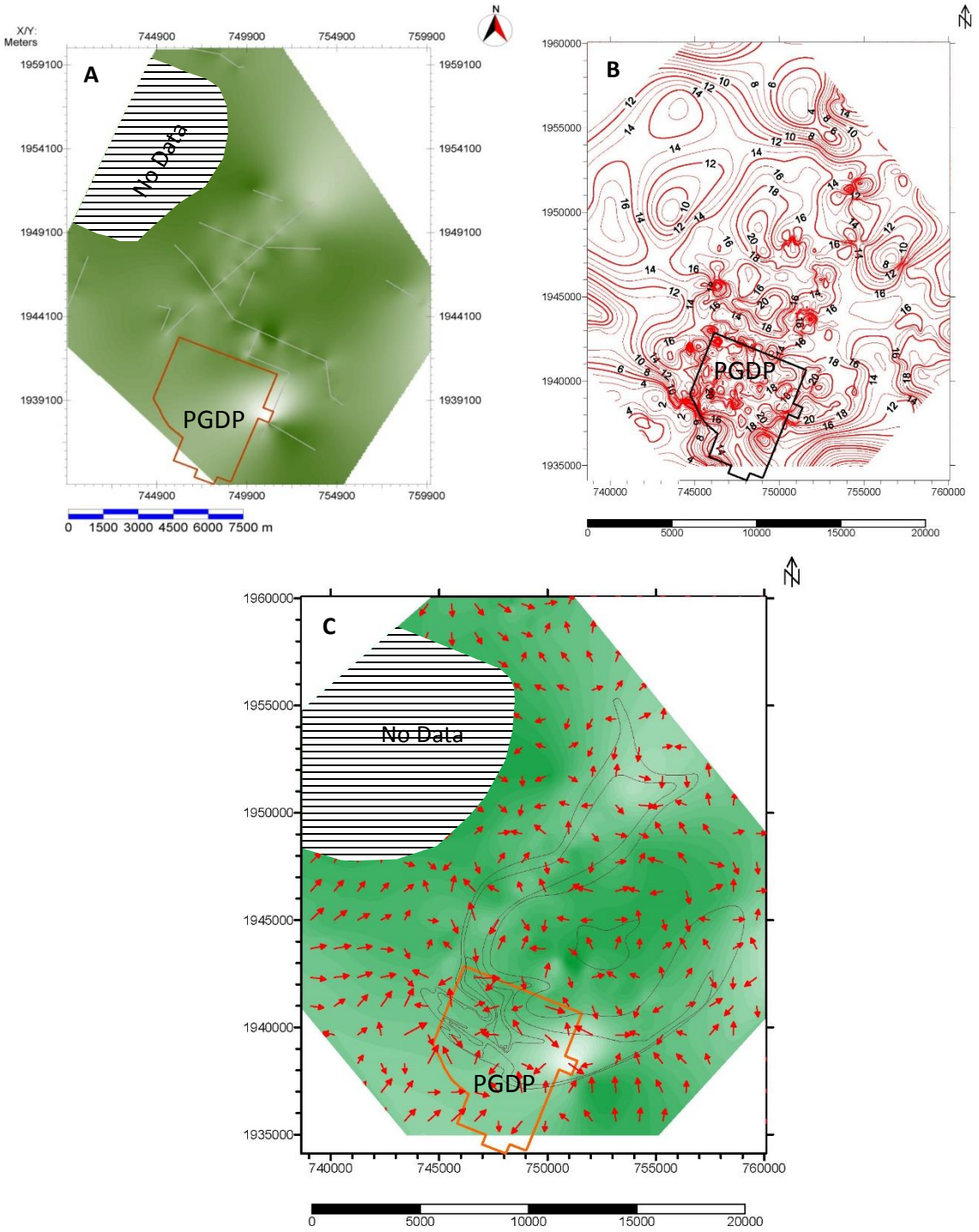

Figure 4.29: (A) Time-structure map of the Mounds Gravel top. (B) Depth contour map of the Mounds Gravel Formation top. (C) Time-structure map and depth vector map of the Mounds Gravel Formation top, correlated spatially with the contamination plume. Depth vector heads point to the deeper areas that are consistent with deeper (white) areas in the time structure map.

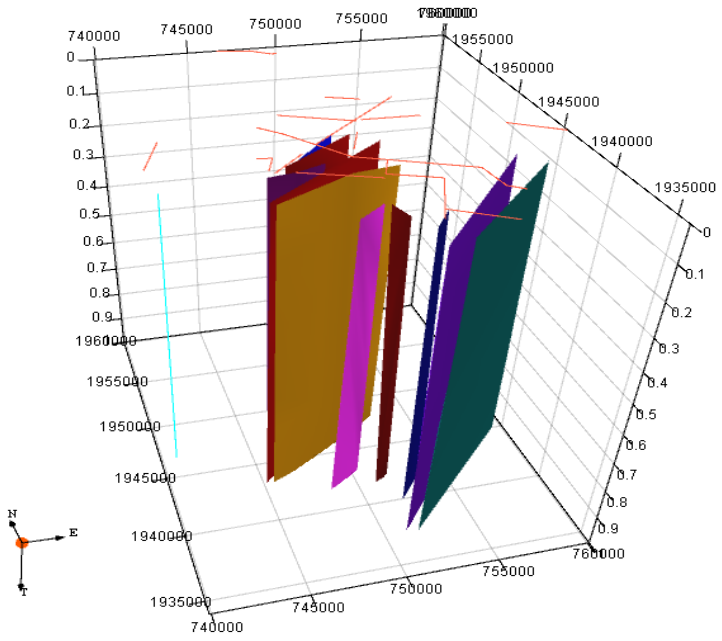

Figure 4.30: A 3D view of the gathered interpreted faults seen on the whole seismic reflection dataset. The general fault planes trend northeast-southwest. The subsurface locations of the interpreted faults are related to the surface location of the seismic profiles.

4.2 Shear-Wave Birefringence Technique

Shear-wave birefringence was first a successful tool in imaging in-situ stresses and fracture orientation in rock layers (Crampin, 1984; Martin and Davis, 1987; Verdon and Kendall, 2011). Later, Harris (1996) used the shear-wave splitting method in unlithified sediments southwest of this study area near the central part of the New Madrid Seismic Zone in order to determine the applicability of the method for seismic-hazard evaluation. He found that azimuthal anisotropy can be detected in the near-surface sediment, and attributed it to differential stress conditions and/or microfractures associated with nearby faults. Shear-wave birefringence evaluation in the thick water-saturated sediment overburden that conceals bedrock structure at this study site was considered a potentially significant tool for performing a near-surface fault assessment, particularly since the multiple reflection profiles provide excellent constraint on fault location, something that

was not available for the Harris (1996) study. The experiment in this study was conducted along the southern part of profile J1 where a high-resolution fault image and location (identified as FZ-3) is interpreted (Fig. 2.6). The experiment evaluated the practical ability for detecting azimuthal anisotropy associated with fault displacement in unlithified sediment, and if detectable, measuring the magnitude of the anisotropy imparted to the sediment by the structural inclusion.

4.2.1 Determining the Shear-Wave Window

At the free surface, shear-waves undergo phase, amplitude, and mode changes that generate precursory and subsequent phases beyond the critical angle (*ic*) (Crampin, 1985).

$$ic = sin^{-1} (Vp/Vs)^{-1} \quad \text{(Crampin, 1985)} \qquad (4.3)$$

Therefore, near-surface shear-wave splitting experiments using rotated reflection data can become problematic and difficult to interpret without a defined shear-wave window. Changes or disturbances in the wavelet characteristics do not exist or are much less for data inside the shear-wave window where the incident events can have near-vertical propagation paths to target depths. In order to remove the free-surface effect on the dataset, a shear-wave window was calculated by measuring Vp and Vs for the first layer using first-break arrivals (Appendices E and F). The calculated P-wave velocities ranged between 620 m/s and 468 m/s, and the corresponding S-wave velocities between 234 m/s and 213 m/s (Fig. 4.31). Thus, *Vp/Vs* ratios ranged between 2 and 2.9. These values are well within the minimum limits stated by Dohr and Janle (1980), as well as the Harris (1996) findings for near-surface sediments. Twelve meters was the average depth for which *Vp/Vs* ratios were calculated (Fig. 4.32). The *Vp/Vs* ratio is used to calculate the maximum width range of the shear-wave window in the surface sediments according to the relationship defined by equation 4.3. The velocity variation allowed a maximum width range for the shear-wave window to be calculated = $\sin^{-} (Vp/Vs)^{-1}$ ……. at ~12 m depth:

$$= \sin^{-} (2.0)^{-1} = 30°$$

$$= \sin^{-} (2.9)^{-1} = 20°.$$

Based on the four reflectors' approximate depths (e.g., Br = 100 m, Mc = 44 m, MG = 24 m, and Me = 10 m) and minimum and maximum offsets (2 m and 48 m), incident angles are between 0.5° and 13° for Br, 1° and 28° for Mc, 2° and 45° for MG, and 5° and 67° for Me were calculated. These values demonstrate that the deeper reflector (Br) was recorded within the shear-wave window, which means no phase distortion or alteration is expected. Parts of shallower reflectors (Mc, MG, and Me) do fall outside the shear-wave window and have likely been altered (Fig. 4.33). In order to eliminate this effect, the useable data were narrowed to exclude contaminated signals from outside the shear-wave window.

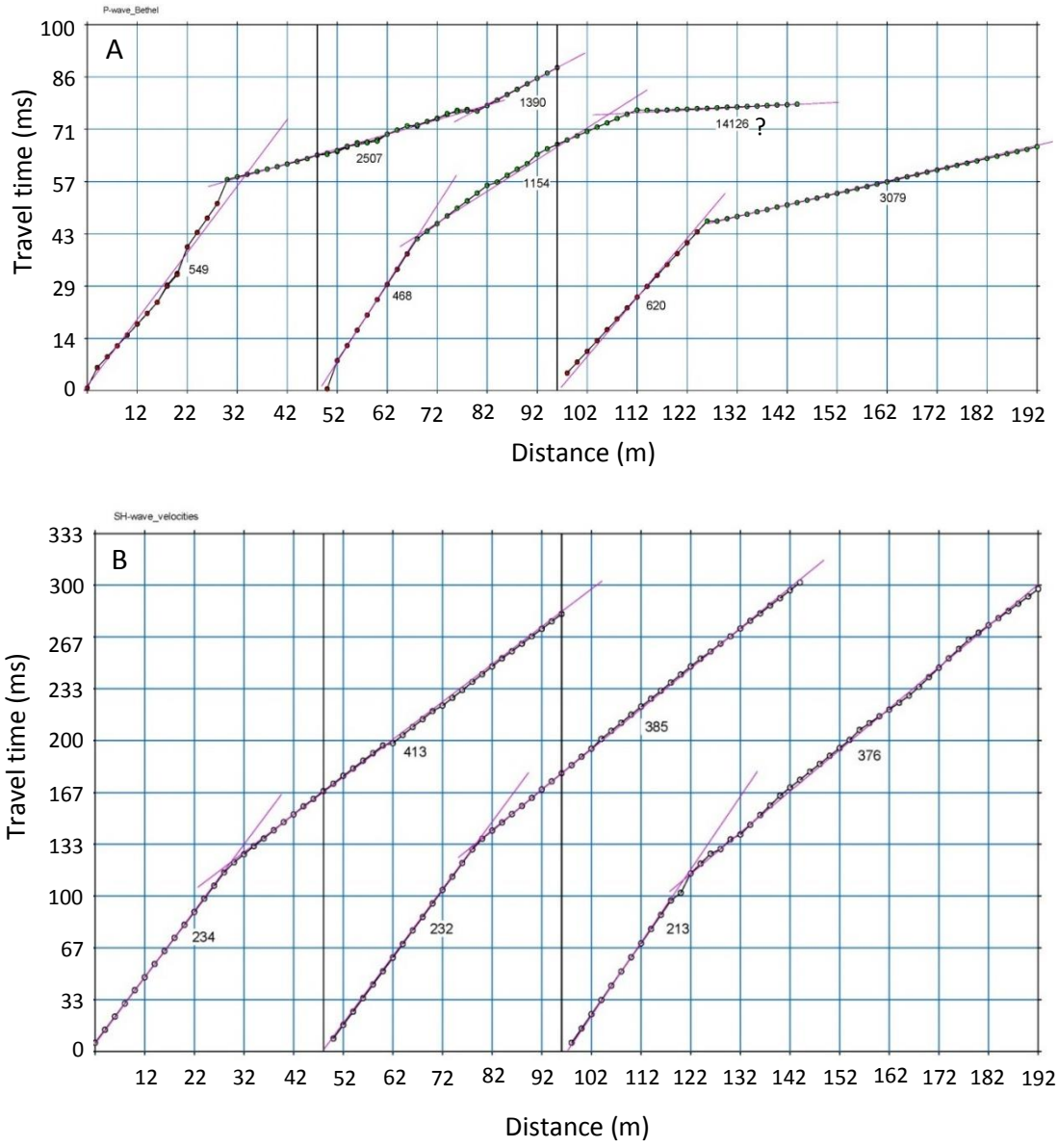

Figure 4.31: Time-distance curves of three consecutive individual (48-channel) field files as they appear in Plotrfra of SeisImger ver. 2.9. First breaks were picked in Pickwind of SeisImager (Appendices E and F). (A) Converted SP-wave velocity measurements. (B) SH-wave velocity measurements.

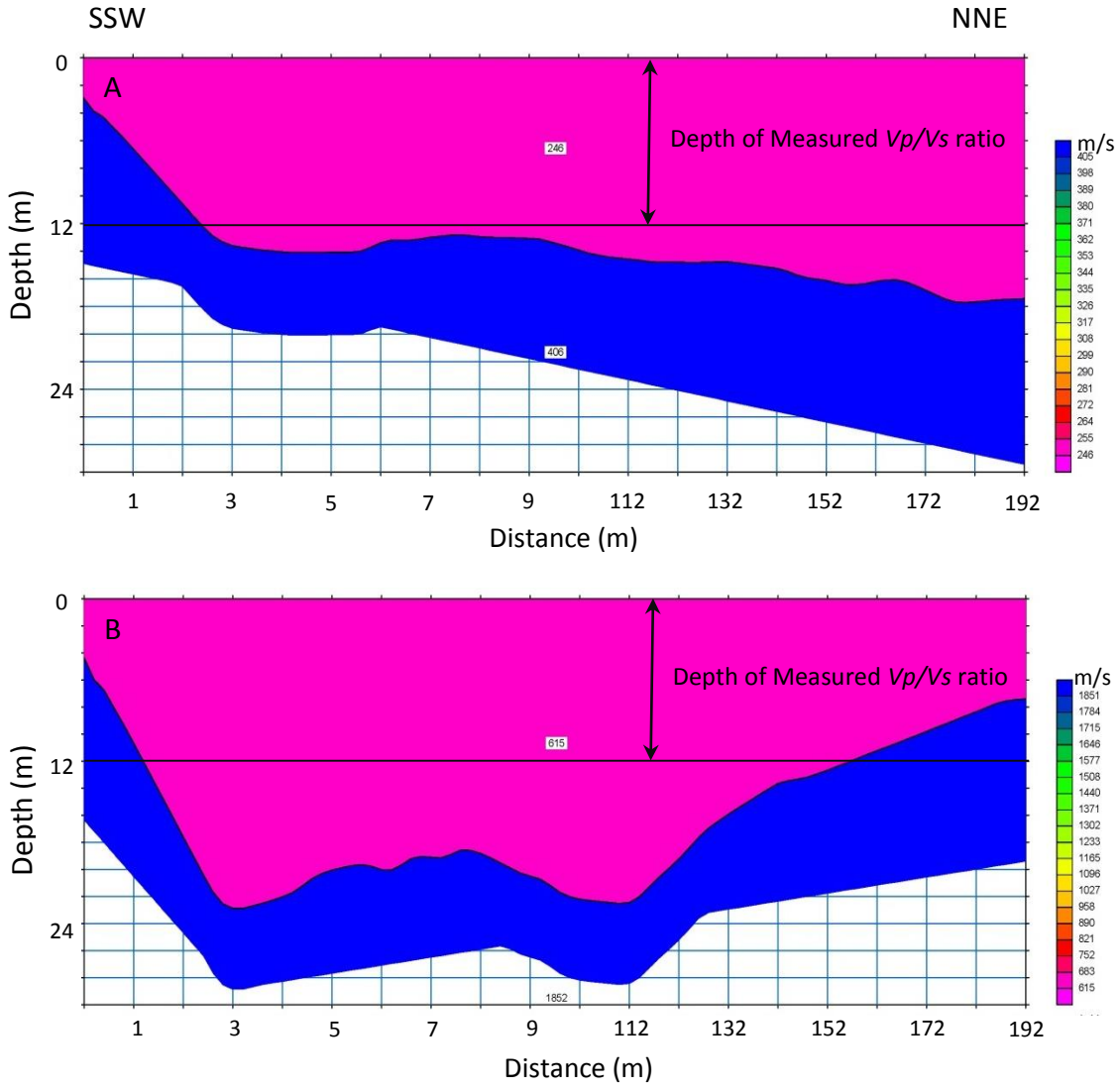

Figure 4.32: A tomographic profile of three consecutive individual (48-channel) field files. The common depth of the measured Vp and SH-wave velocities was 12 m. (A) First-layer average SH-wave velocity was calculated at 246 m/s. (B) First-layer average P-wave velocity was calculated at 615 m/s.

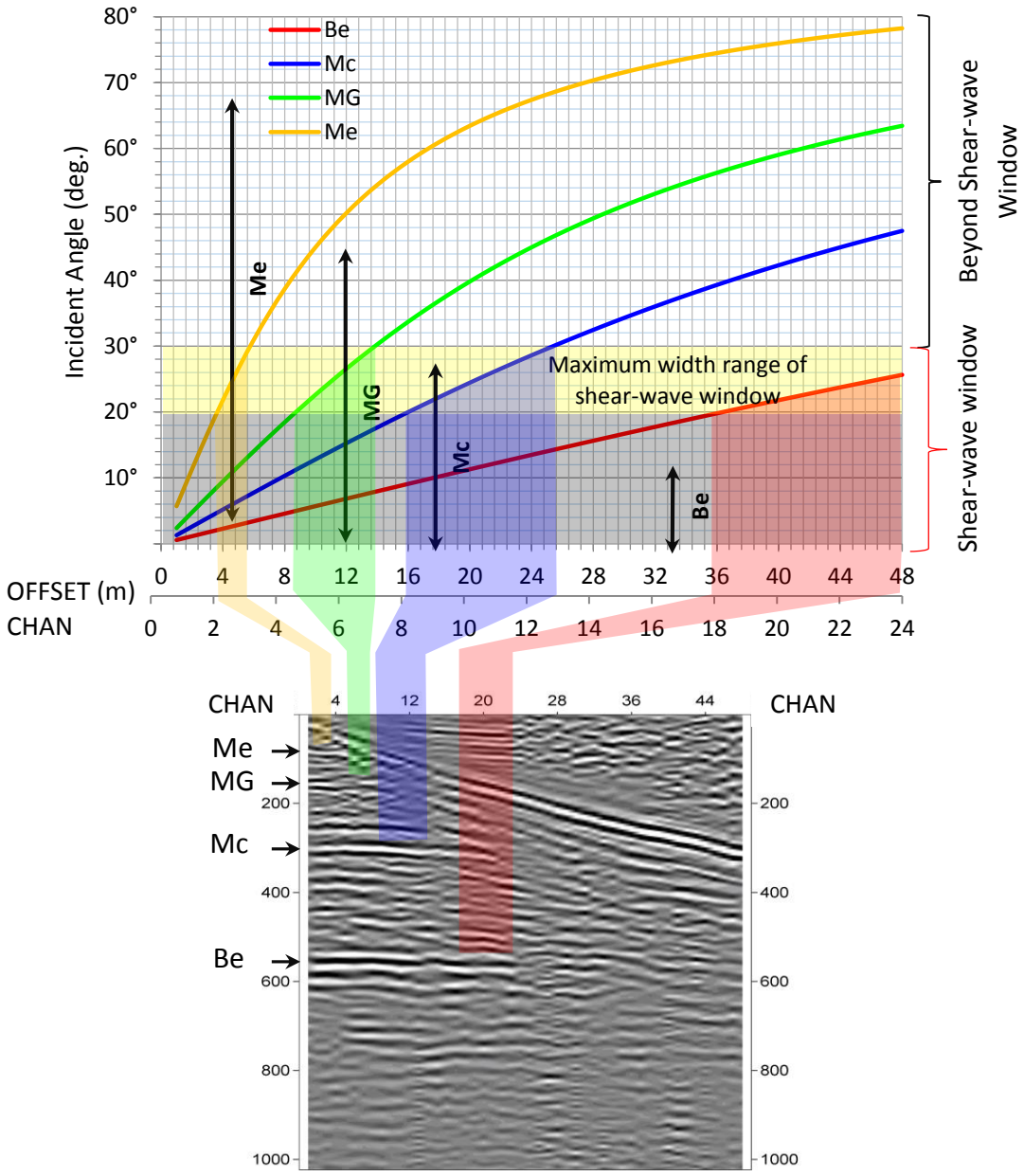

Figure 4.33: Shear-wave window and reflectors' incident angles in correspondence with example field file record. Red, blue, green, and brown transparent areas show the maximum width range of the shear-wave window. On the left side of each transparent area, signals are recorded within the shear-wave window. On the right of any transparent area, signals are recorded outside the window, where amplitude, phase changes occur. For example, the incident angles of the Br reflector are between 0.5° and 13°, which means it is recorded within the shear-wave window; after channel 24, the signal was distorted. The maximum width of the shear-wave window was calculated at 12 m depth, which correspond to a 30° incidence angle.

4.2.2 Data Processing and Rotation

Each shot record was composed of 24 transverse-oriented geophones (SH) and 24 radial-oriented geophones (SV) that was generated with either a transverse-oriented (SH) or radial-oriented (SV) energy source. In any source direction, six total impacts were applied at each shot location, three strikes on each side. Each strike was saved individually in order to check for inadvertent time delays prior to stacking the data. The three hammer strikes per side were stacked into a single record, and a polarity reversal was performed on the second side before both sides were stacked into a single record. The stacking process was performed to enhance the signal/noise ratio. This process was repeated separately for both the transverse and radial datasets. Regardless of transverse or radial source, the transverse-oriented geophones were separated from radial-oriented geophones, creating two datasets for each source orientation (Fig. 4.34). Since the transverse-oriented geophones were assigned an odd channel number (1–47) and radial-oriented geophones were assigned an even channel number (2–48) in the field operation, data headers of each dataset were reindexed in order to set channel numbers from 1–24 for each dataset, TT, TR, RT, and RR. This is an important step for setting the field geometry and for calculating velocities in the subsequent processing steps.

Each dataset was processed identically, following the same processing procedure to collect seismic-reflection data (Fig. 3.1, Table 3.1), but before the velocity analysis step was performed, the GEDCO (2012) algorithm of data matrix rotation was used to determine the direction of the natural coordinate system. The correct rotation angle was postulated as the maximum signal energy of wave polarization that aligned parallel to the sediment's inclusion direction. Minimum signal energy of wave polarization is aligned perpendicular to the sediment's inclusion direction. In other words, maximum and minimum signal energy is an indication of wave polarization that is also coincident with the natural axis of fast and slow directions. The estimation of correct rotation angle was visually and numerically determined. Rotation was performed to each component (i.e., TT, TR, RT, and RR) separately at 5° rotation increment, between 0° and 180° clockwise. A visual inspection was performed to each field file in the datasets of the same source direction. Then, the TT component was compared with the TR component because they are perpendicular to each other and generated from the same energy source; the same is

true with RT with RR. Figure 4.35 is an example of the visual inspection of TT and TR components. Between 35° and 50° rotation, maximum energy was initially noted on the TR component whereas minimum energy was noted on the TT component at the same rotation angle range.

	Transverse-geophone	Radial-geophone
Transverse-source (0°)	TT	TR
Radial-source (90°)	RT	RR

Figure 4.34: Data organization of four components, corresponding to different directions of source impact and receiver component orientation.

For more specific estimation of correct rotation angle, the amplitude spectrum was calculated for each dataset at 5° rotation increments (Appendix G). In Figure 4.36A, the maximum amplitude ratio difference between TR rotated/Initial) and TT rotated/Initial is at 40° clockwise rotation. This indicates that the TR component is aligned with the natural coordinate system where the reflection energy is focused. The minimum amplitude ratio difference of TT/I – TR/I at 40° indicates that the TT component is aligned perpendicular to the natural coordinate system of minimum reflection energy. After a 40° rotation, the maximum amplitude ratio difference of TR/I – TT/I decreased gradually until the 130° rotation to the minimum reflection energy. If 40° rotation represents the fast direction, the 130° rotation, which is perpendicular to 40° rotation, is the slow direction for the same component (TR); the opposite was observed on TT/I – TR/I.

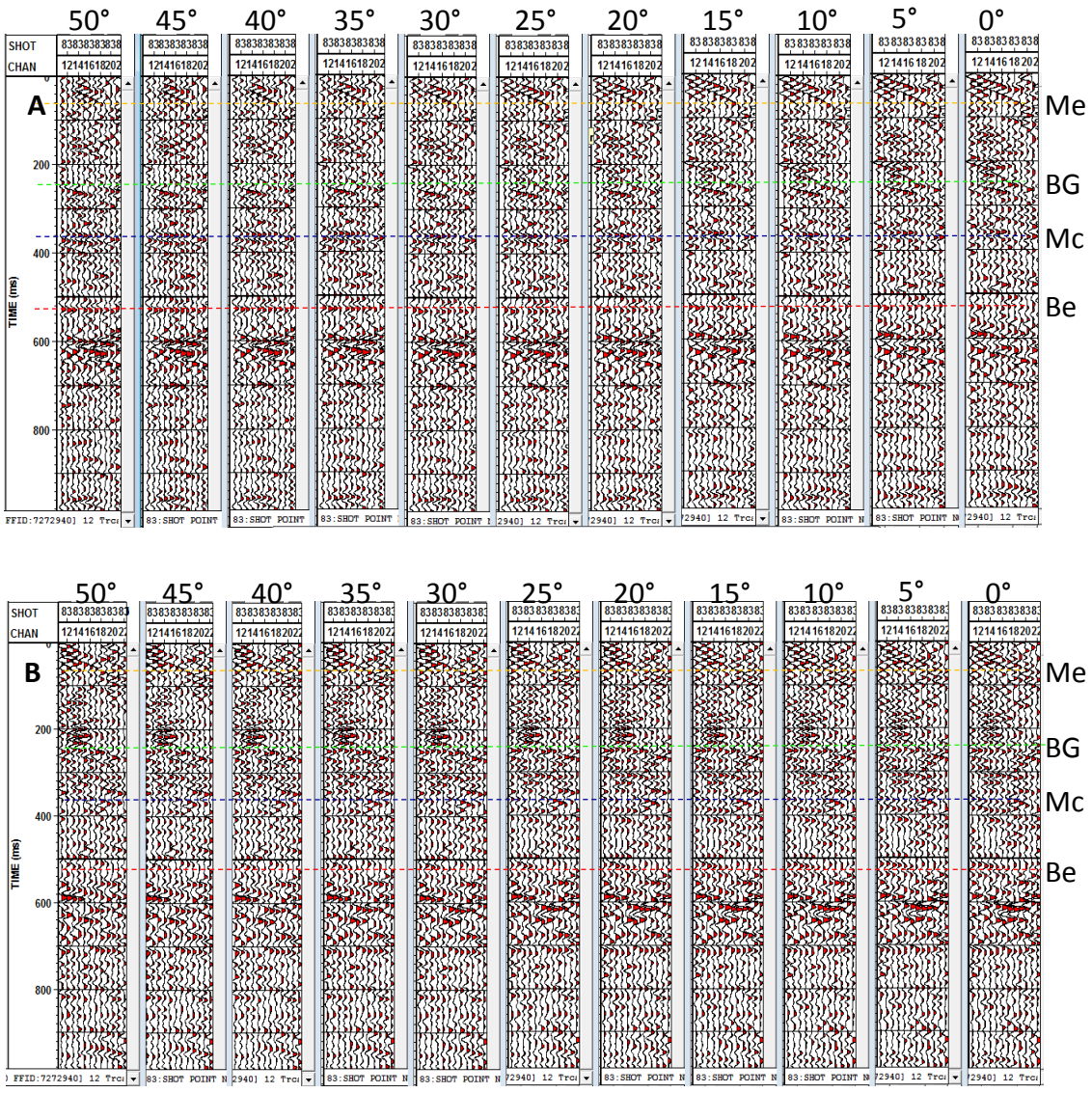

Figure 4.35: Visual inspection was used to determine the correct rotation angle. (A) Transverse-source radial-receiver. (B) Transverse-source transverse-receiver. Both datasets were rotated at 5° increments clockwise. The rest of the rotation degrees (i.e., 55° to 180°) are displayed in Appendix H.

In Figure 4.36B, the maximum and minimum amplitude ratio differences of RR/I – RT/I and RT/I – RR/I are picked at 90° clockwise rotation. This likely indicates no shear-wave splitting has occurred because waves of SV-source converted to SP-wave mode. These maximum and minimum amplitude ratio differences are interpreted as not expressing any

geologic/anisotropic characteristic, but are related to preferential source-receiver direction. For example, at radial source, rotating transverse receiver polarization at 90° leads to a radial polarization (parallel to the source polarization, RR). This causes the maximum amplitude ratio difference at 90° clockwise rotation.

According to the rotation experiment, only TT and TR field datasets at 40° rotation were used in the rest of the processing procedure. Post-rotation processing steps were velocity analysis (NMO correction), noise attenuation, sorting, and stacking. The geographic bearings of the fast and slow directions were calculated at N60°E and N30°W, respectively.

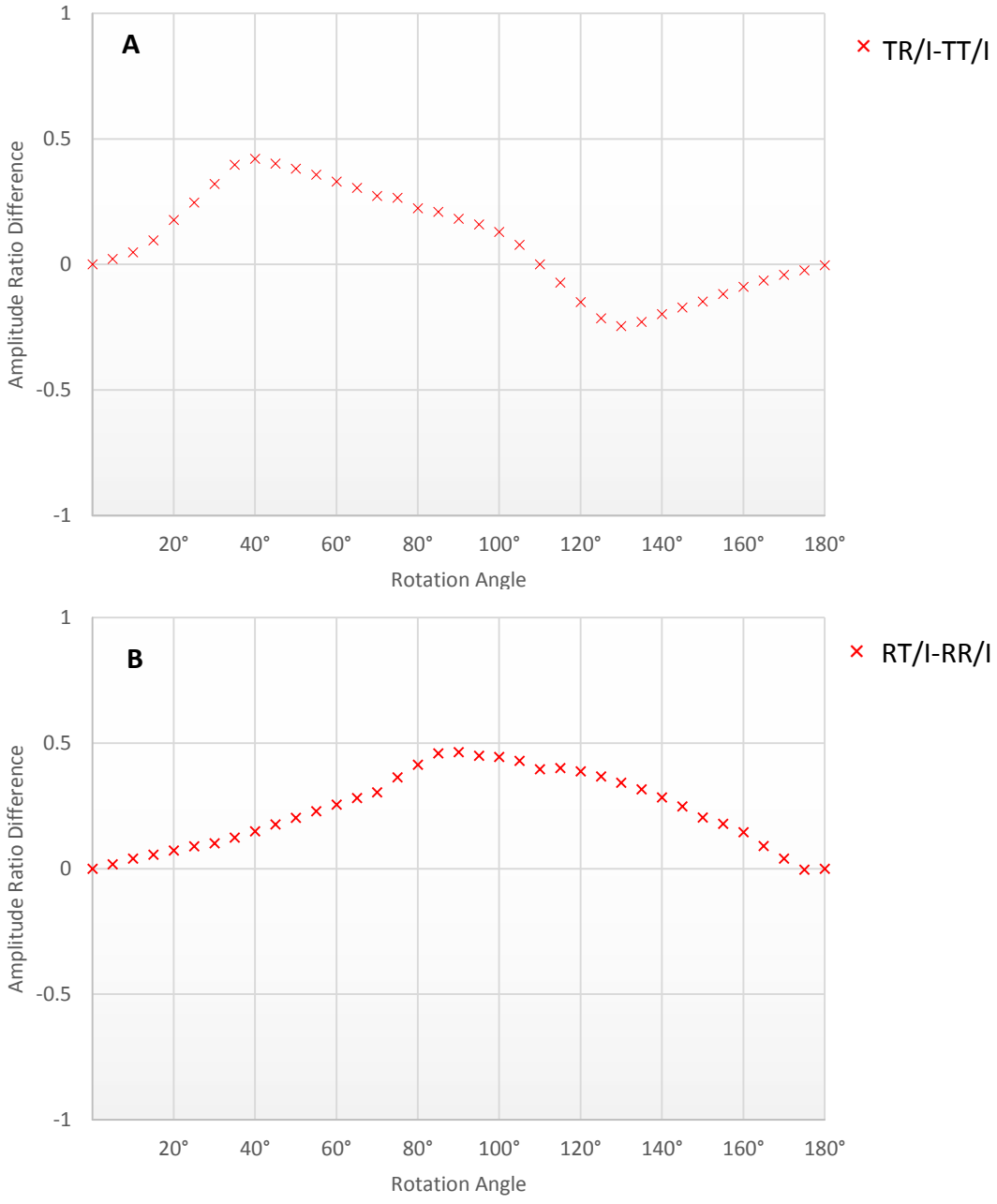

Figure 4.36: Plot of amplitude spectrum ratio (rotated/initial) difference. (A) Transverse source; red crosses represent ratio differences (the amplitude of rotated transverse-geophone/initial value minus the amplitude of rotated radial-geophone/initial value). (B) Radial source; same calculation procedure as used for transverse source.

For easier comparison between the fast and slow directions, field files (fast and slow) and stacked profiles (fast and slow) were spliced to show the reflection time shifts, called dynamic mis-ties (Figs. 4.37–4.38). The dynamic mis-tie provides a measure of the subsurface anisotropy as a function of fracture intensity and orientation (Martin and Davis, 1987), and can be measured directly from the time-delay (ΔT) between the fast and slow directions at any given reflector. Dynamic mis-tie is an essential parameter for calculating the average azimuthal anisotropy (η) which is can be calculated by equation (4.4).

$$\eta = \Delta T / T_{Fast} \quad \text{.....(4.4)}$$

Where

$$\Delta T = T_{Fast} - T_{Slow}$$

(Martin and Davis, 1987)

T_{Fast} and T_{Slow} are the two-way travel times at a given reflector.

Dynamic mis-tie and average azimuthal anisotropy were calculated for Be, Mc, and MG (Table 4.3), but not for the Me reflector because data quality was not coherent enough to estimate these factors.

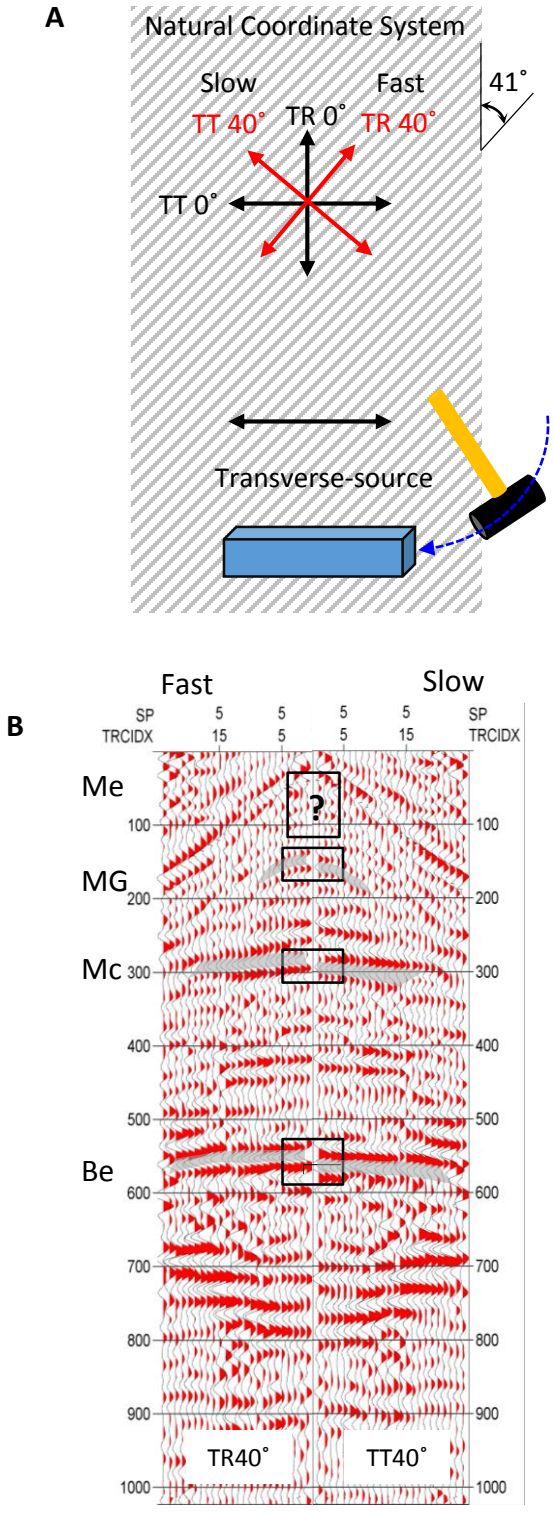

Figure 4.37: (A) A simplified schematic diagram shows receiver polarization in relation with natural coordinate system (fast and slow direction) after 40˚ rotation. (B) Spliced field files of fast TR and slow TT components showing the dynamic mis-tie.

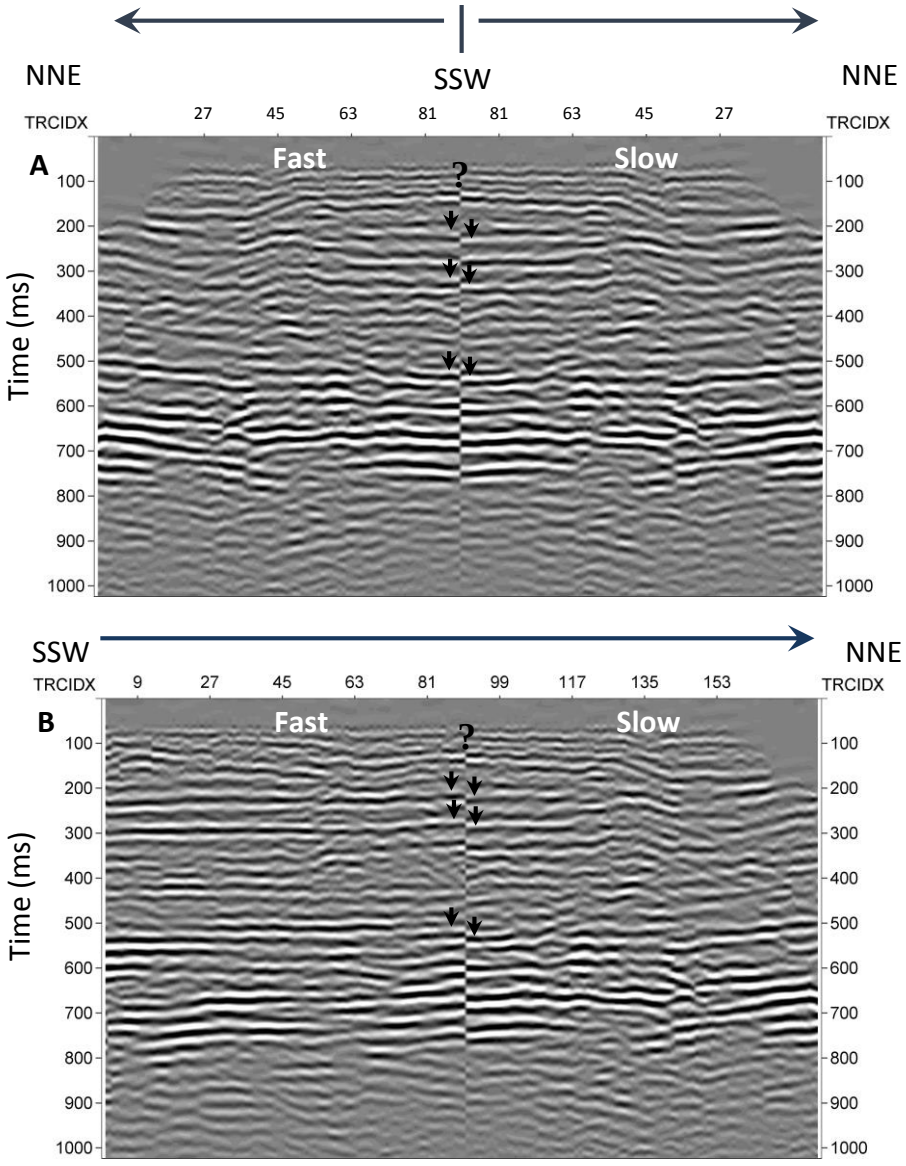

Figure 4.38: A spliced section of fast (TR) and slow (TT) components. Black arrows show the dynamic mis-tie at individual reflectors on the stacked sections. (A) Mirror splice of fast and slow directions. (B) Lateral splice of fast and slow directions.

Table 4.3: Dynamic mis-tie and average azimuthal anisotropy values

	Depth (m)	T_{Fast} (ms)	T_{Slow} (ms)	Dynamic mis-tie	η (%)
Be	100	516	531	15	2.9
Mc	44	278	287.5	9.5	3.4
MG	24	215	224.5	9.5	4.4

The calculated values of average azimuthal anisotropy (Ƞ) fall within the regular value limits stated by Crampin and Lovell (1991). The tabulated reflector depths and (Ƞ) values were plotted in order to depict the sediment's behavior with depth in terms of average azimuthal anisotropy (Fig. 4.39). Although shear-wave splitting and polarization are observed by rotating the two horizontal components of shear-wave reflection, average azimuthal anisotropy decreases with depth. This can be related to the different physical geometry and dimensions of fluid-filled inclusions (physical configuration) in the lithology (Crampin and Lovell, 1991). Thus, it can be the case for near-surface unlithified sediments, poorly consolidated sediments, and bedrock's physical configurations. However, these observations remain speculation because of the surface shear-wave splitting limitation, which preserves only the last or near-surface anisotropy in the record. Therefore, a downhole geophone measurement at each vertical elevation can further support these observations.

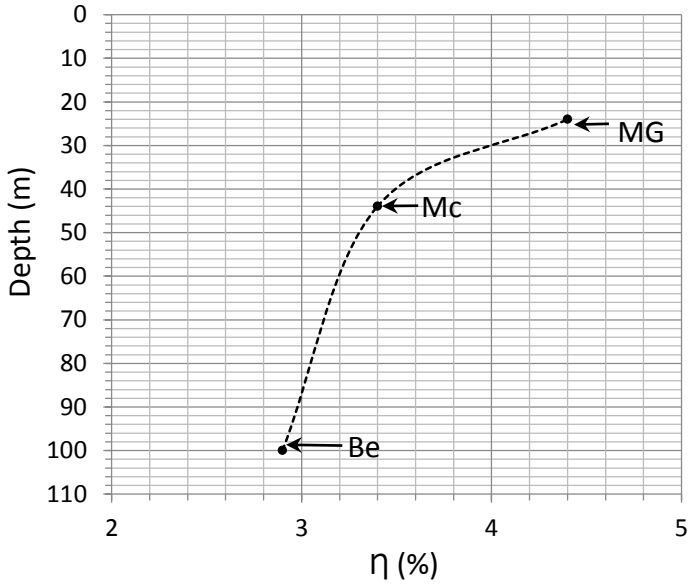

Figure 4.39: Relationship between depths of Be, Mc, and MG and average azimuthal anisotropy. Average azimuthal anisotropy decreasing with depth indicates that the physical configuration of the sediment particles changes with depth.

4.2.3 Interpretation of Shear-Wave Birefringence

Shear-wave splitting has proved to be a successful tool to relate azimuthal anisotropy with geologic causes (e.g., field stresses and cracks) in near-surface sediments and rocks (e.g., Martin and Davis, 1987; Harris, 1996). The geographic bearing of the fast direction is N60°E, which corresponds with the geographic bearing of the interpreted fault strike of N61°E observed on SH-wave profile J1 and P-wave profiles J2 and I (Fig. 4.40). The fault caused an azimuthal anisotropy of 2.9 percent, 3.4 percent, and 4.4 percent at Be, Mc, and MG, respectively. Increasing azimuthal anisotropy from bedrock to the shallow sediments (Fig. 4.39) suggests two possible explanations: (1) Although it has been postulated that general features of shear-wave splitting are alike in many different rock types (Crampin and Lovell 1991), physical configurations of sediment particles can differ within the same formation and thus influence the observation; therefore, the reactivated fault can affect the physical configuration of unlithified sediments more than it does semilithified sediments and much more than rock. (2) The multiple or episodic reactivation of the fault has differentially affected the lithologic material. These

observations are speculative due to the anisotropic "overprinting" that can occur in surface measurements (Harris, 1996). In order to resolve the vertical variation in the sediment overburden a downhole seismic investigation utilizing a directional- controlled 3-component geophone.

Amplitude variations between fast and slow directions (Fig. 4.38) are associated with the azimuthal anisotropy caused by the northeast-southwest fault orientation. In context of decreasing azimuthal anisotropy with depth, a similar observation can be made for reflector amplitudes. Maximum amplitude dissimilarity is observed on the shallow reflectors whereas it is minimal on the bedrock reflector.

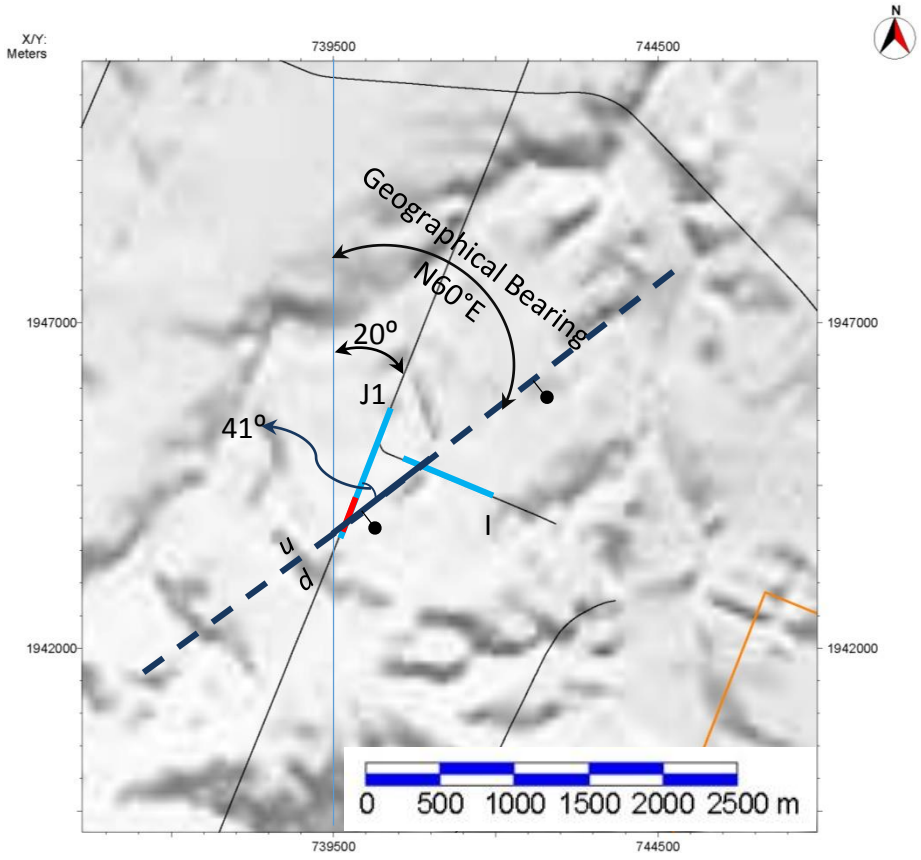

Figure 4.40: Base map showing the locations of profiles J and I, SH-wave and P-wave reflection profiles. The small red line is the location of the shear-wave splitting experiment and P-wave reflection profile. Geographically, the interpreted fault observed on profile I intersects profile J at 41° (N61°E). The fault strike is coincident with the geographic bearing of the fast direction at 40° rotation (N60°E).

4.3 Electrical Resistivity Method Versus Shear-Wave Velocities

The locations of electrical resistivity datasets were selected coincident with seismic reflection profiles to support seismic data interpretation. Blits (2008) collected ER datasets to image the relative displacement across the faulted zones. The same datasets were reprocessed for this study to add another line of evidence supporting the seismic observations pertaining to fault effects on physical properties and configuration of near-surface sediments. Shear-wave interval velocities were overlaid on seismic-reflection profiles. Since shear-wave velocity is directly related to rigidity or shear modulus (equation 4.5), it can provide information regarding variation of the physical properties for the near-surface sediments affected by the fault.

$$Vs = \sqrt{\frac{G}{\rho}} \quad \text{…….. (4.5)} \quad \text{(Burger et al., 2006)}$$

where *Vs*: shear-wave velocity ($m.s^{-1}$)

G: Shear modulus ($kg.m.s^{-2}$)

ρ: Density ($kg.m^{-3}$)

The inverted electrical resistivity tomography (ERT) profiles were inspected for variations in vertical and lateral resistivity values. Lows in electrical resistivity values are interpreted as higher porosity zones filled with increased amounts of pore water whereas high values represent lithology with lesser porosity. Because the shear-waves do not propagate through water, their velocity lows are related to deformation zones (i.e., rigidity modulus lows), not to the existence of pore water. In other words, faulted or deformed zones have lows associated with resistivity and shear-wave velocity.

4.3.1 ERT-1 Versus Shear-Wave Velocity Overlaid Profile H

The ERT-1 profile of 498 m length was collected coincident with seismic profile H of 500 m length. The maximum depth surveyed by ERT-1 profile was 71 m, which overlaps approximately two-thirds of the depth to the Br reflector on seismic-reflection profile H. The principal water-bearing units around the ERT-1 profile are the Metropolis Formation, Mounds Gravel, and McNairy Formation (Jacobs EM Team, 1998). Advanced

Geosciences Inc. (2007a) defined a resistivity value range between 1 and 100 Ohm-m as fresh water; variation of resistivity values within this range depend on dissolved ion content and temperature. ERT-1 has low resistivity values, with slight lateral variation between 10 and 23 Ohm-m at depths between 1 and 9 m. At depths between 9 and ~18 m, resistivity values increased to ~50 Ohm-m, with little or no lateral variation. Generally, the measured resistivity values from 1 to 18 m depth fall within the range of freshwater resistivity values. Therefore, relatively low resistivity values are caused by water-saturated media at this depth range. Information from boring logs (e.g., 27 and MW201) at 9 to 18 m depths correlated with upper Continental deposits. At depths between 20 and 45 m, they correlated with lower Continental deposits and upper McNairy Formation according to boring information, and had large lateral resistivity anomalies. The first anomaly was observed between electrodes 312 and 360 (Fig. 4.41). The resistivity values dropped from 250 to 112 Ohm-m, which is consistent with low shear-wave velocity between trace numbers 300 and 400. The correlated anomalies between the two methods are interpreted as electrical and elastic variation associated with Neotectonic deformation. Shear-wave velocity decrease leads to decreasing rigidity modulus of the sediments, which indicates the fracture zone; coincident low resistivity values added a third line of evidence for the same structural feature effects. Burger et al. (2006) and Chambers et al. (2006) stated that low apparent resistivity values correspond to fault effects. In other words, shear-wave velocity and resistivity lows are associated with the interpreted fault that caused the sediment's changes in physical characteristics and configuration. Similar observations were seen between electrodes 204 and 238, which correspond to trace numbers 150 to 250 and between electrodes 120 and 138, which corresponds to trace numbers 100 to 150. The area between electrodes 1 and 96 was not interpreted because the data quality was not as good as in the middle areas of the profile.

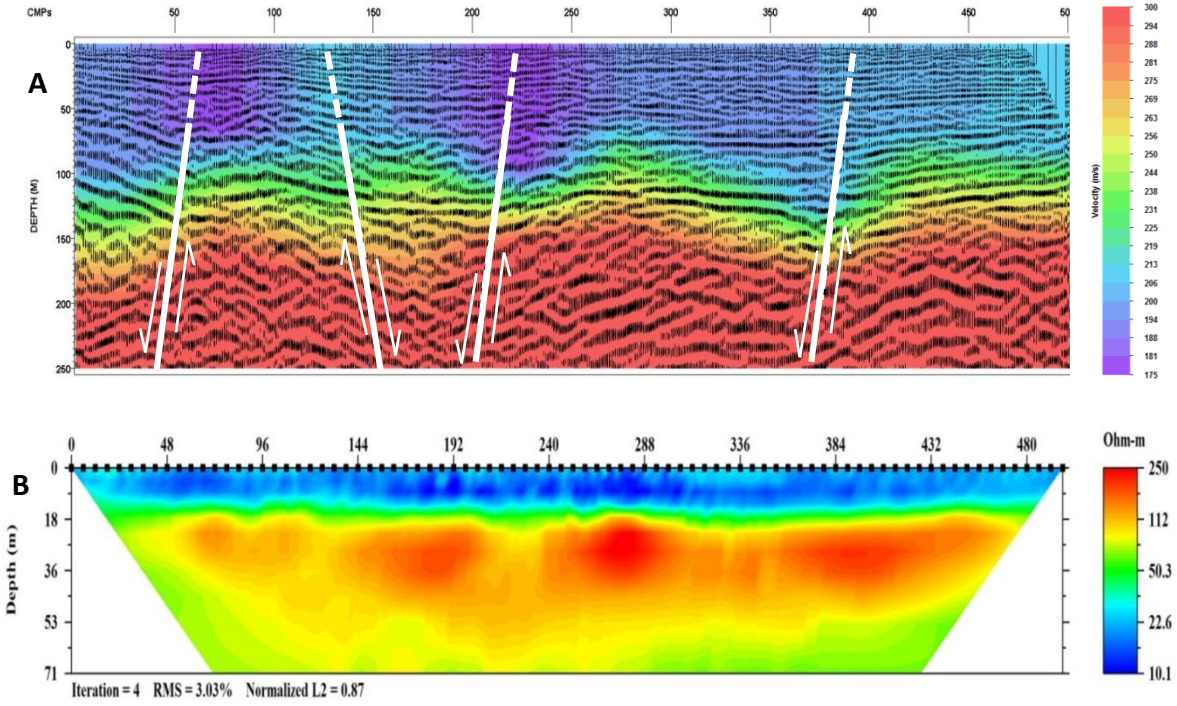

Figure 4.41: (A) Shear-wave velocity overlaid on seismic-reflection profile H. (B) Electrical resistivity tomography profile ERT-1. Fault effects on the physical characteristics of the sediments are clear on the shear-wave velocity and resistivity values.

4.3.2 ERT-2 Versus Shear-Wave Velocity Overlaid Profile L

The ERT-2 profile of 972 m length was collected coincident with seismic profile L of 713 m length. The maximum depth surveyed by the ERT-2 profile was 50 m, which overlaps approximately half of the depth to the Br reflector on seismic-reflection profile L. The principal water-bearing units around ERT-2 are the Metropolis Formation, Mounds Gravel, and McNairy Formation (Jacobs EM Team, 1998). Advanced Geosciences Inc. (2007a) defined a resistivity value range between 1 and 100 Ohm-m as fresh water; variation of resistivity values within this range depend on dissolved ion content and temperature. ERT-2 has low resistivity values, with slight lateral variation between 10 and 25.6 Ohm-m at depths between 1 and 11 m. At depths between 11 and ~13 m, resistivity values increased to ~32 Ohm-m, with little or no lateral variations.

Generally, the measured resistivity values from 1 to 13 m depth fall within the range of freshwater resistivity values. Therefore, relatively low resistivity values are because of water-saturated media within this depth range. The 11 to 13 m depths may be correlated with upper Continental deposits. At depths between 13 and 50 m, which correlate with lower Continental deposits and upper McNairy Formation, large lateral resistivity anomalies were seen. The first anomaly was observed between electrodes 288 and 586 (Fig. 4.42). The resistivity values dropped from 100 to 31.6 Ohm-m, which is consistent with the shear-wave velocity low between trace numbers 125 and 275. Similar observations were seen between electrodes 816 and 960, which corresponds to trace numbers 300 to 350.

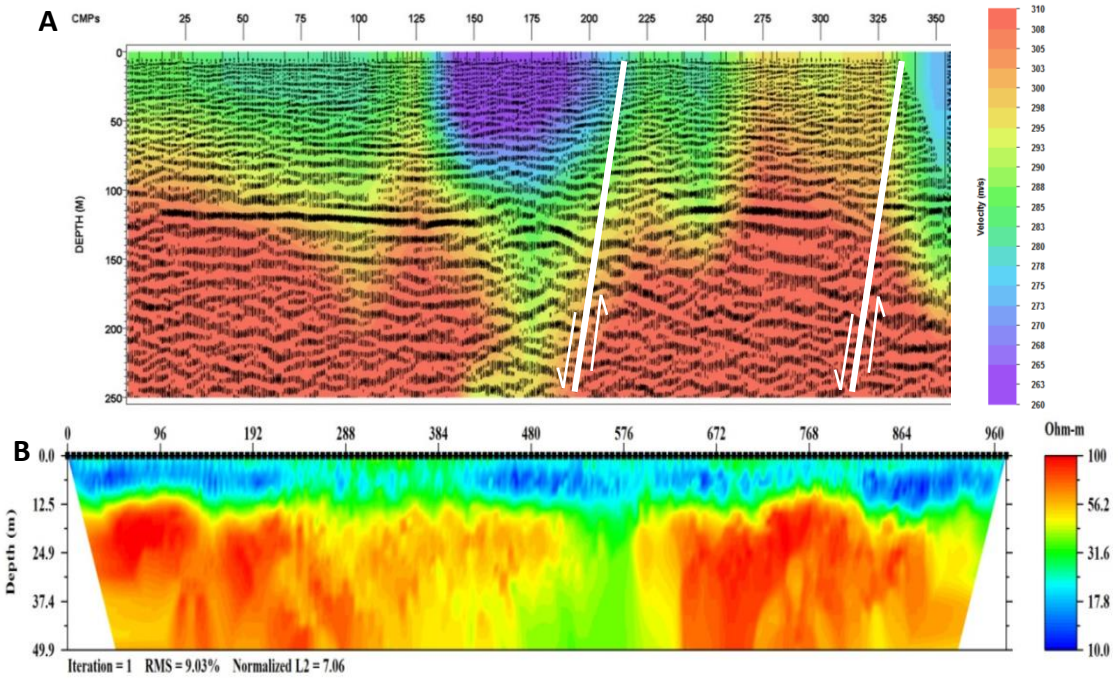

Figure 4.42: (A) Shear-wave velocity overlaid on seismic-reflection profile L. (B) Electrical resistivity tomography profile ERT-2. Fault effects on the physical characteristics of the sediments are clear on the shear-wave velocity and resistivity values.

4.3.3 ERT-3 Versus Shear-Wave Velocity Overlaid Profile J1

The ERT-3 profile of 498 m length was collected coincident with almost half of seismic profile J1 of 789 m length. The maximum depth surveyed by the ERT-3 profile was 50 m, which overlaps approximately half of the depth to the Br reflector on seismic-reflection profile J1. Low resistivity values with slight lateral variation between 8 and 26.7 Ohm-m were noted on the profile at depths between 1 and 6 m. At depths between 6 and 25 m, a large lateral resistivity anomaly was seen between electrodes 216 and 330 (Fig. 4.43). The resistivity values dropped from 88 to ~26 Ohm-m, which is consistent with a shear-wave velocity low between trace numbers 75 and 275. Relatively low resistivity values are because of water-saturated media within this depth range. Groundwater level varies between 2 and 13 m in the vicinity of PGDP (Jacobs EM Team, 1998), which may lower the overall resistivity values on the profile.

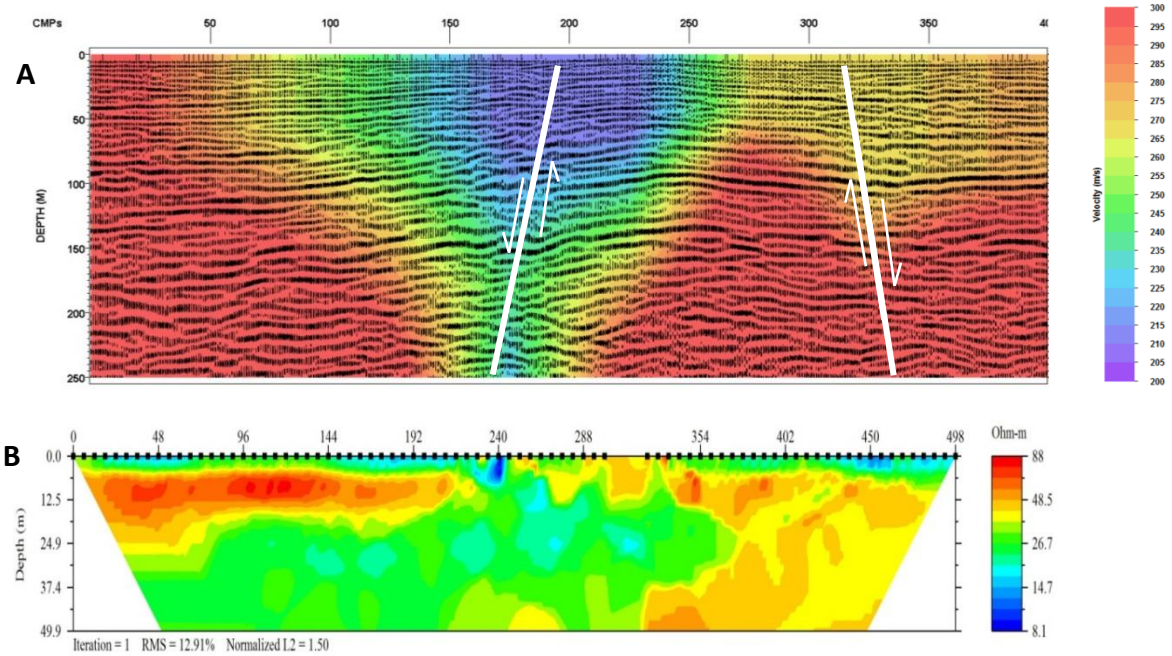

Figure 4.43: (A) Shear-wave velocity overlaid on seismic-reflection profile J1. (B) Electrical resistivity tomography profile ERT-3. Fault effects on the physical characteristics of the sediments are clear on the shear-wave velocity and resistivity values.

The above interpretation suggests that Neotectonic deformation affects the near-surface sediment's physical configuration, which is consistent with shear-wave velocity and resistivity lows. This particular physical particle configuration may offer a preferential flow path for groundwater carrying the contamination plume. Therefore, a fundamental understanding of the near-surface structure will aid in strategies to mitigate contamination within the study area.

CHAPTER FIVE

5 DISSCUSSION

5.1 General Inventory and Justification

In late 1988, DOE reported that the PGDP, a large part of the study area, was a source of trichloroethylene and technetium-99 contamination, and entered into an Administrative Consent Order with the U.S. Environmental Protection Agency. These contaminants can cause serious human health problems according to EPA reports, and so in 1994 the PGDP was designated a Superfund site. As such, intensive on- and off-site investigations were conducted in order to define the specific contamination source and to estimate the spatial extent of the groundwater contamination. Among the many types of investigations (i.e., biological, hydrological, ecological, geochemical, engineering, etc.), geophysical studies were conducted because of the need for noninvasive characterization of the subsurface geology in order to minimize the potential for vertical cross-contamination of the groundwater movement. A significant amount of unprocessed geophysical data, uncorrelated processed geophysical data, and thousands of borehole well logs were available from DOE. This database and newly acquired geophysical data were used to construct a subsurface geologic model in order to identify potential geologic conditions that control the anomalous groundwater/contaminant migration path across the site, thus allowing for a more effective and efficient mitigation design.

Specifically, SH- and P-wave seismic-reflection, electrical-resistivity, VSP, and borehole lithogic logs and Vp and Vs sonic suspension logs were mined from the DOE database. In addition, shear-wave birefringence data were newly acquired in order to further investigate anisotropic conditions imposed on the Quaternary sediment by reactivated faults. The variety of datasets has provided redundancy and constraint for the interpretive models in this complex geologic setting. The primary data used for subsurface imaging were SH- and P-wave seismic-reflection data. The data quality and resolution was fair to good overall, with a few exceptionally high-quality datasets. They, and the SH-wave data in particular, provided a relatively high-resolution set of two-dimensional images for

modeling of the subsurface. The borehole data also provide a high-resolution first-order constraint of the geologic conditions, but the potential for rapid lateral geologic variation away from the annulus of the borehole and the imperfect match between geologic and seismic acoustical boundaries result in some degree of uncertainty. Having said that, the borehole information assisted in the seismic-stratigraphic interpretation in two aspects. First, synthetic seismograms were created from Vp and Vs logs; in addition, the VSP data aided in the correlation of reflection events on the 2D images with stratigraphic units. Second, depths of target lithology that represented formations tops (i.e., McNairy-Clayton Formation and Mounds Gravel) were picked from the lithologic logs, then gridded and contoured in order to recognize the general behavior (i.e., deepening and shallowing) of the formation tops. Thus, spatial correlation between time-structure maps of formations tops from seismic-reflection data and depth contour maps from borehole lithologic logs were constructed to validate seismic interpretation in terms of structural control (Figs. 4.28–4.29).

Although seismic-reflection profiles are the primary method for imaging and assessing faults, variations in shear-wave velocity models and electrical resistivity tomography can further delineate the mechanical effects that faults can have on the near-surface sediment's physical characteristics. The changes in the sediment's physical configuration because of fault deformation also result in azimuthal anisotropy that is larger than other mechanical sources for the anisotropy (e.g., depositional fabric, etc.). Thus, surface-acquired shear-wave splitting experiments were attempted across a well-constrained fault to delineate the azimuthal anisotropy associated with this fault.

An accurate, high-quality seismic-reflection interpretation is a function of proper field acquisition and laboratory signal-processing procedures. Generic untested arrayed data acquisition and common processing procedures do not necessarily result in an interpretable subsurface geophysical image. Both seismic data processing and acquisition are necessary for an adequate interpretation. Overprocessing, as well as underprocessing, can result in unwanted noise and/or artifacts, diminishing, obscuring, and biasing the effective signal (Baker, 1999). The results of the current processing procedures were compared with previous processing procedure (Blits, 2008) for the same datasets (Figs.

5.1–5.4). Although the current processing procedure used more advanced algorithms (VISTA 12.0) compared with those Blits (2008) utilized (VISTA 7.0), the basic processing functions remain the same (e.g., geometry definition, mute, bandpass-filter, NMO, scaling, etc.). Because in this study the processing parameters were fine-tuned, the results were better than Blits (2008) processing procedure.. Additional steps in the current processing procedure, such as prestack deconvolution (Figs. 3.7 and 3.8), poststack deconvolution, adaptive subtraction of fk-filter rejected noise (Figs. 3.4 and 3.5), and post-stack depth migration processing steps add valuable constraints. The velocity estimations used for the NMO correction along with the post-stack depth migration was an important step in correlating the seismic-reflection images with the borehole stratigraphy. Three prominent stratigraphic horizons were consistently imaged across the study area: the Paleozoic bedrock, Cretaceous McNairy-Clayton Formation, and Tertiary Mounds Gravel. These are the surfaces used for the time-structure maps and geologic model. The shallower Metropolis Formation and Pleistocene loess interface was resolved on lines J1 and H, but were inadequate for deriving a time-structure surface.

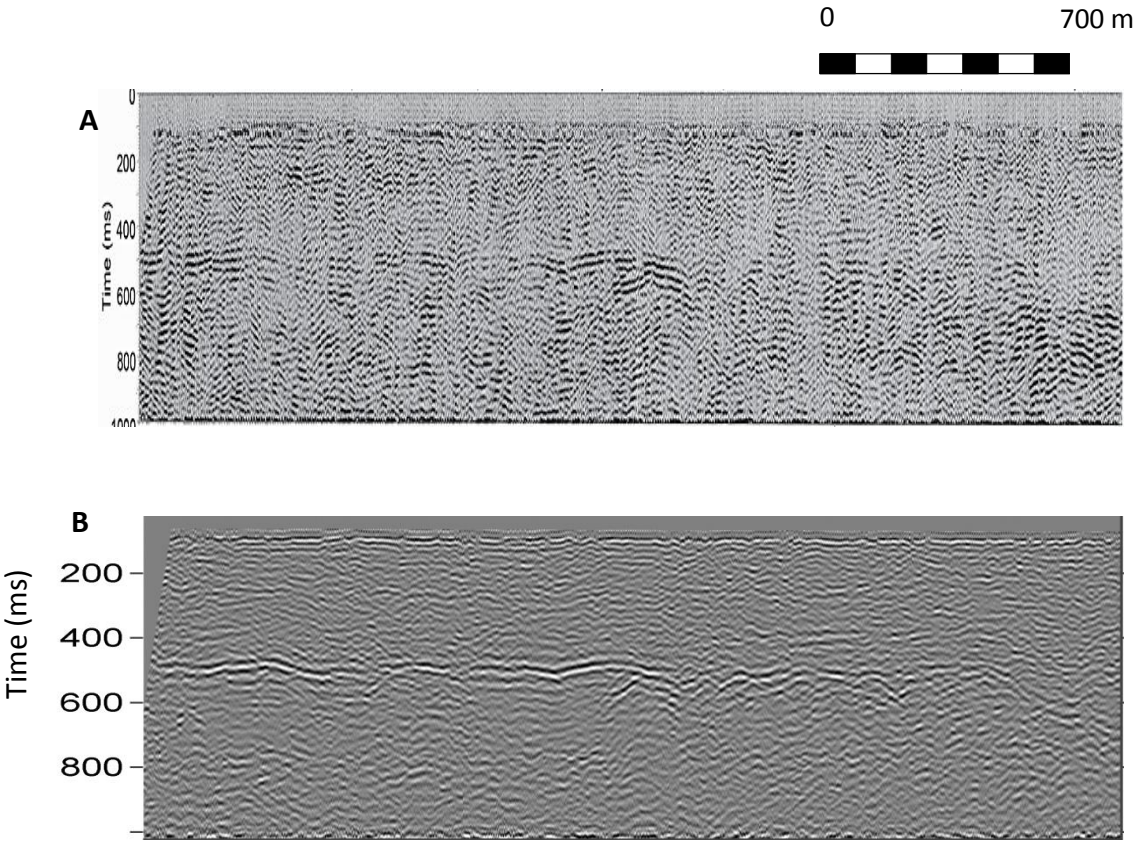

Figure 5.1: Different seismic data-processing procedures give different results for the same datasets, profile G1. (A) Processing result from Blits (2008). (B) Processing result from current study. A very strong bedrock reflector at 500 ms was almost faded out because of processing artifact, and this gives an indication of what happens to the inherent near-surface weak reflectors.

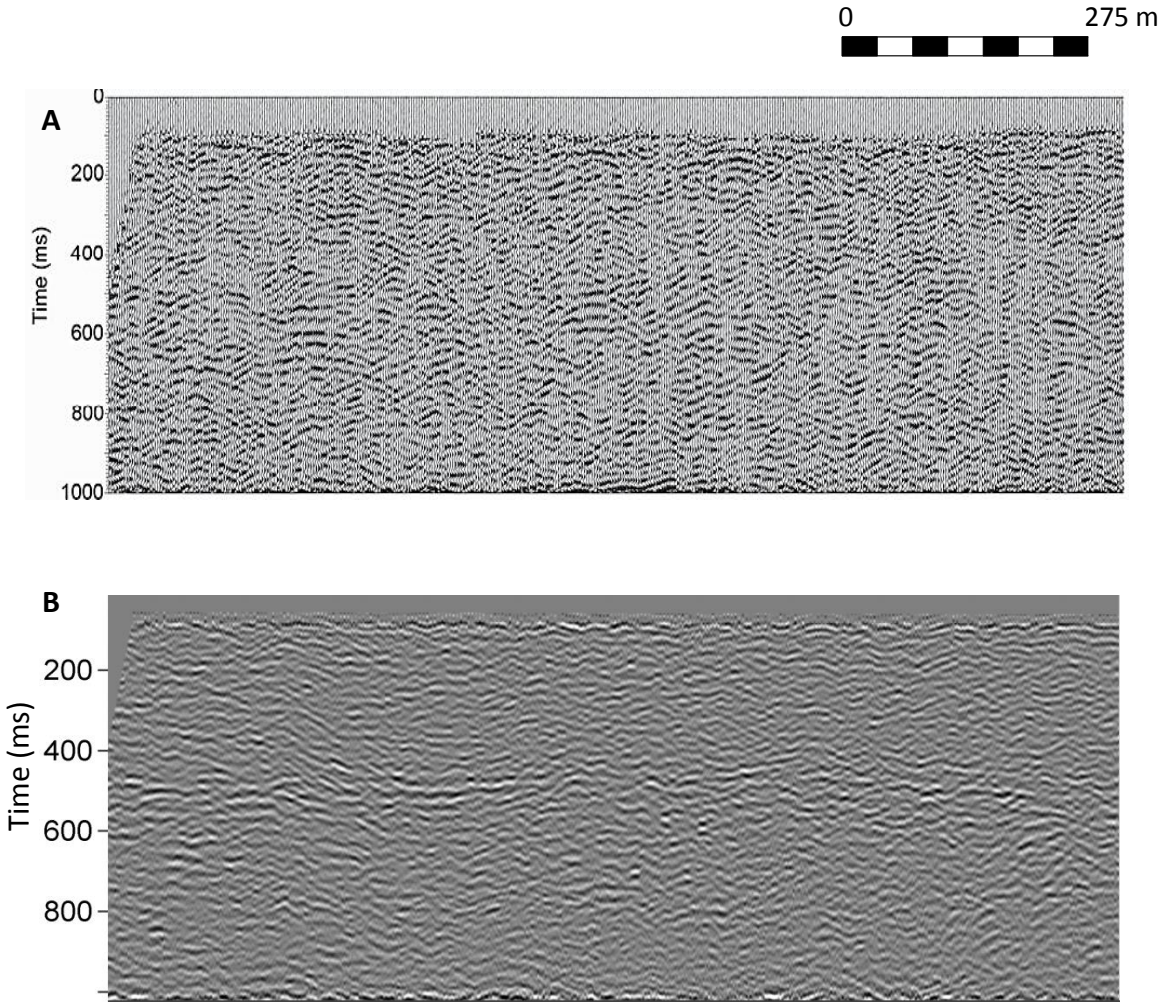

Figure 5.2: Different seismic data-processing procedures give different results for the same dataset, profile G2. (A) Processing result from Blits (2008). (B) Processing result from current study. Subtle bedrock reflector at 500 ms was lost because of processing artifact, and this gives an indication of what happens to the inherent near-surface weak reflectors.

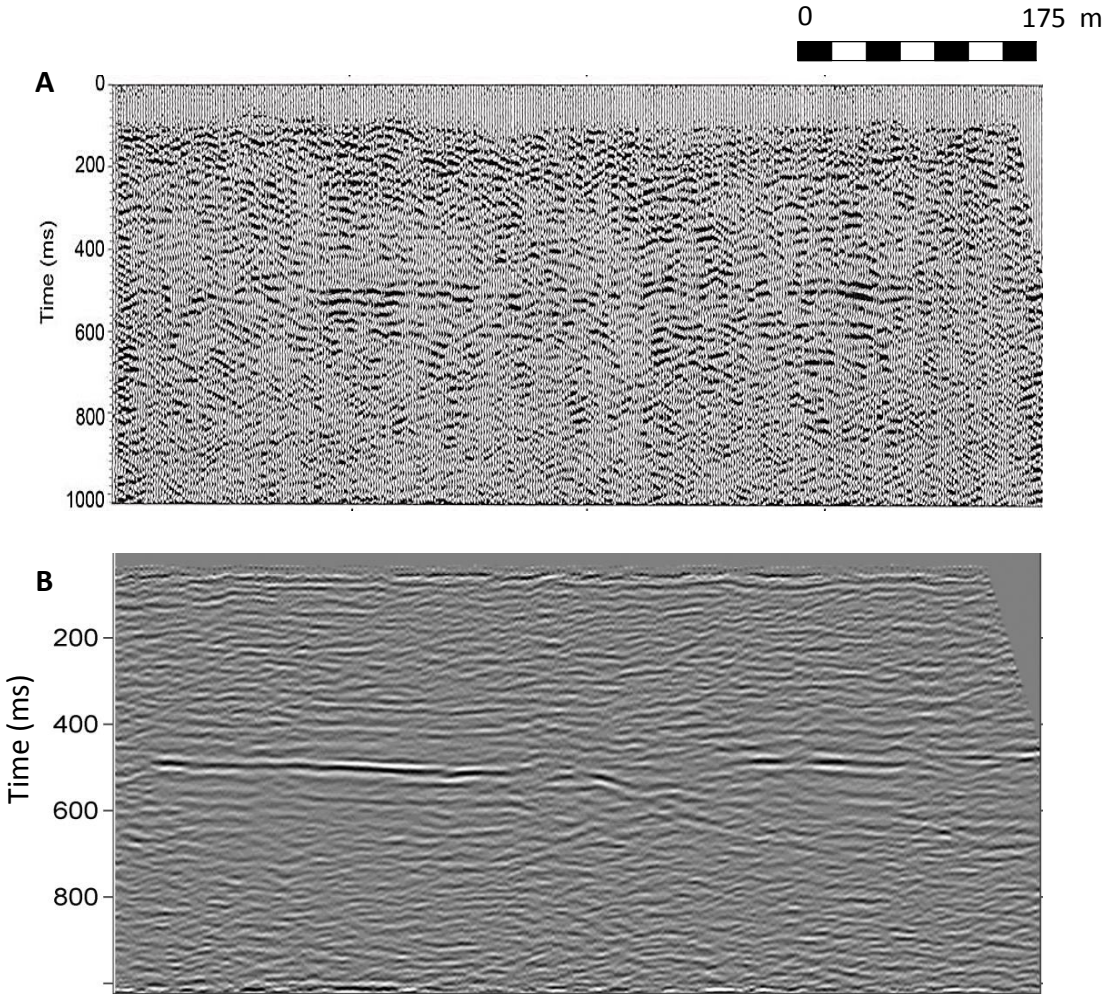

Figure 5.3: Different seismic data-processing procedures give different results for the same dataset, profile L. (A) Processing result from Blits (2008). (B) Processing result from current study. Very strong bedrock reflector at 500 ms was almost faded out because of processing artifact, and this gives an indication of what happens to the inherent near-surface weak reflectors.

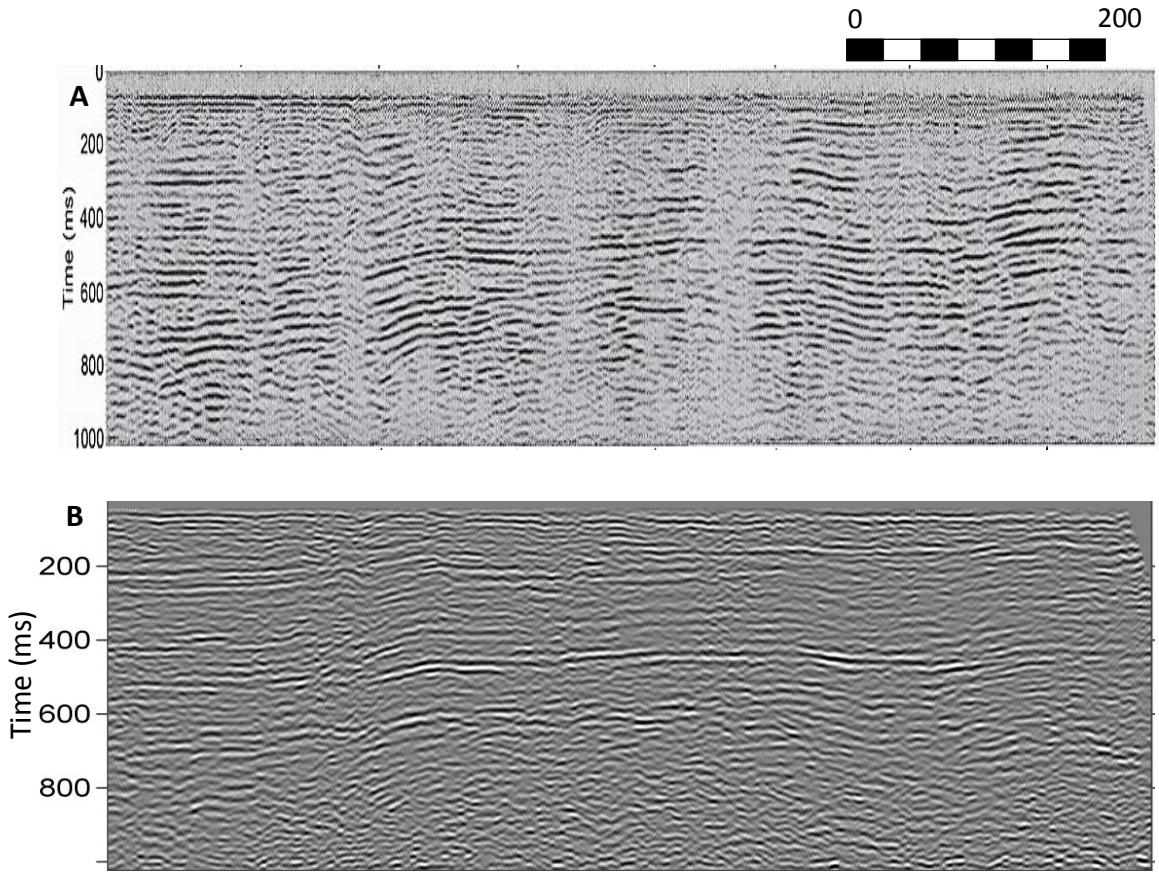

Figure 5.4: Different seismic data-processing procedures give different result for the same dataset, profile J1. (A) Processing result from Blits (2008). (B) Processing result from current study. Strong bedrock reflector at 500 ms was mixed with multiples and reverberations. Also, near-surface reflectors are discontinuous and incoherent.

5.2 Geologic Model

The seismic-reflection images identified clusters of normal faults that were correlated across the study area in a general northeast-southwest orientation. Specifically, three major fault or deformation zones were interpreted. Fault zone 1 (FZ-1) includes the observed fault clusters on profile A3, the eastern part of profile B, and profile C1 (Fig. 5.5). It has an approximate width of 600 m and remains relatively uniform between profile A1 and the eastern part of profile B. The strike is approximately N40°E, and it has an apparent dip to the southeast. The fault throw is manifested by the anomalous time depression along the bedrock time-structure surface (Fig. 4.24). Reduced temporal depressions are also exhibited on the McNairy Formation and Mounds Gravel time-structure maps with a similar orientation (Figs. 4.25–4.26). This is evidence for the reactivation of the older Paleozoic FAFC structures affecting Quaternary horizons. Woolery et al. (2009) used optically stimulated luminescence techniques to suggest that the latest deformation was approximately 25,000–18,000 YBP. A noticeable bend in the fault zone orientation occurs along strike to the southwest, and alters the strike to approximately N60°E, as seen on profiles B and C1. Fault zone 2 (FZ-2) includes the observed fault clusters interpreted on profile A2 and the central part of profile B (Fig. 5.6). It has an approximate width of 450 m and remains relatively uniform between the two profiles. The strike is approximately N40°E, and it has an apparent dip to the northwest. The fault throw is exhibited in the anomalous time depression in the bedrock time-structure map. Reduced temporal depressions are also present on the McNairy Formation and Mounds Gravel time-structure maps, with a similar orientation. This is evidence for reactivation of the early Paleozoic FAFC structures affecting Quaternary sediment. Fault zone 3 (FZ-3) is composed of the fault clusters that were observed on profiles H, A3, I, and J1, and the western part of profile B (Fig. 5.7). It has a relatively narrow 300-m width across profile H and broadens to approximately 1,500 m across profiles J1 and K1. The strike is approximately N35°E, and it has an apparent dip to the southeast. The fault throw is exhibited as an anomalous time depression in the bedrock time-structure map, as well as at the overlying McNairy and Mounds Gravel time-structure horizons. This is evidence that reactivation of the early Paleozoic FAFC affected Quaternary sediment horizons. Not surprisingly, three fault-zone orientations are

generally consistent with the primarily northeast–southwest-striking structure reported from mapped surface faults in southern Illinois (e.g., Kolata and Nelson, 1991; Nelson, 1997) (Fig. 1.3), and are interpreted as the southwest extension of the FAFC (Figs. 5.8–5.10). The fault zone also resulted in significant relief across the time-structure maps. In other words, the primary structures form two major subparallel grabens that are composed of secondary substructure. The time-structure models are also supported by depth-contour and vector maps derived from the borehole database (Figs. 4.28–4.29). Depth vectors for the top of the McNairy Formation point to areas of deepening depth, and are generally coincident with the temporal depressions (i.e., white zones) in the time-structure map. In addition, the mapped locations of the northwest and northeast contaminant plumes are bounded by primary graben structures. This suggests that the structures and their internal deformation may act as a preferential fluid flow path; however, this requires a favorable change in the hydraulic conductivity, and is evaluated in the following sections.

The imaged structural framework appears to have formed in sequential tectonic episodes, as evidenced from the seismic-reflection profiles and using observational approaches followed by Woolery et al. (2003) and Stephenson et al. (1999). Significant thickening and steeply dipping intraformational reflectors associated with the Tertiary and Quaternary sediment on the downthrow of the fault indicate that the majority of the reactivated deformation was syndepositional with these units and post-Cretaceous (Figs. 5.11–5.13). In addition, the more subtle thickening and lack of steeply dipping or onlapped reflectors associated with the Cretaceous sediment suggest a more quiescent period in which deposition draped and filled the earlier Paleozoic structural blocks. On both profiles J1 and H, within the available average vertical (~2 m) and horizontal (~436 m) resolutions for Tertiary and Quaternary sediments, similar vertical deformation and reflector slopes on opposite sides of the fault zone exist at Tertiary and Quaternary impedance boundaries. These are geometrically consistent features and are further evidence that the majority of the deformation was not reactivated until at least the Tertiary and/or early Quaternary Period subsequent to its extensional genesis in the late Precambrian and Early Cambrian. The general reversal of the extensional stress to a compressive stress regime in the Tertiary suggests the possibility for structural inversion.

An evaluation of the highest-resolution images (i.e., lines H and J1) does suggest reflection characteristics in the Tertiary and Quaternary sediment sequences that are indicative of structural inversion (Tertiary?). Evidence includes the antiformal folds in the hanging-wall reflectors, as well as small-amplitude force folds that may also be present in the Quaternary intraalluvial horizons, although the data quality of these very near-surface horizons makes this interpretation less definitive. Although the impedance boundary separating the Metropolis and overlying loess deposits is not resolved uniformly across the site, it is imaged in profiles J1 and H. Moreover, this boundary appears to have a throw reversal across the major faults at trace numbers 200 and 130, respectively.

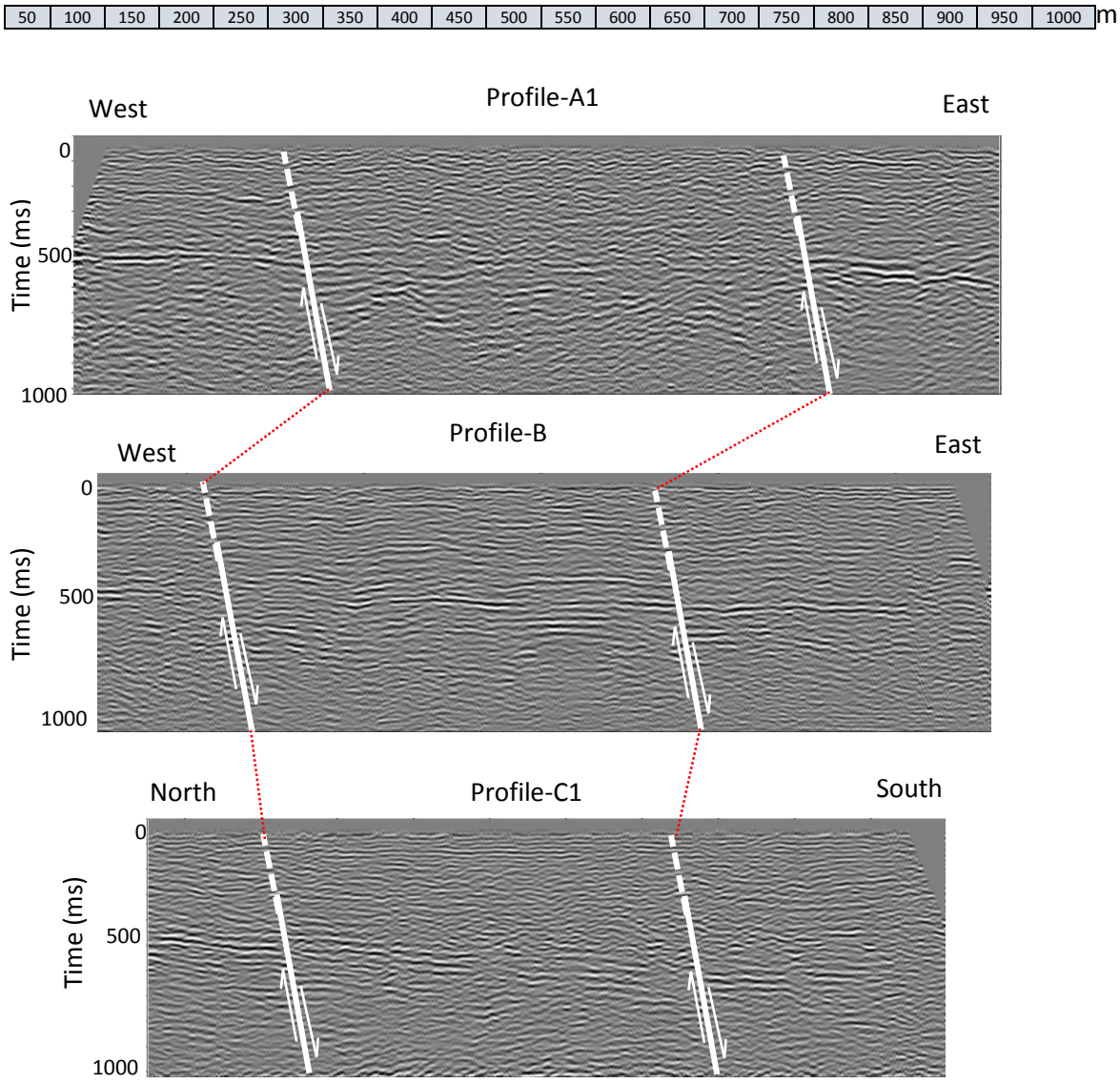

Figure 5.5: Spatial correlation of the fault cluster seen on profiles A1, B, and C1 to form Fault zone 1.

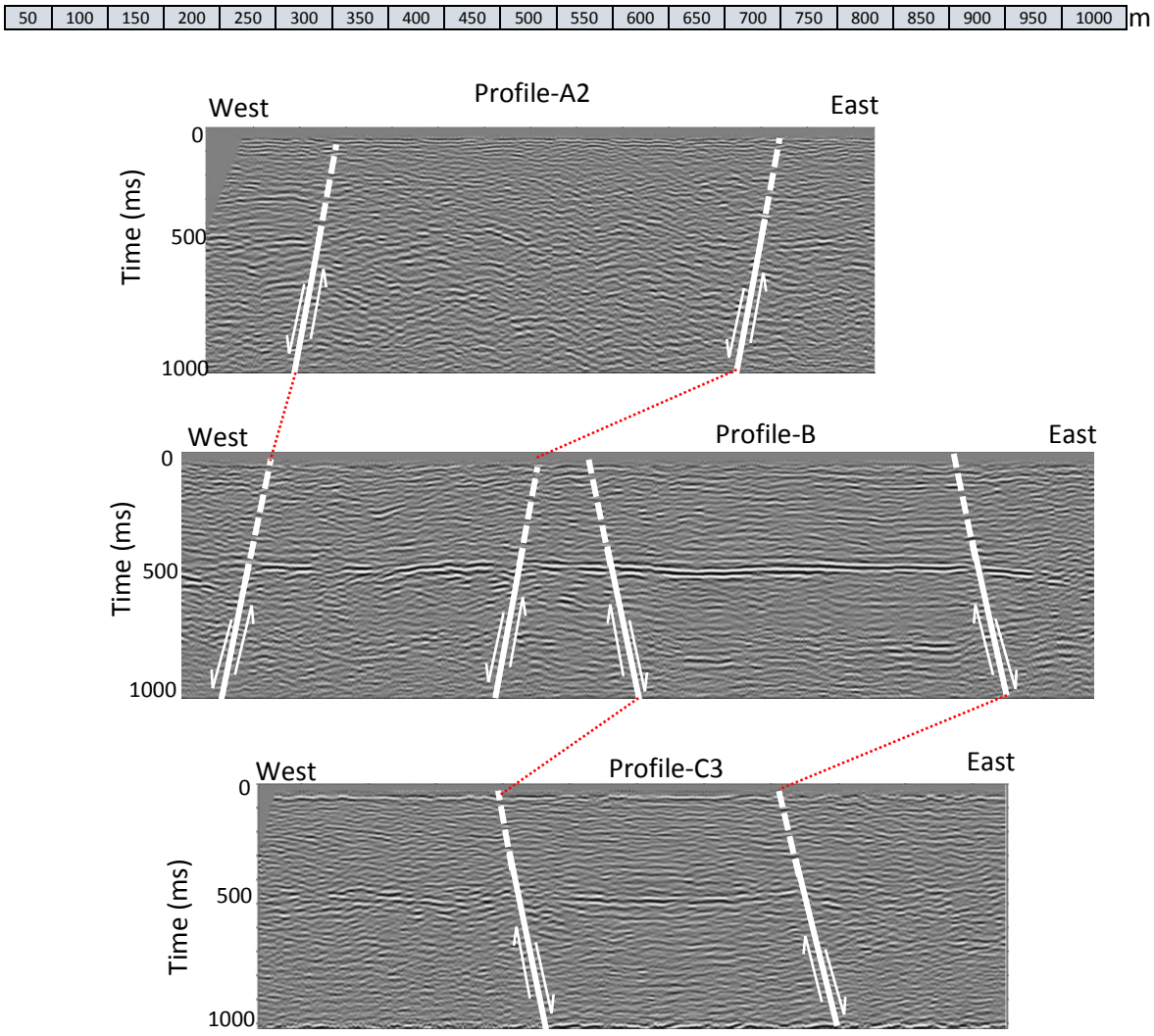

Figure 5.6: Spatial correlation of the fault cluster seen on profiles A2, B, and C3 to form Fault zone 2.

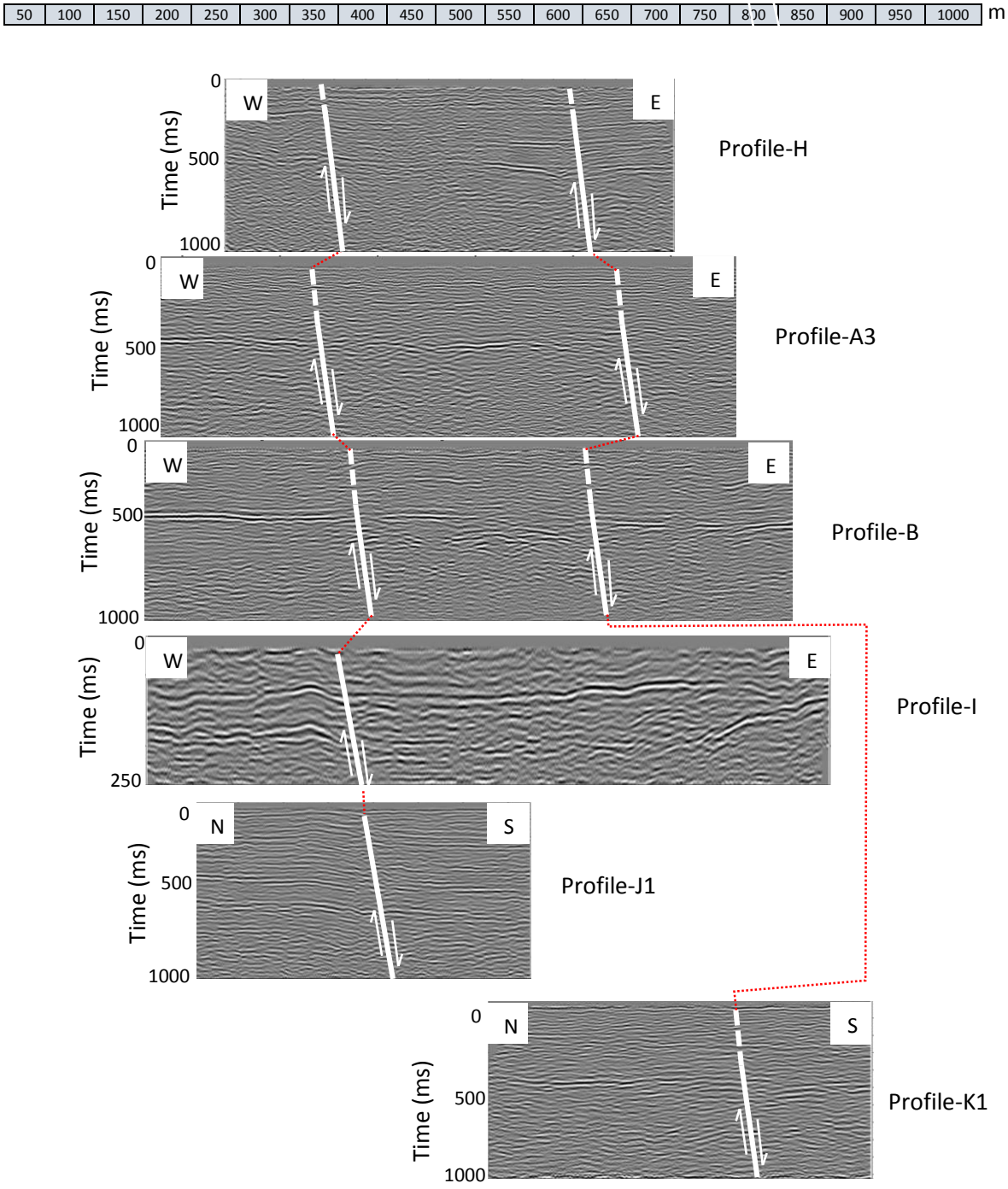

Figure 5.7: Spatial correlation of the fault cluster seen on profiles H, A3, B, I, J1, and K1 to form Fault zone 3.

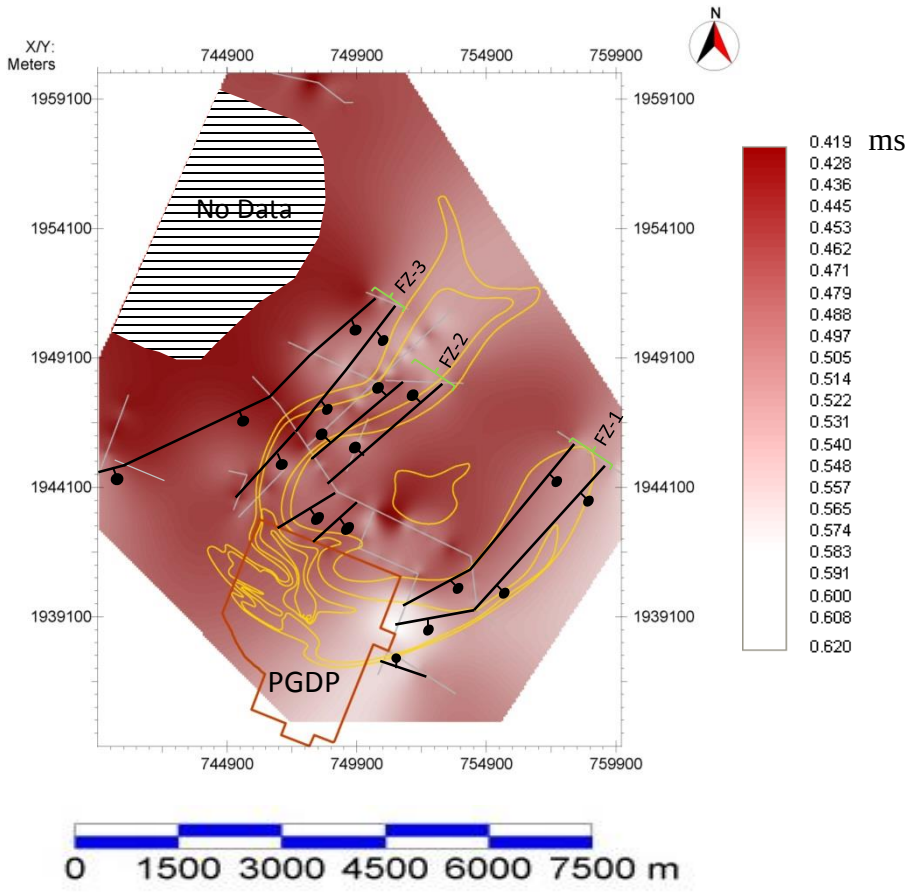

Figure 5.8: (A) Time-structure map of Paleozoic bedrock correlated spatially with the three speculated fault zones and the contamination plume.

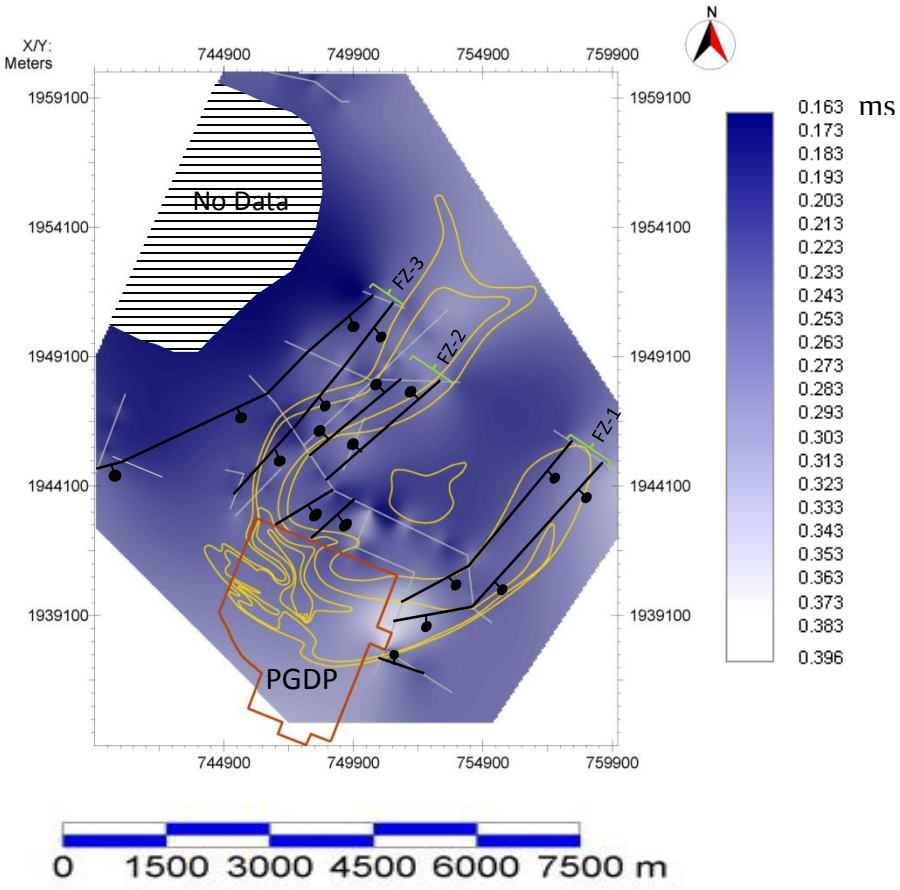

Figure 5.9: Time-structure map of Cretaceous McNairy top correlated spatially with the three speculated fault zones and the contamination plume.

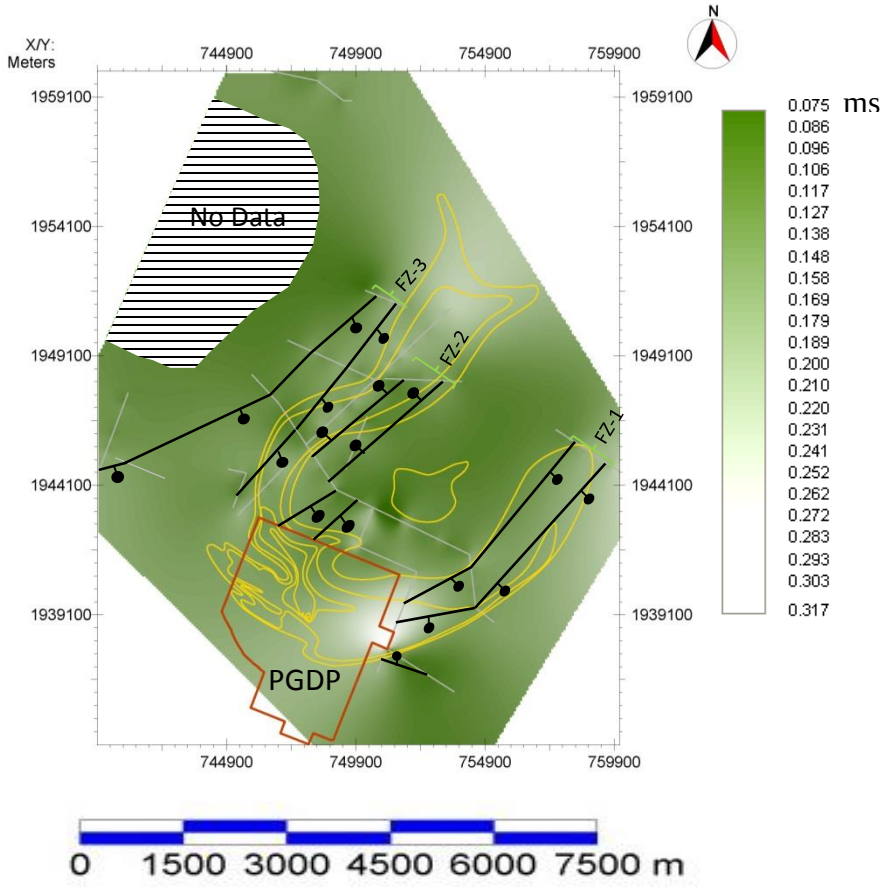

Figure 5.10: Time-structure map of Tertiary Mounds Gravel top correlated spatially with the three speculated fault zones and the contamination plume.

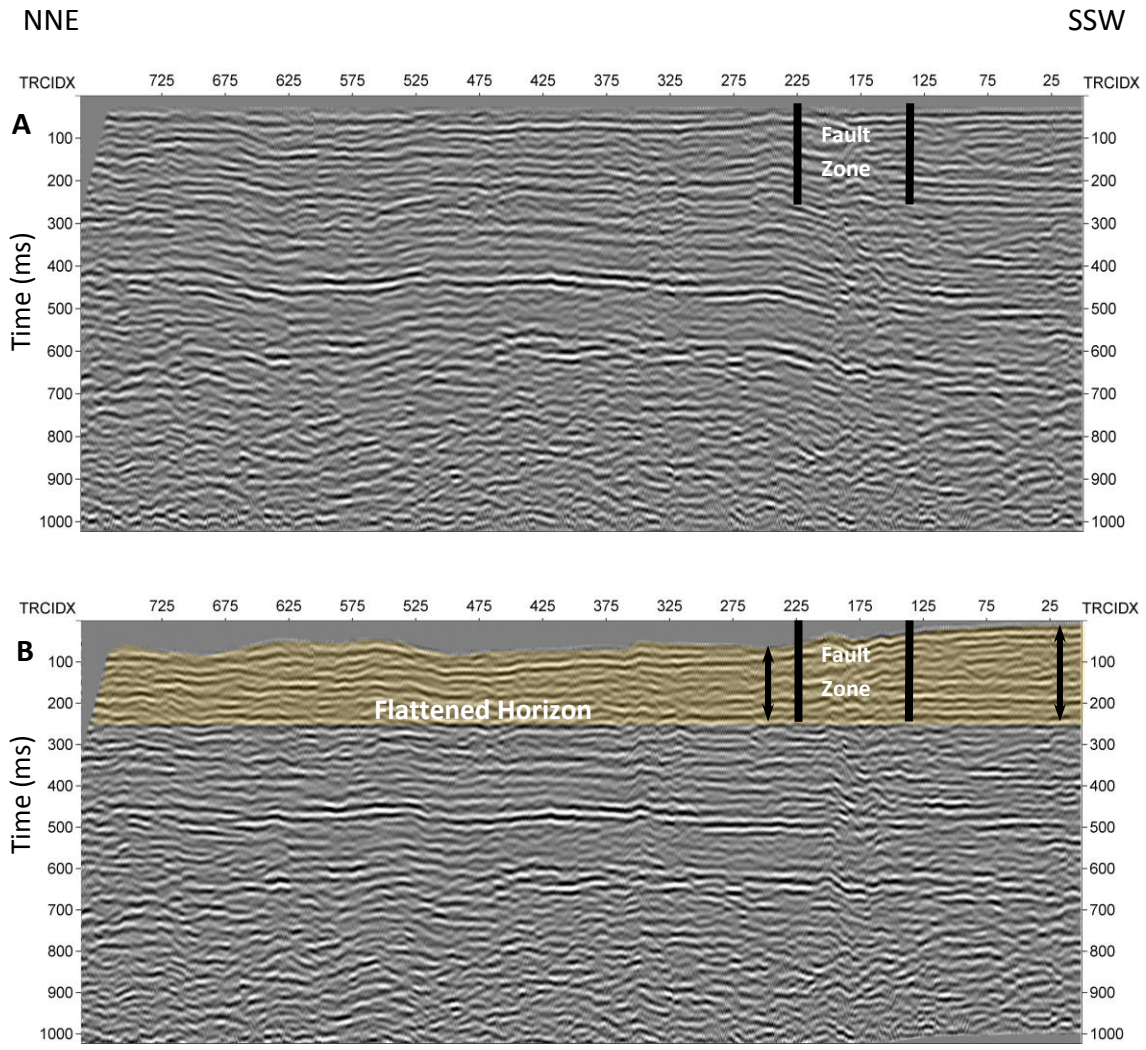

Figure 5.11: (A) Profile J1 non-flattened shows the identified fault zone. (B) Flattened, the fault zone bounded approximately between trace numbers 130 and 225. The slight southward thickening (yellowish shaded area) of the Cretaceous, Tertiary, and Quaternary sections are constant across the fault zone. If much of the apparent vertical deformation on these boundaries occurred prior to the deposition of the Cretaceous through Tertiary to Quaternary strata, then a linear projection of these contacts across the fault zone would not be possible. Therefore, most fault motion occurred afterward.

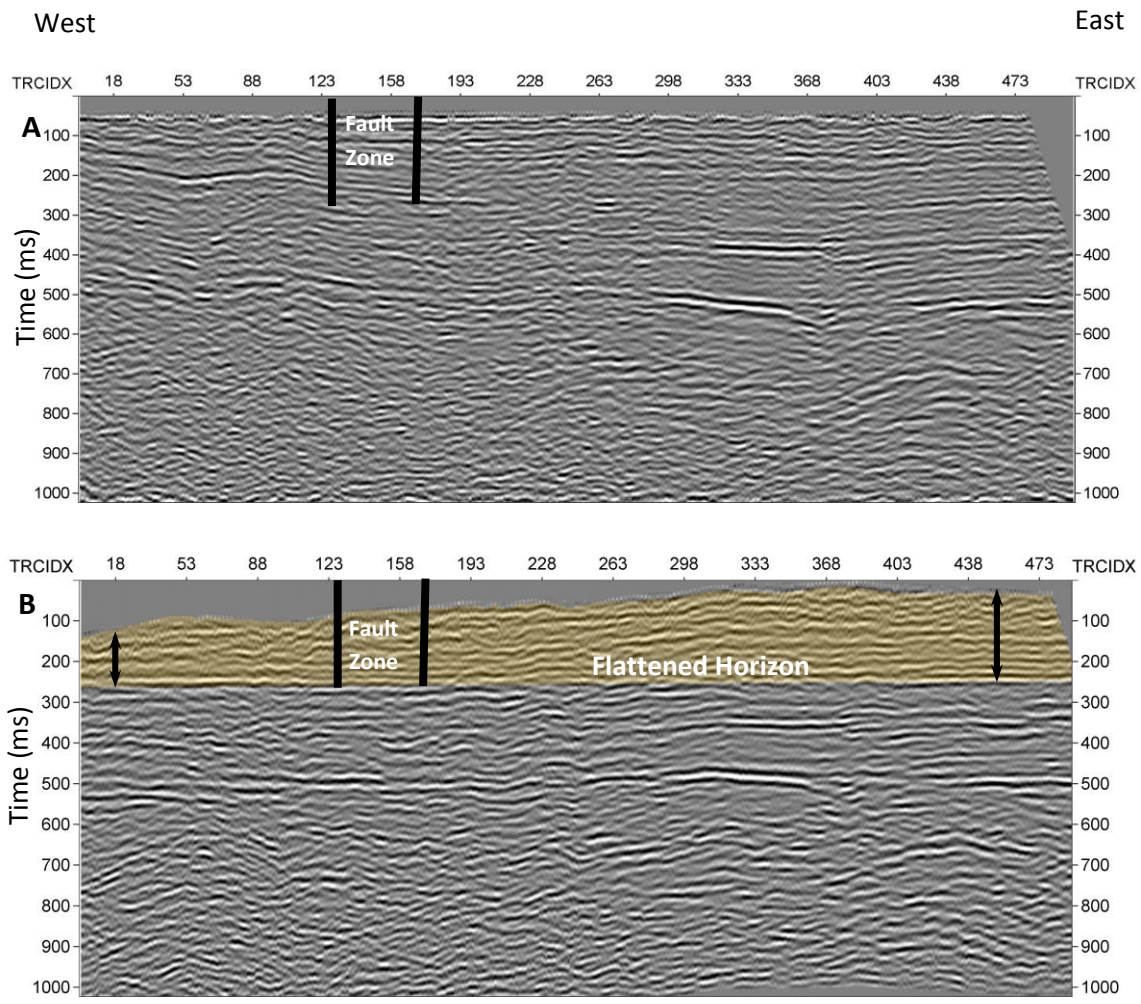

Figure 5.12: (A) Profile H non-flattened shows the identified fault zone. (B) Flattened, the fault zone bounded approximately between trace numbers 125 and 165. The eastward thickening (yellowish shaded area) of the Cretaceous, Tertiary, and Quaternary sections is constant across the fault zone. Slope and the displacement differences in the McNairy top and Mounds Gravel and Metropolis tops across the fault zone imply deformation prior to the development of the McNairy. Similar offsets between MG and Me showed reactivation of the preexisting fault movement. If much of the apparent vertical deformation on these boundaries occurred prior to the deposition of the Tertiary and Quaternary strata, then a linear projection of these contacts across the fault zone would not be possible. Therefore, fault motion occurred after deposition of the Cretaceous strata and reactivated after the deposition of Tertiary and Quaternary strata.

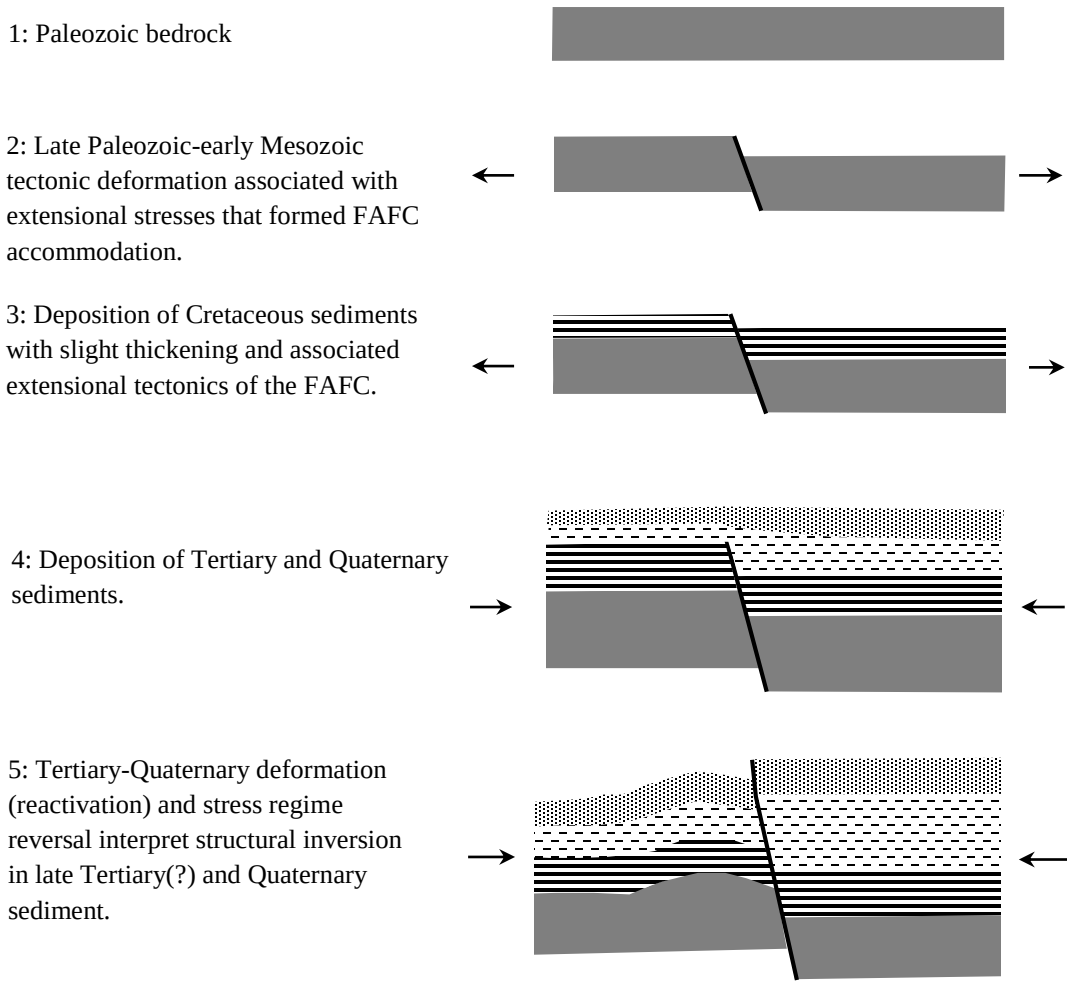

Figure 5.13: A suggested simplified schematic diagram articulates episodic tectonic events that observed on profiles-H and J1.

5.3 Shear-Wave Birefringence

Shear-wave splitting has been successfully used as an industry tool to identify the subsurface anisotropy associated with fractures, faults, and depositional fabrics in rocks. Harris (1996) was the first to use the technique for near-surface studies in unlithified sediments. His investigation successfully identified azimuthal anisotropy, which he attributed to differential stress conditions and/or microfractures associated with nearby faults. In this study, the technique was applied specifically to a geometrically well-constrained fault that high-resolution SH-wave images indicate disturbs the completely

resolvable sediment column. Specifically, FZ-3 was best resolved in SH-wave profile J1, and its local strike was well constrained by adjacent and orthogonal profiles J1/J2 and I. The J1 and I profiles clearly define a localized strike for FZ-3 of N60°E (Fig. 4.40), and the deformation associated with the fault extends above the Paleozoic bedrock to include the boundary separating the Metropolis Formation and overlying loess. Because shear-wave splitting measurements from the surface only provide a measure of the last encountered anisotropic filter prior to recording (i.e., surface birefringence methods do not discriminate between changing anisotropy vertically through the media of propagation), a fault extending across all or most of the sediment overburden was thought to minimize the effects of this technical limitation. Any azimuthal anisotropy caused by other inclusions, such as stratigraphic or sedimentlogical cross-cutting relationships, depositional fabric, and differential stress, would be insignificant relative to the deformation associated with the fault.

Each pair of orthogonal components was generated from the same energy source (i.e., TT and TR and RT and RR) and rotated separately in order to determine the natural coordinate system corresponding to fast and slow directions. The plot of the amplitude spectral ratios difference (Fig. 4.36) showed a relational maximum ratio from the orientation of the acquisition array along the county highway (Bethel Church Road). At 40º rotation, the TR component showed the maximum amplitude ratio (i.e., the maximum focused energy) because SH-wave polarization is aligned parallel to the natural coordinate system whereas the TT component showed the minimum focused energy because it is polarized perpendicular to the natural coordinate system. The resultant fast direction transformed into a geographic bearing is coincident with the well-constrained fault strike of N60ºE. Figures 4.37and 4.38 show a symmetrically mirrored, unstacked field file and stacked CMP processed after each side has been rotated into the natural coordinate system (i.e., fast and slow direction). The measured dynamic mis-tie exhibited in the natural coordinate system ranged between 15 and 9.5 ms for the bedrock, Cretaceous, and Tertiary horizons. Consequently, average azimuthal anisotropy ranged between 2.9 and 4.4 percent. Although the fault has not been active in the Holocene, the azimuthal anisotropy indicates that a permanent alteration in the lithologic

mechanical/elastic properties has occurred (i.e., the relative quiescence during the Holocene Epoch has not healed the fault zone).

5.4 Fault Properties in Unlithified Sediment

In order to further evaluate the physical change in the fault deformation zones properties, shear-wave velocity variations were mapped across the seismic profiles and electrical-resistivity surveys coincident with the seismic-reflection profiles and the interpreted faults were evaluated for variation in their electrical conductivity properties. The imaged faults along the seismic profiles exhibited significantly lower shear-wave velocities relative to either side of the deformed area. These velocity decreases are coincident with the significantly lower electrical-resistivity values that occur in the faulted zone (Figs. 4.41–4.43). These low values can be related to the change in the particle's physical configuration (e.g., from dense to loose packing of non-cohesive materials and from face-to-face to edge-to-face association of cohesive materials) associated with fault strike (Fig. 5.14). Together with the azimuthal anisotropy, the reduced shear-wave velocity (i.e., reduced rigidity modulus) and low electrical resistivity (i.e., increased hydraulic conductivity) indicate that the initial fault effects on the sediment's physical properties are not healed over a relatively significant geologic time period. In addition, this also suggests that subsurface fluid movement can be controlled to some degree by the increased hydraulic conductivity imparted to the lithology by the structural azimuthal anisotropy; therefore, the coincidence of the plume migration with the deformation zones of the Mounds Gravel (regional gravel aquifer) suggests a preferential pathway that accounts for the anomalous orientation of the local contaminant flow path with respect to an expected potentiometric surface in a homogeneous isotropic environment (Figs. 5.8–5.10) (Heath, 1983).

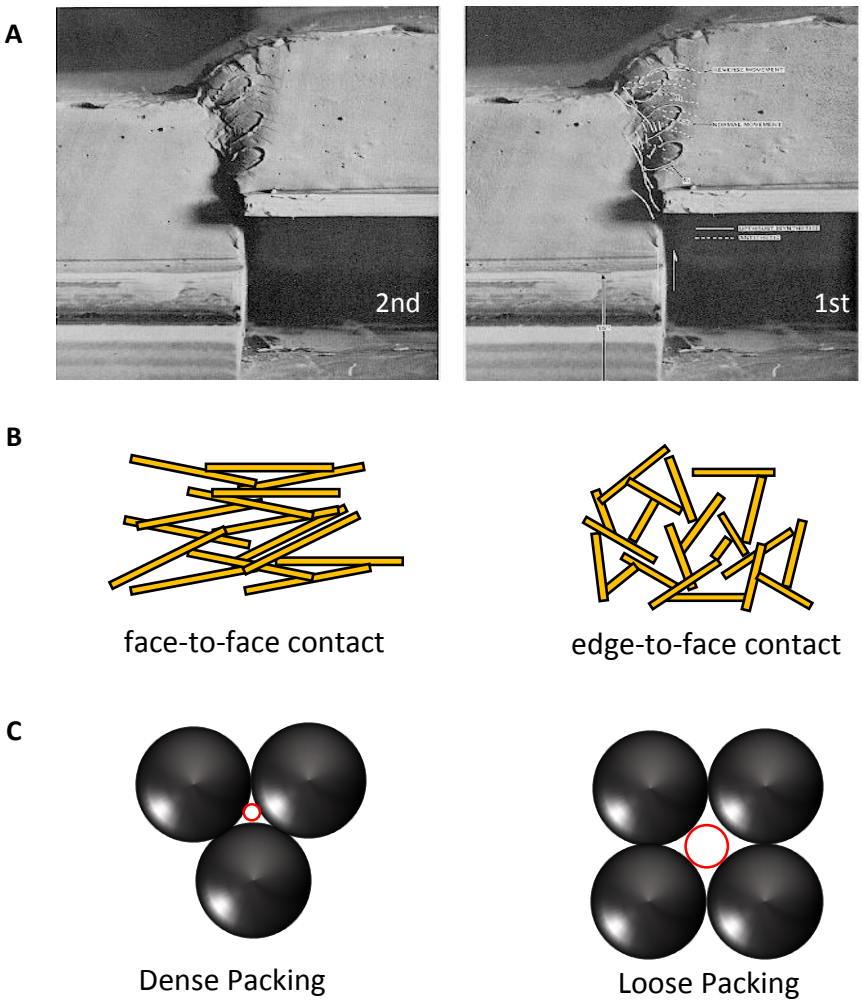

Figure 5.14: Fault effects on sediment particle's physical configuration. (A) Two stages of laboratory shear-stress test on soils (fault effects implication). (B) Cohesive material: Rearranging from face-to-face association to edge-to-face association that increase the total volume. (C) Non-cohesive materials: Rearranging physical particle configuration has led to a transformation from dense to loose packing that increases the pore space (red circle is for visual pore size estimation). Part C is modified from Santamarina et al. (2001).

CHAPTER SIX

6 CONCLUSIONS

The lack of subsurface geologic exposures in the unlithified, water-saturated Cretaceous, Tertiary, and Quaternary sediments that cover and conceal Paleozoic bedrock throughout the northern Mississippi Embayment, including McCracken County, Kentucky, near the Paducah Gaseous Diffusion Plant, make characterizing and defining the geologic conditions problematic. Remote geophysical imaging, seismic-reflection methods in particular, provides the most effective solution; however, the resolution provided by the conventional P-wave seismic-reflection method has proven less effective because of a limited spatial and temporal optimum window and the masking effect of the groundwater in the low-velocity near-surface sediment. Although more labor intensive to acquire, the SH-wave seismic-reflection method is a more efficient substitute, because it provides a relatively broader spatial and temporal optimum recording window and an inherently greater resolving power, approximately two to three times greater in the subject research area. Consequently, approximately 21 km of SH-wave seismic-reflection and 1.5 km of P-wave profiles have been acquired and compiled to image and construct a near-surface geologic model that resolves the primary stratigraphic horizons, as well as the subtle structural framework as shallow as ~7 m.

The resultant model indicates that there are three general northeast–southwest-oriented fault zones that are consistent with the geometry of the mapped surface faults outside of the embayment cover in southern Illinois. These fault zones are southwestern extensions of the FAFC and form two significant subparallel grabens with ancillary substructure in the study area. The FAFC structure is interpreted to have undergone episodic tectonic deformation since its late Precambrian and Early Cambrian formation. Significant thickening and steeply dipping reflectors are imaged on the downthrown blocks, particularly within Tertiary and Quaternary sediment, suggesting most of the reactivation occurred post-Cretaceous. Subtle thickening and lack of steeply dipping intraformational reflectors in the Cretaceous suggest a more quiescent period, with sediment deposition

unconformably draping and filling the earlier Paleozoic structural blocks. Kolata et al. (1981) also noted overthickened Cretaceous sediment in southernmost Illinois, but were reluctant to attribute this to fault activity. The high-quality and high-resolution profiles H and J1 provide the primary evidence for the interpretations for this study. In addition, the reactivation in the Tertiary and early Quaternary also indicate a reversal in the stress regime (i.e., from extensional to compressional). The primary evidence for this interpretation is the antiformal folds seen in the hanging-wall reflectors and the potential small-amplitude force folds in the Quaternary alluvium. In addition, a displacement inversion is evident along the Metropolis-loess seismic horizon on both lines J1 and H. These observed variations in structural style were confined to a relatively small area of the northern Mississippi Embayment and may indicate another event in an ongoing cycle of shifting tectonic activity in the northern part of the embayment during the last few tens of millions of years, also suggesting that the observed anomalous fault behavior may represent localized inconsistent trends such that stresses vary spatially and/or temporally rather than a single stress field representative of a specific tectonic event.

Shear-wave splitting in near-surface unlithified sediment is measurable for significant azimuthal anisotropic inclusions such as fault deformation zones. A shear-wave birefringence experiment showed azimuthal anisotropy coincident with a well-constrained N60ºE fault strike identified by adjacent orthogonal seismic profiles. This provides another efficient and effective tool for characterizing shallow subsurface geologic features in low-impedance water-saturated sediment environments. This also provides evidence that faults inactive during significant geologic intervals (i.e., the Holocene) do not "heal".

The integrated shear-wave velocity models and electrical resistivity tomography provide additional evidence regarding the physical character of deformed sediment. Relatively low electrical-resistivity values and low shear-wave velocities within the deformation zones compared with values outside the boundaries suggest that the sediment particle configuration changes from a denser to a more loosely packed sediment arrangement that provides an increase in the overall porosity and permeability (i.e., hydraulic conductivity). An increase in hydraulic conductivity along the azimuthally anisotropic

deformation zones can provide a preferential path for fluid migration, and can wholly or in large part explain the anomalous contaminant plume migration path and its coincidence with the deformation boundaries of the Mounds Gravel, the regional groundwater aquifer.

REFERENCES

Advanced Geosciences Inc., 2006, Instruction manual for EarthImager 2D 2.3.0: Resistivity and IP Inversion Software, Austin, Texas, Advances Geosciences Inc., 134 p.

Advanced Geosciences Inc., 2007a, Seminar of resistivity imaging: AGI resistivity imaging seminar, September 11–12, Austin, Texas.

Advanced Geosciences Inc., 2007b, Seminar of resistivity imaging: AGI resistivity imaging seminar, September 13–14, Austin, Texas.

Baker, G.S., 1999, Processing near-surface seismic-reflection data: A primer, Society of exploration geophysics, Course notes series, Roger A. Young series.

Bay Geophysycal, Inc, 2010, personal communication.

Bechtel Jacobs Co. LLC, 2003, Technical memorandum for the C-746-U landfill fault study at the Paducah Gaseous Diffusion Plant, Paducah, Kentucky: A report prepared for U.S. Department of Energy Office of Environmental Management.

Bexfield, C.E., McBride, J.H., Pugin, A.J., Ravat, D., Biswas, S., Nelson, W.J., Larson, T.H., Sargent, S.L., Fillerup, M.A., Tingey, B.E., Wald, L., Northcott, M.L., South, J.V., Okure, M.S., and Chandler, M.R., 2006, Integration of P- and SH-wave high-resolution seismic reflection and micro-gravity techniques to improve interpretation of shallow subsurface structure: New Madrid Seismic Zone: Tectonophysics, 420, 5−21.

Blits, C.A., 2008, Integrated geophysical imaging of subsurface geologic conditions across a contaminant plume, McCracken County, Kentucky: A master's thesis submitted to the Graduate School at the University of Kentucky, 299 p.

Braile, L.W., Hinze, W., Keller, G.R., Lidiak, E.G., and Sexton, J.L., 1986, Tectonic development of the New Madrid rift complex, Mississippi Embayment, North America: Tectonophysics, 131, 1−21.

Braile, L.W., Keller, G.R., Hinze, W.J., and Lidiak, E.G., 1982, An ancient rift complex and its relation to contemporary seismicity in the New Madrid Seismic Zone: Tectonics, 1, 225–237.

Burger, H.R., Sheehan, A.F., and Jones, C.H., 2006, Introduction to applied geophysics: Exploring the shallow subsurface: New York, W.W. Norton, 600 p.

Burke, K., and Dewey, J.F., 1973, Plume-generated triple junctions: Key indicators in applying plate tectonics to old rocks: Journal of Geology, 81, 406−433.

Chambers, J.E., Kuras, O., Meldrum, P.I., Ogilvy, R.D., and Hollands, J., 2006, Case history: Electrical resistivity tomography applied to geologic, hydrogeologic and engineering investigations at a former waste-disposal site: Geophysics, 71(6), B231–B239.

Clausen, J.L., Douthitt, J.W., Davis, K.R., and Phillips, N.E., 1992, Groundwater investigation phase III for Paducah Gaseous Diffusion Plant, Paducah, Kentucky: A final report prepared for the U.S. Department of Energy under contract no. DEAC0f76OR00001, Martin Marietta Energy System, Inc.

Clement, W.P., Carbonell, R., and Smithson, S.B., 1994, Shear-wave splitting in the lower crust beneath the Archean crust of south Greenland: Tectonophysics, 232, 195–210.

Crampin, S., Chensonkov, M., Hipkin, R., 1994, Seismic anisotropy: the state of the art II: Geophysics, 76, 1-16.

Crampin, S., 1985, Evaluation of anisotropy by shear-wave splitting: Geophysics, 50(1), 142–152.

Crampin, S., and Lovell, J.H., 1991, A decade of shear-wave splitting in the Earth's crust: What does it mean? What use can we make of it? And what should we do next?: Geophysical Journal International, 107, 387–407.

Dahlin, T., and Zhou, B., 2004, A numerical comparison of 2D resistivity imaging with 10 electrode arrays: Geophysical Prospecting, 52, 379–398.

Deidda, G.P., and Balia, R., 2001, An ultrashallow SH-wave seismic reflection experiment on a subsurface ground model: Geophysics, 66(4), 1097–1104.

Dobrin, M.B., 1976, Introduction to geophysical prospecting [3rd ed.]: New York, McGraw-Hill, Inc., 630 p.

Dohr, G., and Janle, H., 1980, Improvements in the observation of shear-wave: Geophysical Prospecting, 28, 208–220.

Dolinar, B., and Tranuner, L., 2007, The impact of structure on the undrained shear strength of cohesive soils: Engineering Geology, 92, 88–96.

Drahovzal, J.A., and Hendricks, R.T., 1996, Geological features relevant to ground-water flow in the vicinity of the Paducah Gaseous Diffusion Plant: Final report submitted to Federal Facilities Oversight Unit; Environmental Remediation for the Paducah Gaseous Diffusion Plant.

Francese, R., Giudici, M., Schmitt, D.R., and Zaja, A., 2005, Mapping the geometry of an aquifer system with a high-resolution reflection seismic profile: Geophysical Prospecting, 53, 817–828.

Francese, R.G., Hajnal, Z., and Prugger, A., 2002, High-resolution images of shallow aquifers—A challenge in near-surface seismology: Geophysics 67(1), 177–187.

GEDCO (Geophysical Exploration and Development Corporation), 2012, VISTA® 2D/3D seismic data processing manual.

Guy, E.D., Nolen-Hoeksema, C., Daniels, J.J., and Lefchik, T., 2003, High-resolution SH-wave seismic reflection investigations near a coal mine-related roadway collapse feature: Journal of Applied Geophysics, 54, 51–70.

Harris, J.B., 1996, Shear-wave splitting in Quaternary sediments: Neotectonic implications in the central New Madrid Seismic Zone: Geophysics, 61(6), 1871–1882.

Harris, J.B., 2005, Observation of shear-wave splitting in Quaternary sediments of the New Madrid Seismic Zone: An indicator of in-situ stress conditions: 11th European Meeting of Environmental and Engineering Geophysics, Best of SAGEEP.

Harris, L.D., 1975, Oil and gas data from the Lower Ordovician and Cambrian rocks of the Appalachian Basin: U.S. Geological Survey Miscellaneous Investigations Series Map I-917 D1, 2, 3.

Harrison, R.W., and Litwin, R.J., 1997, Campanian coastal plain sediments in southeastern Missouri and southern Illinois—Significance to the early geologic history of the northern Mississippi Embayment: Cretaceous Research, 18, 687–696.

Heath, R.C., 1983, Basic ground-water hydrology: U.S. Geological Survey Water-Supply Paper 2220.

Helbig, K., 1986, Shear-waves: What they are and how they can be used: Applied seismic anisotropy, theory, background, and field studies: Society of Exploration Geophysicists, Geophysics Reprint Series, 20, 19–38.

Hickman, J.B., Jr., 2011, Structural evolution of an intracratonic rift system; Mississippi Valley Graben, Rough Creek Graben, and Rome Trough of Kentucky, USA: A doctoral dissertation submitted to the Graduate School at the University of Kentucky, 185 p.

Hildenbrand, T.G., and Keller, G.R., 1983, Magnetic and gravity features of western Kentucky—Their geologic significance: U.S. Geological Survey, Open-File Report, 83, 164 p.

Hunter, J.A., Pullan, S.E., Burns, R.A., Gagne, R.M., and Good, R.L., 1984, Shallow seismic reflection mapping of the overburden-bedrock interface with the engineering seismograph─Some simple techniques: Geophysics, 49, 1381–1385.

Jacobs EM Team, 1997, Ground-water conceptual model for the Paducah Gaseous Diffusion Plant, Paducah, Kentucky; prepared for the U.S. Department of Energy under contract no. DE-AC05- 93OR22028, Paducah, Ky.

Jacobs EM Team, 1998, Record of decision for waste area groups 1 and 7 at the Paducah Gaseous Diffusion Plant, Paducah, Kentucky: A report prepared for U.S. Department of Energy Remediation Management Group: EPA/ROD/R04-98/112.

Kane, M.F., Hildenbrand, T.G., and Hendricks, J.D., 1981, Model for the tectonic evolution of the Mississippi Embayment and its contemporary seismicity: Geology, 9, 563–568.

Kolata, D.R., and Hildenbrand, T.G., 1997, Structural underpinnings and Neotectonics of the southern Illinois Basin: Seismological Research Letters, 68, 499–510.

Kolata, D. R., Terworgy, J. D., and Masters, J. M., 1981, Structural framework of the Mississippi embayment of southern Illinois: Illinois State Geological Survey, Circular 516, 38 p.

Kolata, D.R., and Nelson, W.J., 1990, Interior cratonic basins: American Association of Petroleum Geologists Memoir 51, chapter 18, p. 267.

Kolata, D.R., and Nelson, W.J., 1991, Tectonic history of the Illinois Basin, *in* Interior cratonic basins, special issue: American Association of Petroleum Geologists Memoir, 51, 2663–2285.

Kolata, D.R., and Nelson, W.J., 1997, Role of the Reelfoot Rift/Rough Creek Graben in the evolution of the Illinois Basin, *in* Ojakangas, R.W., Dickas, A.B., and Green, J.C., eds., Middle Proterozoic to Cambrian rifting, central North America: Geological Society of America Special Paper 312.

Langston, C., McIntyre, J., Street, R., and Harris, J., 1998, Investigation of the shallow subsurface near the Paducah Gaseous Diffusion Plant using SH-wave seismic methods: Expanded abstracts, 62nd International Meeting of the Society of Exploration Geophysicists, 13–18, New Orleans, La., 62, 878–880.

Lee, M.W., and Balch, A.H., 1983, Computer processing of vertical seismic profile data: Geophysics, 48(3), 272–287.

Long, M.D., and Silver, P.G., 2009, Shear wave splitting and mantle anisotropy: Measurements, interpretations, and new direction: Survey in Geophysics, 30, 407–461.

Lowrie, W., 2007, Fundamentals of geophysics [2nd ed.]: New York, Cambridge University Press, 381 p.

Martin, M.A., and Davis, T.L., 1987, Shear-wave birefringence: A new tool for evaluating fractured reservoirs: The Leading Edge, 6(10), 22–28.

Mayne W.H., 1962, Common reflection point horizontal data stacking techniques: Geophysics, XXVII(6), 927–938.

Mayne, W.H., 1967, Practical considerations in the use of common reflection point techniques: Geophysics, XXXII(2), 225–229.

McBride, J.H., Nelson, W.J., and Stephenson W.J., 2002, Integrated geological and geophysical study of Neogene and Quaternary-age deformation in the northern Mississippi Embayment: Seismological Research Letters, 73, 597–627.

McBride, J.H., and Nelson, W.J., 2001, Seismic reflection images of shallow faulting, northernmost Mississippi Embayment, north of the New Madrid Seismic Zone: Bulletin of the Seismological Society of America, 91(1), 128−139.

Mooney, W.D., Andrews, M.C., Ginsburg, A., Peters, D.A., and Hamilton, R.M., 1983, Crustal structure of northern Mississippi Embayment and a comparison with other continental rift zones: Tectonophysics, 94, 327–348.

Nelson, K.D., and Zhang, J., 1991, A COCORP deep reflection profile across the buried Reelfoot Rift, south-central United States: Tectonophysics, 197, 271−293.

Nelson, W.J., 1998, Bedrock geology of the Paducah 1° × 2° CUSMAP quadrangle, Illinois, Indiana, Kentucky, and Missouri: U.S. Geological Survey Bulletin 2150-B.

Nelson, W.J., Denny, B.F., Devera, J.A., Follmer, L.R., and Masters, J.M., 1997, Tertiary and Quaternary tectonic faulting in southernmost Illinois: Engineering Geology, 46, 235–258.

Nelson, W., and Lumm, D., 1987, Structural geology of southeastern Illinois and vicinity: Illinois State Geological Survey Circular, 538, 70 p.

Nelson, W.J., Denny, F.B., Follmer, L.R., and Masters, J.M., 1999, Quaternary grabens in southernmost Illinois: Deformation near an active intraplate seismic zone: Tectonophysics, 305, 381−397.

Odum, J.K., Stephenson, W.J., Shedlock, K.M., and Pratt, T.L., 1998, Near-surface structural model for deformation associated with the February 7, 1812, New Madrid, Missouri, earthquake: Geological Society of America Bulletin, 110(2), 149−162.

Olive, W.W., 1980, Geologic maps of the Jackson Purchase Region, Kentucky: U.S. Geological Survey Miscellaneous Investigations Series, I-1217.

Olive, W.W., and McDowell, R.C., 1986, The geology of Kentucky—A text to accompany the Geologic Map of Kentucky: Cretaceous and Tertiary Systems: U.S. Geological Survey Professional Paper 1151-H.

Oliver, J., Dobrin, M., Kaufman, S., Meyer, R., and Phinney, R., 1976, Continuous seismic reflection profiling of the deep basement, Hardeman County, Texas: Geological Society of America Bulletin, 87(11), 1537–1546.

Omens, G., 1978, Exploring with SH-waves: CSEG National Convention, Calgary, May 11.

Palmer, J.R., Hoffman, D., Stephenson, W.J., Odum, J.K., and Williams, R.A., 1997, Shallow seismic reflection profiles and geological structure in the Benton Hills, southeast Missouri: Engineering Geology, 46, 217−233.

Pugin, A.J., Larson, T.H., Sargent, S.L., McBride, J.H., and Bexfield, C.E., 2004, Near-surface mapping using SH-wave and P-wave seismic land-streamer data acquisition in Illinois, U.S.: The Leading Edge, 23, 677–682.

SAIC Engineering Inc., 2004, Seismic investigation report for siting of a potential on-site CERCLA waste disposal facility at the Paducah Gaseous Diffusion Plant, Paducah, Kentucky: A final report prepared for the U.S. Department of Energy Office of Environmental Management, DOE/OR/07-2038&D2.

Santamarina, J. C., Klein, K. A., and Fam, M. A., 2001, Soils and waves: Particlate materials behavior, characterization and process monitoring, John Wiley and Sons Ltd, Baffins Lane, Chishester, West Sussex PO19 1UD, England, 488 P.

Schoenberg, M., Sayers, M., 1995, Seismic anisotropy of fractured fock: Geophysics, 60(1) 204–211.

Sexton, J.L., 2006, Lithologic and stratigraphic compilation of near-surface sediments for the Paducah Gaseous Diffusion Plant, McCracken County, KY: A master's thesis submitted to the Graduate School at the University of Kentucky, 250 p.

Sexton, J., and Jones, P.B., 1986, Evidence for recurrent faulting in the New Madrid Seismic Zone from Mini-Sosie high-resolution reflection: Geophysics 51(9), 1760–1788.

Shaowu, G., Guoan, L., and Bo, Z., 2009, Elimination of the mono-frequency interference based on an adaptive subtraction: CPS/SEG International Geophysical Conference and Exposition, Beijing, China, 24–27 April: 103.

Silver, P.G., Savage, M.K., 1994, The interpretation of shear-wave splitting parameters in the presence of two anisotropic layers: Geophysical Journal International, 119, 949-963.

Soderberg, R.K., and Keller, G.R., 1981, Geophysical evidence for deep basin in western Kentucky: American Association of Petroleum Geologists, 65(2), 226–234.

Steeples, D.W., and Miller, R.D., 1990, Seismic-reflection methods applied to engineering, environmental, and ground-water problems, *in* Ward, S., ed: Society of Exploration Geophysicists, Investigations in Geophysics, Review and Tutorial, 1(5), 1–30.

Stephenson, W.J., Odum, J.K., Williams, R.A., McBride, J.H., and Tomlinson, I., 2012, Characterization of intrabasin faulting and deformation for earthquake hazards in southern Utah Valley, Utah, from high-resolution seismic imaging: Bulletin of the Seismological Society of America, 102(2), 524–540.

Stephenson, W.J., Odum, J.K., Williams, R.A., Pratt, T.L., Harrison, R.W., and Hoffman, D., 1999, Deformation and Quaternary faulting in southeast Missouri across the Commerce Geophysical Lineament: Bulletin of the Seismological Society of America, 89(1), 140–155.

Street, R., Wang, Z., Woolery, E., Hunt, J., and Harris, J., 1997, Site effects at a vertical accelerometer array near Paducah, Kentucky: Engineering Geology, 46, 349–367.

Tatham, R.H., McCormack, M.D., 1991, Multicomponent seismology in petroleum exploration: Society of Exploration Geophysics, 248 p.

Thomas, W.A., 2011, The Appalachian-Ouachita rifted margin of southeastern North America: Geological Society of America Bulletin, 103, 415–431.

Thomsen, L., 1988, Reflection seismology over azimuthally anisotropic media: Geophysics, 53(3) 304-313.

Tripathi, G.N., 2009, Use of surface geophysical techniques to locate a karst conduit in the Cane Run–Royal Spring Basin, Kentucky: A master's thesis submitted to the Graduate School at the University of Kentucky, 115 p.

U.S. Environmental Protection Agency, 2000, Tricholoroethylene hazard summary: EPA79-01-06, Office of Research and Development, Washington, D.C.

U.S. Environmental Protection Agency, 2007, Technetium-99. : http://www.epa.gov/radiation/radionuclides/technetium.html.

Verdon, J.P., and Kendall, J.M., 2011, Detection of multiple fracture sets using observation of shear-wave splitting in microseismic data: European Association of Geoscientists and Engineers, Geophysical Prospecting, 1–16.

Wheeler, R.L., 1997, Boundary separation of the seismically active Reelfoot Rift from the sparsely seismic Rough Creek Graben, Kentucky and Illinois: Seismological Research Letters, 68(4), 586–598.

Winterstein, D.F., and Meadows, M.A., 1991, Changes in shear-wave polarization azimuth with depth in Cymric and Railroad Gap oil fields: Geophysics, 56, 13449–1364.

Woolery, E.W., 2002, SH-wave seismic reflection images of anomalous foundation conditions at the Mississippi Dam, Indiana: Journal of Environmental & Engineering Geophysics, 7(4), 161−168.

Woolery, E., Baldwin, J., Kelson, K., Hampson, S., Givler, R., and Sundermann, S., 2009, Site-specific fault hazard assessment—Fluorspar Area Fault Complex, western Kentucky: Seismological Research Letters, 80(6), 1035–1044.

Woolery, E.W, Schaefer, J.A., and Wang, Z., 2003, Elevated lateral stress in unlithified sediment, Midcontinent, United States—Geotechnical and geophysical indicators for a tectonic origin: Tectonophysics, 368, 139–153.

Woolery, E.W., and Street, R., 2002, Quaternary fault reactivation in the Fluorspar Area Fault Complex of western Kentucky: Evidence from shallow SH-wave reflection profiles: Seismological Research Letters, 73(5), 628–639.

Woolery, E., and Street, R., 2003, An integrated geophysical assessment of Late Quaternary Neotectonics along the Northern Mississippi Embayment extension of the Fluorspar Area Fault Complex: U.S. Geological Survey National Earthquake Hazards Reduction Program Final Technical Report 01HQGR0044, 36 p.

Woolery, E.W., Street, R.L., Wang, Z., and Harris, J.B., 1993, Near-surface deformation in the New Madrid Seismic Zone as imaged by high resolution SH-wave seismic methods: Geophysical Research Letters, 20(15), 1615−1618.

Woolery, E.W., and Wang, Z., 2005, Seismic velocity measurements at expanded network sites: A final report prepared for United States Department of Energy Portsmouth/Paducah Project Office, UK/KRCEE Doc. P8.3.

Yilmaz, Ö., 2008, Seismic data analysis: Inversion and interpretation of seismic data: Society of Exploration Geophysicists (1), 2027 p.

APPENDECES

Appendix A

Band pass filter test to SH-wave reflection field shot-gathers

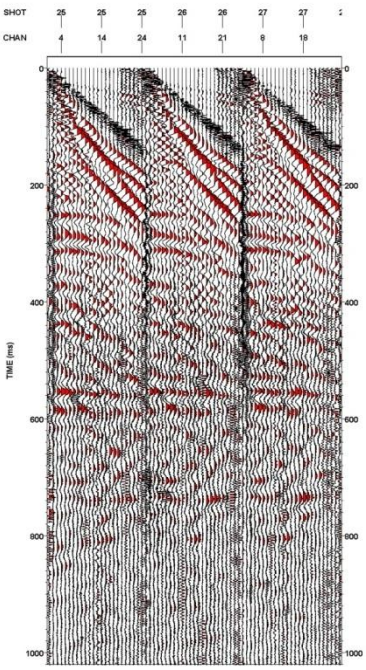

Raw data

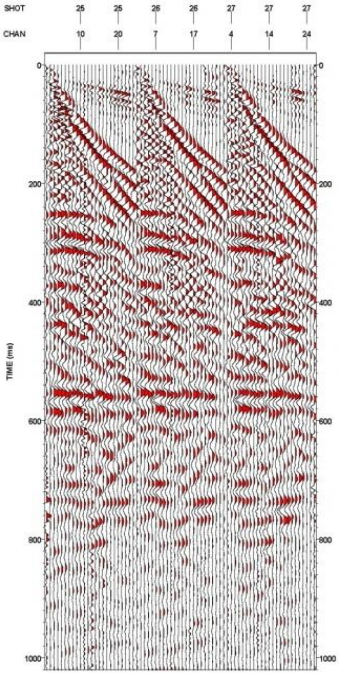

BP filter
(15 25 125 145) Hz

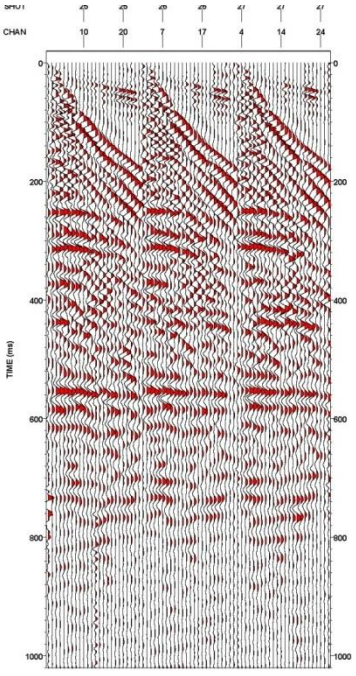

BP filter
(20 30 100 120) Hz

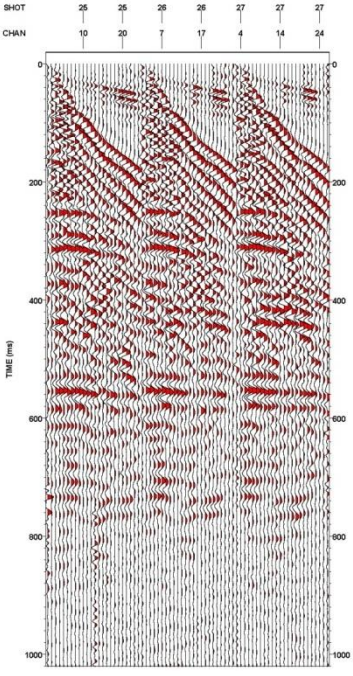

BP filter
(20 40 100 120) Hz

Appendix A: Continued

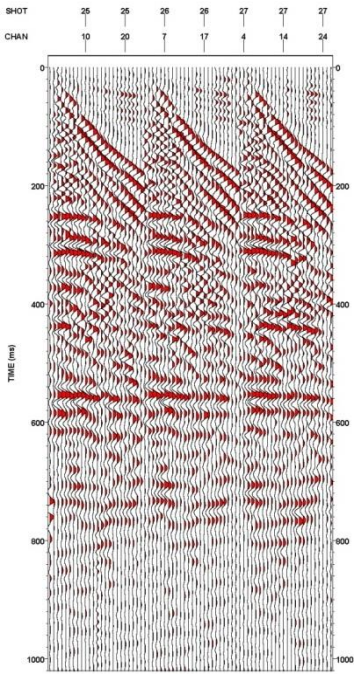

BP filter
(20 30 75 85) Hz

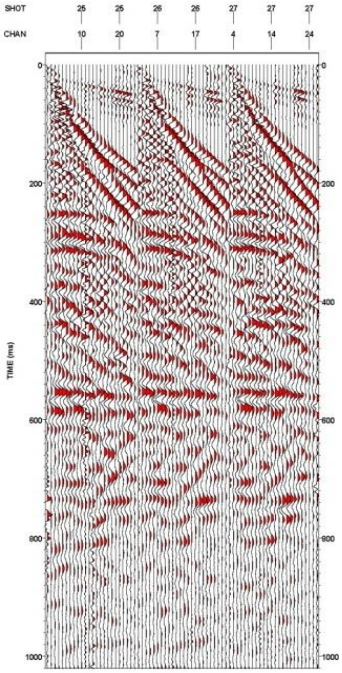

BP filter
(10 20 130 150) Hz

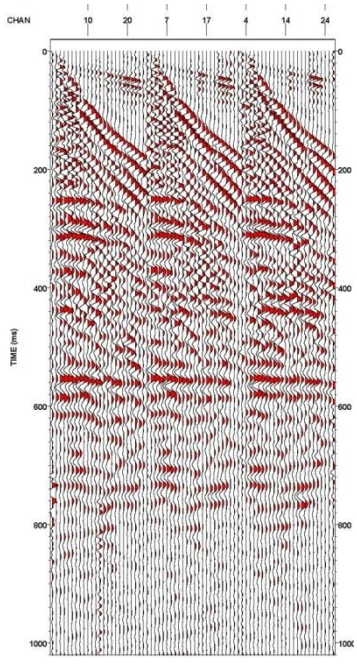

BP filter
(15 35 100 120) Hz

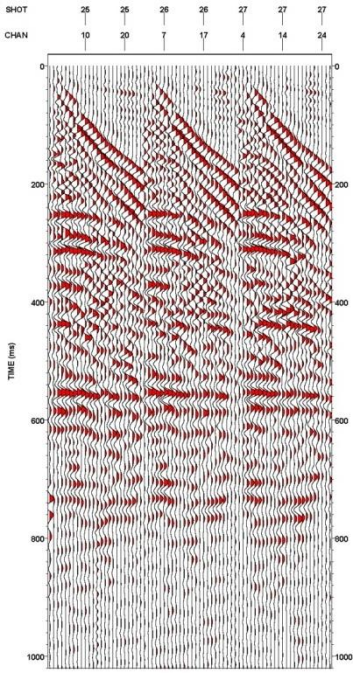

BP filter
(20 30 70 80) Hz

Appendix B:

Band pass filter test to P-wave reflection field shot-gathers

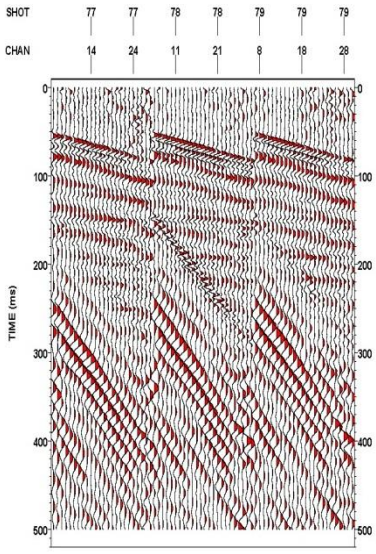

BP filter
(10 30 180 200) Hz

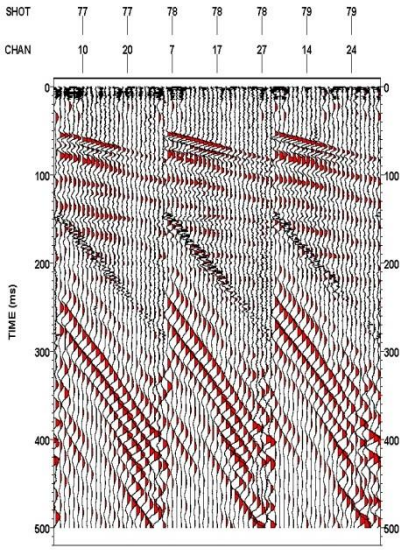

Raw data

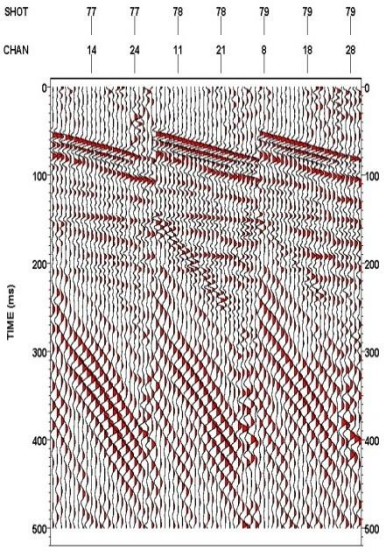

BP filter
(30 50 140 160) Hz

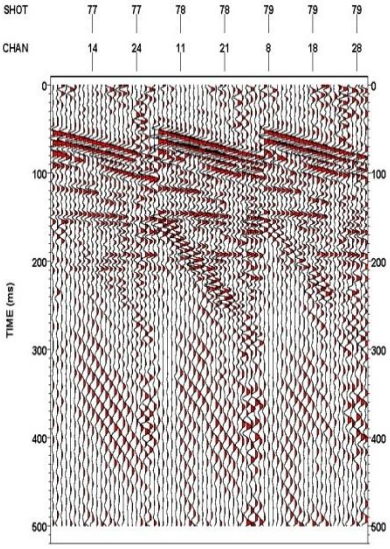

BP filter
(40 60 140 160) Hz

Appendix B: Continued

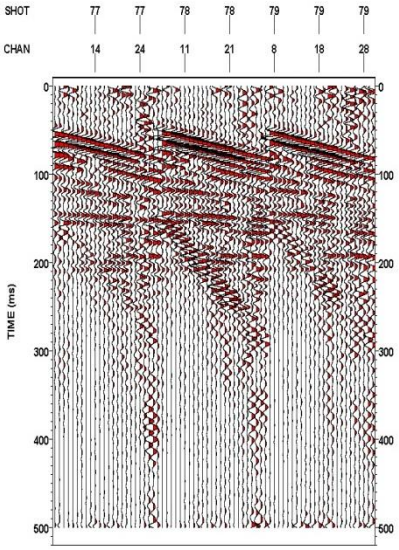

BP filter
(10 30 180 200) Hz

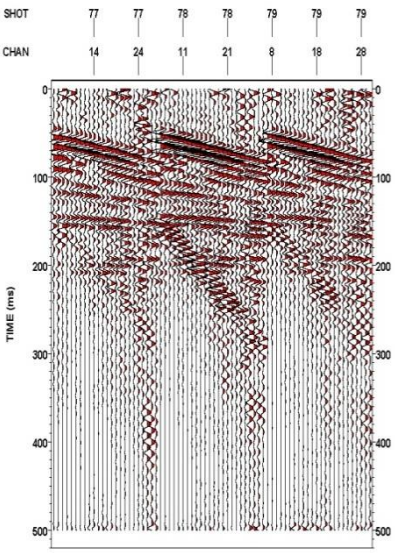

BP filter
(60 80 140 160) Hz

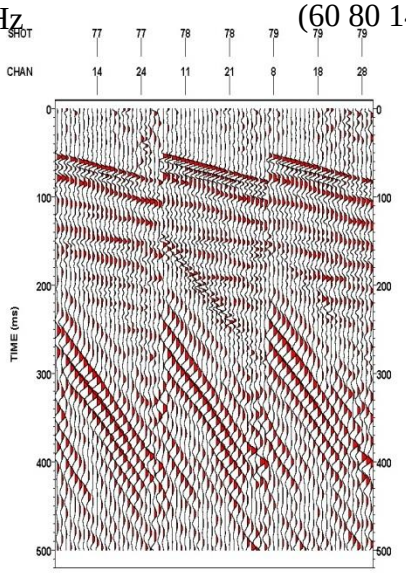

BP filter
(20 40 160 180) Hz

Appendix C:

P-wave seismic-reflection profiles. The data were processed, but not been interpreted because of location inconsistency.

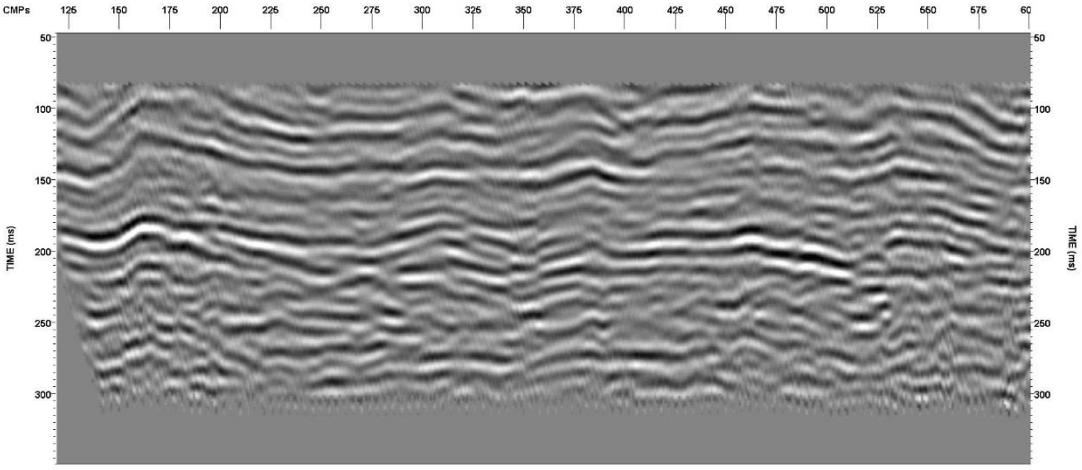

Profile P1

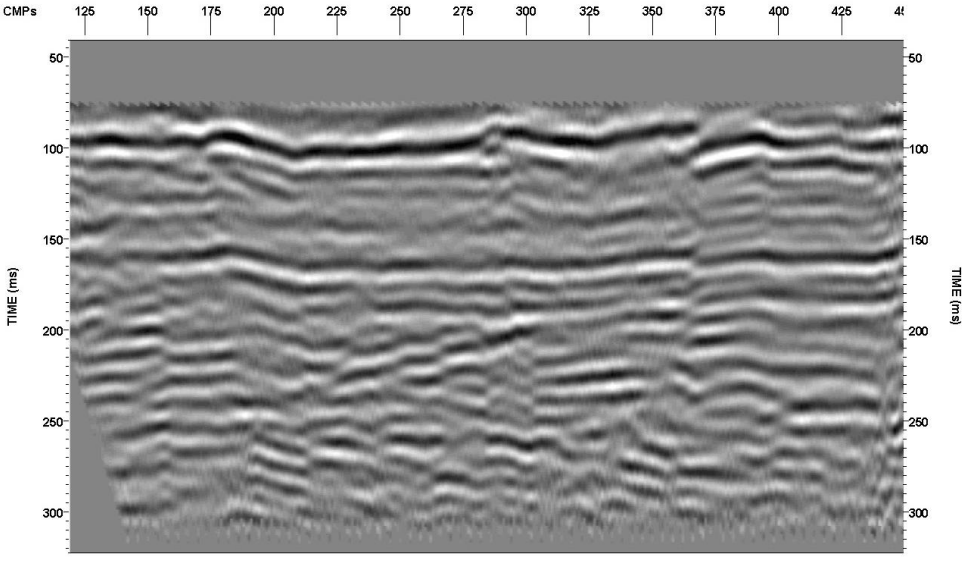

Profile P2

Appendix C: Continued

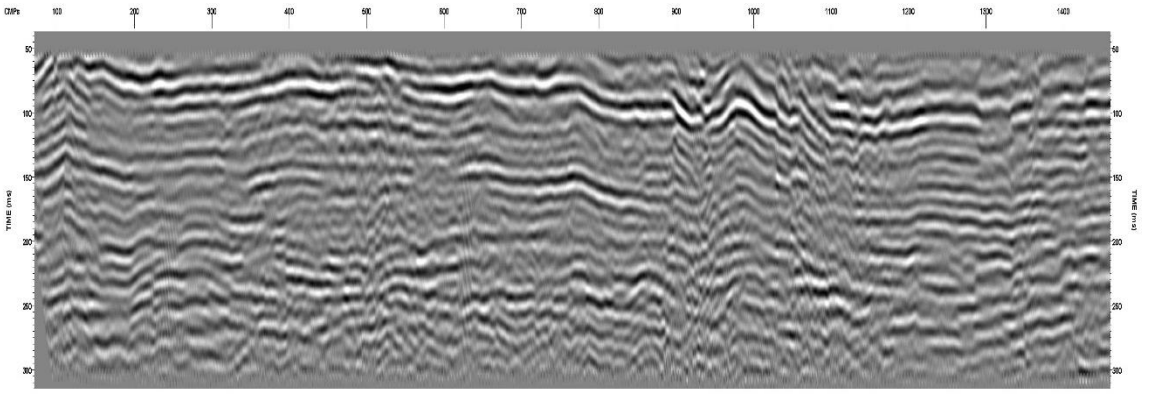

Profile P4

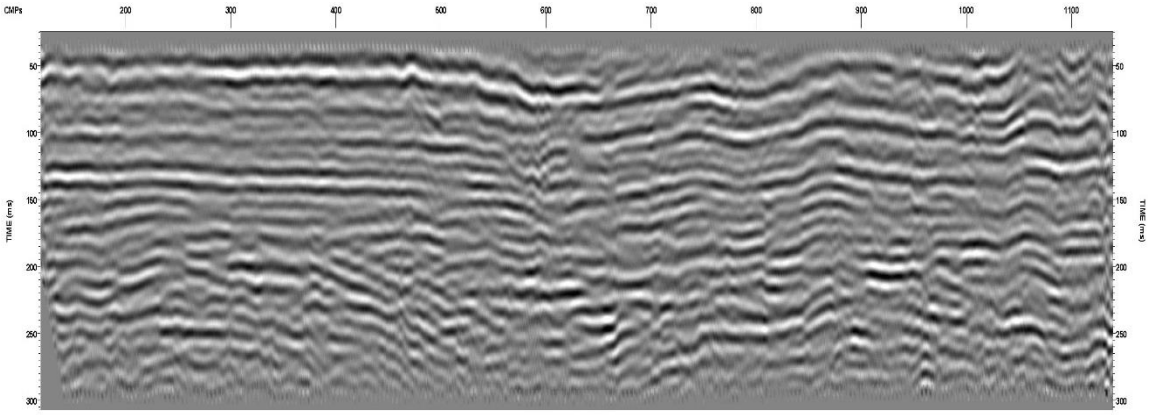

Profile P5

Appendix C: Continued

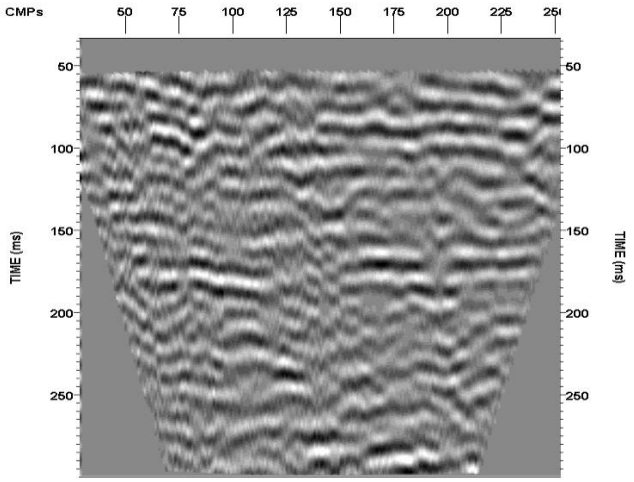

Profile P6

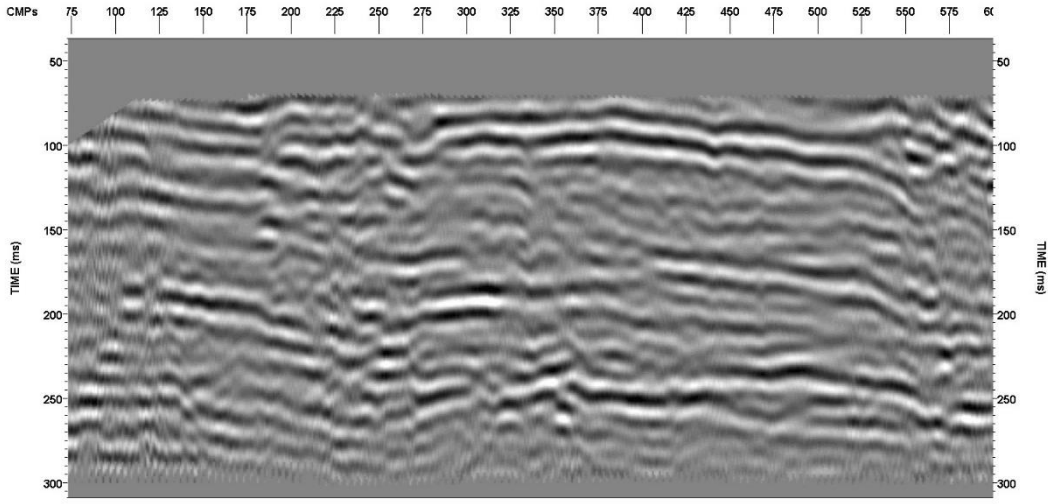

Profile P7

Appendix D:

SH-wave seismic-reflection profiles. The data were processed, but not been interpreted because of poor data quality.

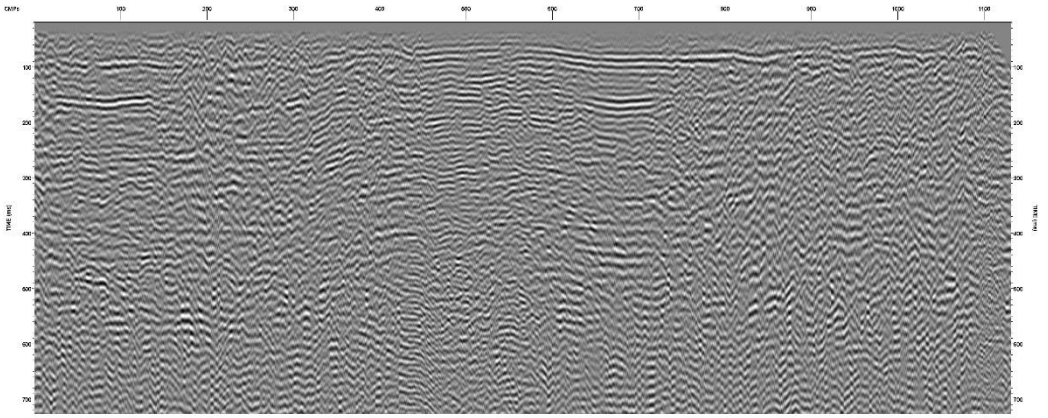

Profile S8

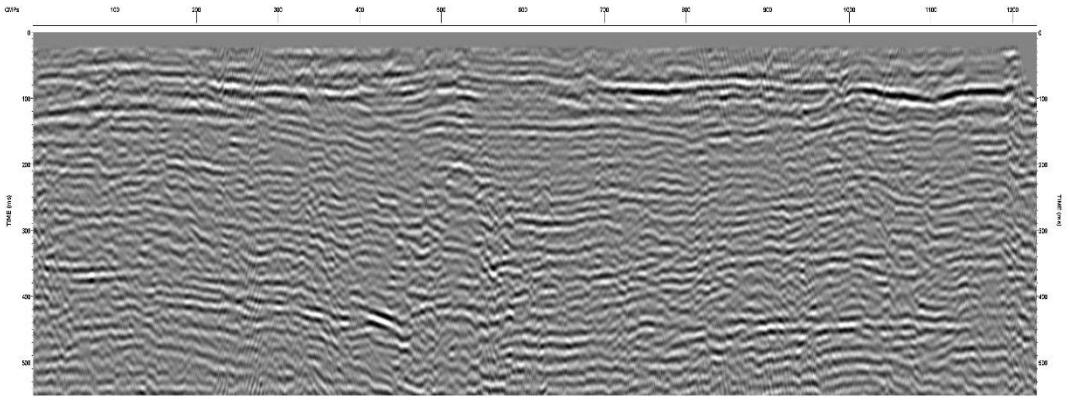

Profile S9

Appendix D: Continued

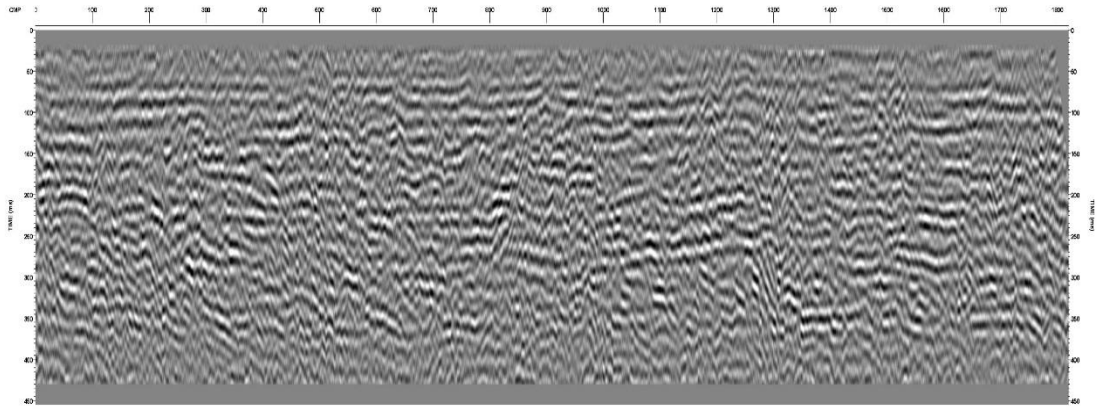

Profile N

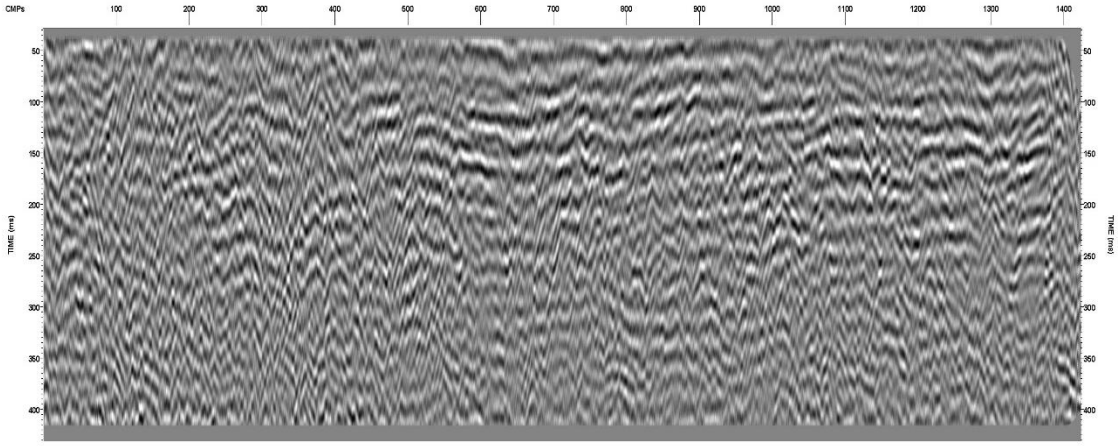

Profile O

Appendix E:

First Beaks picking on field filed records in order to estimate S-wave velocities.

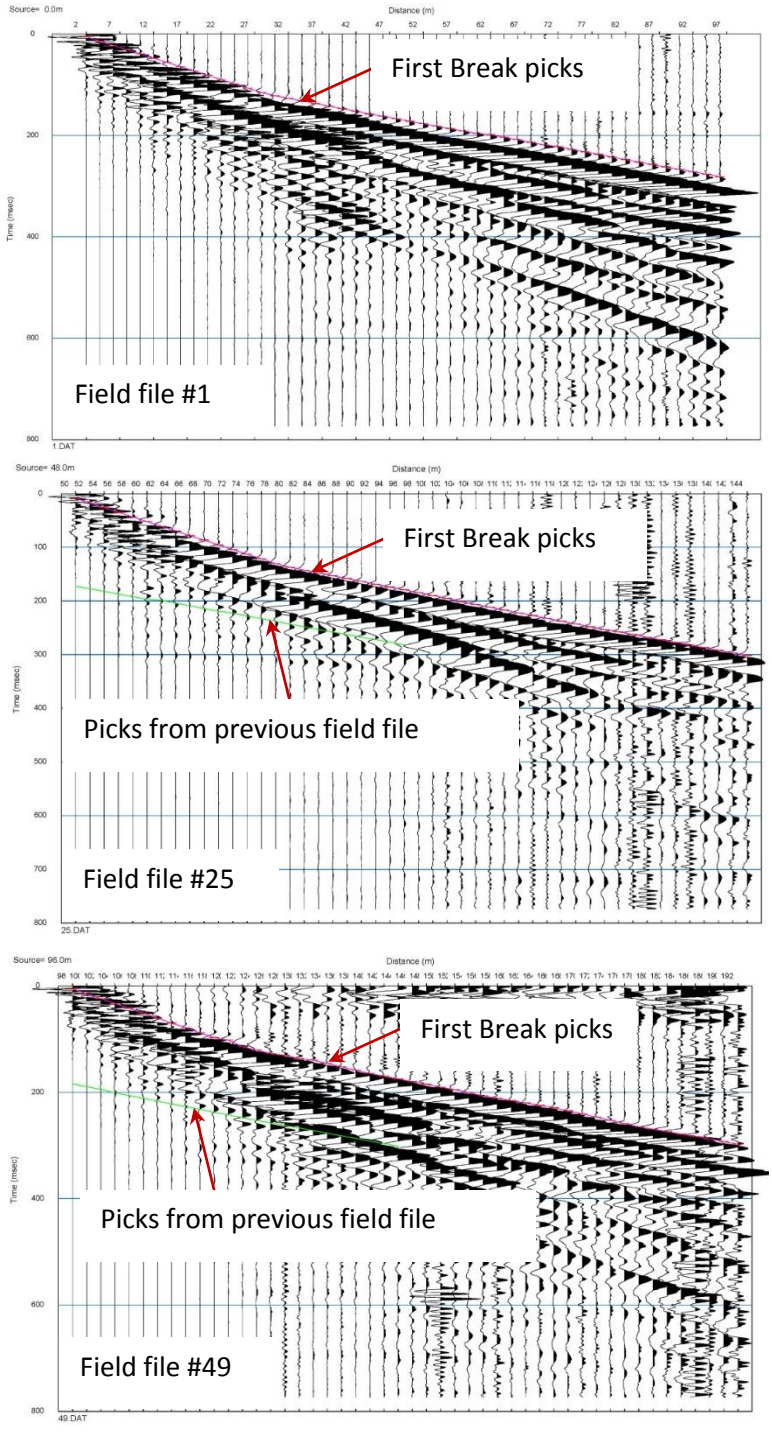
First Break picks
Field file #1
First Break picks
Picks from previous field file
Field file #25
First Break picks
Picks from previous field file
Field file #49

.

Appendix F:

First Beaks picking on field filed records in order to estimate P-wave velocities

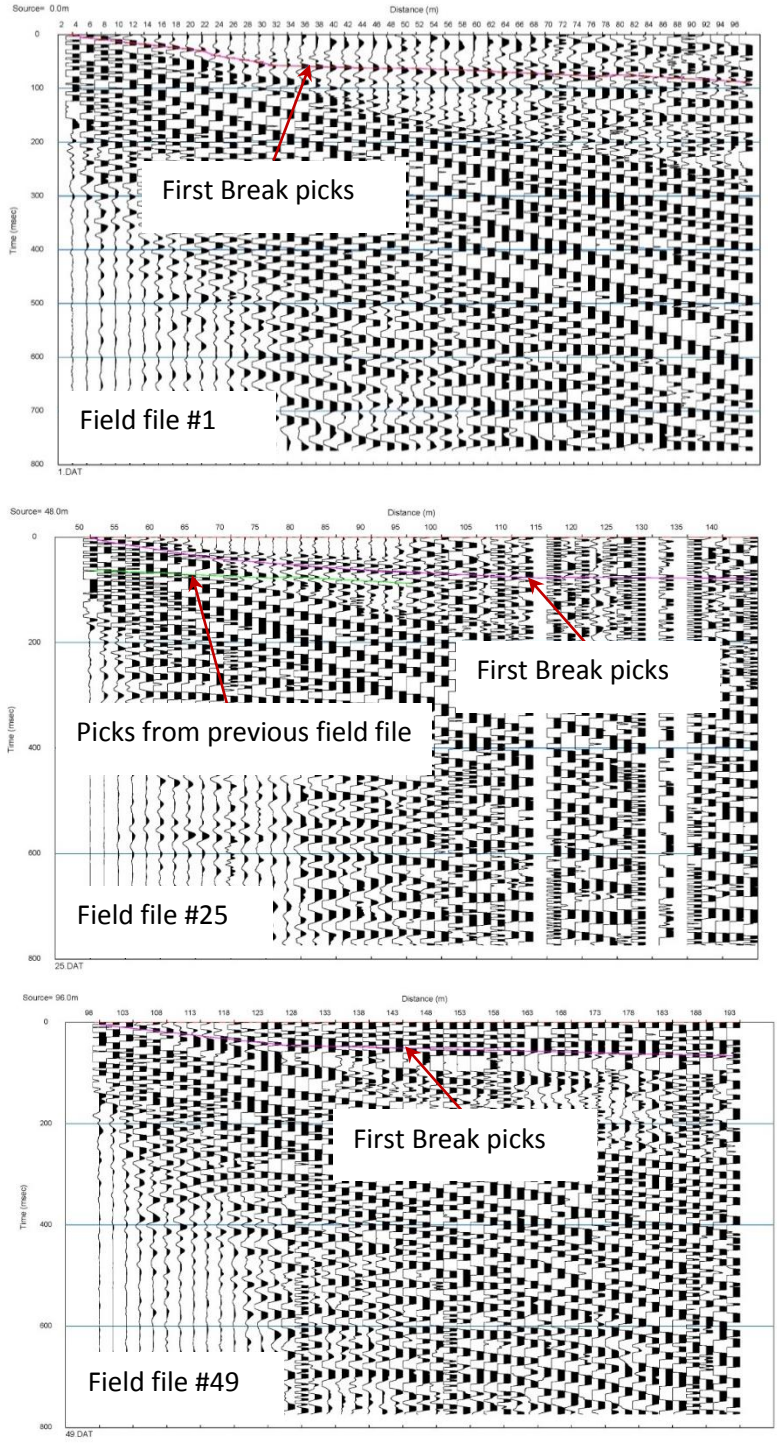
Source= 0.0m
Distance (m)
Time (msec)
First Break picks
Field file #1
1.DAT
Source= 48.0m
Distance (m)
Time (msec)
First Break picks
Picks from previous field file
Field file #25
25.DAT
Source= 96.0m
Distance (m)
Time (msec)
First Break picks
Field file #49
49.DAT

Appendix G:

Amplitude spectrum of the rotated data sets. Each component (i.e., TT, TR, RR, RT) were rotated at 5˚ increment. Maximum amplitude indicates the reflection energy at any particulate rotation.

1) Transverse source (East-West hammer strikes)

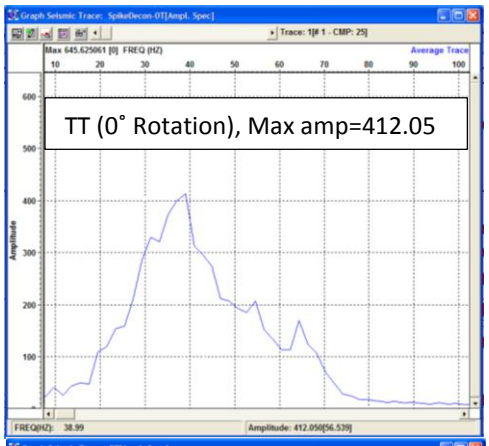
TT (0˚ Rotation), Max amp=412.05

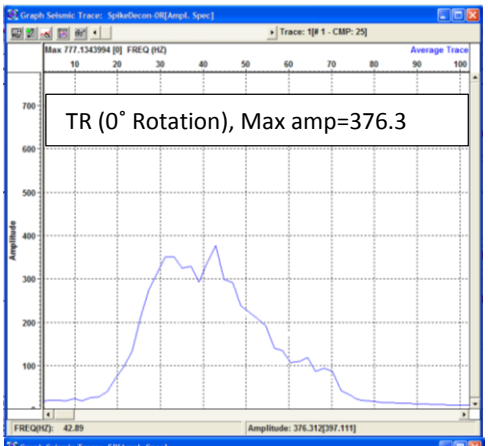
TR (0˚ Rotation), Max amp=376.3

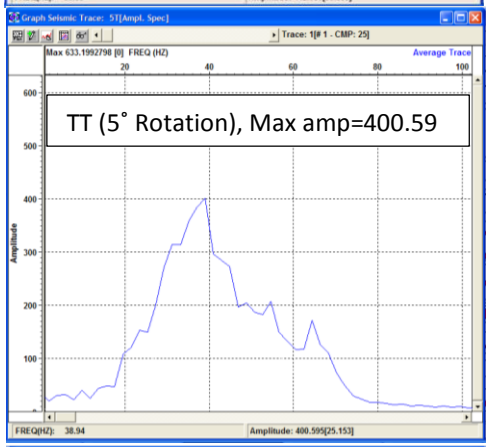
TT (5˚ Rotation), Max amp=400.59

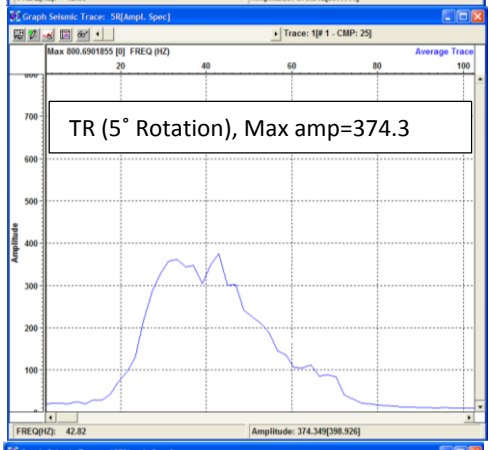
TR (5˚ Rotation), Max amp=374.3

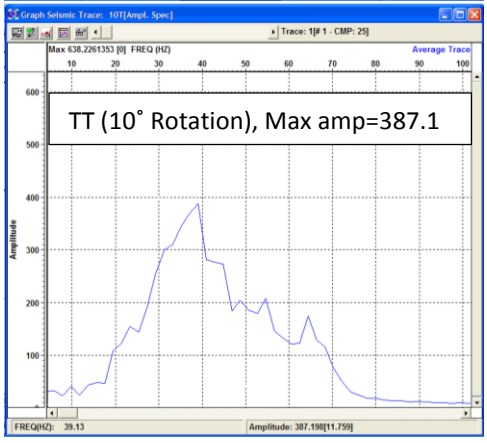
TT (10˚ Rotation), Max amp=387.1

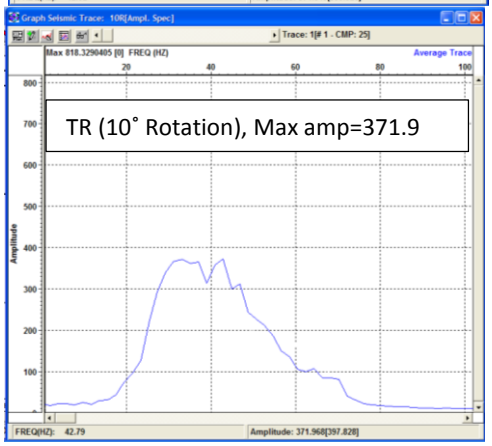
TR (10˚ Rotation), Max amp=371.9

Appendix G-1: Continued

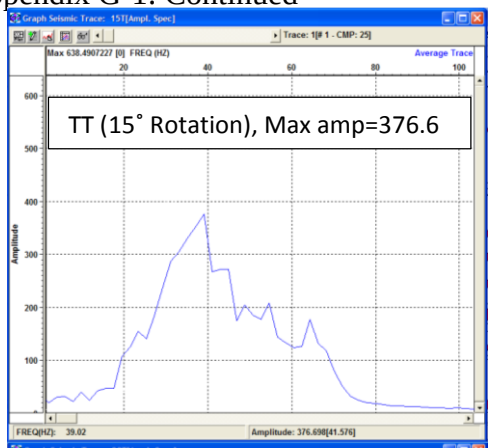

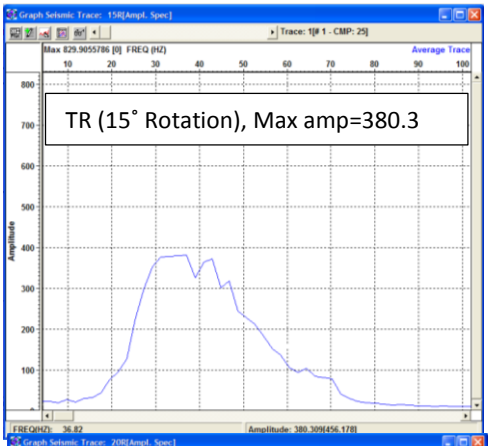

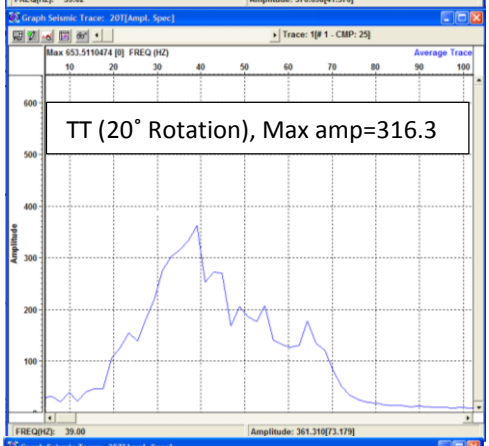

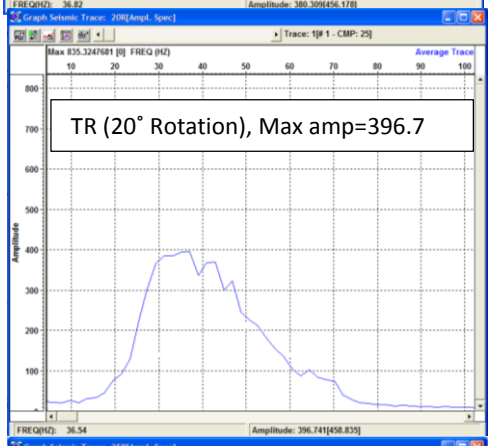

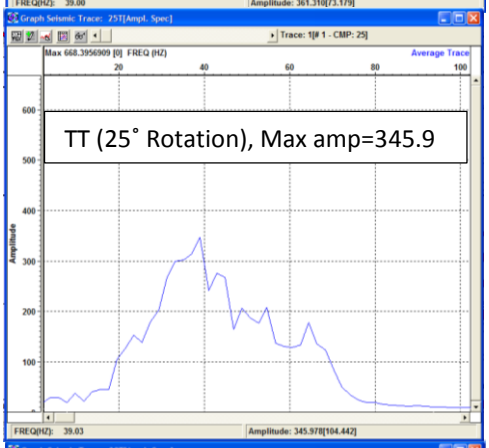

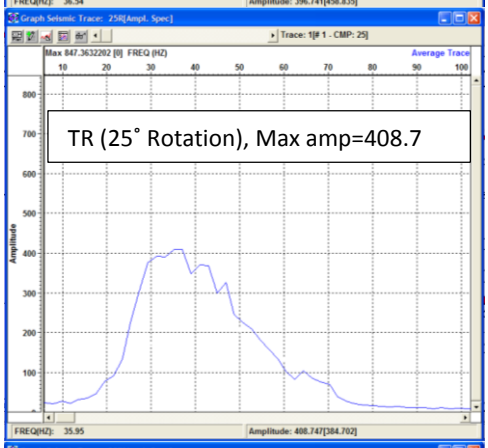

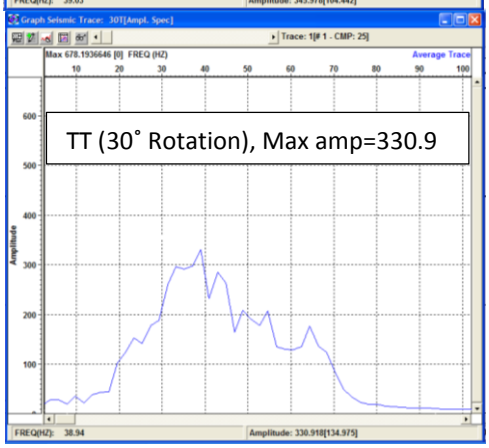

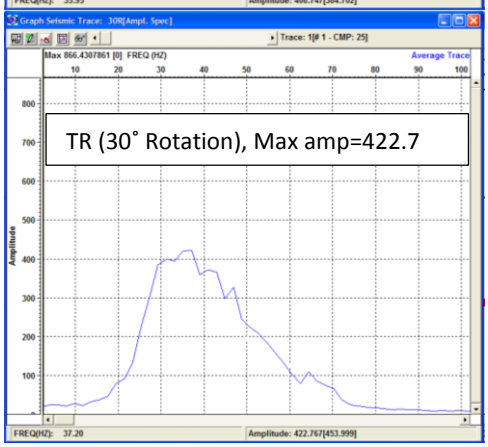

Appendix G-1: Continued

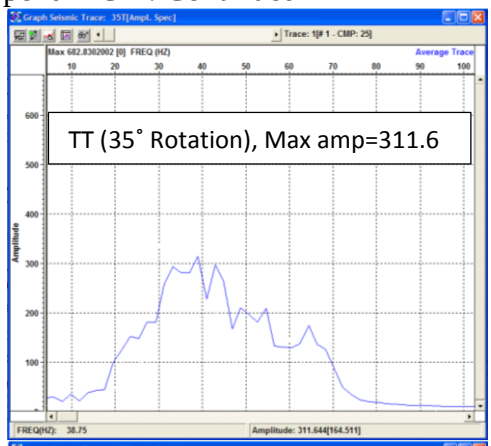

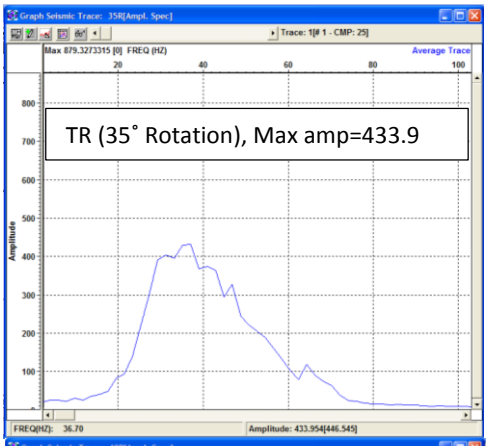

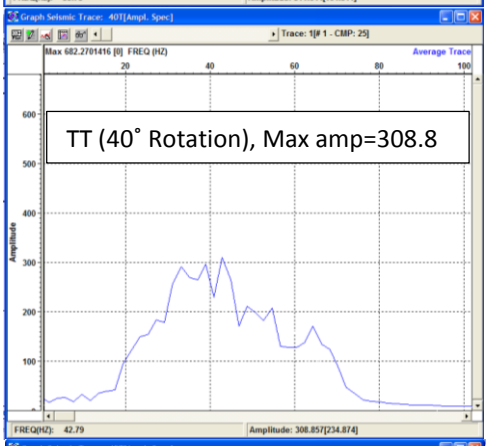

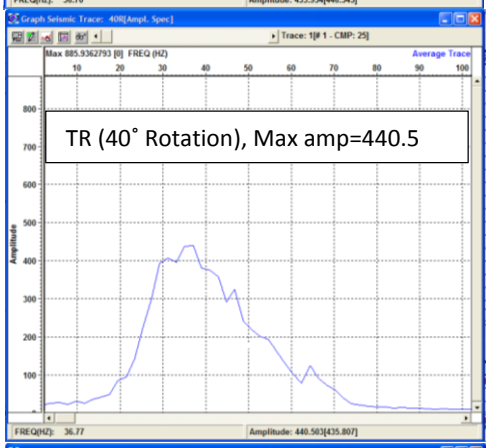

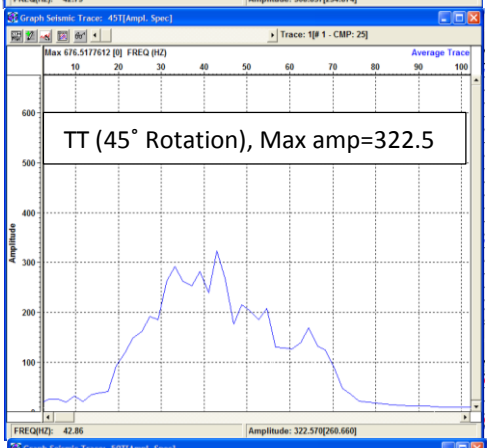

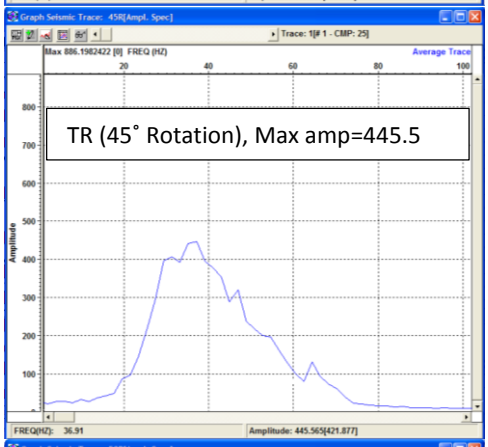

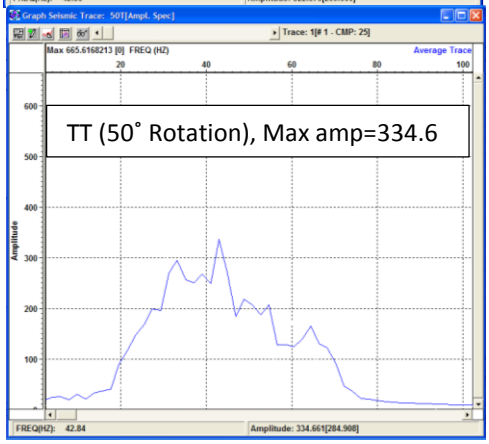

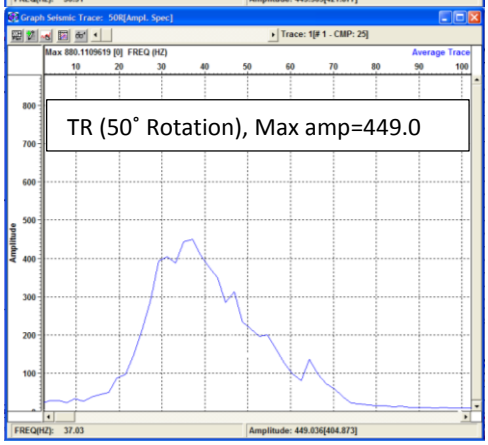

Appendix G-1: Continued

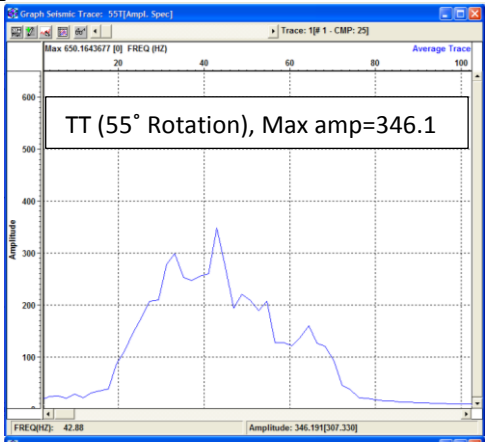

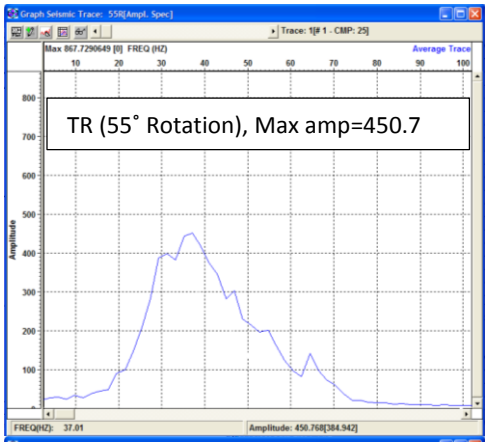

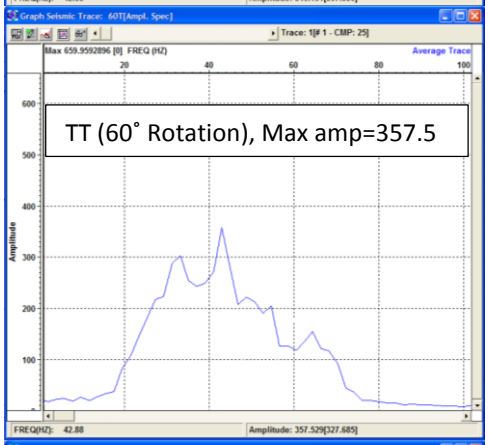

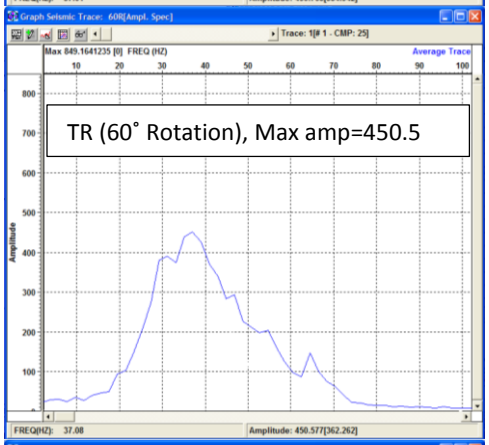

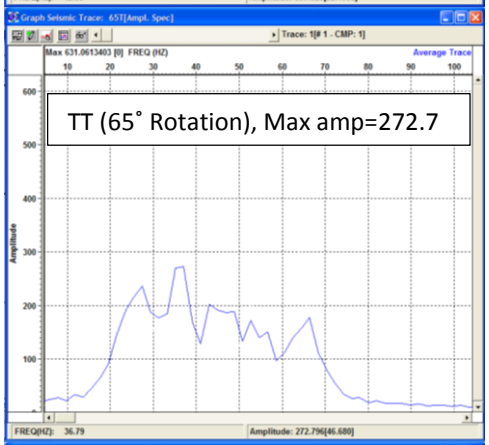

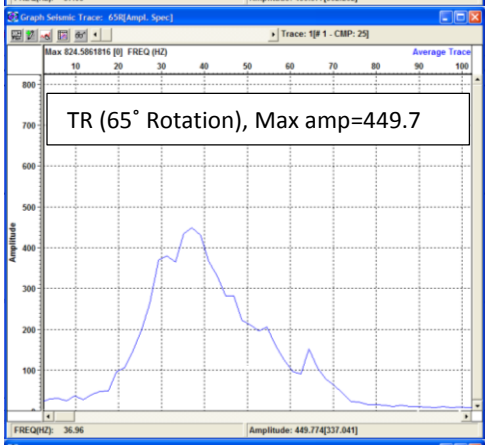

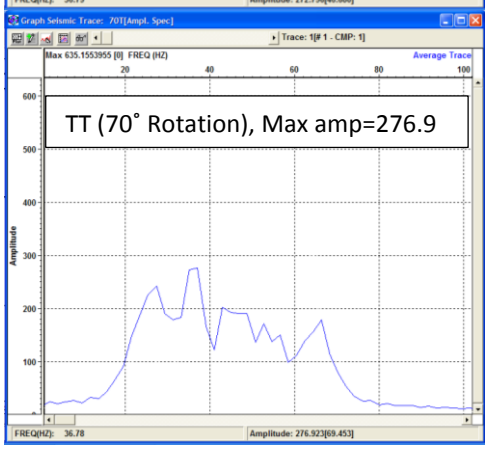

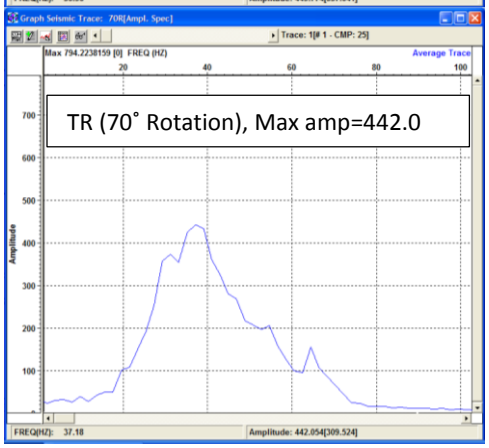

Appendix G-1: Continued

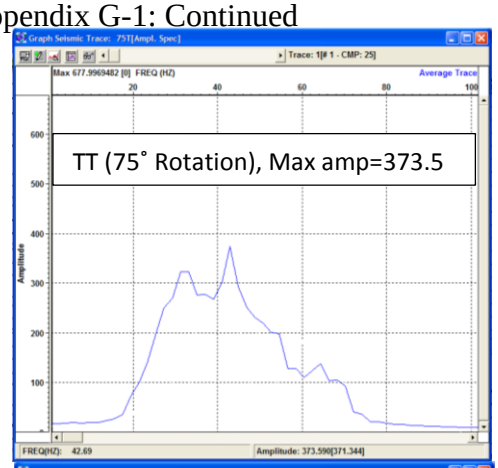

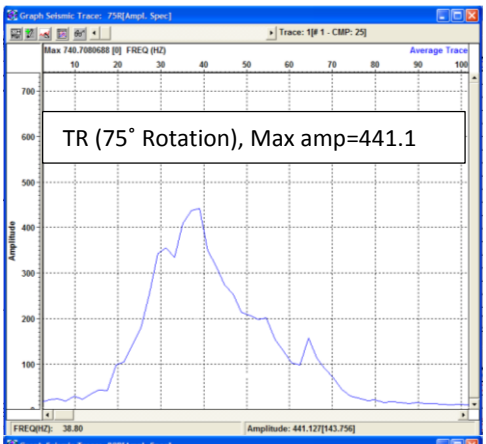

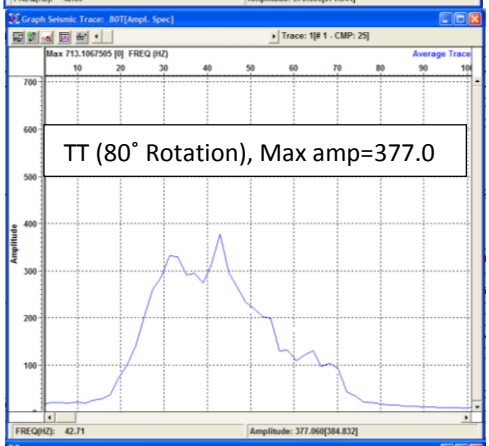

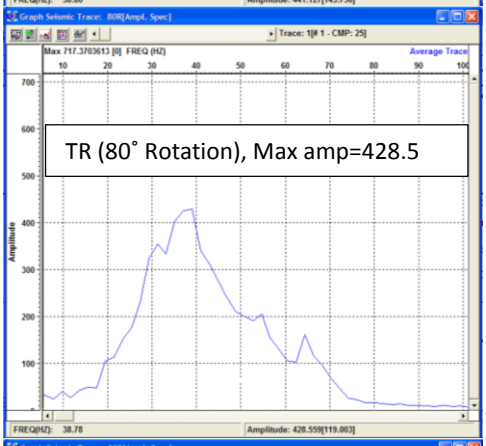

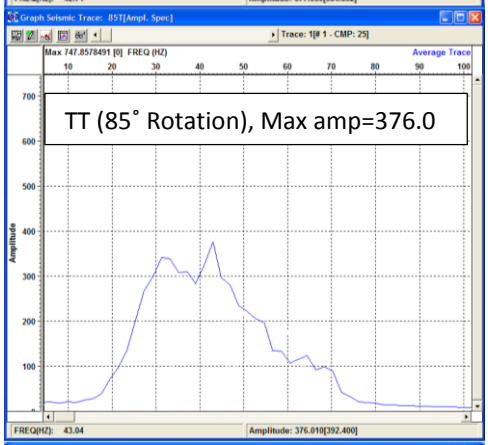

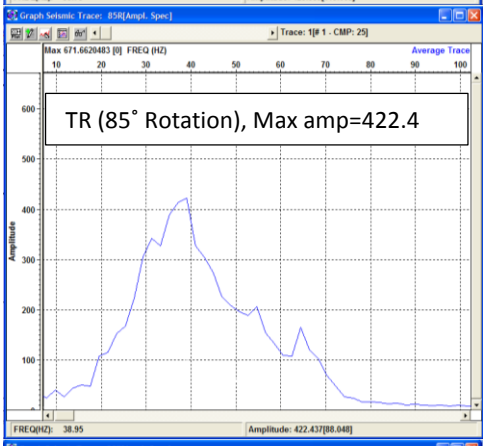

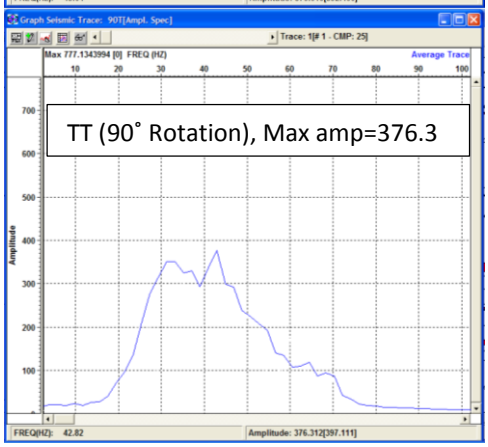

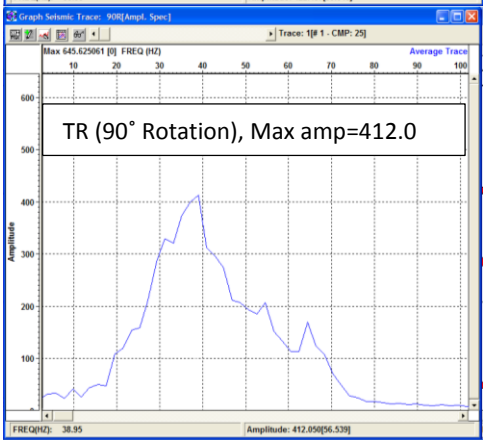

Appendix G-1: Continued

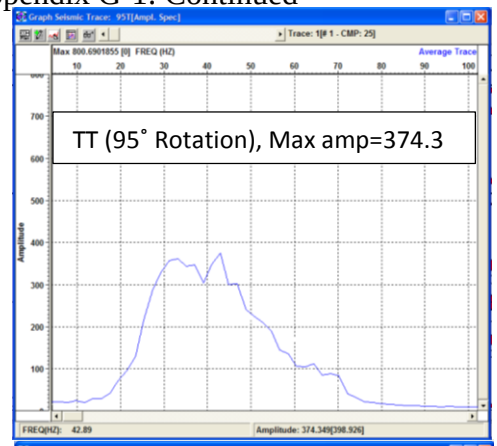

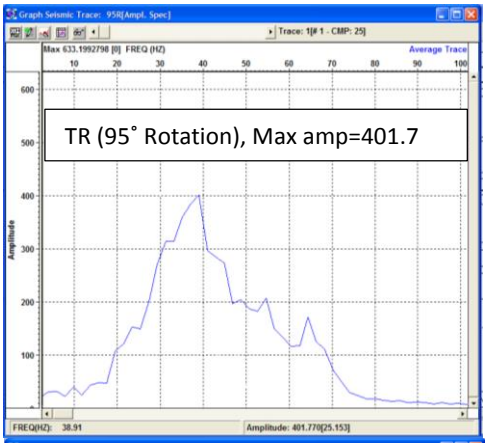

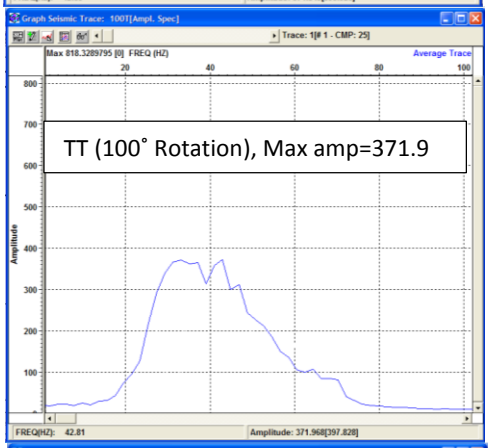

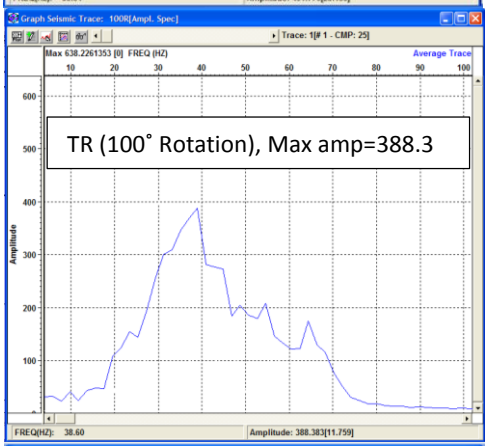

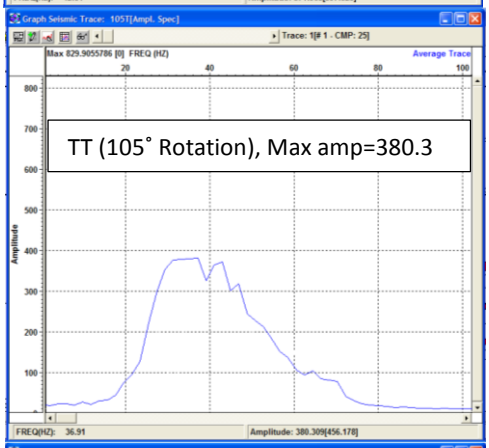

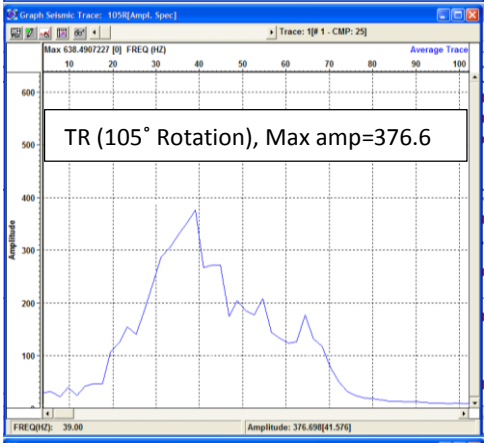

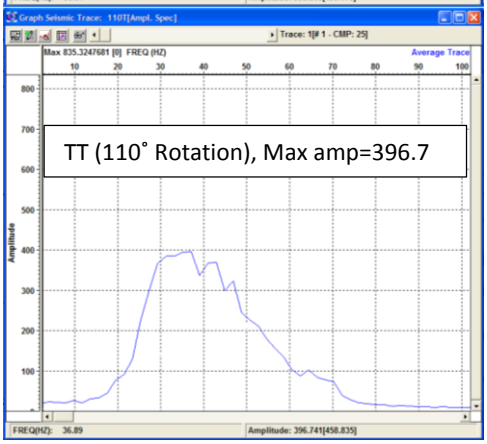

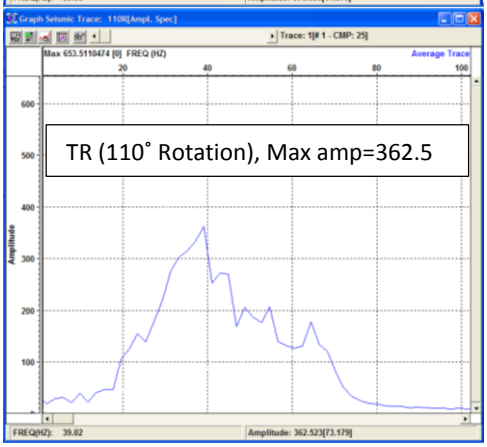

Appendix G-1: Continued

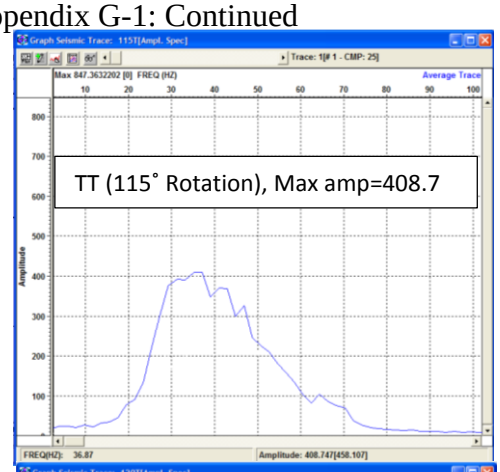

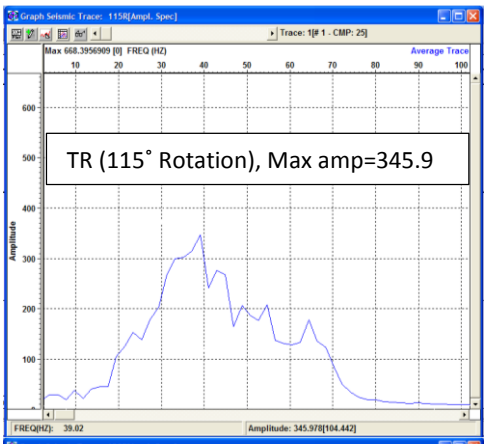

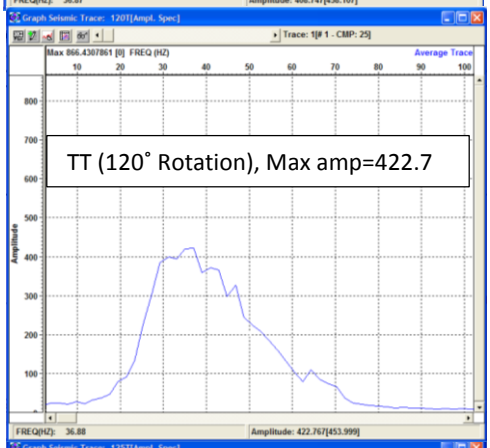

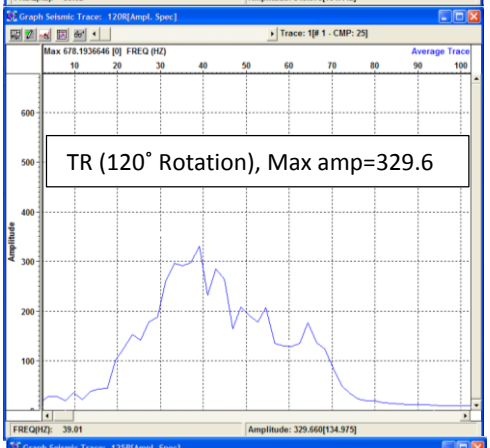

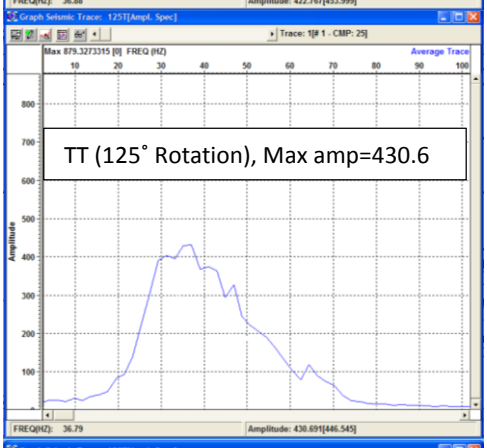

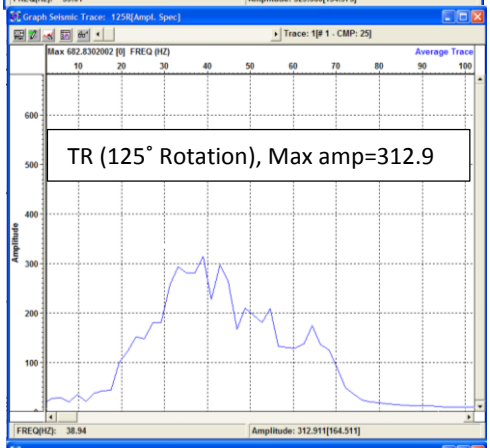

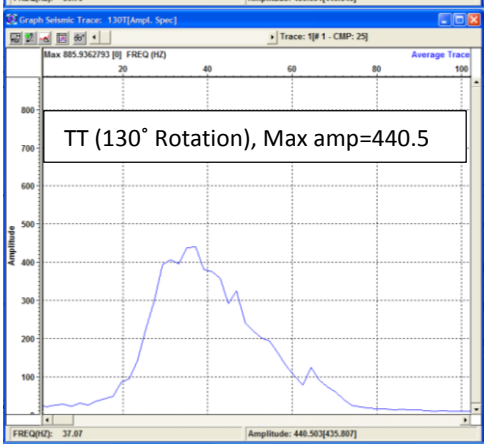

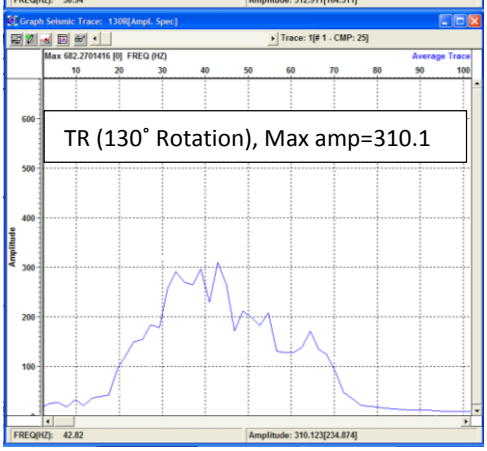

Appendix G-1: Continued

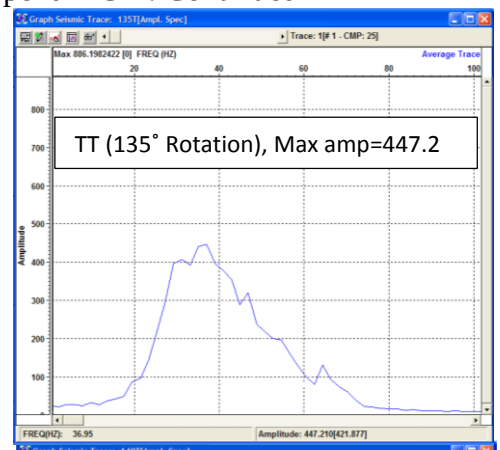

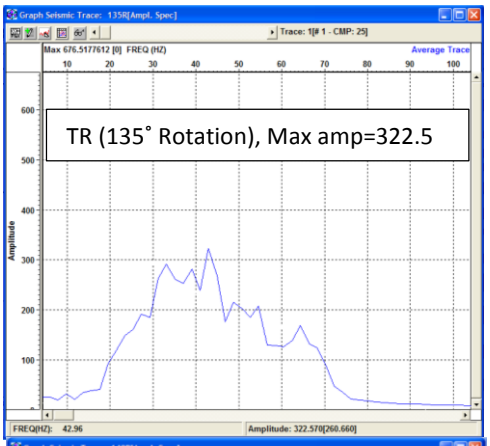

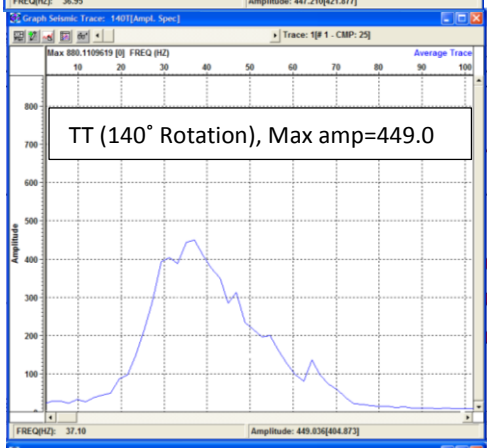

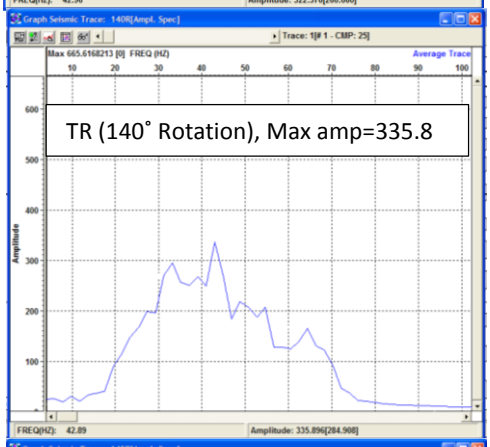

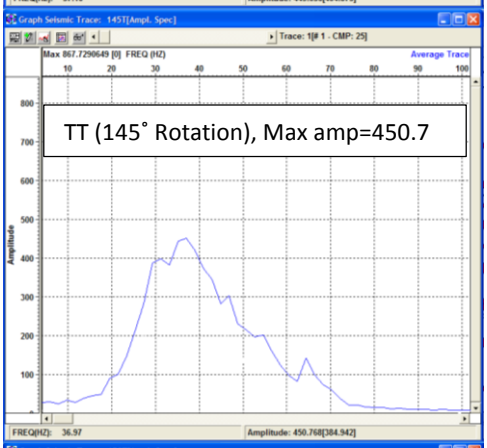

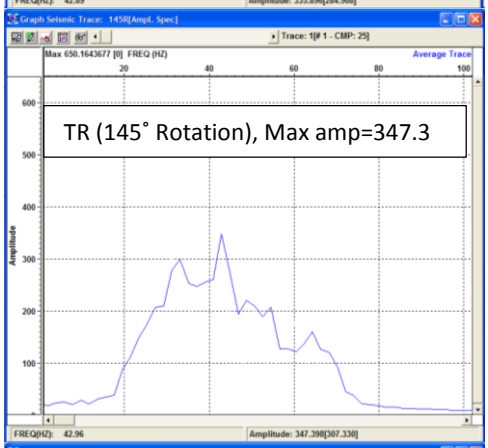

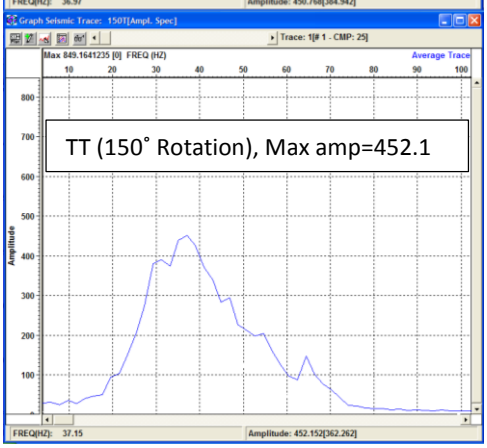

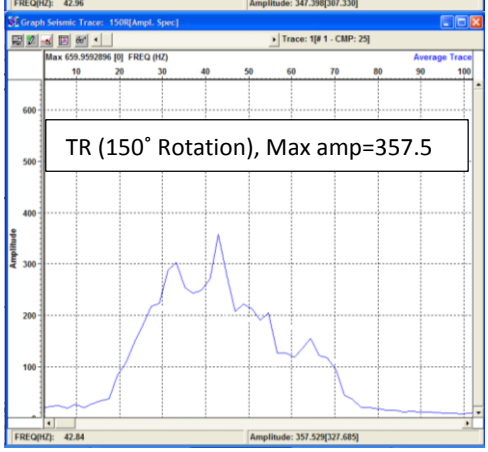

Appendix G-1: Continued

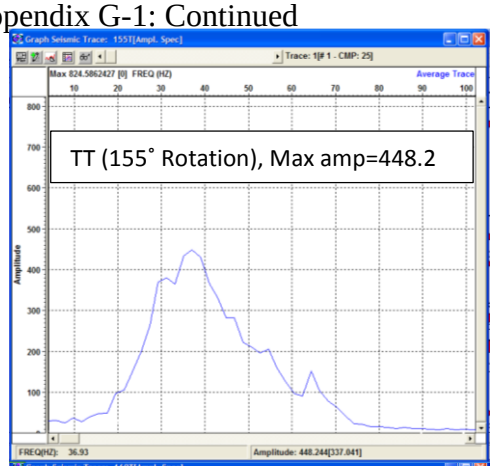

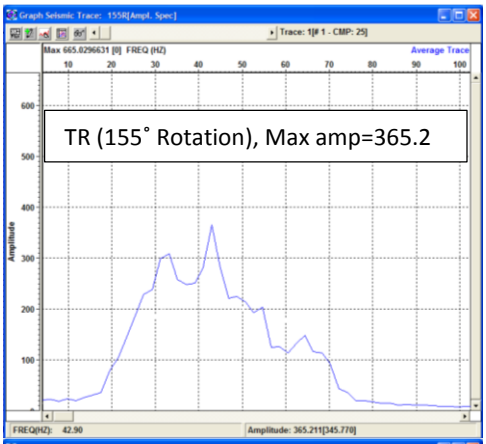

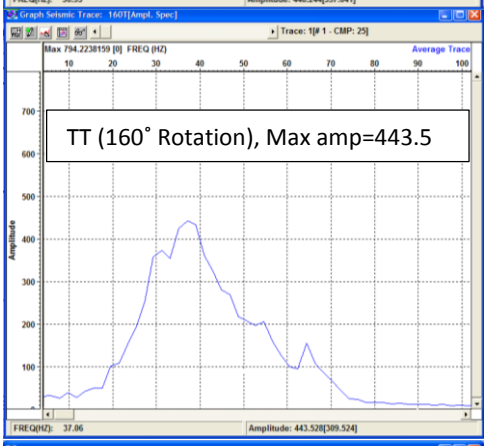

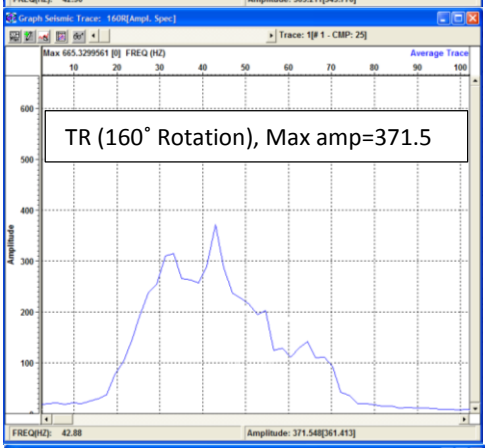

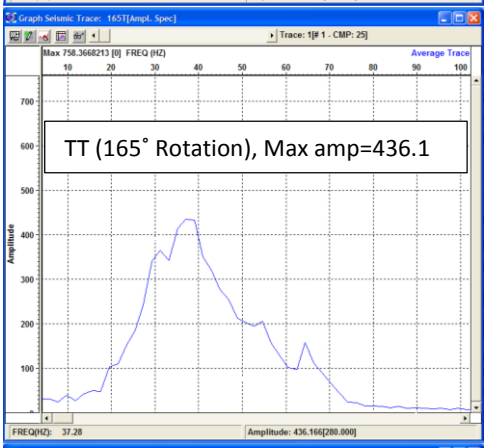

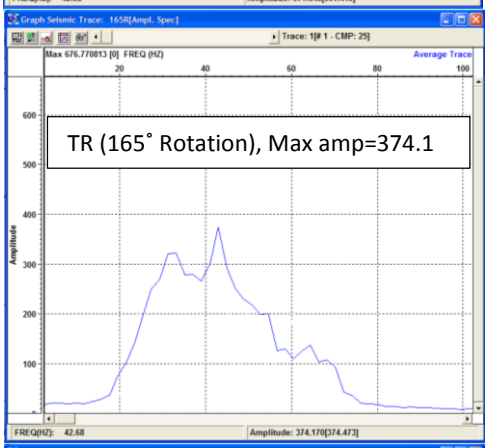

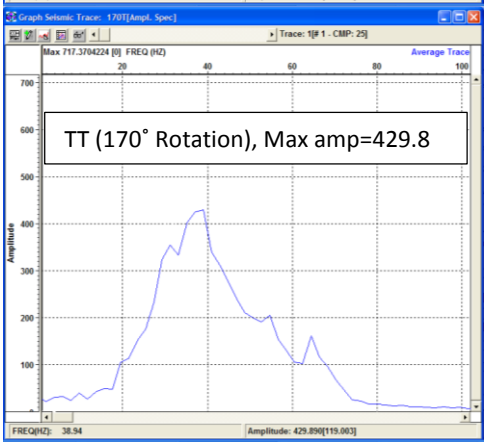

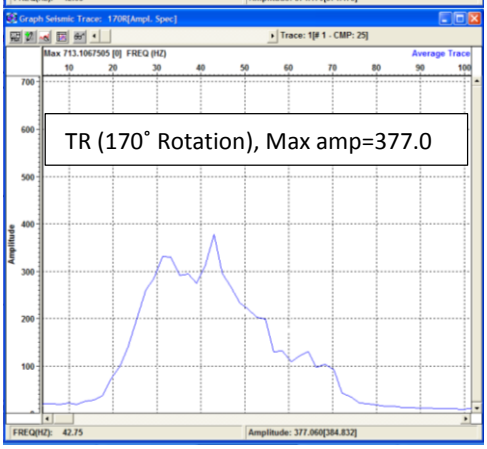

Appendix G-1: Continued

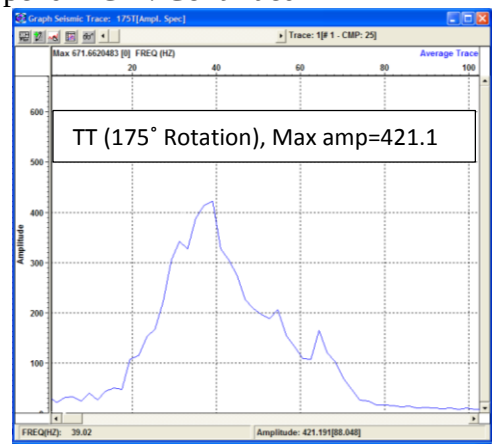

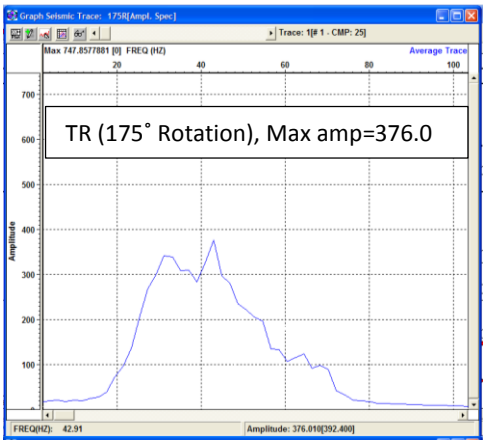

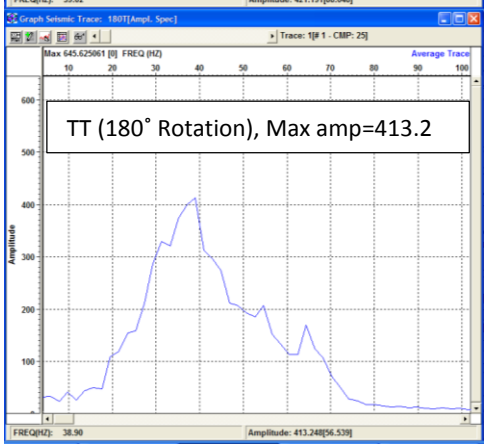

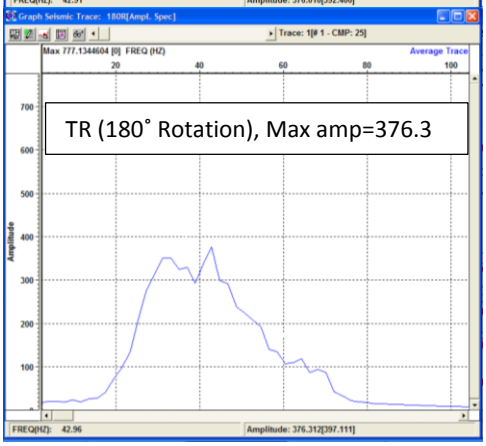

2) Radial source (North-South hammer strikes)

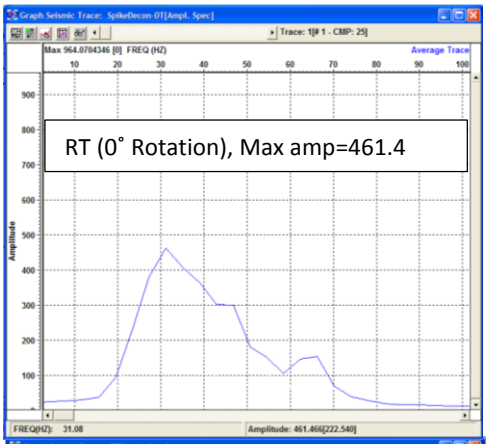
RT (0˚ Rotation), Max amp=461.4

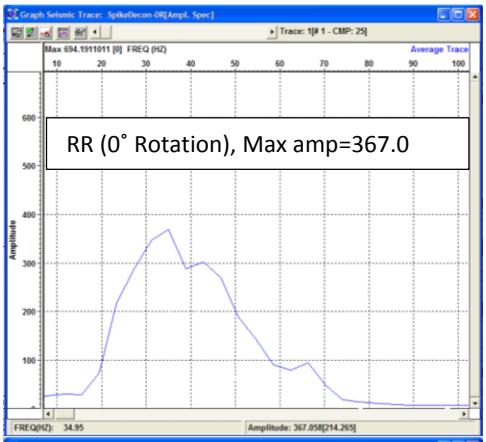
RR (0˚ Rotation), Max amp=367.0

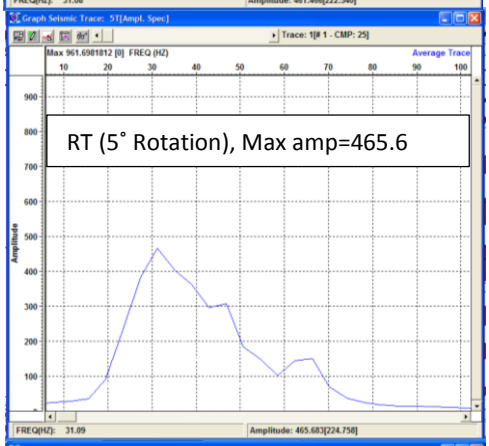
RT (5˚ Rotation), Max amp=465.6

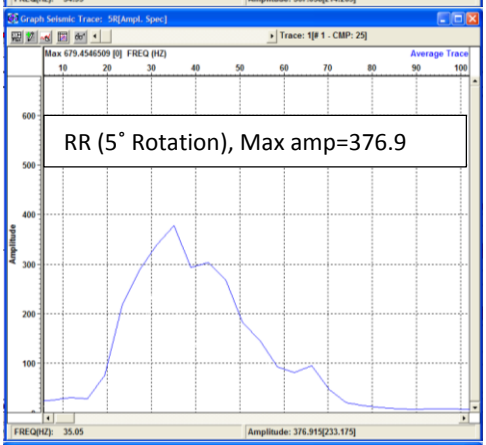
RR (5˚ Rotation), Max amp=376.9

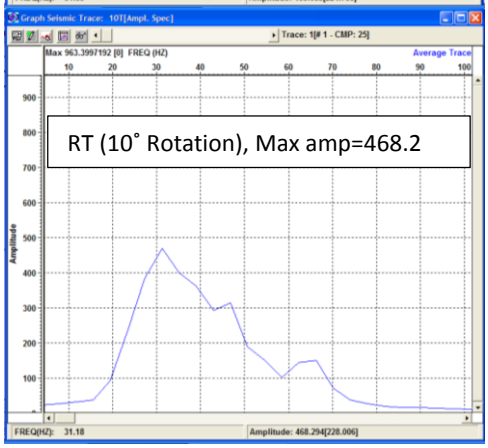
RT (10˚ Rotation), Max amp=468.2

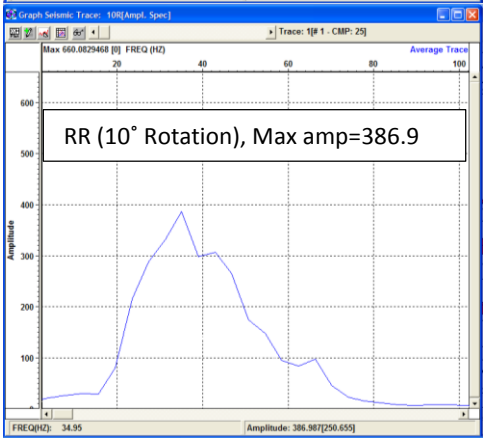
RR (10˚ Rotation), Max amp=386.9

Appendix G-2: Continued

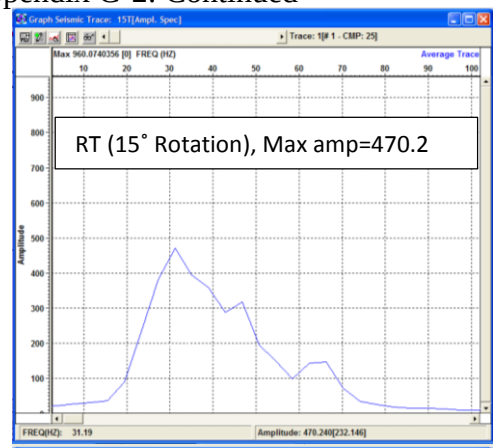

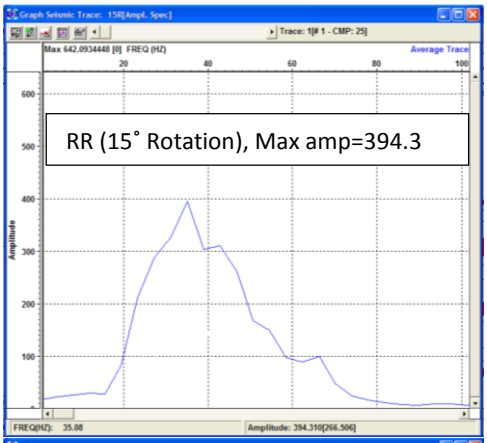

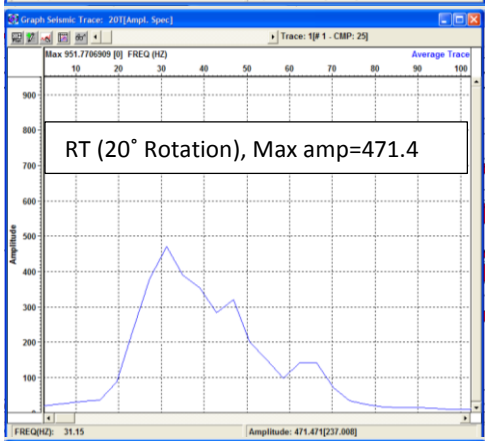

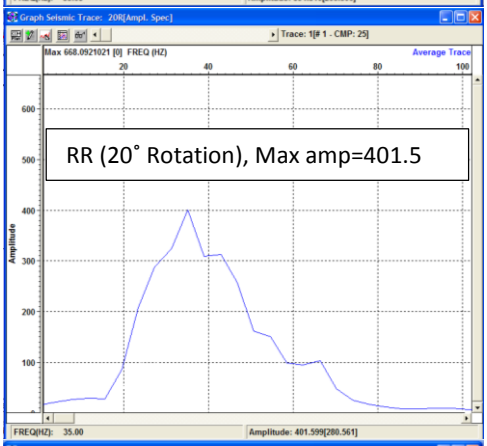

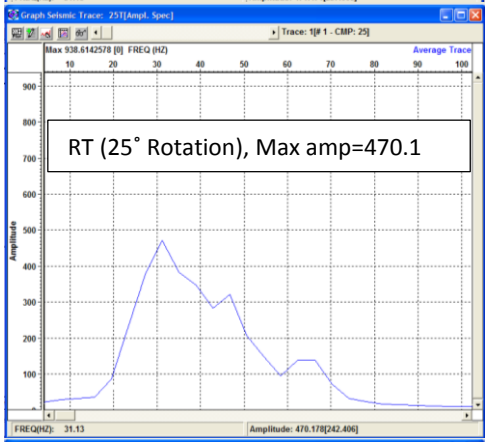

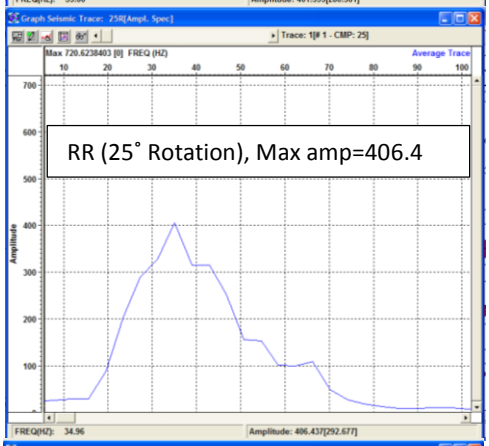

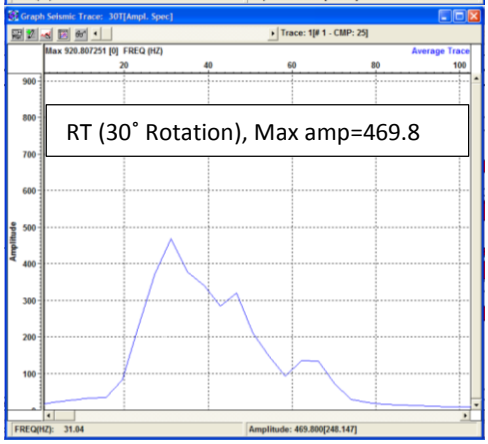

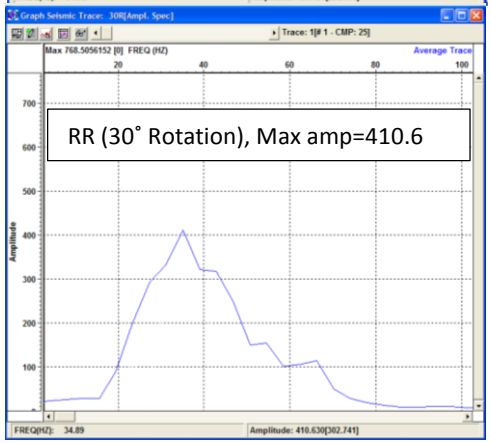

Appendix G-2: Continued

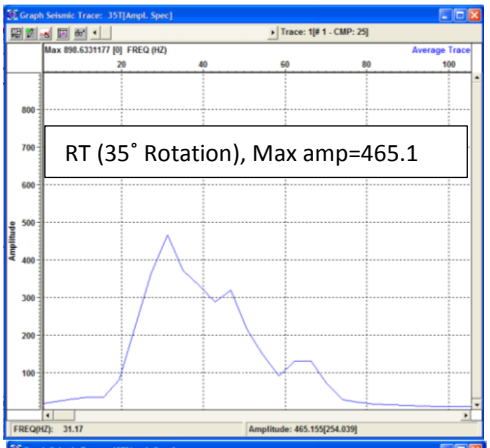

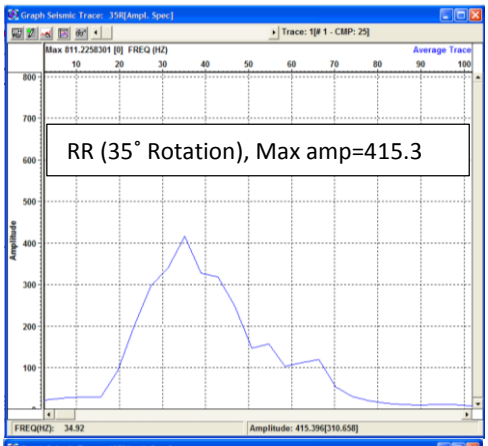

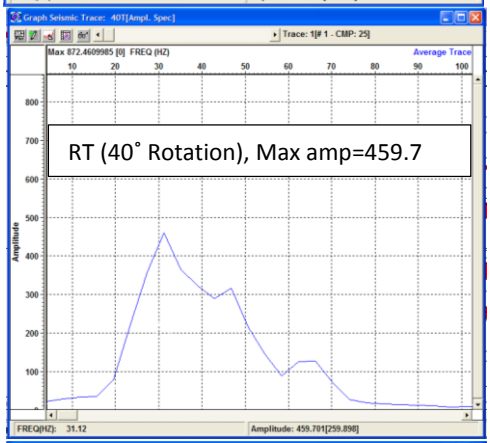

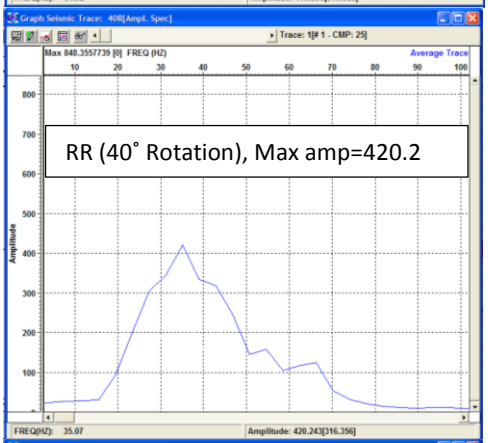

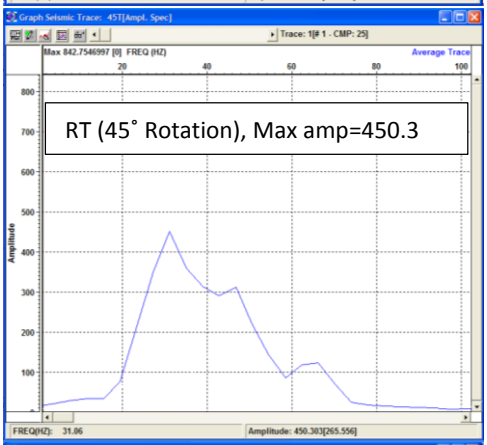

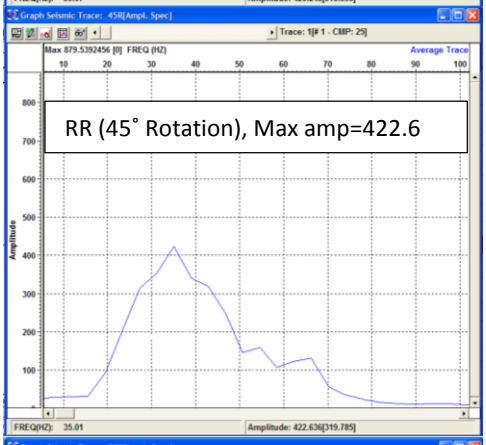

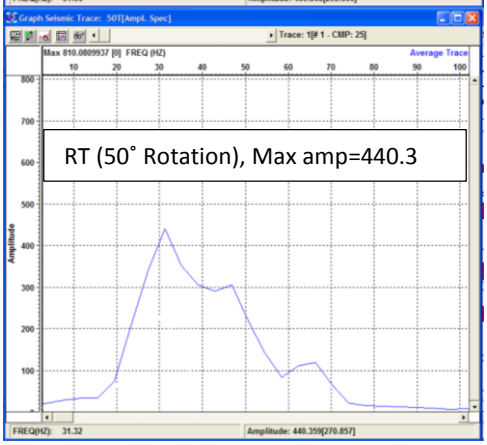

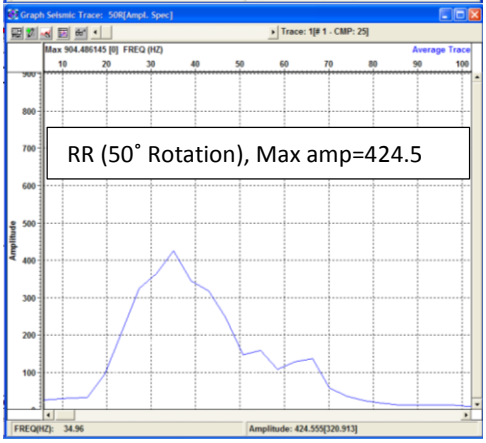

Appendix G-2: Continued

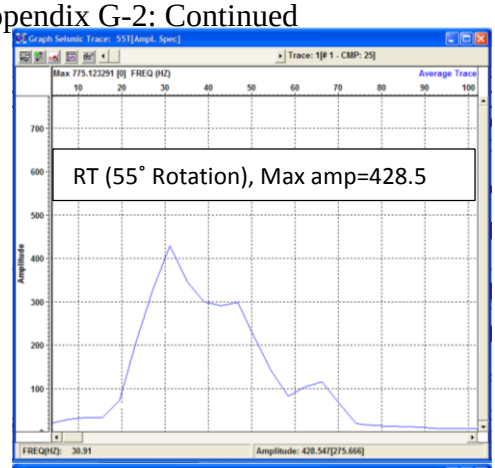

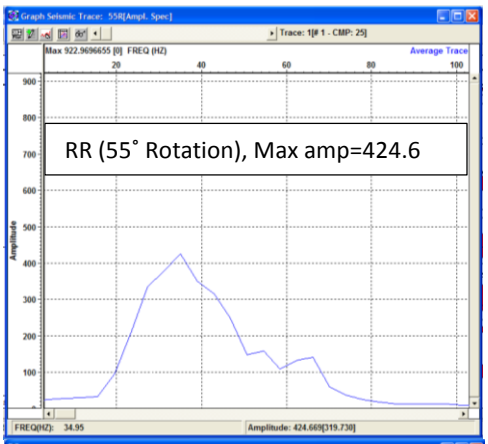

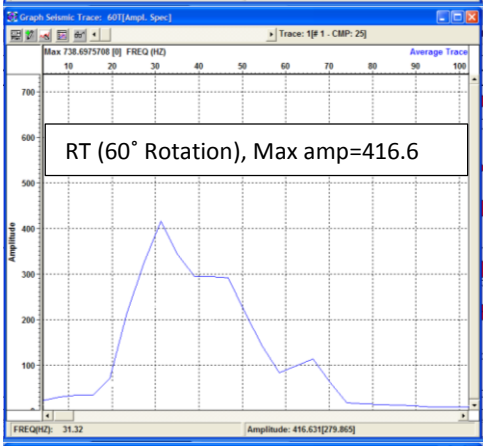

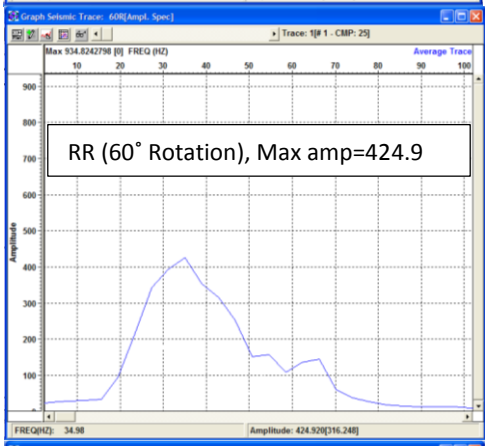

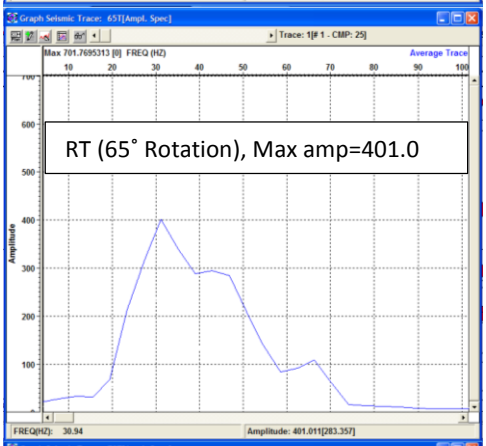

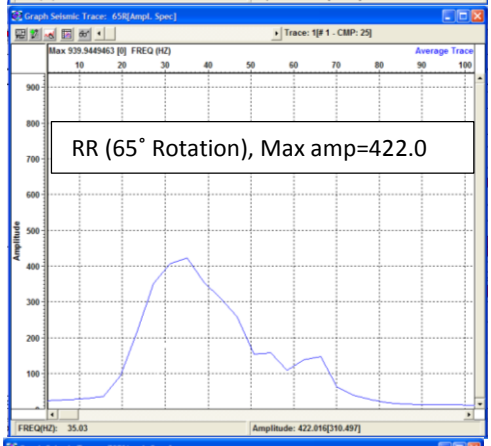

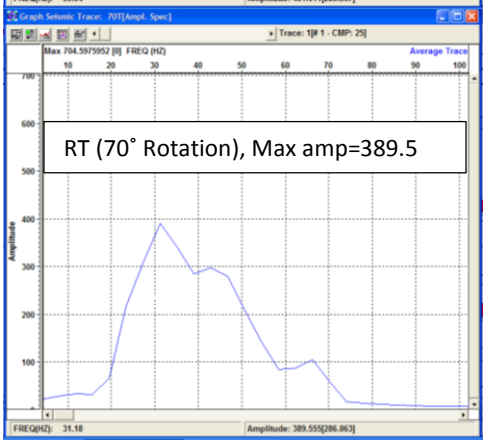

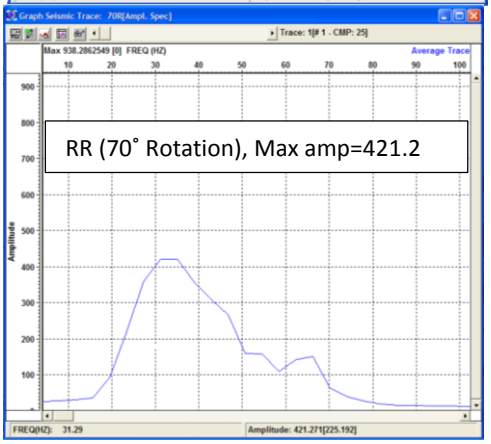

Appendix G-2: Continued

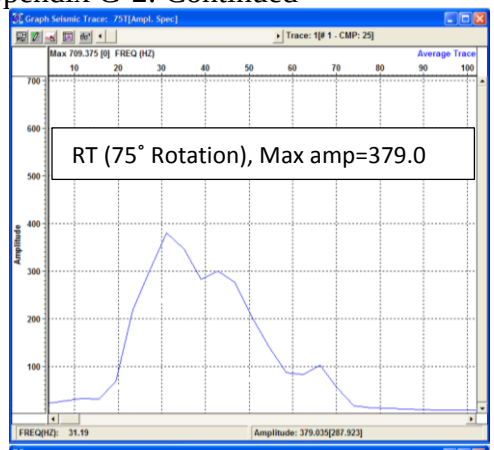

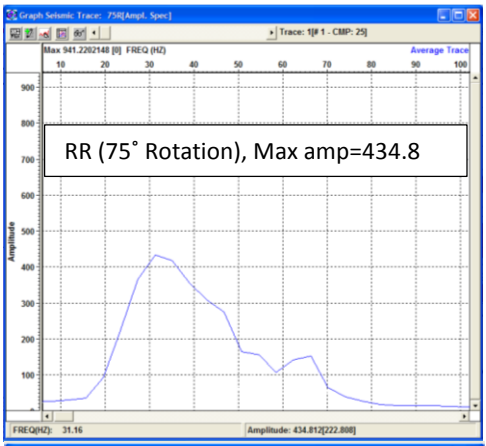

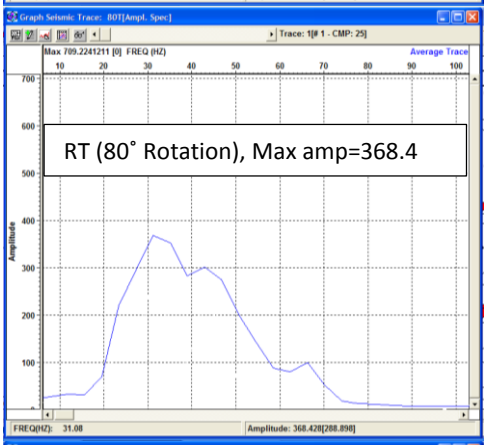

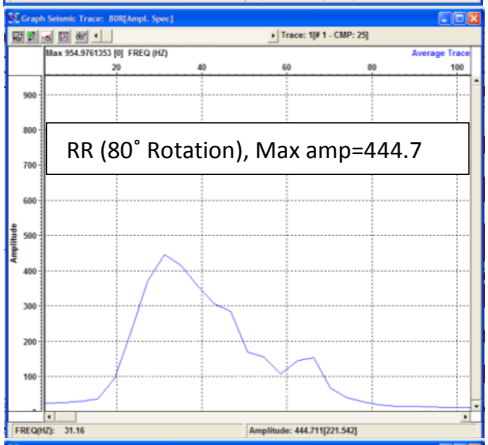

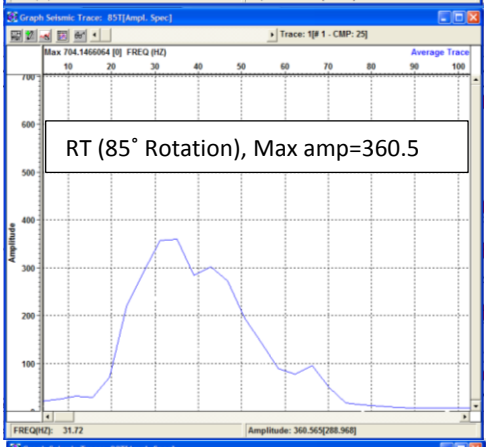

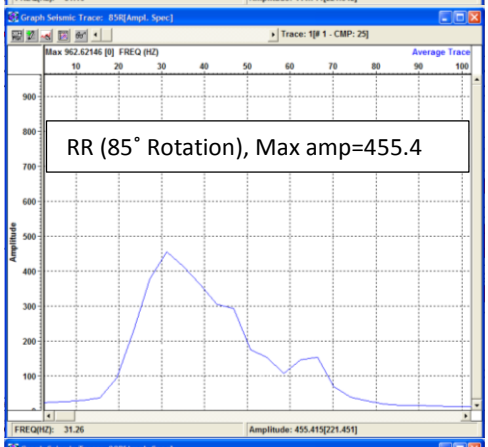

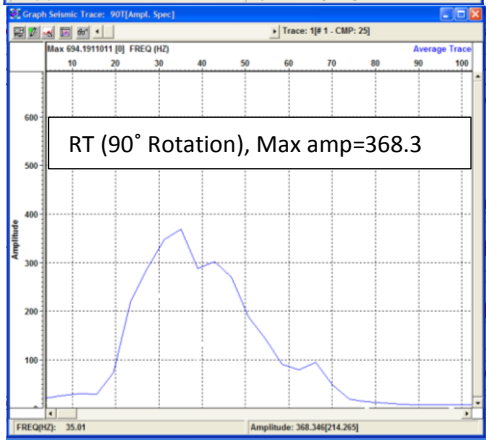

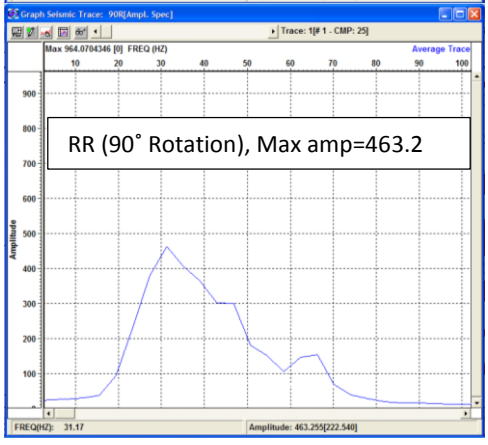

Appendix G-2: Continued

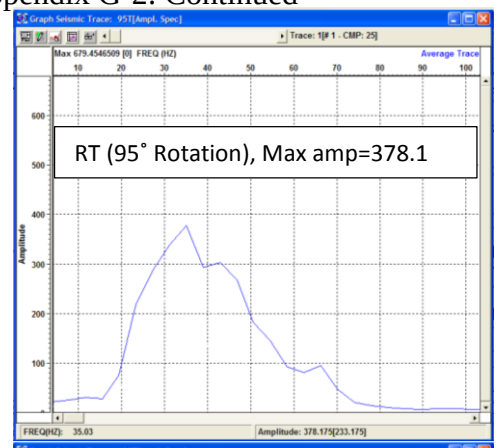

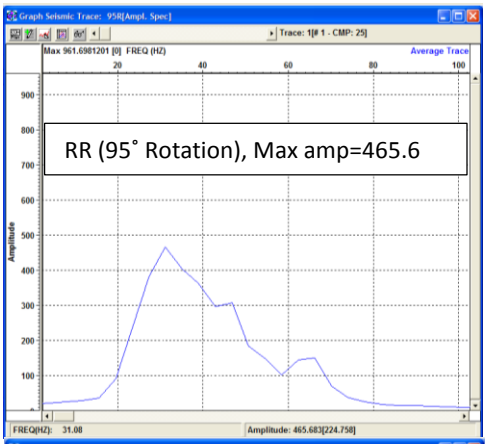

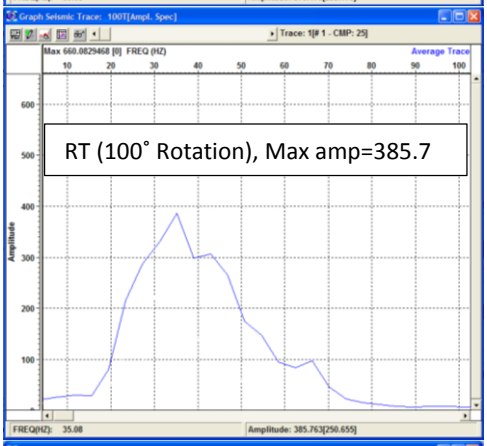

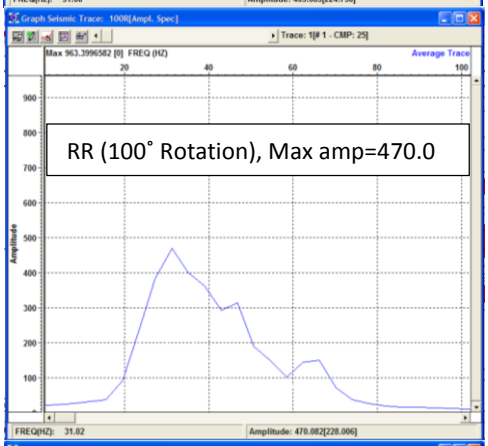

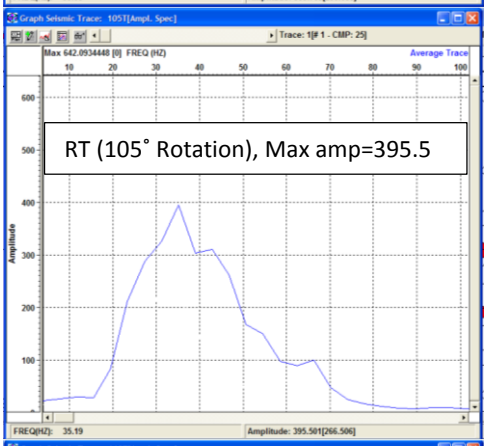

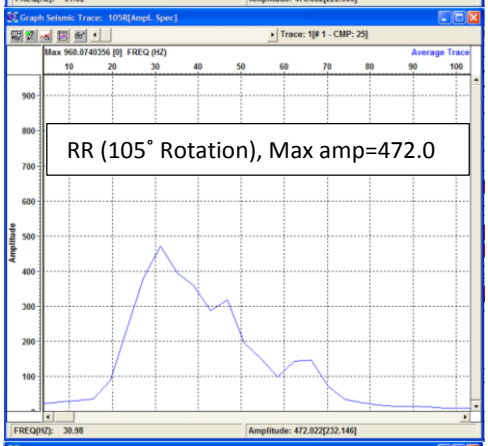

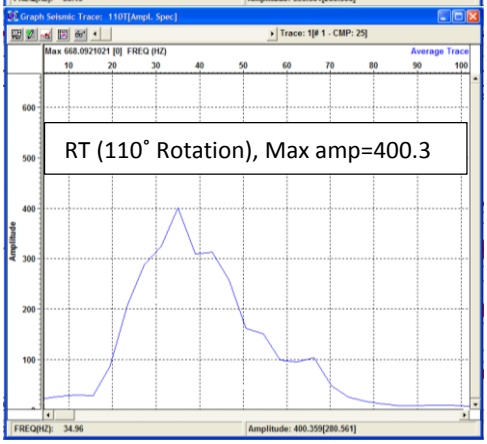

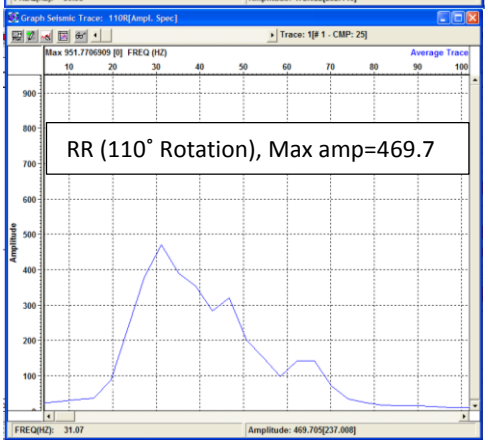

Appendix G-2: Continued

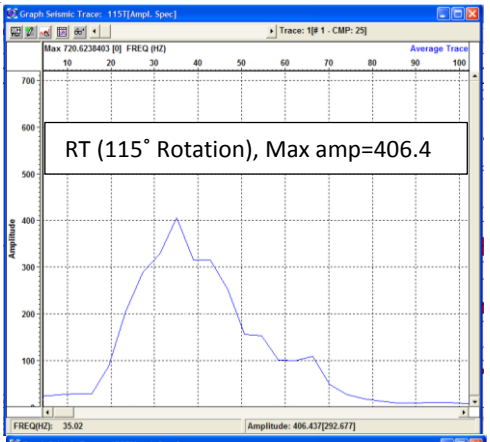

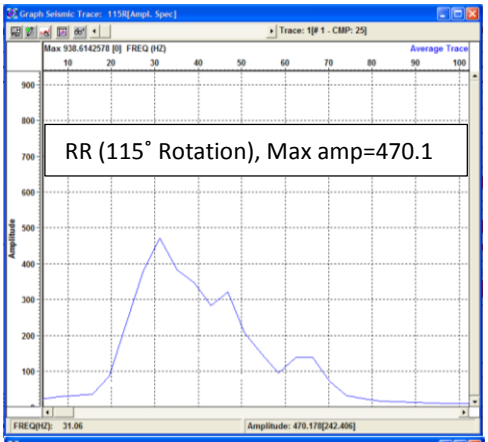

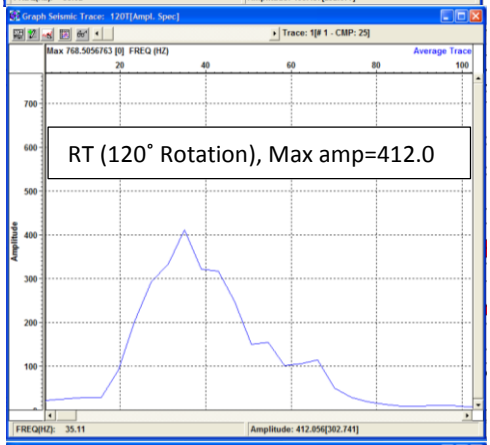

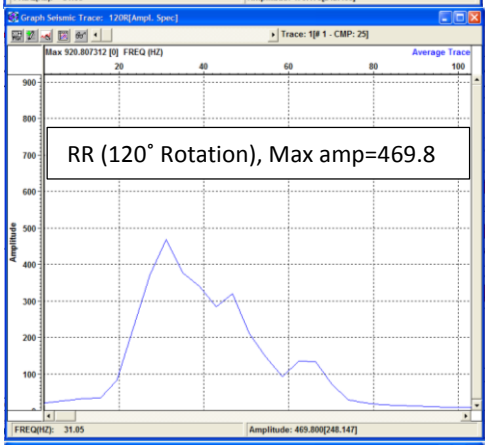

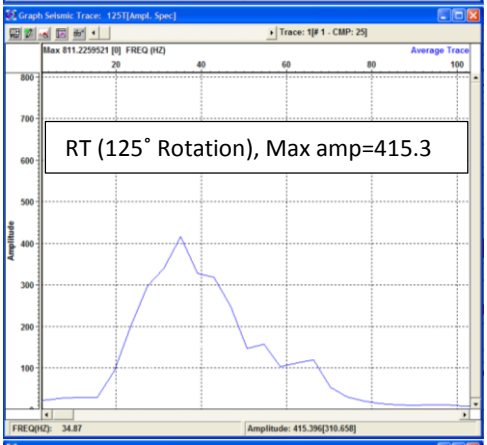

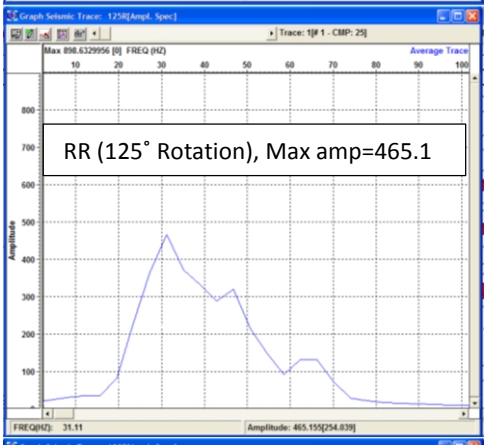

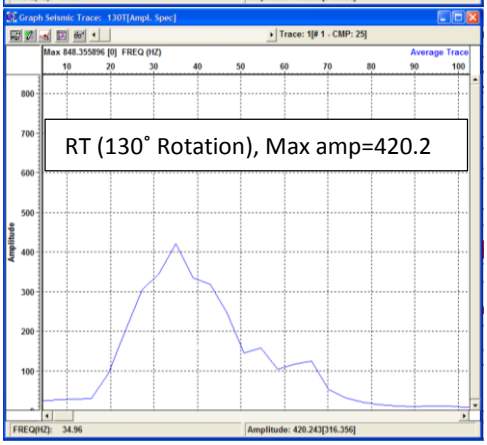

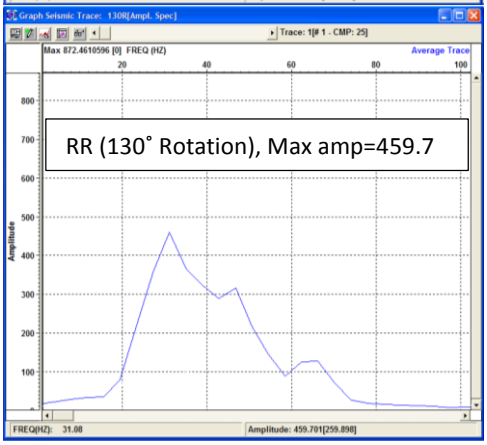

Appendix G-2: Continued

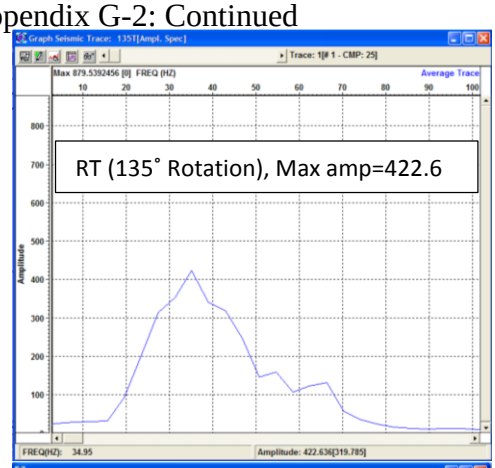

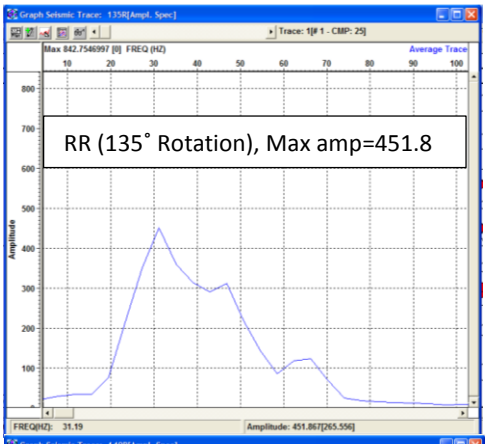

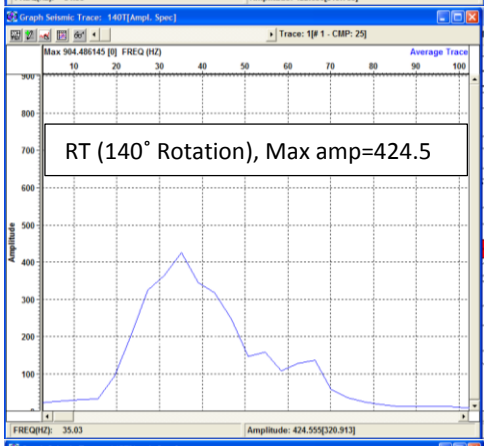

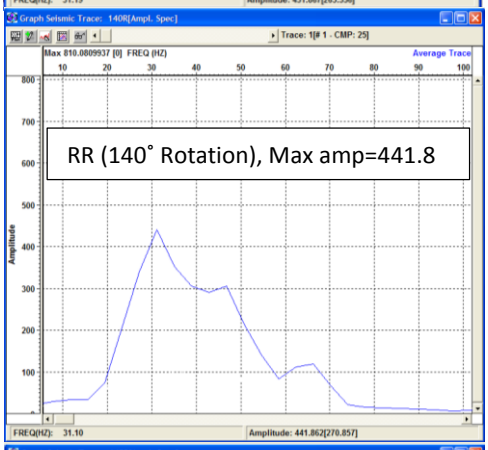

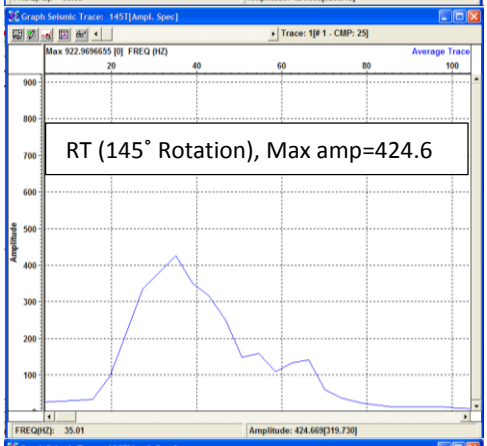

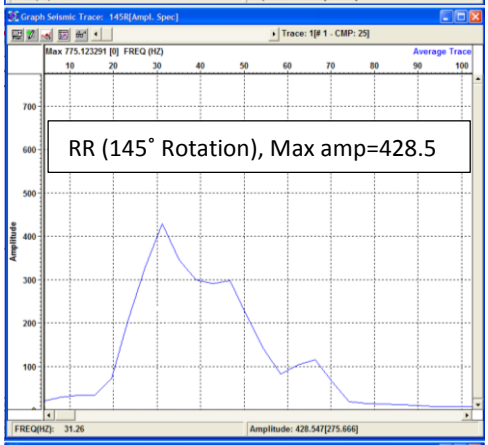

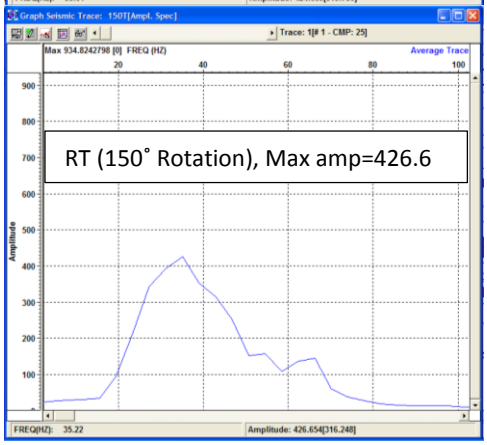

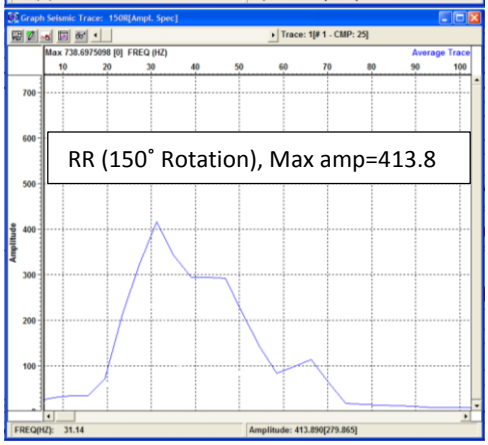

Appendix G-2: Continued

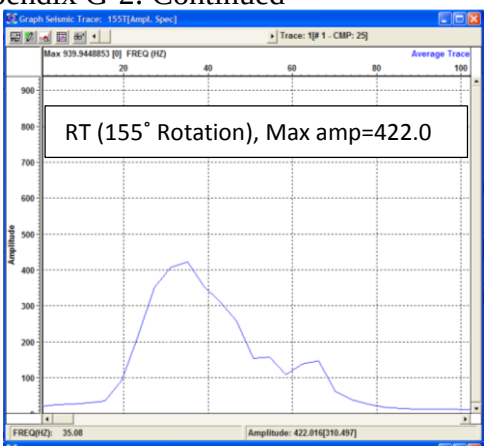

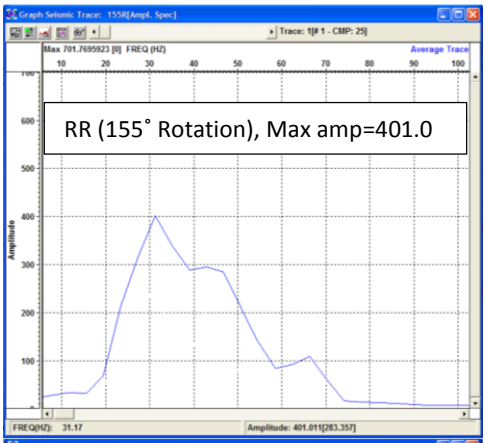

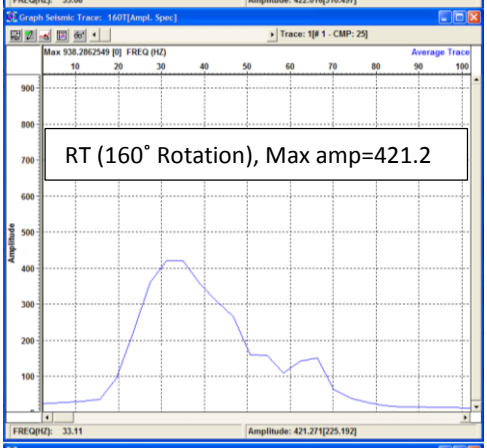

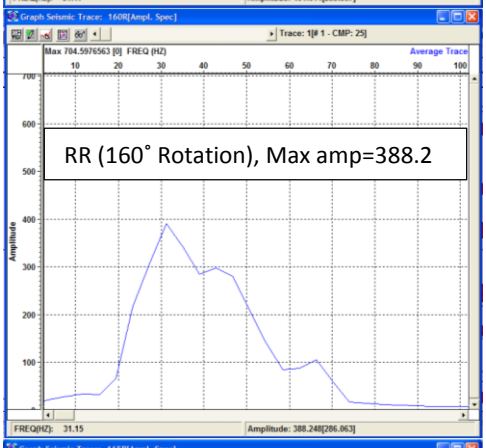

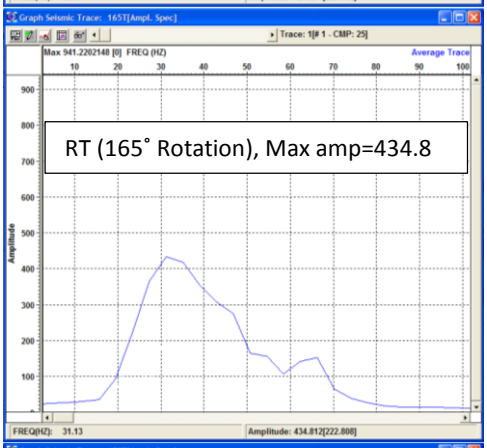

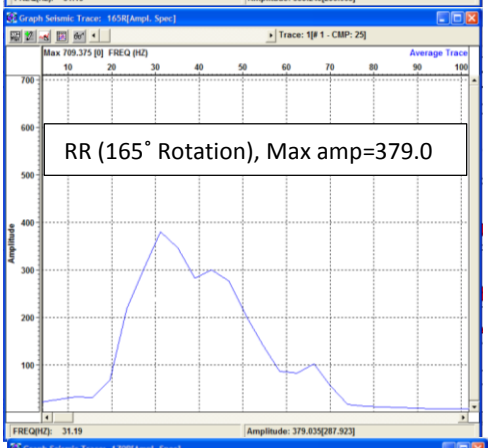

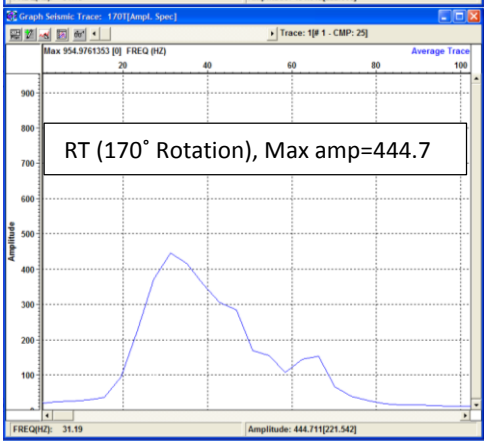

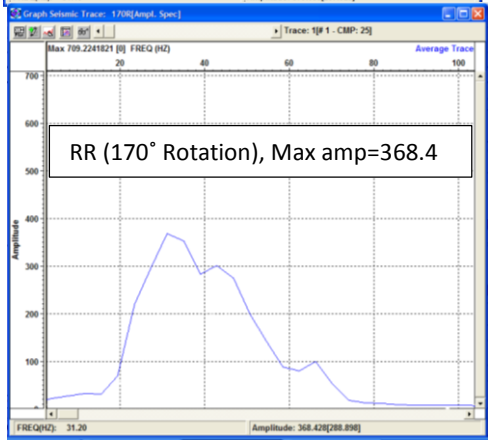

Appendix G-2: Continued

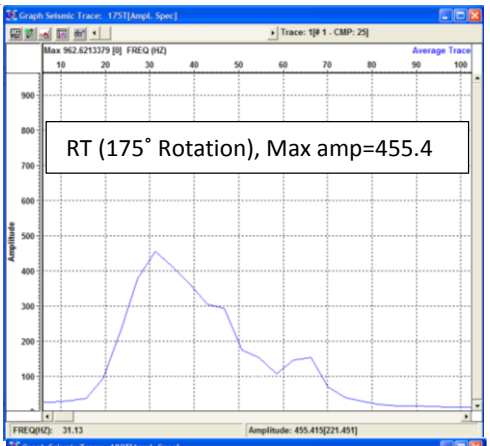

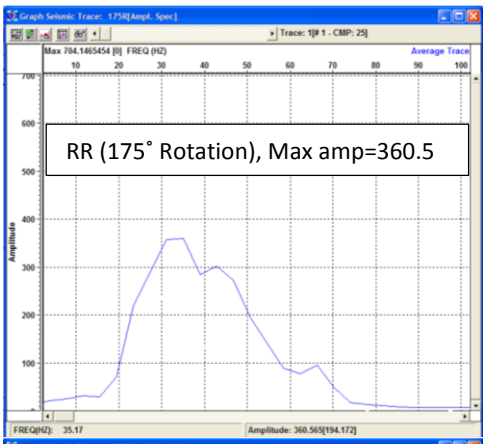

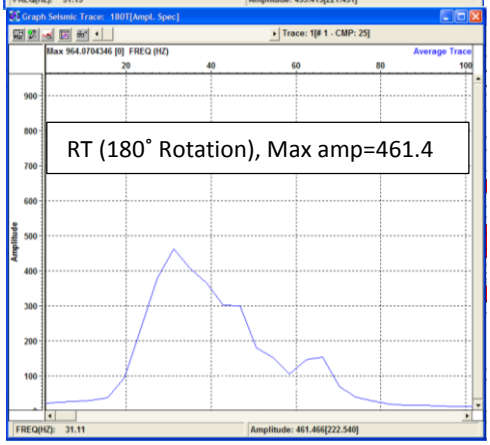

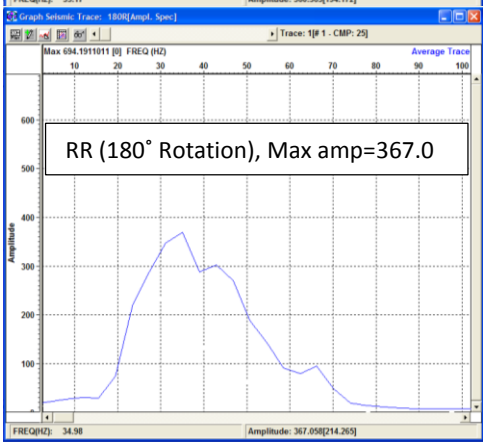

VITA

Ali Z. Almayahi

EDUCATION

Fall 2008-Fall 2009	Missouri University of Science and Technology, Rolla, MO Six classes (Coursework only) Geophysics related GPA: 4.0/4
June 2002	University of Baghdad, Baghdad, Iraq M.Sc. Degree in Seismic Exploration GPA 82.6/100 Master's thesis title: Seismic Data Processing Directed Toward Stratigraphic interpretation
August 1999	University of Basra, Basra, Iraq B.Sc. Degree in Geology GPA 74.5/100

SELECTED PUBLICATIONS

Almayahi, A. Woolery, E. Hampson, S., 2011, SH-Wave Imaging of Near-Surface Geologic Controls on Contaminant Plume Migration — Fluorspar Area Fault Complex, Western Kentucky USA. In preparation to be submitted to Journal of Applied Geophysics.

Woolery, E. and Almayahi, A., 2013, Near-Surface SH-Wave Reflection and Birefringence Applications for Fault Assessment in Unlithified Sediment, Central United States: accepted abstract at SSA annual meeting.

Kursheed, S., Alkarasan, E., Almayahi, A., 2007, P- and S- waves Evaluation for Engineering Site Investigation of a Hostel Complex Inside Basra University, Southern Iraq. Basra Journal of Science, no. 483A.

Almayahi, A., Abass, N., and Alhadad, F., 2005, Seismic Signal Processing Directed Toward Stratigraphic Interpretations. Basra Journal of Science, no. 423A. (From master thesis).

LANGUAGE SKILLS

Arabic: Native Language
US English: Speaking: Fluently, Writing: Very good

HONORS

Delta Epsilon Iota, Academic Honor society, 2011- present

ORGANIZATIONS MEMBERSHIPS

*Society of Exploration Geophysicists (**SEG**)*
*American Association of Petroleum Geologists (**AAPG**)*
*American Geophysical Union (**AGU**)*
*The Geological Society of America (**GSA**)*
Society of Petroleum Engineers (**SPE**)